INAUGURAL – DISSERTATION

zur

zur Erlangung der Doktorwürde

der

Gesamtfakultät für Mathematik, Ingenieur- und Naturwissenschaften

der Ruprecht-Karls-Universität

Heidelberg

Vorgelegt von

Flora Kluge

Geboren in: Aachen, Deutschland

Tag der mündlichen Prüfung: 21.10.2022

Airborne glyoxal measurements in different regions of the globe: Its atmospheric fate, comparison with TROPOMI observations and EMAC simulations, and inferred biomass burning emission factors for glyoxal and methylglyoxal

Gutachter:

Prof. Dr. Klaus Pfeilsticker

Prof. Dr. Thomas Wagner

Zusammenfassung

Anhand von 72 Messflügen des Forschungsflugzeuges DLR HALO im Zeitraum 2014 bis 2019 wurden weltweite troposphärische Messungen von Glyoxalkonzentrationen und vertikalen Säulendichten (VCDs) durchgeführt. Über dem Amazonas Regenwald wird die Erprobung durch simultane Formaldehyd- und Methylglyoxalmessungen ergänzt. Die Glyoxal VCDs werden mit guter Übereinstimmung mit tagesaktuellen Satellitenmessungen des TROPOMI Instrumentes validiert und ein Vergleich mit globalen Glyoxalsimulationen des chemischen Transportmodelles (CTM) EMAC durchgeführt. Abweichungen von TROPOMI Glyoxalmessungen ergeben sich für Flugzeugbeobachtungen von Schadstoffwolken mit geringer räumlicher Ausdehnung sowie solche innerhalb der planetaren Grenzschicht. Letzteres führt insbesondere zu geringeren Glyoxalsäulendichten des Satelliteninstrumentes über Städte- und Industriezentren. Erhöhtes, bisher unerklärtes Glyoxal wurde wiederholt in gealterten Abgasfahnen von Biomassebränden sowie in marinen Reinluftgebieten der Tropen beobachtet. Über dem Regenwald werden Emissionsfaktoren für Regenwaldfeuer bestimmt (0.11–0.52 $\mathrm{g_{Glyoxal}\,kg_{fuel}^{-1}}$, 0.50–8.64 $\mathrm{g_{Methylglyoxal}\,kg_{fuel}^{-1}}$) sowie Isopren als potentielles Glyoxal- und Methylglyoxalvorläufergas oberhalb der planetaren Grenzschicht identifiziert. Der Vergleich mit EMAC zeigt deutlich höhere Glyoxalmessungen als die Simulationen in nahezu allen Regionen nahelegen, insbesondere in der planetaren Grenzschicht und Abgaswolken. Dies weist auf eine Unterschätzung der photochemischen Aktivität von Glyoxal und seinen Vorläufergasen durch EMAC hin, mit entsprechenden Konsequenzen für den Einfluss dieser Gase auf die troposphärische Oxidationskapazität sowie die Ozon- und sekundäre organische Aerosolbildung und damit auf den Strahlungstransport.

Abstract

Tropospheric glyoxal mixing ratios and vertical column densities were measured during 72 research flights with the German research aircraft DLR HALO over different regions between 2014 and 2019. Over the Amazon rainforest, the observations are complemented by simultaneous formaldehyde and methylglyoxal measurements. The glyoxal measurements are confirmed by same-day observations of the TROPOMI satellite instrument and compared to simulations of the photochemical transport model EMAC. Deviations of air- and spaceborne glyoxal are found for spatially small pollution plumes and those located near the surface. This causes smaller satellite glyoxal measurements around urban centres. Unexplained glyoxal enhancements are detected repeatedly in aged biomass burning plumes and the tropical marine boundary layer. Over the rainforest, emission factors are estimated for tropical forest fires (0.11–0.52 $\mathrm{g_{glyoxal}\,kg_{fuel}^{-1}}$, 0.50–8.64 $\mathrm{g_{methylglyoxal}\,kg_{fuel}^{-1}}$) and isoprene is identified as a potential glyoxal and methylglyoxal precursor above the boundary layer. The comparison to EMAC shows an underestimation of modelled glyoxal in most regions, especially in the boundary layer and pollution plumes. This is indicative of an underestimation of glyoxal and its precursors by EMAC, with consequences for the tropospheric oxidative capacity as well as the formation of ozone and secondary organic aerosols and hence for the radiative forcing.

Contents

Chapter 1

Introduction

Emissions of reactive trace gases into the atmosphere impact the photochemistry, the oxidation capacity and in particular the atmospheric burden of greenhouse gases. All these processes have direct or secondary impact on the radiative balance of the atmosphere and hence on the climate of the Earth. In the past (and coming) decades, anthropogenically induced changes in the atmospheric composition and photochemistry are expected to increasingly alter this radiative balance and hence the radiative forcing[1] of the climate system. To estimate the impact of these changes, in the past decades an increasing scientific effort has been put into understanding the atmosphere and its countless components, interactions, chemistry, and feedback-mechanisms. However, due to the enormous complexity of the atmospheric system and its multiple interaction cycles, major uncertainties still exist in many fields.

Among all trace gases, organic carbon compounds (VOCs[2]) are key atmospheric constituents that are highly reactive and largely impact the tropospheric photochemistry, in particular the formation of ozone, and the tropospheric oxidative capacity, i.e the formation and destruction of OH. Since many VOCs with carbon-oxygen double bonds are also considerably water soluble, they contribute via hydration and oligomerization to the formation of secondary organic aerosols (SOA). As a consequence, VOCs can have a direct influence on the radiative forcing through scattering and absorption of solar light, but likewise importantly, they exert an indirect effect by altering the concentrations and lifetimes of tropospheric ozone and organic aerosols. Due to the large variety of different VOCs and feedback mechanisms, the overall impact of VOCs on atmospheric photochemistry and climate forcing is still largely uncertain and many of the involved indirect climate feedback mechanisms are not yet fully understood (e.g. Seinfeld et al. [2016]; Sporre et al. [2019]; Zhu et al. [2019a]). It is therefore crucial to better understand anthropogenic and biogenic VOC emissions as well as their individual and combined impact on the atmospheric composition, photochemistry, and radiative forcing of the climate system.

This thesis aims at gaining further insight into the atmospheric abundance of the VOCs formaldehyde, glyoxal, and methylglyoxal in different air masses around the globe. All three gases are detectable by the applied Differential Optical Absorption Spectroscopy (DOAS) technique [Platt and Stutz, 2008] and important oxidation intermediates of VOCs, but many aspects of their atmospheric fate and hence their impact on the photochemistry of the troposphere are still

---

[1] Following the Fifth Assessment Report of the Intergovernmental Panel on Climate Change (IPCC), (effective) radiative forcing is defined as 'the change in net TOA [top of the atmosphere] downward radiative flux after allowing for atmospheric temperatures, water vapour and clouds to adjust, but with global mean surface temperature or a portion of surface conditions unchanged' [G. Myhre and Zhang, 2013].

[2] The term VOC is defined ambiguously: commonly, VOCs refer to all reactive chemicals that contain carbon-hydrogen or carbon-carbon bonds and quickly evaporate (high water vapour pressure at ambient temperature). The category VOCs hence combines a myriad of different organic compounds and can be further differentiated, e.g. into biogenically emitted VOCs (bVOC), non-methane VOCs (NMVOC), non-methane hydrocarbons (NMHC),or oxygenated VOCs (OVOC).

poorly understood.

Tropospheric ozone is a greenhouse gas that results predominantly from in situ photochemical production from the oxidation of methane and NMVOCs in the presence of NO_X ($NO + NO_2$; Logan [1985]; Sillman et al. [1990]; Monks et al. [2015]). For all these ozone forming trace gases, the atmospheric concentrations have continuously increased in the past decades due to anthropogenic activities [IPCC, 2001], even though this trend has started to slow down in the past decade as a result of global air pollution control measures [P.A. Arias, 2021]. The resulting increase of tropospheric ozone has a large impact on regional air pollution and thus on the global climate. Especially near the surface, elevated ozone not only impacts both air quality and human health [Lelieveld et al., 2015, 2019], but also affects vegetation and forest growth by inhibiting plant CO_2 uptake[3] [Heck et al., 1982; Sitch et al., 2007].

In addition, the atmospheric HO_X ($OH + HO_2$) concentration is largely controlled by surface VOC emissions and VOC photochemistry in the atmosphere. However, a significant fraction of the OH reactivity is still unknown and attributed to reactions with NMHCs [Yang et al., 2022]. In fact, the current lack of knowledge of VOC photochemistry and oxidation pathways of intermediate VOCs is one of the major uncertainties in quantifying the current day atmospheric oxidative capacity [Taraborrelli et al., 2012] and hence also its reaction to changing VOC emissions due to global warming. This significantly limits confident estimates on the current and future lifetime of major greenhouse gases like ozone or methane and thus on their radiative forcing [G. Myhre and Zhang, 2013; P.A. Arias, 2021]. Better knowledge of the concentrations and atmospheric fates of VOCs that act as OH sources and sinks and their development under a warming climate are therefore urgently needed.

As ozone both interacts with short- and longwave radiation, changes in the ozone distribution and concentration directly affect the radiative forcing of climate change. Tropospheric ozone dominates the total ozone impact on the radiative forcing with $0.4\ \mathrm{W\,m^{-2}}$ (0.2 to $0.6\ \mathrm{W\,m^{-2}}$) as of 2011[4] [Stevenson et al., 2013; G. Myhre and Zhang, 2013], even if only approximately 10% of the atmospheric ozone is actually located in the troposphere. Of the total radiative forcing of tropospheric ozone, current estimates attribute 9% of it to result from emissions of NMHCs (Fig. 2.8 and Stevenson et al. [2013]).

Besides their impact on atmospheric photochemistry, VOCs from both biogenic and anthropogenic emissions also contribute significantly to the formation of secondary pollutants like secondary organic aerosols (e.g. Went [1960]; Pandis et al. [1991]; Kroll and Seinfeld [2008]). As for ozone formation, the secondary organic aerosol (SOA) yield from VOCs is highly dependent on the individual chemicals, their concentrations, ambient conditions, and in particular on the presence of anthropogenic pollutants like ozone and nitrogen oxides (e.g. Seinfeld and Pandis [2013]; Camredon et al. [2007]).

After significant increases since pre-industrial records, conflicting findings exist for the overall trend of the atmospheric aerosol abundance in the past decades [P.A. Arias, 2021]. Organic aerosols have a significant cooling effect on the climate via scattering and absorption of incoming radiation and cloud formation or modification. Due to the large efforts to quantify the total radiative forcing of aerosols and in particular to differentiate the anthropogenic and natural fractions of the aerosol climate forcing, numerous studies have been performed to quantify the aerosol formation potential of individual VOCs (e.g. McCormick and Ludwig [1967]; Andreae [1995]; Hoffmann et al. [1997]; Mahilang et al. [2021]). However, due to its complexity and known

---

[3] Depending on the plant species, Heck et al. [1982] observed average crop yield reductions between 1% and 8% per 10 ppb ozone increase above 60 ppb over a 7 h time period.

[4] The latest IPCC estimate for the effective radiative forcing of tropospheric and stratospheric ozone combined is $0.47\ \mathrm{W\,m^{-2}}$ (1750–2019). To compare, the radiative forcing of atmospheric CO_2 is $2.0\ \mathrm{W\,m^{-2}}$ as of 2019 and the total 1750–2019 net anthropogenic radiative forcing of the atmosphere is estimated to be $2.72\ \mathrm{W\,m^{-2}}$ [P.A. Arias, 2021]

and unknown involved feedback mechanisms, large uncertainties still exist regarding the formation of secondary organic aerosol from VOCs [Carslaw et al., 2010; Hoyle et al., 2011; Mahilang et al., 2021; Fan et al., 2022].

In conclusion, organic carbon species have a significant and not yet sufficiently understood impact on the global atmospheric photochemistry and radiative forcing, and further investigation is required to better assess their current and future impact on the global climate.

Continuous global satellite observations of column integrated concentrations only exist for a few selected VOCs with unique optical properties (e.g. formaldehyde and glyoxal), but these satellite observations do not provide any altitude resolved information and have limited spatial resolution and coverage [Vrekoussis et al., 2009; Chan Miller et al., 2014, 2017; Lerot et al., 2021]. Due to the large variety of different VOCs and oxidation intermediates, systematic investigations on a global scale are still needed for many VOC species and overall indicate deficits in the simulation of VOC chemistry by current photochemical transport models (e.g. Stavrakou et al. [2009a]; Myriokefalitakis et al. [2008]; Liu et al. [2012]; McDonald et al. [2018]; Silva et al. [2018]; Zhu et al. [2019b]). This includes in particular unexplained observations of shorter-lived VOCs in aged pollution plumes, such as enhanced glyoxal concentrations in long-range transported biomass burning plumes (e.g. Alvarado et al. [2020]). Measurements of the transport, the composition and the evolution of fresh and aged plumes are however rare for many species, e.g. glyoxal and methylglyoxal [Andreae and Merlet, 2001; Akagi et al., 2011; Stockwell et al., 2015; Andreae, 2019]. Equally, the role of oceanic emissions of VOCs is still not well studied. Whether the micro-layer at the oceanic surface or the water body of the ocean is a source or sink for organic species is highly latitudinal, seasonal, temperature, biological composition, and species dependent [Guenther et al., 1995; Brüggemann et al., 2018]. Recent findings indicate an overall larger production of organic species in the ocean surface layer and transport therefrom into the atmosphere than previously assumed [Brüggemann et al., 2018; Rocco et al., 2021]. Whether rising sea surface temperatures increase or decrease the marine VOC emissions depends on the involved chemicals and ambient conditions, but estimates of their extent are still uncertain (e.g. Dayan et al. [2020]). In particular in the tropical regions, marine emissions of VOCs need to be better understood and quantified, because the efficient tropical convection may cause significant vertical transport of such VOCs up into the intertropical convergence zone (ITCZ[5]; Williams [2004]).

Overall, these findings hint at significant deficits in our current understanding of the photochemistry of VOCs and their individual precursors, source strengths, and fate in the atmosphere, with equal consequences for the formation of tropospheric ozone, organic aerosol, and OH from organic compounds. Insights into this matter require systematic and extensive field measurements of organic species close and far from their sources throughout the entire troposphere and comparison of the findings with up-to-date global photochemical transport models to assess differences between assumed oxidation pathways and real air oxidation chemistry as well as gas-to-particle partitioning.

The composition of the myriad of different VOCs in different atmospheric regimes (e.g. biogenic, anthropogenic, pristine or marine air) is highly variable [Altshuller, 1983; Miller and Moran, 1997; Atkinson, 2000; Volkamer et al., 2001; Friedfeld et al., 2002; Volkamer et al., 2005b]. However, many VOCs with carbon-hydrogen bonds oxidize at some point of their oxidation chain to formaldehyde, glyoxal, or methylglyoxal (e.g. Finlayson-Pitts and J. N. Pitts [1986]; Fu et al. [2008]). The three gases are the smallest atmospheric carbonyl compounds and have only minor direct emission sources as compared to their secondary formation during VOC oxidation. The detection of these three gases may thus provide insights into the distribution and burden of a

---

[5] The intertropical convergence zone is located approximately at 5° N. It marks a band of strong vertical convergence and surface winds [Goosse et al., 2010].

large range of precursor VOCs and the photochemical activity of the atmosphere. In particular, the precursor VOCs of glyoxal and methylglyoxal are among the most important ozone forming non-methane VOCs [Gu et al., 2021]. Due to its widespread distribution, the impact of glyoxal on the formation of ozone and organic aerosols has recently been the subject of great interest: different studies point to a larger and more widespread distribution of glyoxal both regionally as well as vertically than currently understood. The impact of glyoxal and its precursor VOCs in the atmosphere is therefore expected to be more important than previously assumed [Stavrakou et al., 2009b; Myriokefalitakis et al., 2008; Liu et al., 2012; Silva et al., 2018]. Recent unexplained observations of glyoxal in long-range transported biomass burning plumes as well as unexpected large glyoxal concentrations in the pristine marine boundary layer in the tropics further indicate an insufficient understanding and quantification of glyoxal and its precursor VOCs [Zhou and Mopper, 1990; Sinreich et al., 2010; Coburn et al., 2014; Mahajan et al., 2014; Lawson et al., 2015; Volkamer et al., 2015; Chiu et al., 2017; Alvarado et al., 2020; Walker et al., 2022].

The present thesis systematically investigates the global tropospheric glyoxal abundance based on concentration and simultaneous vertical column density (VCD) measurements from 72 worldwide flights of the research aircraft DLR HALO[6] between 2014 and 2019. The data represent the most extensive glyoxal data set yet with unique geographic and altitudinal coverage from several hundred meters altitude up to the lowermost stratosphere. The observations reach from the marine atmosphere over different oceans between 70° N down to 70° S as well as to the continental atmosphere over regions far from any anthropogenic activities, over large human agglomerations, during the local biomass burning seasons as well as to air masses negligibly, or in contrast, heavily affected by biogenic VOC emissions. Over one of the most photochemically active global regions, the Amazon rain forest, the glyoxal observations are complemented by simultaneous formaldehyde measurements and the first airborne observations of methylglyoxal throughout the troposphere over a tropical rainforest. Combined, the observations contribute to answering open questions on the photochemistry of the three smallest carbonyls in the boundary layer as well as the free and upper troposphere and give new insights into their potential impact on tropospheric ozone, oxidative capacity and organic aerosol formation.

Moreover, this thesis aims at gaining further insights into the following three scientific questions:

1. A thorough assessment of the global glyoxal abundance in rarely or even unexplored air masses. This includes in particular the marine and terrestrial background of glyoxal, the sources of glyoxal in the anthropogenically polluted atmosphere, potential marine emissions of glyoxal or its precursors from the ocean surface in different latitudes, the impact of biomass burning on atmospheric glyoxal in and above the boundary layers, and a thorough comparison of air- and spaceborne detection of glyoxal in all these different air masses.

2. The validation of recent reports of elevated glyoxal in aged biomass plumes by respective globally distributed observations and an analysis of the extent and occurrence of elevated glyoxal in the pristine marine troposphere in the tropics. Both observations suggest additional and yet unknown or underestimated glyoxal formation pathways, which may in part be responsible for the current deficits in the simulation of atmospheric glyoxal by current photochemical transport models both in emission plumes and in the background atmosphere [Myriokefalitakis et al., 2008; Stavrakou et al., 2009a; Lerot et al., 2010].

3. The transport of isoprene oxidation products and ozone precursors from the boundary layer into the tropical free and upper troposphere in low HO_X–low NO_X–high VOC regimes

---

[6] `https://www.HALO.DLR.de/`

dominated by biogenic emissions (Amazon rainforest) and the impact of biomass burning in these regions on their atmospheric profiles.

Further, the glyoxal data analysed within the framework of the present thesis are used in a complementary modelling study by our collaborators from the FZ Jülich (D. Taraborrelli and S. Rosanka, work in progress as of August, 2022) to re-establish the global budget of glyoxal and to unravel its major precursor molecules and their source regions.

The thesis is organized as follows. Chapter 2 provides additional background information on the studied trace gases and the most relevant processes determining their atmospheric fates. Chapter 3 describes the mini-DOAS instrument and the corresponding measurement technique as well as additional instruments and photochemical transport model simulations involved in the analysis. Chapter 4 reports on the deployment and measurements of the mini-DOAS instrument on eight missions of the HALO research aircraft into different global regions between 2014 and 2019 and the complementary spaceborne glyoxal measurements. Chapter 5 presents the airborne mixing ratio and vertical column density (VCD) measurements of glyoxal in different regions all around the globe with particular focus on the tropical rainforest, where the observations are complemented by simultaneous formaldehyde and methylglyoxal measurements. The glyoxal VCDs are compared to collocated total atmospheric column density observations of glyoxal from the TROPOMI satellite instrument. Further, both airborne data sets of glyoxal mixing ratios and VCDs, are compared to simulations of the global ECHAM/MESSy Atmospheric Chemistry model. Chapter 6 discusses the major findings and results and chapter 7 concludes and summarises the thesis.

Chapter 2

Tropospheric photochemistry

The terrestrial atmosphere is the transition zone between the planetary surface and space. It is fundamental for life on earth and extends from the surface up to $10^2 - 10^6$ km altitude[1]. The present thesis focuses on the physics and photochemistry of the lowest part of the atmosphere, the troposphere. It reaches from the surface to the next atmospheric layer, the stratosphere. The altitude of the transition zone in between, the tropopause, varies depending on the season, latitude, and its exact definition. Following the World Meteorological Organisation (WMO) 1957 definition, the bottom level of the tropopause is the lowest altitude at which the temperature lapse rate[2] decreases to 2 $\mathrm{K\,km^{-1}}$ and it extends over the entire layer in which the temperature does not change more than 1 $\mathrm{K\,km^{-1}}$ [Meteorology, 1957]. The tropopause is located at $\sim$ 8 km (at the poles) and $\sim$ 16 km (at the equator) altitude above the surface. The troposphere and stratosphere are inherently different regarding their chemical, physical, and dynamical characteristics. The troposphere is characterised by a large temperature lapse rate, i.e. a quick change of the air temperature with altitude. Accordingly, it is a zone of low vertical stability and is a highly dynamic mixing and transport layer [Goosse et al., 2010].

The following chapter provides an overview of the aspects of tropospheric photochemistry that are relevant for the present thesis. This includes details on the formation and climate relevance of tropospheric ozone, the atmospheric oxidation capacity, and the impact of VOCs in the atmosphere. Special emphasis is put on the trace gases formaldehyde, glyoxal, and methylglyoxal, which are the focus of this thesis. The sources, sinks, and photochemical and climate importance of these gases, in particular with respect to their potential as secondary organic aerosol precursors, is discussed.

2.1 Ozone and oxidative capacity

Emissions of gaseous compounds from the Earth's surface into the atmosphere and their subsequent removal from it form a continuous photochemical cycle. Without this decomposition, the gases would accumulate in the atmosphere and no quasi steady-state could evolve. The two main atmospheric removal processes of trace gases are light-initiated photolysis and their reaction with

---

[1] The transition between the atmosphere and space is not unambiguously defined. There is no distinct boundary of the atmosphere, it rather fades out continuously into space. Up to $\sim$ 100 km altitude, particles experience gravitation and are homogeneously mixed (homosphere). At higher altitudes, no mixing occurs and the molecules increasingly escape into space (heterosphere).

[2] The temperature lapse rate refers to the rate of change of the air temperature with increasing atmospheric altitude. In the troposphere, the air is the warmest above the planetary surface and the air temperature decreases continuously at higher altitudes with a positive lapse rate of $\sim$ 6.5 $\mathrm{K\,km^{-2}}$ (depending on horizontal heat transport, season, latitude, and convection); Goosse et al. [2010]). In the stratosphere, this gradient is reversed and the temperature increases with altitude (negative lapse rate). This is largely a result of the absorption of shortwave radiation by the ozone layer.

hydrogen radicals, in particular with the hydroxyl radical (OH). For sufficiently water-soluble species, dry and wet removal by aerosol and cloud particles is a further important process. The efficiency of the reaction of gases with OH is described by the so-called oxidative capacity of the atmosphere. It quantifies how efficiently trace gases are removed from the atmosphere by oxidation. This makes the entire photochemistry of Earth's atmosphere and its radiative balance highly dependent on hydrogen radicals. As a major oxidation pathway for VOCs [Levy, 1971], OH plays a key role in atmospheric ozone and organic aerosol formation and largely controls the atmospheric lifetime and abundance of VOCs, such as methane, and hence their impact on the radiative forcing.

Ozone is an important atmospheric oxidant and greenhouse gas. The predominant fraction is located in the stratosphere between 20 and 60 km altitude, where it absorbs harmful ultraviolet radiation. However, ozone is also present in the troposphere [Hartley, 1881; Chapman, 1942], where it is part of a complex and tightly coupled photochemical system of NO_X, CO, VOCs, and hydrogen radicals [Fishman and Seiler, 1983]. Tropospheric ozone impacts the climate forcing by acting as a greenhouse gas and by participating in the formation of secondary aerosols, and is toxic to humans as well as to the ecosystem [Monks et al., 2015; Wallington et al., 2019; Archibald et al., 2020].

Tropospheric ozone partly results from the stratosphere–troposphere exchange, with a net transport of ~ 340 [3]$\mathrm{Tg\,y^{-1}}$ into the troposphere [Wang and Fu, 2021]. However, over ~ 10 times more ozone is formed during photochemical reactions in the troposphere with a yearly net production of 5000 Tg [Hartley, 1881; Chapman, 1942; Young et al., 2013; Monks et al., 2015]. When accounting for dry and wet deposition and chemical loss processes, the global tropospheric ozone burden is $\sim 335 \pm 10$ Tg, however with a large spatial inhomogeneity [Monks et al., 2015]. Globally, the tropospheric ozone concentration has increased by 30% (30–70% in the northern hemisphere) since the pre-industrial records with large seasonal and latitudinal variations [P.A. Arias, 2021]. Consequently, its impact on radiative forcing has steadily increased to 0.4 $\mathrm{W\,m^{-2}}$ as of 2010 (Fig. 2.1). Since the pre-industrial era (1750), northern hemispheric background ozone has increased by ~ 30 ppb [4] (1–5 $\mathrm{ppb\,decade^{-1}}$; Cooper et al. [2014]) up to 80 ppb near the surface during summer [IPCC, 2001]. Even higher mixing ratios are found in urban regions and during heat waves, e.g. over Berlin [Churkina et al., 2017]. The positive trend of tropospheric ozone concentrations during the past century is mainly a result of enhanced emissions of its two main precursors NO_X and VOCs [Crutzen, 1988; Sillman, 1999]. In fact, in situ production of ozone in the troposphere was firstly recognized due to the significant ozone concentrations in the photochemical smog around Los Angeles in the 1940's caused by the photo-oxidation of NMVOCs [Haagen-Smit et al., 1952; Crutzen, 1988]. Due to the dependence on VOCs, the average tropospheric ozone production is largest in regions with constantly high VOC emissions, in particular in the tropics, and especially during the tropical dry season. During this period, extended biomass burning activities cause additional large enhancements in VOC and NO_X emissions.

The main photochemical ozone source in the troposphere is photolysis of NO_2. In fact, during the daytime ozone and NO_X convert to each other and form a photochemical equilibrium [Leighton, 1961]:

NO_2 quickly photolyses ($j \approx 10^{-2}\ \mathrm{s^{-1}}$ [Parrish et al., 1983]) producing a ground electronic state oxygen atom,

$$\mathrm{NO_2 + h\nu \rightarrow NO + O(^3P)}, \tag{2.1}$$

---

[3] $1\ \mathrm{Tg} = 10^{12}\ \mathrm{g}$

[4] $1\ \mathrm{ppb_v} = 10^{-9}\ \mathrm{v\,v^{-1}}$

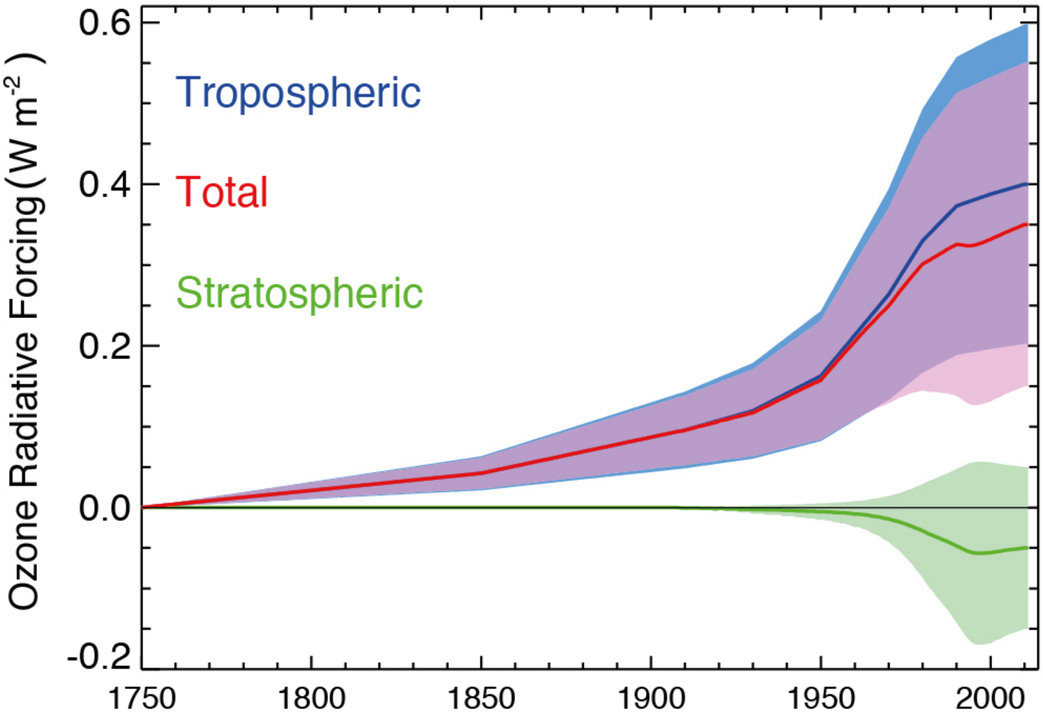

Figure 2.1: Radiative forcing of tropospheric and stratospheric ozone from 1750 to 2010. Figure taken from G. Myhre and Zhang [2013].

that recombines in a three-body reaction with molecular oxygen to form ozone

$$O^3P + O_2 + M \rightarrow O_3 + M, \tag{2.2}$$

with M being an arbitrary additional collision partner. At the same time, NO from NO_2 photolysis titrates O_3 and re-forms NO_2 according to

$$O_3 + NO \rightarrow NO_2 + O_2 \tag{2.3}$$

[Tan et al., 2018]. This closed NO_X–O_3–system without a net loss or gain of its components (during daytime) is disturbed by the presence of hydroxyl and organic peroxy radicals (HO_2 and RO_2). They cause additional NO–NO_2–conversion processes and hence a net O_3 gain or loss (via removal of molecular oxygen without production of O_3, e.g. $NO_2 + OH \rightarrow HNO_3$). In fact, the concentration and distribution of HO_X radicals is tightly coupled to those of ozone, VOCs and nitrogen oxides. This so called O_3–NO_X–VOC–sensitivity is discussed in detail in the following.

The main tropospheric source of hydroxyl radicals (OH) is the photolysis of ozone,

$$O_3 + h\nu_{\leq\lambda<320\ \mathrm{nm}} \rightarrow O(^1D) + O_2(^1\Delta_g), \tag{2.4}$$

and reaction of $O(^1D)$ with H_2O,

$$O(^1D) + H_2O \rightarrow OH + OH \tag{2.5}$$

[Bates and Nicolet, 1950; Levy, 1971; Seinfeld and Pandis, 2013; P.A. Arias, 2021]. Secondary OH sources and reactions exist, but a large fraction is still poorly understood and quantified, e.g. OH production during OH-initiated isoprene oxidation [Taraborrelli et al., 2012]. Despite these uncertainties, latest estimates of global OH report an overall stable (or slightly positive) abundance [P.A. Arias, 2021]. Among others, additional OH sources are formaldehyde from methane oxidation as well as acetone and hydrogen peroxide. Depending on the local NO_X level, OH mostly reacts with CO (reaction 2.7) and methane (to H_2O and CH_3O_2) and ultimately acts as an ozone sink (at low NO_X), or ozone source (at high NO_X)[5]. The presence of NMVOCs in the air complicates this reaction scheme via additional O_3 formation. Briefly summarized, this additional ozone formation pathway consists of (1) oxidation of VOCs or CO via OH,

$$RH + OH(+O_2) \rightarrow RO_2 + H_2O, \tag{2.6}$$

or

$$CO + OH \rightarrow CO_2 + H \tag{2.7}$$

and subsequently

$$H + O_2 + M \rightarrow HO_2 + M. \tag{2.8}$$

(2) Conversion of NO to NO_2 and reformation of OH via the resulting hydroxyl/organic peroxy radical,

$$RO_2 + NO \rightarrow \text{secondary } RO + NO_2, \tag{2.9}$$

$$RO + O_2 \rightarrow R_{-H}O + HO_2, \tag{2.10}$$

and/or

$$HO_2 + NO \rightarrow NO_2 + OH \tag{2.11}$$

[Orlando and Tyndall, 2012; Fittschen, 2019], (3) photolysis of NO_2 producing a single oxygen atom, and (4) recombination of the oxygen atom with molecular oxygen forming O_3 according to reactions 2.1 and 2.2 (e.g. [Monks, 2005]). This reaction cycle of ozone formation competes with loss processes of hydrogen radicals, e.g. via

$$OH + NO_2 + M \rightarrow HNO_3 + M. \tag{2.12}$$

Consequently, VOC initiated NO–NO_2 conversion leads to O_3 formation without simultaneous O_3 destruction as in reaction 2.3. However, the different reaction cycles and the VOC–NO_X–O_3–coupling also depend on the VOC species involved, and on ambient conditions (e.g. temperature and humidity; Sillman and He [2002]). In the atmospheric regimes that are dominated by biogenic emissions, i.e. high bVOC and low NO_X levels, HO_X removal occurs via HO_X–HO_X reactions and is insensitive to NO_2. Under these conditions, the local NO_X concentration controls the ozone yield from VOCs (NO_X limited regime). Increasing NO_X concentrations then lead to increases in ozone, but changing VOC concentrations have little impact on ozone formation (Fig. 2.2, bottom right corner). In highly polluted regions with very high NO and low VOC concentrations, O_3 titration via reaction 2.3 causes net O_3 to NO_2 conversion, which can be outweighed by additional O_3 formation from VOC oxidation (VOC limited; Fig. 2.2, upper left corner). For mixed polluted regimes (NO_X–VOC–ratio along the diagonal in Fig. 2.2), O_3 formation increases both with increasing NO_X and VOC concentrations.

In the remote and upper troposphere, methane oxidation via formaldehyde production is the most important secondary O_3 source. This is a result of the long methane lifetime of ~ 12 years and the corresponding long-range transport far from its emission sources [Council et al., 1992] in combination with its generally high (and increasing) atmospheric mixing ratio of ~ 1909 ppb as

---

[5] A detailed description of atmospheric HO_X photochemistry can be found e.g. in Wennberg et al. [1998]; Monks [2005].

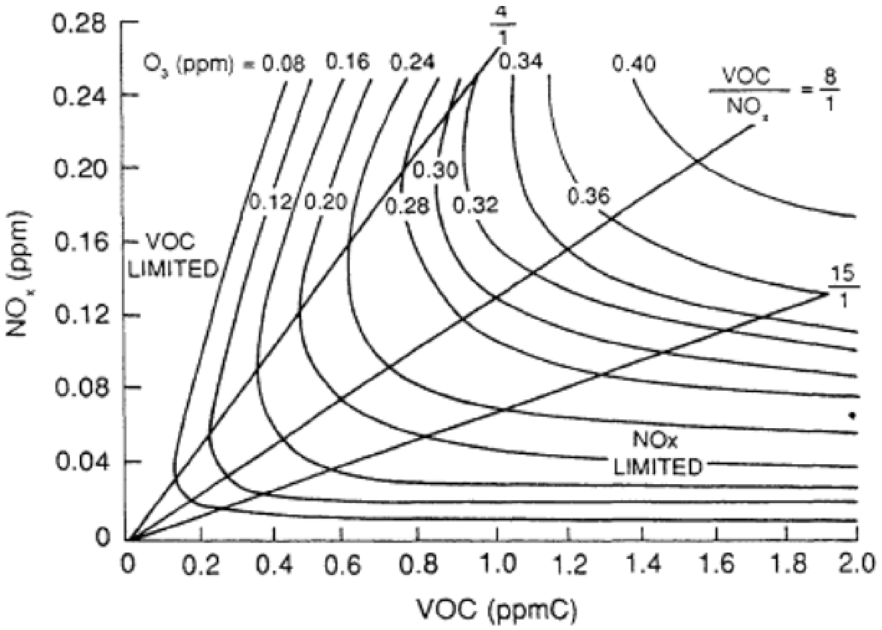

Figure 2.2: NO_X–VOC–O_3-coupling in the troposphere. For $\frac{\text{VOC}}{\text{NO}_\text{X}} < \frac{8\text{ ppb C}}{1\text{ ppb}}$ (left of the central diagonal), ozone (O_3) formation is limited by the VOC budget (VOC sensitive regime), for $\frac{\text{VOC}}{\text{NO}_\text{X}} > \frac{8\text{ ppb C}}{1\text{ ppb}}$ (right of the central diagonal), O_3 formation is limited by the NO_X concentration (NO_X sensitive regime). The threshold between the regimes can be approximated by the involved rate coefficients (see text). The isopleths (black curves) show constant maximum O_3 mixing ratios that can result from the given NO_X–VOC mixtures. VOCs are expressed in units of their carbon equivalent (ppm C or ppb C). Figure taken from Council et al. [1992].

of February 2022 [6]. In biogenically or anthropogenically polluted air masses, NMVOCs dominate the VOC impact on ozone formation. The oxidation of NMVOCs is highly complex and produces thousands of partially oxidised intermediates [Carter and Atkinson, 1996; Aumont et al., 2005]. In fact, organic species account for 14.000 of the $\sim$ 17.000 reactions in the latest version of the Master Chemical Mechanism [Jenkin et al., 2015]. VOC chemistry and oxidation is consequently a key process in atmospheric photochemistry and uncertainties in the RO_2 chemistry are reflected in estimates of ozone [Dibble, 2008], SOAs (sect. 2.3), and also have significant impacts on the HO_X–NO_X photochemistry. Better knowledge of VOC oxidation and measurements of its oxidation products in the atmosphere are therefore crucial to better assess their individual and combined impact on the atmospheric OH reactivity in the present and under a changing atmospheric composition and climate [Yang et al., 2022].

2.2 Volatile organic compounds

In the troposphere, the degradation of volatile organic compounds in the presence of NO_X leads to the formation of secondary gaseous and particulate products [Calvert, 1976]. Important products of the coupled NO_X–VOC photochemistry are tropospheric ozone (O_3) and secondary organic aerosols (SOA). Both impact air quality, the climate system, and in particular the radiative forcing. The degradation of the numerous photochemical reactions of atmospheric VOCs is highly complex and depends on numerous feedback mechanisms [Atkinson et al., 2004, 2006]. However, there are several small hydrocarbons that are intermediate oxidation products of many larger VOCs and only have minor or negligible alternative emission sources. Therefore, they can be used as proxies for the long chain precursors VOCs and give a handle on their atmospheric

---

[6] `https://gml.noaa.gov/ccgg/trends_ch4/`; last access: June, 2022.

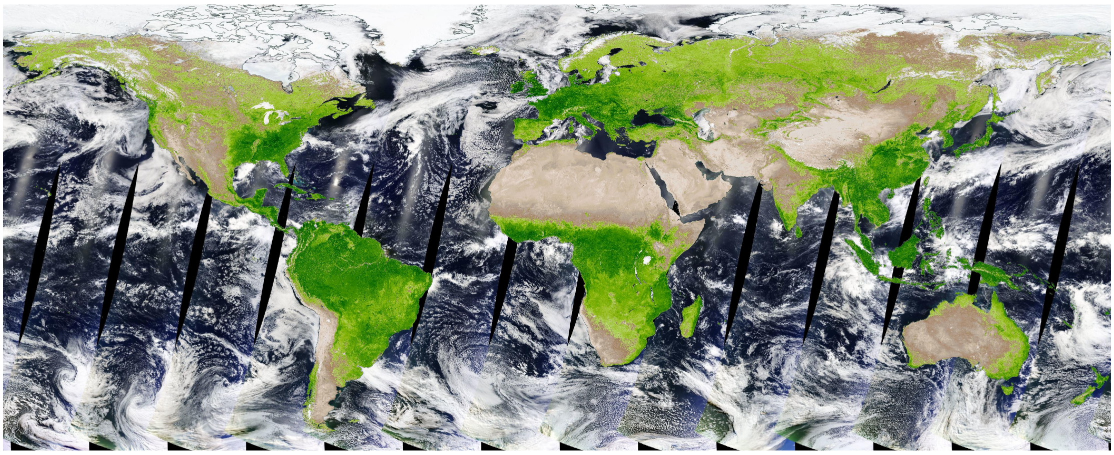

Figure 2.3: Global vegetation index provided by the MYD13A3 v061 MODIS/Aqua Vegetation Indices Monthly L3 Global 1 km SIN Grid classification scheme [Didan, 2021] for May 2022. The colour scale ranges from no/few vegetation (brown) to high vegetation (dark green). Figure created with NASA Worldview (`https://worldview.earthdata.nasa.gov/`).

emissions and fates, and on the atmospheric VOC–NO_X–HO_X cycle [Fried et al., 1997]. Such VOCs are formaldehyde, glyoxal, and methylglyoxal [Calvert et al., 2002; Myriokefalitakis et al., 2008; Luecken et al., 2012], which this thesis focuses on.

2.2.1 Isoprene

The largest common precursor VOC of formaldehyde, glyoxal, and methylglyoxal is isoprene (C_5H_8). Globally, isoprene oxidation is believed to account for 47% of the atmospheric glyoxal and 79% of methylglyoxal. While methane oxidation dominates the formaldehyde formation in the background and upper troposphere, 67% of the boundary layer formaldehyde is thought to result from isoprene oxidation [Lee et al., 1998; Fu et al., 2008; Wennberg et al., 2018]. Accordingly, the global patterns of formaldehyde, glyoxal, and methylglyoxal are expected to be similar to that of isoprene (Fig. 2.4).

Isoprene is a biogenic VOC, which is almost exclusively emitted into the atmosphere by vegetation. With yearly emissions of ~ 350 Tg, isoprene is the most prevalent NMVOC. It alone accounts for roughly one third of the global bVOC emissions. As isoprene is purely biogenically emitted, its concentration in the atmosphere is the largest over regions with dense vegetation (compare Figs. 2.3 and 2.4). Owing to the high complexity of their oxidation and interaction pathways, such biogenic VOC emissions represent one of the major uncertainties in estimates of the regional and global tropospheric O_3 concentrations [Archibald et al., 2011]. However, it is generally acknowledged that their potential as O_3 precursors is significant [Fiore et al., 2011; Hewitt et al., 2011; Situ et al., 2013; Tagaris et al., 2014]. In the rural northern hemisphere, O_3 was found to increase by as much as 11% when accounting for bVOC emissions [Zare et al., 2014]. In urban regions, bVOC emissions are responsible for a highly variable fraction between 6 and 60% of the elevated ozone, depending on the ambient conditions and anthropogenically emitted VOC species [Churkina et al., 2017]. Lee et al. [2014] even reported an O_3 increase of ~ 37 ppb due to bVOC emissions in the urban region of Shanghai. The same applies to anthropogenic VOC emissions [Dalsøren et al., 2018].

Globally, the Amazon rainforest is the largest source region of isoprene with mixing ratios exceeding 6 ppb in the boundary layer by the end of the dry season [Gu et al., 2017; Fu et al., 2019]. Uncertainties in the isoprene O_3 yield therefore have significant effects in particular in the tropics, where isoprene accounts for 30–50% of the bVOC emissions [Guenther et al., 1995]. Isoprene is

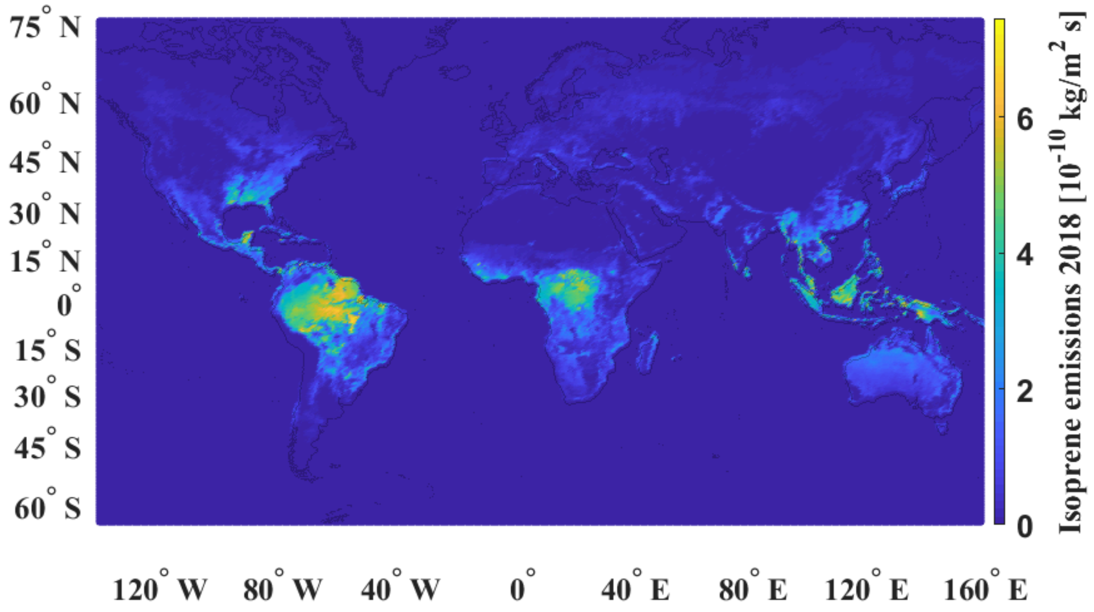

Figure 2.4: Yearly averaged MEGAN-MOHYCAN isoprene emissions (ALBERI dataset) at 0.5° × 0.5° resolution for 2018 [Opacka and Müller, 2021]. Data taken from `https://emissions.aeronomie.be/index.php/bottom-up/isoprenev2021`, last access: June, 2022. The global isoprene emission pattern is strongly correlated to the primary production of vegetation (Fig. 2.3). Clearly visible are the isoprene emission hotspots over tropical forests, in particular over the Amazon basin.

highly reactive and quickly oxidises in the atmosphere. Its atmospheric abundance is therefore generally limited to lower altitudes. However, depending on the local NO_X concentrations, the lifetime of isoprene may range from 4 h (global average) up to 36 h over the Amazon rainforest. In that region, Fu et al. [2019] suspected unusually low NO_X and high isoprene concentrations to lead to low OH, which prohibits efficient oxidation. This finding is of particular importance in the tropics, where convection enables efficient vertical transport. In particular over the Amazon rainforest, the potentially longer lifetime of isoprene may cause its transport into higher altitudes than otherwise possible. Such vertically transported isoprene in the free troposphere could be a significant in situ source of its oxidation products, e.g. glyoxal and methylglyoxal. Based on model simulation, Paulot et al. [2012] estimated 20% of the tropical isoprene to be oxidised in the free troposphere and not within the boundary layer. This is a matter of concern, since the lifetime of O_3 is significantly longer in the free and upper troposphere than in the boundary layer (6 vs 105 days [Jacob et al., 1996]), where bVOC photo-oxidation is usually located. Due to the longer lifetime, the climate forcing of O_3 from potential isoprene oxidation in the free troposphere is significantly larger than the radiative forcing of boundary layer ozone [Paulot et al., 2012]. The rapid urbanisation of the tropics and enhanced agricultural activities may significantly enlarge this phenomenon due to increasing NO_X emissions into extremely bVOC rich airmasses [Paulot et al., 2012]. Consequences of this development include changes of the radiative forcing of O_3, but also of air quality and crop yield [Sitch et al., 2007; Van Dingenen et al., 2009]. Previous studies on the tropical isoprene-O_3-chemistry are to the best of the author's knowledge mostly based on model simulations [Roelofs and Lelieveld, 2000; Pfister et al., 2008; Paulot et al., 2012] and space borne measurements of formaldehyde vertical columns [Barkley et al., 2008, 2013; Palmer et al., 2003]. However, under low NO_X conditions, formaldehyde cannot be linked directly to isoprene emissions [Paulot et al., 2012; Barkley et al., 2013; Wolfe et al., 2016; Wennberg et al., 2018]. Methylglyoxal on the other hand is believed to result to $\sim 80\%$ from isoprene oxidation [Fu et al., 2008]. Field measurements of isoprene oxidation products , such as methylglyoxal or glyoxal, in the free or even upper troposphere both over the remote tropical forest and in vicinity to urban centres are therefore needed to better assess the impact of isoprene oxidation in the free troposphere on O_3 formation and the potential consequences of current and future anthropogenic activities on this system.

2.2.2 Formaldehyde

Formaldehyde (CH_2O) is a partially oxygenated organic compound that is ubiquitous in the atmosphere. It is secondarily formed during the oxidation of methane [Jaeglé et al., 2001] and NMVOCs [Pfister et al., 2008], and to a lesser degree directly emitted by fossil fuel combustion [de Serves, 1994], biomass burning [Lee et al., 1997], and vegetation [Kesselmeier et al., 2002; Lathiere et al., 2006]. Formaldehyde is one of the pre-final oxidation products of many longer chained VOCs. It is therefore a measure for both the photochemical activity as well as emissions or transport of most hydrocarbons. Oxidation of methane is the main atmospheric formaldehyde source. Due to its long lifetime, methane is distributed in all tropospheric altitudes and global regions. Its oxidation,

$$\mathrm{CH_4 + OH \rightarrow CH_3 + H_2O} \tag{2.13}$$

produces a methyl CH_3 radical, which reacts with molecular oxygen to the methyl peroxy radical,

$$\mathrm{CH_3 + O_2 + M \rightarrow CH_3O_2 + M.} \tag{2.14}$$

Atmospheric CH_3O_2 can react with various species, including with itself, NO, HO_2, or ClO, e.g. directly producing formaldehyde and methanol

$$\mathrm{CH_3O_2 + CH_3O_2 \rightarrow CH_2O + CH_3OH + O_2.} \tag{2.15}$$

Methanol equally oxidises to formaldehyde by reaction with OH. There are numerous possible methane oxidation pathways, all of which end with the production of formaldehyde from the carbon atom of methane [Brasseur and Solomon, 2005a]. Methane oxidation therefore causes a constant ubiquitous formaldehyde background on the order of several 10 ppt in steady-state equilibrium at daytime [Jaeglé et al., 2001; Brasseur and Solomon, 2005b]. Methane oxidation to formaldehyde is particularly important in the pristine and upper troposphere, where no or few additional formaldehyde sources are present [Fried et al., 2008]. In biogenically or anthropogenic emission affected air masses and in the planetary or marine boundary layer, surface emissions and NMVOC precursors are a significant additional formaldehyde sources [Palmer et al., 2003; Pfister et al., 2008; Stavrakou et al., 2009b]. As a consequence, atmospheric formaldehyde concentrations are the largest over regions with high biogenic emissions, e.g. tropical rainforests, and over industrial hotspots, e.g. the Italian Po Valley. Globally, the largest NMVOC source of formaldehyde is isoprene emissions from plants [Palmer et al., 2003, 2006; Pfister et al., 2008].

Formaldehyde is quickly removed from the atmosphere to approximately equal parts via photolysis and oxidation with the hydroxyl radical (OH) or to a lesser degree oxidation with the nitrate radical (NO_3; Cooke et al. [2010]). During daytime, the atmospheric lifetime against photolysis or oxidation is on the order of 1–2 h only [Logan et al., 1981]. Photolysis of formaldehyde either directly forms CO,

$$\mathrm{CH_2O + h\nu \rightarrow H_2 + CO} \tag{2.16}$$

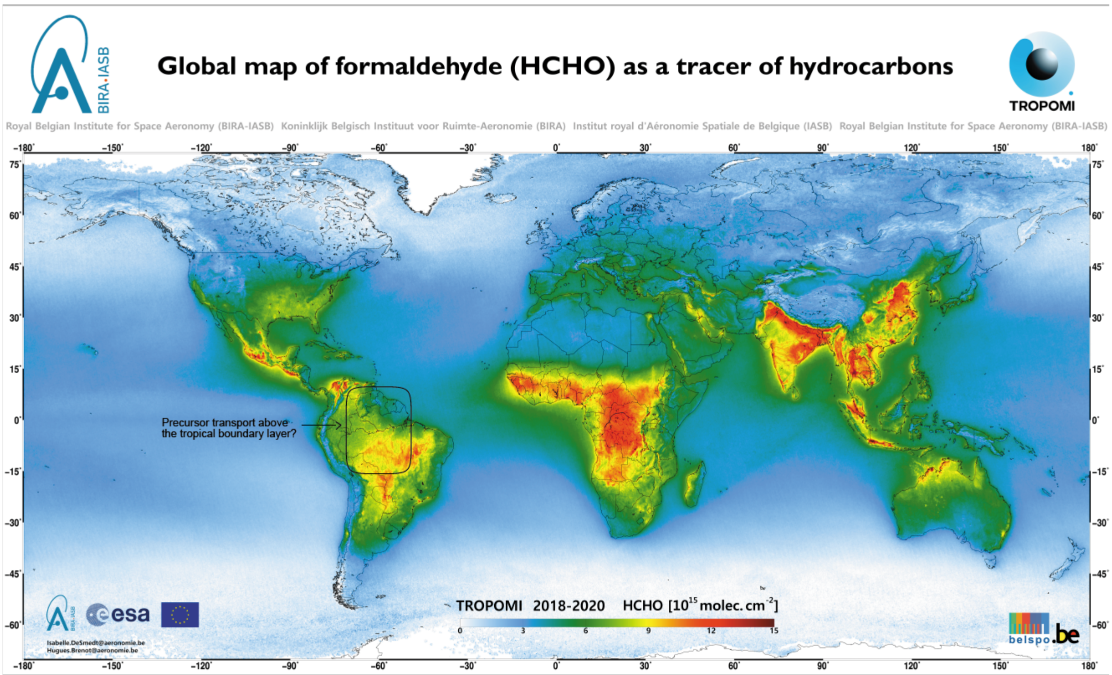

Figure 2.5: Global map of TROPOMI formaldehyde VCD measurements between 2018 and 2020 (3 years average). The black square marks the region and scientific scope of the present formaldehyde measurements. Figure taken from `https://uv-vis.aeronomie.be/data/TROPOMI_posters/`, last access: June 2022. Copyright: Contains modified Copernicus Sentinel data (2018-2020)/processed by BIRA-IASB.

or the hydroperoxyl radical (HO_2) via H and HCO,

$$CH_2O + h\nu \rightarrow H + HCO. \tag{2.17}$$

The HCO radical is quickly converted to CO and either H or HO_2 by photolysis or reaction with O_2 (e.g. Brasseur and Solomon [2005a]). Reaction of H and HCO with O_2 yields two hydroperoxyl radials (HO_2) per formaldehyde molecule. HO_2 reacts to OH in the presence of O_3 and NO. At high solar zenith angles, when $O(^1D)$ formation by O_3 photolysis is inefficient, formaldehyde is therefore one of the major atmospheric OH sources. This is in particular the case in the upper troposphere, where formaldehyde is an important HO_X source due to its constant background formation from methane oxidation [Logan et al., 1981; Wennberg et al., 1998] and upwards transport [Fried et al., 2008]. The latter is of particular importance in the tropical upper troposphere, where deep tropical convection causes efficient upwards transport of HO_X precursors like formaldehyde or formaldehyde precursors [Jaeglé et al., 2001]. In fact, mixing ratios on the order of 70 ppt formaldehyde were observed in the upper tropical troposphere, presumably due to upwards transport of biomass burning emissions [Steck et al., 2008]. Due to the strong correlation between upper tropospheric O_3 and HO_X [Jaeglé et al., 1998], formaldehyde is frequently used as a proxy for the local and in particular upper tropospheric HO_X and O_3 chemistry [Fried et al., 2008].

While biogenic VOC emissions globally dominate the formaldehyde production from NMVOCs, biomass burning emissions can have significant local and seasonal impact [Finlayson-Pitts and J. N. Pitts, 1986; Munger et al., 1995; Andreae and Merlet, 2001; Wagner et al., 2002; Akagi et al., 2011; Seinfeld and Pandis, 2013; Stockwell et al., 2015]. In the past, formaldehyde emissions from different fuel types have been studied both in the field and laboratory (e.g., Finlayson-Pitts and J. N. Pitts [1986]; Andreae and Merlet [2001]; Wagner et al. [2002]; Akagi et al. [2011]; Seinfeld and Pandis [2013]; Stockwell et al. [2015]; Andreae [2019]). Further, since CH_2O is considerably water soluble, it may participate in either acid or base catalysed aldol-condensation reactions in the aerosol phase, hence contributing to secondary organic aerosol formation [Wang et al., 2010]. Since formaldehyde is also observable from space, its global vertical column densities have been monitored by spaceborne instruments almost constantly since the employment of the GOME instrument in 1998 [Thomas et al., 1998; Chance et al., 2000] and photochemical transport models appear to reasonably well reproduce atmospheric formaldehyde observations both from space [Dufour et al., 2009; Stavrakou et al., 2009b; Boeke et al., 2011; Bauwens et al., 2016] and within the atmosphere [Arlander et al., 1995; Fried et al., 2008; Borbon et al., 2012; Kaiser et al., 2015; Chan Miller et al., 2017].

2.2.3 Glyoxal

Glyoxal ($C_2H_2O_2$) is a short lived dicarbonyl that has significant importance in air quality and climate due to its role as an intermediate in the oxidation of hydrocarbons (e.g. Finlayson-Pitts and J. N. Pitts [1986]; Volkamer et al. [2001]; Fu et al. [2008]; Myriokefalitakis et al. [2008]; Vrekoussis et al. [2009]; Nishino et al. [2010]; Li et al. [2016]; Chan Miller et al. [2017]; Wennberg et al. [2018]) as well as an important precursor for secondary organic aerosol formation and thus for the aerosol forcing of climate (e.g. Jang and Kamens [2001]; Liggio et al. [2005b]; Volkamer et al. [2007]; Parrish et al. [2012]; Lim et al. [2013]; Knote et al. [2014]; Kim et al. [2022]). Glyoxal is directly emitted into the atmosphere by fossil fuel combustion [Kean et al., 2001] and biomass burning [Hays et al., 2002], and more importantly secondarily produced during the oxidation of both anthropogenic and biogenic precursor VOCs. Due to its large number of precursors, glyoxal is one of the most abundant atmospheric dicarbonyls. Globally, direct glyoxal emissions are negligible compared to its secondary production. Even over emission hotspots like urban areas, where direct glyoxal emissions are expected to be much larger than over rural areas, secondary production prevails [Volkamer et al., 2005a]. Therefore, the presence of glyoxal in the atmosphere can be used as an indicator for VOC oxidation, photochemical activity, and VOC–O_3–NO_X–coupling [Volkamer et al., 2005a; Liu et al., 2021].

Important glyoxal sources are the oxidation of aromatic or unsaturated hydrocarbons [Volkamer et al., 2001; Taraborrelli et al., 2021], the reaction of O_3 and OH with alkenes [Grosjean et al., 1996; Newland et al., 2022], unsaturated OVOCs [Magneron et al., 2002] and aldehydes [Chiu et al., 2017], as well as the oxidation of other anthropogenic VOCs, e.g. acetylene [Xiao et al., 2007], or biogenic VOCs, e.g. glycolaldehyde [Magneron et al., 2002]. In urban areas, anthropogenic precursor VOCs like acetylene or aromatics dominate the glyoxal production [Kim et al., 2022]. Globally, glyoxal formation from biogenically emitted VOCs dominates its atmospheric concentration [Fu et al., 2008; Wennberg et al., 2018]. Isoprene oxidation is the largest single glyoxal source and contributes via intermediates, e.g. glycolaldehyde, approximately 47% of the global glyoxal budget [Saunders et al., 2003; Volkamer et al., 2007; Fu et al., 2008; Chan Miller et al., 2017]. On a local and seasonal scale, additional direct and secondary glyoxal emissions due to biomass burning also contribute significantly [Andreae, 2019; Akagi et al., 2011; Stockwell et al., 2015; Zarzana et al., 2017, 2018]. As a result, the global distribution of glyoxal is similar to that of formaldehyde, with the largest concentrations occurring in the boundary layer over regions of high bVOCs emissions, such as the tropical rainforests. Fu et al. [2008] estimated the global source strength of glyoxal to 45 $\mathrm{Tg\,a^{-1}}$. In the marine or pristine atmosphere, glyoxal mixing ratios are on the order of several ppt. 7–23 ppt of glyoxal were found over the South Pacific [Lawson et al., 2015], or up to 10 ppt at the Cape Verde Atmospheric Observatory (CVAO, Sao Vicente island) over the Tropical Atlantic [Walker et al., 2022], and Mahajan et al. [2014] reported average glyoxal mixing ratios of 25 ppt from 10 field campaigns over the open oceans

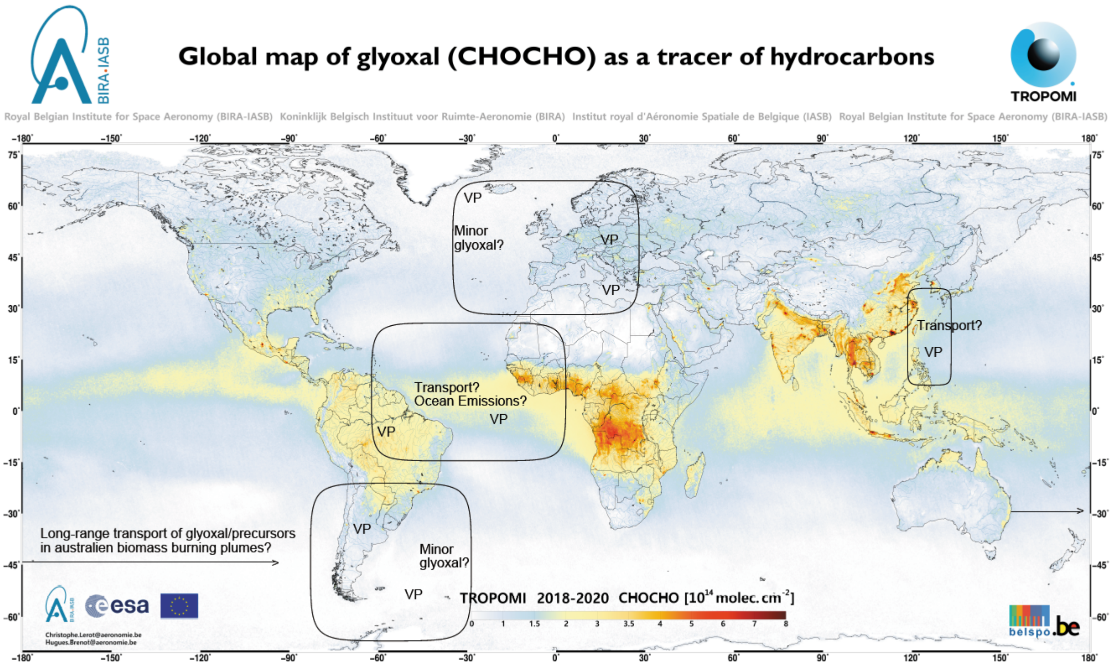

Figure 2.6: Global map of TROPOMI glyoxal VCD measurements between 2018 and 2020 (3 years average) and open scientific questions addressed within this thesis. Black squares mark the airborne mini-DOAS measurements. Regions, for which vertical profiles are inferred, are marked with VP. Figure adapted from `https://uv-vis.aeronomie.be/data/TROPOMI_posters/`, last access: June 2022. Copyright: Contains modified Copernicus Sentinel data (2018-2020)/processed by BIRA-IASB.

in different parts of the world. Over regions with high biogenic or anthropogenic emissions or in biomass burning plumes, glyoxal mixing ratios may reach a few 100 ppt [Lee et al., 1998; Volkamer et al., 2005a, 2007; Fu et al., 2008; Sinreich et al., 2010; Baidar et al., 2013; Kaiser et al., 2015; Volkamer et al., 2015; Chan Miller et al., 2017; Kim et al., 2022].

Glyoxal has an atmospheric lifetime of ∼ 3 h. Its removal occurs mainly via photolysis, reaction with OH [Plum et al., 1983; Zhu et al., 1996; Tadić et al., 2006]), and uptake on aerosols and cloud droplets [Kim et al., 2022]. During daytime, photolysis is the predominant removal pathway [Tadić et al., 2006]. Glyoxal photolysis is a source of radicals,

$$\mathrm{CHOCHO} + \mathrm{h}\nu \rightarrow \mathrm{HCO} + \mathrm{HCO}, \tag{2.18}$$

or formaldehyde

$$\mathrm{CHOCHO} + \mathrm{h}\nu \rightarrow \mathrm{H_2CO} + \mathrm{CO}, \tag{2.19}$$

or direct decay into CO,

$$\mathrm{CHOCHO} + \mathrm{h}\nu \rightarrow \mathrm{H_2} + 2\,\mathrm{CO} \tag{2.20}$$

[Tadić et al., 2006]. The formation of two HCO radicals per glyoxal molecule was found to be the predominant photolysis pathway in the daytime atmosphere [Zhu et al., 1996; Tadić et al., 2006]. Due to its high water solubility (effective Henry's law coefficient $H^{cp} = 4100\,\mathrm{mol\,m^{-3}\,P^{-1}}$ [Sander, 2015]), high hydration and oligomerization potential [Liggio et al., 2005a], and aqueous-phase oxidation in cloud droplets, glyoxal partitions efficiently into organic or inorganic aerosol [Jang and Kamens, 2001; Liggio et al., 2005a,b; Schaefer et al., 2015; Zhang et al., 2021; Kim et al., 2022]. In a laboratory study, the SOA yield from glyoxal was found to be as large as 2.33% [Jang and Kamens, 2001]. The first field measurements attributed 15% of the total SOA over Mexico

City to glyoxal [Volkamer et al., 2007]. Fu et al. [2008] estimated the yearly SOA production from glyoxal to 2.6 $\mathrm{TgC\,y^{-1}}$, of which 90% are attributed to uptake onto cloud droplets. A more recent modelling study estimated the SOA production of isoprene-derived glyoxal alone to yield 0–0.8 $\mu\mathrm{g\,m^{-3}}$ [Li et al., 2016]. Since additional glyoxal from sources other than isoprene was not considered in that study, this is only a lower limit for the total SOA yield. The contribution of glyoxal to organic aerosols is of particular importance due to the high hydration reactivity of glyoxal and its widespread global distribution from the various precursors [Liggio et al., 2005a]. However, the gas-phase glyoxal formation, the glyoxal aerosol yield and uptake pathways, its contribution to global SOA formation, and how this affects atmospheric photochemistry and the radiative balance are still uncertain and subject to current research [Li et al., 2016; Zhang et al., 2021; Kim et al., 2022].

Like formaldehyde, glyoxal is detectable from space by satellites applying a similar technique (Differential Optical Absorption Spectroscopy [Platt and Stutz, 2008]) as used for the airborne data in the present thesis. Accordingly, since the first glyoxal observations of UV/vis Nadir observing spectrometers (e.g. from the Scanning Imaging Absorption Spectrometer for Atmospheric Chartography (SCIAMACHY);Wittrock et al. [2006]), numerous studies with ever increasing observation capabilities and spatial resolution have been reported for spaceborne measurements of vertical column densities (VCD) of glyoxal (e.g. from the instruments SCIAMACHY (Scanning Imaging Absorption Spectrometer for Atmospheric Chartography), OMI (Ozone Monitoring Instrument), and TROPOMI (TROPOspheric Monitoring Instrument; Wittrock et al. [2006]; Stavrakou et al. [2009a]; Vrekoussis et al. [2009]; Lerot et al. [2010]; Vrekoussis et al. [2010]; Chan Miller et al. [2014]; Alvarado et al. [2020, 2014]; Lerot et al. [2021], and many others).

Ground-, air-, and spaceborne observations of glyoxal together with modelling have been used in the past years to gain increasing knowledge on VOC oxidation, the formation of SOA from carbonyls, and the photochemistry of biomass burning plumes [Stavrakou et al., 2009b; Lerot et al., 2010; Boeke et al., 2011; Chan Miller et al., 2014; Knote et al., 2014; Bauwens et al., 2016; Li et al., 2016; Stavrakou et al., 2016; Liao et al., 2019; Lim et al., 2019]. Simultaneous space- or airborne observations of glyoxal and formaldehyde have further been used to study the photochemistry and emissions of their different precursors (e.g. Stavrakou et al. [2009b]; Lerot et al. [2010]; Boeke et al. [2011]; Chan Miller et al. [2014]; Bauwens et al. [2016]; Stavrakou et al. [2016]). In particular, both gases are produced by both anthropogenic and biogenic precursors. However, their relative yields from these precursor groups vary between species. Therefore, the direct comparison of their ratio [$CH_2O\,/\,C_2H_2O_2$] enables the characterization (biogenic or anthropogenic) and study of the photochemical evolution of pollution plumes. The same applies to biomass burning plumes, where the fraction of formaldehyde and glyoxal has been used to study the reactivity and evolution of the complex photochemical mixture of emitted VOCs [Lee et al., 1998; Wittrock et al., 2006; Vrekoussis et al., 2010; DiGangi et al., 2012; MacDonald et al., 2012; Kaiser et al., 2015; Bauwens et al., 2016; Li et al., 2016; Chan Miller et al., 2017; Zarzana et al., 2017; Hoque et al., 2018; Behrens et al., 2019; Alvarado et al., 2020]).

All combined, recent air- and spaceborne observations together with photochemical transport modelling revealed significant deficits in the current understanding of atmospheric glyoxal. This includes in particular the following open issues which are addressed by the present thesis:

1. Its occurrence in biomass burning plumes far downwind of their origins [Alvarado et al., 2020].

2. Its occurrence in presumably pristine or marine air masses [Sinreich et al., 2010; Volkamer et al., 2015].

3. The insufficient reproduction of atmospheric glyoxal by current models both in emission

plumes and the background atmosphere [Myriokefalitakis et al., 2008; Stavrakou et al., 2009a; Lerot et al., 2010].

Due to its short lifetime, glyoxal hours to days or even weeks downwind of its sources likely does not result from atmospheric transport processes, but suggests sufficiently long-lived precursor VOCs co-emitted at the emission sources. Equally, recent observations of glyoxal in the marine atmosphere and in particular in the tropical marine boundary layer require yet unidentified precursor VOCs [Lawson et al., 2015; Walker et al., 2022]. Unexpected large glyoxal mixing ratios were observed e.g. in the marine boundary layer of the Eastern Pacific up to 3000 km from the continental coast by shipborne (up to 140 ppt [Sinreich et al., 2010]) and during airborne measurements (32–36 ppt [Volkamer et al., 2015]). These observations revealed a yet unknown marine source of glyoxal, possibly from ozone-driven reactions with the organic microlayer at the sea surface, which in idealised seawater laboratory experiments have been shown to produce glyoxal [Zhou et al., 2014], and/or secondary formation from oxidised VOC precursor molecules, such as acetaldehyde, acetylene, and others [Wang et al., 2019].

2.2.4 Methylglyoxal

Many atmospheric characteristics of glyoxal also apply to methylglyoxal ($C_3H_4O_2$). The two gases are the two smallest dicarbonyls in the atmosphere, are produced by a large range of anthropogenic and biogenic precursor VOCs, have similar lifetimes around 2 h against photolysis, and are highly water soluble. The latter favours their uptake by aqueous aerosols and cloud particles (reactive uptake coefficients $\gamma = 2.9 \times 10^{-3}$ [Liggio et al., 2005a,b; Zhao et al., 2006]), and hence, via subsequent hydration or oxidation, their global contribution to the formation of secondary organic aerosols and the climate forcing of aerosols. With 140 $\mathrm{Tg\,y^{-1}}$, the global methylglyoxal budget was estimated to be approximately 3 times larger than that of glyoxal [Fu et al., 2008], indicating a respectively larger impact on the atmospheric photochemistry and formation of secondary aerosols. However, information on methylglyoxal in the atmosphere is even more rare than of glyoxal, since satellite measurements of methylglyoxal are not yet available and atmospheric measurements of methylglyoxal are still sparse. This is a consequence of the moderate spectral resolution of space- and airborne optical measurements, which suffer from the spectral interference of the major but only weakly structured absorption bands of methylglyoxal with those of other dicarbonyls (mainly 2,3-butanedione) in the blue spectral region [Meller et al., 1991; Horowitz et al., 2001; Thalman et al., 2015; Zarzana et al., 2017]. Potential interferences with the 7ν absorption band of water vapour at 442 nm further complicate the spectral retrieval [Thalman et al., 2015; Zarzana et al., 2017]. In situ measurements of methylglyoxal using different techniques have only recently become available [Kawamura et al., 2013; Lawson et al., 2015; Michoud et al., 2018; Mitsuishi et al., 2018; Lv et al., 2019; Ling et al., 2020; Liu et al., 2020]. The very limited number of measurements in conjunction with insufficient detection limits are still preventing comprehensive studies of methylglyoxal in the atmosphere.

As for formaldehyde and glyoxal, the largest single source of methylglyoxal is isoprene. It alone accounts for 79% of the total global methylglyoxal emissions, followed by acetone (7%) [Fu et al., 2008]. As isoprene and acetone are both biogenic VOCs, the predominant part of the atmospheric methylglyoxal is naturally emitted and only minor parts result from biomass burning and anthropogenic emissions. As a consequence, the largest concentrations are expected over regions of high biogenic activity, in particular the tropical rainforests. However, to the best of the author's knowledge airborne measurements of methylglyoxal do not yet exist over these regions. For this reason, the present thesis aims at improving the knowledge on the atmospheric concentrations and the vertical gradient of methylglyoxal over one of the largest tropical rainforests, the Amazon basin.

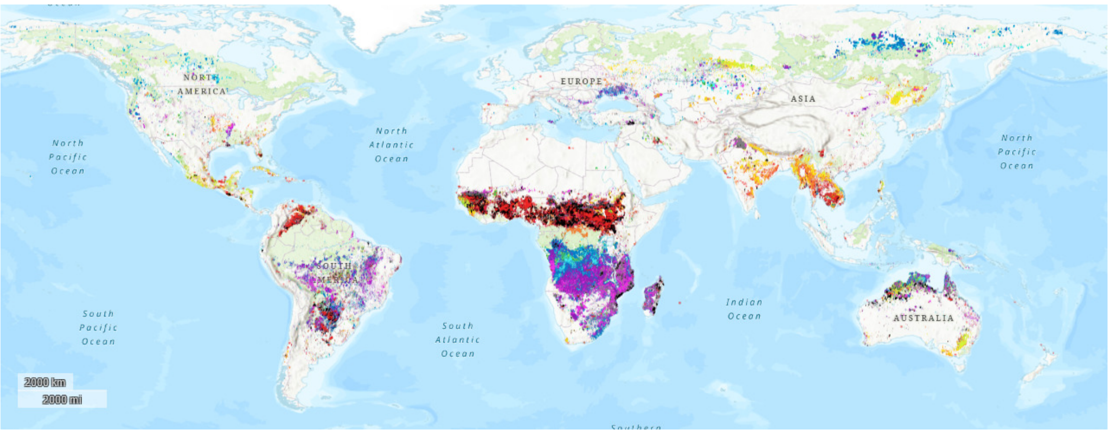

Figure 2.7: Globally burned area due to biomass burning in 2021 as detected by MODIS Collection 61 [Giglio et al., 2018]. Different colours correspond to biomass burning in different months. Figure created with FIRMS (`https://firms.modaps.eosdis.nasa.gov/map/`, last access: June 2022).

Like formaldehyde and glyoxal, methylglyoxal is also directly and secondarily emitted by biomass burning. However, its emission strength from different fuel and fire types is still largely uncertain and based on only three previous studies [Hays et al., 2002; Zarzana et al., 2017, 2018]. Based on laboratory measurements, Hays et al. [2002] reported larger glyoxal than methylglyoxal emissions from the analysed fuels. Contrarily, Zarzana et al. [2017, 2018] found larger methylglyoxal and smaller glyoxal emissions. Their findings suggest significantly larger methylglyoxal emissions than previously assumed in model studies, e.g. by Fu et al. [2008]. The recent overview of biomass burning emission factors by Andreae [2019] indicates for most fuels the complete lack of methylglyoxal emission data.

While Kroll et al. [2005] found no evidence for irreversible uptake of glyoxal and methylglyoxal by aerosols, Fu et al. [2008] estimate the SOA source from methylglyoxal to be 8 $\mathrm{Tg C\,y^{-1}}$. This is roughly three times larger than that of glyoxal. The predominant part of this source is located below 1.5 km altitude. Combined with glyoxal, the impact of this potential additional source on the production of SOA is significant. In fact, Fu et al. [2008] found an increase in the global SOA concentration by 40% when including glyoxal and methylglyoxal as SOA sources in the GEOS-Chem model.

2.3 Biomass burning as a source of VOCs

The term biomass burning refers to all kinds of burning processes of vegetation. This covers both naturally occurring wildfires, e.g. induced by lightning ($\sim$ 10% of the fires on the planet [Shi et al., 2020]), and fires that result from human activities, e.g. agricultural field burns or biofuel burning ($\sim$ 90%; Shi et al. [2020]). Globally, 8.7 Pg[7] of dry mass are burned each year [Seiler and Crutzen, 1980; Andreae, 1991]. Depending on the assumed carbon emission rates (e.g. 2500 $\mathrm{kg\,C\,ha^{-1}}$ burned [Van Der Werf et al., 2004]) and the total burned area worldwide ($\sim 1.7 \times 10^6$ $\mathrm{km^2}$ [Hoelzemann et al., 2004]), this corresponds to yearly carbon emissions into the atmosphere on the order of 1.4–2.6 PgC [Hoelzemann et al., 2004; Ito and Penner, 2004; Van Der Werf et al., 2004]. Biomass burning hence contributes $\sim$ 40% to the total annual carbon emissions [IPCC, 2001]. The predominant fraction of global biomass burning occurs in the tropical and subtropical regions (Fig. 2.7 and e.g. Crutzen et al. [1979]; Van Der Werf et al. [2004]; Shi et al. [2020]), in particular in Africa (30–50% of the global fires) and South

---

[7] 1 Pg $= 10^{12}$ kg.

America (15% of the global fires; Shi et al. [2020]). In these regions, the large density of biomass in tropical forests (18% of the global fires) and savannah (43–50% of the global fires) combined with frequent agricultural field cleavage (5–23% of the global fires), and wood fuel use (11–16% of the global fires) cause large biomass burning extends (Hao and Liu [1994]; Andreae [1991]; Shi et al. [2020], and references therein). At the same time, the tropical atmosphere is a chemically and dynamically highly active region. As a result, the efficient vertical and latitudinal transport distributes the fire emissions far away from the sources into the remote and upper troposphere [Koppmann et al., 1992; Andreae and Merlet, 2001].

Biomass burning causes large direct emissions of greenhouse gases, such as carbon dioxide, nitrous oxide, and methane into the atmosphere [Koppmann et al., 2005]. In addition, biomass burning leads to large and concentrated emissions of chemically and radiatively reactive gases like CO, NO, and VOCs [Crutzen and Andreae, 1990; Andreae and Merlet, 2001; Andreae et al., 2001; Andreae, 2019]. Finally, approx. 5% of the total carbon is emitted as particulate matter [Radke et al., 1991; Reid et al., 2005]. Once emitted, the gases quickly react and form a complex and changing mixture of chemicals while being transported downwind of the fires. Biomass burning therefore affects the atmosphere close-by and far away from the fires [Fishman et al., 1996; Jaffe et al., 2004]. Therefore, biomass burning has strong impacts on the photochemistry, in particular tropospheric ozone formation [Fishman et al., 1990, 1996], secondary aerosol formation and composition, and hence cloud formation and radiation, as well as human health [Koppmann et al., 2005; Theys et al., 2020]. Emissions of long-lived halogen species from the fires may even be transported into the stratosphere and impact stratospheric ozone. Numerous studies, both in the field and laboratory were conducted in the past and increasing knowledge has been gained on the emitted species from different fuel types, their individual emission strengths, and the photochemical evolution of the plumes while being transported away from the source [Crutzen and Andreae, 1990; Andreae and Merlet, 2001; Andreae et al., 2001; Akagi et al., 2011; Stockwell et al., 2015; Andreae, 2019]. However, the species and concentrations of primary and secondary emitted gases depend on numerous factors, like the fuel types, the fire sizes and moisture, ambient conditions like temperature and wind, and the combustion efficiency of the fire (smouldering or open flame) and hence the fraction of direct CO_2/CO production [Radke et al., 1991; Koppmann et al., 2005]. For many species, accurate measurements of their pyrogenic emissions and hence their climate impact from biomass burning are still insufficient [Andreae, 2019]. Accordingly, estimates of the global impact of biomass burning on specific trace gas emission budgets are affected by large uncertainties [French et al., 2004].

Among the manifold of NMVOCs released in large amounts by fires or formed in their plumes are carbonyl compounds such as formaldehyde, glyoxal, methylglyoxal, 2,3-butanedione, and many others (see sect. 2.2.2 to 2.2.4). In particular, the ratio of glyoxal and formaldehyde emissions (R_{GF}) has been used in the past as an indication of the precursor VOC species and to differentiate biomass burning plumes from the usually biogenic surroundings [Kaiser et al., 2015; Stavrakou et al., 2016]. Based on OMI satellite and airborne field measurements of pyrogenic plumes, Stavrakou et al. [2016] and Zarzana et al. [2017] recently estimated an R_{GF} of 0.04–0.05. This is up to two orders of magnitude smaller than reported by laboratory measurements of McDonald et al. [2000] (0.5–4.2) and Hays et al. [2002] (1.2–2.7), on which the study of Fu et al. [2008] is based on. The range of reported methylglyoxal emissions relative to formaldehyde (R_{MGF}) is largely uncertain due to the limited number of methylglyoxal studies. In a laboratory study, Hays et al. [2002] estimated an R_{MGF} of 1.1–1.7.

The present thesis uses simultaneous airborne measurements of $C_2H_2O_2$ and $C_3H_4O_2$ over the Amazon to estimate their emission ratios with respect to CH_2O as well as the normalized excess mixing ratios within biomass burning plumes. Combined with previously reported emission

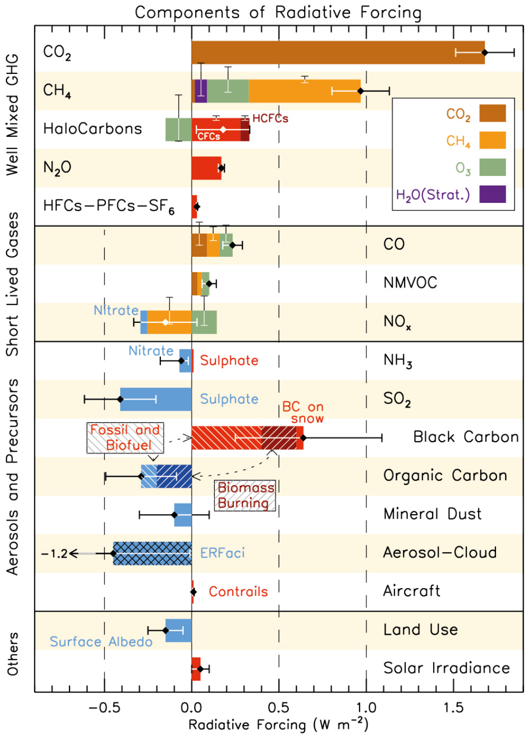

Figure 2.8: Contribution of different atmospheric compounds to the total radiative forcing (1750–2011). GHG indicates greenhouse gases. Via ozone, methane, and CO_2 formation, NMVOCs contribute with approximately 0.1 W m^{-2} to the radiative forcing, whereas aerosols predominantly have a cooling effect on the climate (besides black carbon). Figure taken from the Fifth IPCC assessment report [G. Myhre and Zhang, 2013].

factors of CH_2O (e.g., Andreae [2019]), their emission factors for tropical forest fires are estimated.

2.4. Secondary aerosol formation by organics

Besides gaseous compounds, the atmosphere also contains liquid and solid particles, that are distinguished according to size, composition, and water content into cloud and aerosol particles. Such aerosols may be directly emitted from the surface as primary particulate matter or secondarily produced in the atmosphere from gaseous compounds. Atmospheric aerosols mainly consist of inorganic species (e.g. sulfate), organic species, black carbon, and minerals [G. Myhre and Zhang, 2013]. The atmospheric aerosol composition and concentrations are of particular relevance for the climate system due to the impact of aerosols on the radiative forcing, air pollution [Ostro and Chestnut, 1998; Hoyle et al., 2011; Fan et al., 2022], and heterogeneous reactions that affect the atmospheric gas-phase chemistry.

Fine particulate matter, i.e atmospheric particulates with diameter < 2.5 µm, is considered particularly important for the climate system due to its more efficient transport away from the sources and its size comparable to visible wavelengths, which renders it an efficient scatterer for light at these wavelengths [Kanakidou et al., 2005]. Of the atmospheric submicron particulate matter, organic aerosols account for a varying fraction of 20–90% [Kanakidou et al., 2005]. 10–40% of the organic aerosol is secondarily formed in the atmosphere from the photo-oxidation of VOCs. Making up 90%, the predominant fraction of the resulting secondary organic aerosols (SOA) is believed to be of biogenic origin [Kanakidou et al., 2005; Volkamer et al., 2006]. Primary and secondary organic aerosols contribute directly to the radiative forcing of climate via absorption and reflection of incoming and outgoing radiation (direct aerosol effect, e.g. Dickerson et al. [1997]), as well as secondarily through their impact on tropospheric cloud formation. By serving as cloud condensation nuclei (CCN), hydrophilic aerosols enhance water vapour condensation and hence cloud formation and further also impact the radiative and albedo characteristics of the clouds (so-called Twomey or cloud albedo effect, e.g. Twomey [1974]; Twomey et al. [1984]; Albrecht [1989]; Novakov and Penner [1993]; Corrigan and Novakov [1999]). This increased backscattering of incoming solar radiation and cloud formation or cloud albedo modification causes the production of secondary organic aerosols from VOCs to exhibit a cooling effect on the climate. Latest estimates of the total radiative forcing due to aerosol-cloud and to a lesser degree aerosol-radiation interaction are -1.1 $\mathrm{W\,m^{-2}}$, with a possibly diminishing future trend (Fig. 2.8 and P.A. Arias [2021]).

Secondary organic aerosols are produced from the photo-oxidation of VOCs (e.g. formaldehyde, glyoxal, and methylglyoxal) to increasingly less volatile chemicals that finally partition into the particulate phase. Currently, only $\sim$ 10% of the organic aerosol sources are quantified and photochemical models were found to under predict atmospheric SOA significantly [Aiken et al., 2008; Carslaw et al., 2010; Hoyle et al., 2011; Mahilang et al., 2021; Fan et al., 2022]. Glyoxal and methylglyoxal are particularly efficient contributors to SOA formation due to their high hydration and oligomerization potential. In fact, Fu et al. [2008] estimated the potential additional SOA production when accounting for glyoxal in the tropical marine boundary layer to 1.5 $\mathrm{\mu g\,m^{-3}}$. This could fill previously observed gaps between observed and modelled organic aerosol concentrations [Heald et al., 2006].

Chapter 3

Instrumentation and Methods

The following chapter discusses all instruments that were involved in the analysis as well as the applied measurement methods. The focus of the chapter is put on the measurements of the mini-DOAS instrument, the directly measured and indirectly inferred physical quantities as well as the implications of the applied methods. Their strengths and weaknesses and uncertainties are laid out in detail.

The analysis of the airborne mini-DOAS measurements of UV/vis/near-IR absorbing trace gases involves the following steps: (1) simultaneous measurements of Limb (towards the horizon) and Nadir (in ground direction) scattered skylight; (2) analysis of the measured sunlight spectra for the target gases according to the DOAS method; (3) forward radiative transfer modelling of the optical properties of the atmosphere during the measurements using the Monte Carlo model McArtim [Deutschmann et al., 2011]; and (4a) inferring of trace gas concentrations from the Limb observations by scaling the measured slant column densities (SCDs) using simultaneously measured SCDs of a scaling gas of known concentration (e.g. O_3), or the calculated clear sky extinction of the collisional complex O_2-O_2 (further on called O_4); Hüneke [2016]; Hüneke et al. [2017]; Stutz et al. [2017]; Werner et al. [2017]; Kluge et al. [2020]; Rotermund et al. [2021]); or alternatively (4b) inferring of vertical column densities (VCDs) from the Nadir measured SCDs based on the air mass factors (AMFs) simulated with McArtim.

The present study focuses on the Nadir and Limb measurements of O_4, CH_2O, $C_2H_2O_2$, and $C_3H_4O_2$ by the mini-DOAS instrument made from aboard the German research aircraft DLR HALO during a total of 72 research flights on eight scientific missions covering different regions of the globe in the time 2014 to 2019.

Main parts of this chapter have been published in Kluge et al. [2020], section 2, or are currently under review for publication in Kluge et al. [2022].

3.1 Mini-DOAS instrument

The mini-DOAS instrument is a UV/vis/near-IR six channel optical spectrometer, which has been operated on board the DLR HALO research aircraft since 2011. It detects Nadir and Limb scattered sunlight in the UV (310–440 nm, FWHM[1] = 0.47 nm), visible (420–640 nm, FWHM = 1.1 nm) and near-infrared (1100–1680 nm, FWHM = 10 nm) wavelength ranges [Hüneke, 2016; Hüneke et al., 2017]. The six telescopes (FOV[2] 0.5° × 3.15°) collect the skylight from fixed Nadir and Limb viewing geometries in a UV, visible and near-IR channel in each viewing direction. The Limb telescopes can observe at varying elevation angles (+5 to -90°) when commanded, but

---

[1] Full Width at Half Maximum

[2] Field Of View

Table 3.1: Trace gas absorption cross sections used for the spectral retrieval. For H_2O, gas phase (g) as well as liquid phase (l) absorption cross sections are included.

No.	**Absorber**	**Temperature** [**K**]	**Reference**	**Uncertainty** [%]
1a	O_4	273	Thalman and Volkamer [2013]	4
1b	O_4	293	Thalman and Volkamer [2013]	4
2a	O_3	203	Serdyuchenko et al. [2014]	3
2b	O_3	223	Serdyuchenko et al. [2014]	3
2c	O_3	273	Serdyuchenko et al. [2014]	3
2d	O_3	293	Serdyuchenko et al. [2014]	3
3	NO_2	294	Vandaele et al. [1998]	3
4a	H_2O (g)	293	Rothman et al. [2009]	8
4b	H_2O (g)	296	Polyansky et al. [2018]	1
4c	H_2O (l)	295	Pope and Fry [1997]	1
5	CH_2O	293	Chance and Orphal [2011]	10
6	$C_2H_2O_2$	296	Volkamer et al. [2005b]	3
7	$C_3H_4O_2$	296	Meller et al. [1991]	10
8	$C_4H_6O_2$	223	Horowitz et al. [2001]	4

are normally aligned with a control frequency of 10 Hz at -0.5° below the horizon to compensate for the changing roll angle of the aircraft. Glass fibre bundles conduct the collected light to six optical spectrometers, assembled in an evacuated (10^{-5} mbar) and thermostatic housing (at ideally $\approx 1^\circ$ C) in the otherwise unpressurised and uninsulated boiler room of the aircraft. In the Limb geometry, the mini-DOAS instrument probes air masses perpendicular to the aircraft's flight direction on the starboard side. An IDS uEye camera (FOV 46°) co-aligned with the limb telescopes additionally provides images of the sampled atmosphere at 1 Hz resolution.

More details of the instrument design, its major features and deployment on the HALO aircraft, the measurement method, the spectral retrieval and data processing can be found in Hüneke [2016]; Hüneke et al. [2017]; Stutz et al. [2017]; Werner et al. [2017]; Kluge et al. [2020]; Rotermund et al. [2021].

3.1.1 Spectral retrieval

The measured skylight spectra are analysed for the absorption of the target gases using the DOAS method. A detailed description of the DOAS technique and its application to airborne measurements can be found in Platt and Stutz [2008]. Retrieval details like the applied wavelength ranges, included trace gases and the fitting parameters for each gas are provided in tables 3.1 and 3.2 and are briefly outlined below for each individual gas.

For the processing of the data obtained during different missions, minor adjustments to the retrieval settings (e.g. the lower end of the analysed wavelength range or the temperatures of the included absorption cross sections) are applied when needed. Primarily, these adjustment are necessary to compensate for mechanical modifications of the instrument and hence of the optical imaging (e.g. fibre bundle replacements, which cause changes in the lower wavelength limit of the spectrometers) as well as due to the largely changing ambient conditions during the different research missions.

3.1.1.1 O_4

The absorption structure of the O_2-O_2 collisional complex (briefly called O_4) between 350 and 630 nm is caused by simultaneous transitions of two oxygen molecules from the ${}^3\Sigma_g^- + {}^3\Sigma_g^-$ ground state into electronically excited states [Greenblatt et al., 1990]. To minimize the distance between the absorption bands of the target and scaling gas, O_4 is analysed around its absorption bands

Table 3.2: Details of the DOAS spectral analysis for the analysed trace gases.

Target gas	Spectral interval [nm]	Fitted absorbers (see Table 3.1)	Polyn.	mission (i)
	348-369	1a, 2a, 2c, 3, 5	2	1
O_4 (Limb)	338-370	1a, 2b, 2d, 3, 5	2	2, 3, 4, 5, 6, 7, 8
	460–490	1a, 2a, 2c, 3, 4a	2	1, 2, 3, 4, 5, 6, 7, 8
CH_2O (Limb)	324–354	1a, 2a, 2c, 3, 5	2	1
$C_2H_2O_2$ (Limb)	420–439 and 447–465	1a, 2c, 3, 4a, 6	2	1
$C_2H_2O_2$ (Limb)	435–460	1b, 2b, 3, 4b, 4c, 6	3	6, 8
$C_2H_2O_2$ (Limb)	430–460	1b, 2b, 3, 4b, 4c, 6	3	2, 3, 4, 5, 7
$C_2H_2O_2$(Nadir)	435–460	1b, 2b, 3, 4b, 4c, 6	3	3, 4, 5, 6, 7, 8
$C_3H_4O_2$* (Limb)	420–475	1a, 2c, 3, 4a, 6, 7, 8	2	1

Additional parameters for all spectral retrievals are (1) Offset spectrum (I_{Ofs}); (2) Ring spectrum (R); (3) Ring spectrum multiplied by λ^4 ($R \cdot \lambda^4$).
(i): ACRIDICON-CHUVA (1), OMO (2), EMeRGe-EU (3), WISE (4), EMeRGe-Asia (5), CoMet (6), CAFE (7), SouthTRAC (8).

at 477.3 nm ($^1\Sigma_g^+ + {}^1\Delta_g$ transition) in the visible and 360.8 nm ($^1\Sigma_g^+ + {}^1\Sigma_g^+$ transition) in the UV [Landau et al., 1962].

3.1.1.2 Formaldehyde

The absorption cross section of formaldehyde has several characteristic (vibrational) maxima between 315 and 380 nm ($A^1\,A_2 \leftarrow X^1\,A_1$ transition; Moule and Walsh [1975]). Due to the lower spectral limit of the UV-spectrometer (310 nm) as well as to minimise potential cross correlation with ozone absorption (i.e. with the Hartley and Huggins bands), the lower limit of the analysed spectral range was chosen at the highest possible wavelength (i.e above 320 nm) to minimise the spectral residuum, while at the same time still including as many formaldehyde absorption maxima as possible to optimize the signal to noise of the retrieval. The resulting wavelength range of 324 nm to 354 nm includes the five main vibrational formaldehyde absorption bands. Selecting an even higher lower wavelength limit, e.g. above 330 nm, would slightly reduce the spectral residuum of the retrieval on average by 20%, but at the expense of also reducing the signal to noise on average by 24%. The latter is even more pronounced for measurements in the lower troposphere (Fig. 3.1, panel b). As most formaldehyde measurements over the rainforest and especially the biomass burning plume probing occurred below 3 km altitude (Fig. 4.2), the larger wavelength range from 324 to 354 nm is chosen for the analysis. Exemplary spectral retrievals based on both lower wavelength limits (324 and 337 nm) are shown in Fig. A.1.

3.1.1.3 Glyoxal

The major absorption bands of glyoxal are located in the visible spectral range between 400 and 470 nm ($A^1A_u - X^1A_g$ transition). The centre of the dominating absorption structure is located at 455 nm with an absorption cross section of $\sigma \approx 52 \times 10^{-20}$ cm^2 molec^{-1}. Three slightly smaller ($\sigma < 30 \times 10^{-20}$ cm^2 molec^{-1}) absorption maxima are located at 440 nm, 428 nm and 413 nm. Outside of this wavelength range, for $\lambda < 413$ nm or $\lambda > 457$ nm, σ remains smaller than 7×10^{-20} cm^2 molec^{-1} [Volkamer et al., 2005b]. In particular for Nadir observations in a moist atmosphere and above the ocean, the DOAS analysis of glyoxal is complicated due to its low optical density ($\sim 3 \times 10^{-3}$, see Fig. A.2) and proximity of the main absorption bands to the much stronger 7ν absorption band of water at 442 nm (optical density on the order of 10^{-1} Wei et al. [2019]). Therefore, for such observations, 5–50 consecutively measured spectra are co-added in order to minimise potential spectral interferences while optimising the signal to

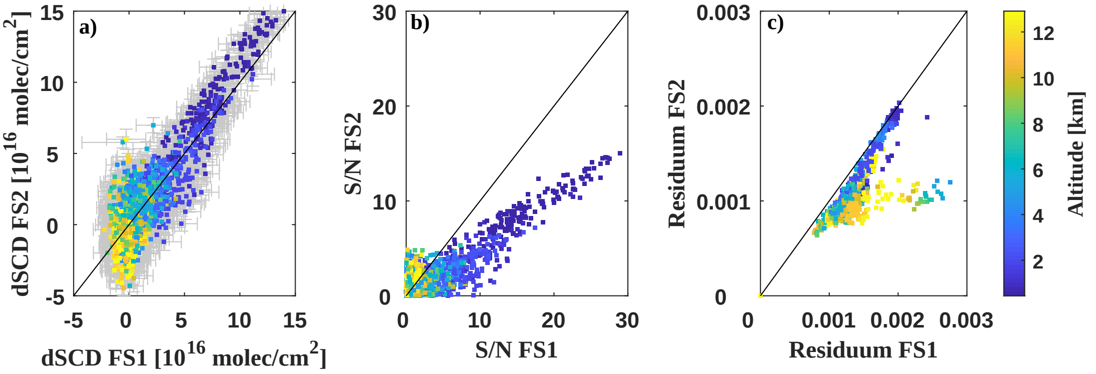

Figure 3.1: DOAS analysis of formaldehyde based on two different retrieval settings with spectral ranges from 324 to 354 nm (FS1, five absorption bands) and 337 to 354 nm (FS2, three absorption bands), respectively. Panels (a) to (c) show the resulting dSCDs, the signal to noise ratios (S/N), and the spectral residuum of the retrievals, all colour-coded by the measurement altitude. Notable is the significant increase in S/N for lower flight altitudes when using the larger spectral range for the retrieval.

noise, at the expense of enlarging the foot-print of the affected measurements (as discussed in detail in sect. 3.1.3). While most satellite or ground based instruments use a continuous spectral range around the two most prominent absorption bands for the glyoxal retrieval (e.g. Lerot et al. [2021]), Mahajan et al. [2014] suggest to simultaneously use two retrieval windows from 420 to 439 nm and 447 to 465 nm, respectively, thus avoiding the 7ν water band. As this study analyses mini-DOAS measurements under all-sky conditions with occasional heavy cloudiness, or even with the spectrometers directly pointing into liquid water (i.e. Nadir observations over the ocean), potential cross correlations of water absorption on the glyoxal retrieval have to be taken into account. Therefore, all measurements are analysed using (a) a continuous wavelength range from 430 (or 435) to 460 nm based on Lerot et al. [2021] and (b) two simultaneous spectral ranges around the 7ν water band (420 to 439 nm and 447 to 465 nm) with all other parameters equal to (a). The direct comparison of both approaches clearly indicates on average a factor of three smaller spectral residua when using the continuous spectral range both in the Limb and Nadir viewing geometry (Fig. 3.2, panels a and d) at approximately constant signal to noise ratio (Fig. 3.2, panels b, and e). In the free troposphere, the resulting dSCDs based on the continuous spectral analysis are systematically larger than those obtained based on the discrete wavelength ranges (Fig. 3.2, panels c and f). This is mainly caused by the larger scatter of the dSCDs around zero when using the discrete wavelength range. Interestingly, no significant influence of the viewing geometry (Fig. 3.2, upper compared to lower row) and especially also when further differentiating into continental compared to marine observations (not shown) is discernable. Thus, for the research missions under only moderately humid and cloudy measurement conditions, the spectral retrieval settings of the Limb and Nadir glyoxal observations are based on the recent TROPOMI glyoxal analysis from Lerot et al. [2021], in support of a better comparability of both data sets (chapter 5.1.2) and a smaller spectral residuum ($< 10^{-4}$). Unlike the TROPOMI glyoxal retrieval, the mini-DOAS measurements are not found to be significantly affected by changing NO_2 concentrations, therefore only a single NO_2 absorption cross section (at a warmer temperature) to account for the tropospheric NO2 absorption is included in the present analysis (Table 3.2).

During the ACRIDICON-CHUVA mission, the large and patchy cloud cover over the tropical rainforest together with generally moist atmospheric conditions during the predominantly low flight altitudes within the planetary boundary layer occasionally caused very high H_2O concentrations, such that the glyoxal retrieval in this region is performed based on the two discrete spectral ranges

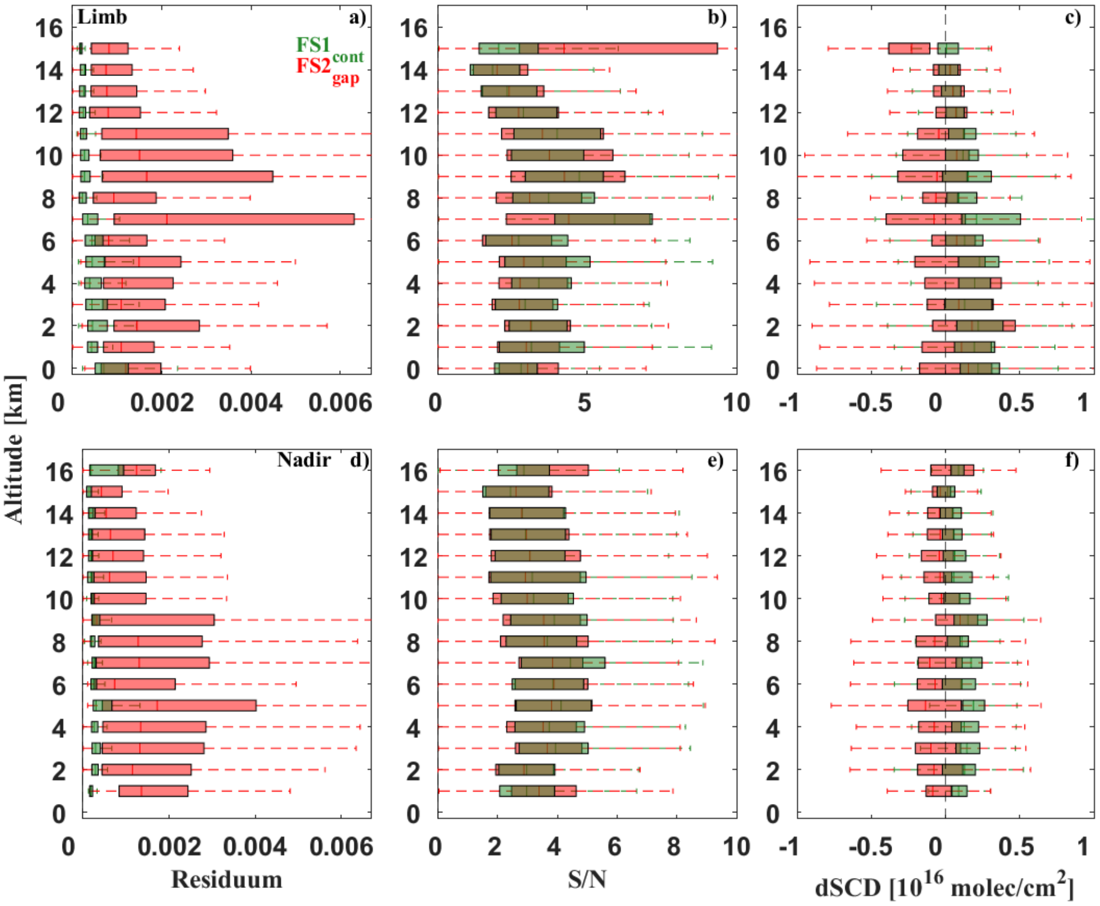

Figure 3.2: DOAS retrieval of glyoxal from all 72 research flights in the Limb (upper row) and Nadir (lower row) viewing geometry based on two different spectral ranges avoiding (FS_{2gap}, red) and including (FS_{1cont}, green) the 7ν absorption band of water, respectively, by using a continuous spectral range from 430 or 435 to 460 nm or two simultaneous ranges from 430 or 435 to 439 nm and 447 to 460 nm. The data are averaged on a 1 km altitude grid. The different panels show the spectral residuum (a, d), the signal to noise ratio (S/N) of the retrieval (b, e) and the resulting dSCDs (c, f).

(Fig. 3.3, red). The different lower limits of the spectral ranges during ACRIDICON-CHUVA and the later measurements (Table 3.2) are mainly caused by shifts in the spectrometers wavelength limits due to mechanical adjustments of the fibre bundles of the instrument. Exemplary spectral retrievals based on one continuous and two discrete wavelength ranges as well as for the Nadir glyoxal measurements are shown in Fig. A.2.

3.1.1.4 Methylglyoxal

Due to the only weakly structured absorption cross section of methylglyoxal (Fig. A.3), its detection by remote sensing instruments deserves a brief discussion. Substituted dicarbonyls such as biacetyl ($CH_3COCOCH_3$), with absorption cross sections in the visible spectral range similar to that of $C_3H_4O_2$, are co-emitted from similar emission sources like those of methylglyoxal (e.g. biomass burning) in significant quantities (e.g. Meller et al. [1991]; Horowitz et al. [2001]; Thalman et al. [2015]; Zarzana et al. [2017]). Owing to the moderate resolution of the min-DOAS spectrometer in the visible spectral range, it is not possible to separately and thus unambiguously detect these substituted dicarbonyls in the atmosphere, unlike in studies employing higher resolving spectrometers (e.g. Thalman et al. [2015]). Accordingly, in the following the weighted

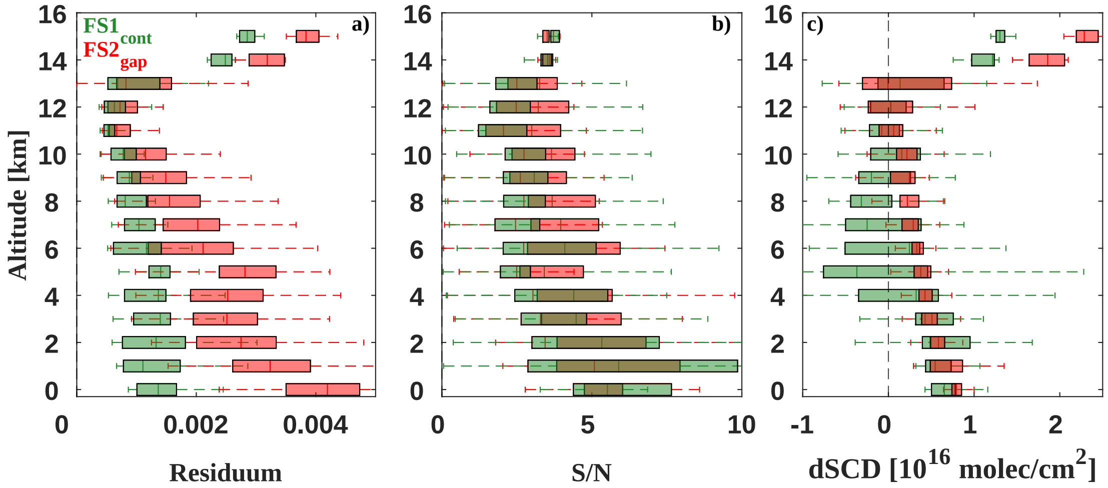

Figure 3.3: DOAS retrieval of glyoxal over the Amazon rainforest (ACRIDICON-CHUVA mission) during all analysed research flights using a continuous spectral range from 420 to 465 nm (FS_{1cont}, green) or two simultaneous ranges from 420 to 439 nm and 447 to 465 nm (FS_{2gap}, red) according to Fig. 3.2.

sum (absorption cross section times concentration) of $C_3H_4O_2$ and that of other substituted dicarbonyls is reported and expressed as $C_3H_4O_2{}^*$. The actual amount of methylglyoxal within $C_3H_4O_2{}^*$ can only roughly be approximated (see sect. 5.2.1.4). However, the observations still provide valuable information on the atmospheric methylglyoxal profile and its approximated (upper limit) concentration, especially when considering that airborne methylglyoxal measurements are still rare, and in the case of satellite instruments, completely lacking. Exemplary spectral retrievals of methylglyoxal are shown in Fig. A.3.

3.1.1.5 Fraunhofer reference spectra and detection limit

Since the DOAS method infers a differential slant column density (dSCD) relative to a solar Fraunhofer reference spectrum (SCD_{ref}), the total slant column (SCD) has to be inferred by adding the fraction of absorption in (SCD_{ref}),

$$SCD = SCD_{ref} + dSCD. \tag{3.1}$$

For the retrieval of formaldehyde, glyoxal, and methylglyoxal, SCD_{ref} is determined from Limb measurements at high altitudes above which insignificant (or no) absorption is expected, or, if a sufficient flight altitude was not reached (EMeRGe-Europe and EMeRGe-Asia missions), by using a reference from a different research flight which fulfils the above conditions. For the retrieval of the O_4 extinction, SCD_{ref} is determined using a high resolution solar reference spectrum [Thuillier et al., 1998].

Based on an exposure time of 300 ms, a saturation of 60 %, and 100 added readouts (30 s integration time), the mini-DOAS detection limit for glyoxal $dSCD_{dl}$ is $2.6 \cdot 10^{14}$ molec cm^{-2} [Platt and Stutz, 2008]. Depending on SCD_{ref} and the related air mass factors (Sect. 3.1.2) and hence flight altitude, for Limb measurements, this results in a detection limit ranging from 1 ppt (during clear skies, for a light path of about 100 km at maximum cruising altitude of the aircraft) up to several 100 ppt (for very short line-of-sight photon paths, e.g. in dense clouds; Kluge et al. [2020]). For the Nadir measurements, the typical detection limit $[VCD_{dl}]$ is $1.5 \cdot 10^{14}$ molec cm^{-2}, but depending on the flight altitude and cloud cover and thus columnar air mass factor, it can be as low as $6.7 \cdot 10^{13}$ molec cm^{-2} or as large as $2.6 \cdot 10^{14}$ molec cm^{-2}.

3.1.2 Retrieval of concentrations (Limb) and vertical column densities (Nadir)

The following section discusses the conversion of the inferred SCDs to mixing ratios (Limb measurements) and to total vertical column densities (Nadir measurements).

The Limb measured slant column densities $\mathrm{SCD_{limb}}$ are converted into trace gas mixing ratios using the O_4-scaling method, as described in detail in Hüneke [2016]; Hüneke et al. [2017]; Stutz et al. [2017]; Werner et al. [2017]; Kluge et al. [2020]. Accordingly, the concentration of a trace gas $[X]$ in the flight altitude j is inferred from $SCD_{limb,X}$ by comparing the measured optical depth SCD_{limb,O_4} with the calculated clear sky extinction $[O_4]_j$ to quantify the atmospheric radiative transfer during each single measurement:

$$[\mathrm{X}]_j = \frac{\alpha_{X_j}}{\alpha_{O_{4,j}}} \cdot \frac{SCD_{limb,X}}{SCD_{limb,O_4}} \cdot [\mathrm{O_4}]_j, \tag{3.2}$$

with the correction factors α_{X_j} and $\alpha_{O_{4,j}}$ (see below). This approach is justified based on the equivalence theorem in optics, which states that for a given wavelength, the photon path length distribution and hence the mean photon path lengths are the same for weak absorbers with similar atmospheric distribution [Irvine, 1963]. Evidently, this criterium is in good approximation fulfilled when using O_4 as scaling gas for all trace gases with sources at the ground and sinks in the troposphere, such as formaldehyde, glyoxal, and methylglyoxal. Remaining differences in the profile shapes of target and scaling gas and their centre wavelengths of absorption are accounted for by the so called α-factors. The α-factors express the fraction of the line-of-sight absorption at the measurement altitude to the total atmospheric absorption, which -while similar- may slightly differ for the gas of interest compared to the scaling gas, due their different profile shapes. For the simulation of the α-factors, the present thesis relies on the Monte-Carlo radiative transfer inverse model McArtim by Deutschmann et al. [2011]. McArtim is capable to treat the radiative transfer in 2D (or 3D), calculate the refraction, and also account for the sphericity of the Earth. Each detected photon is modelled backward (i.e. from the detector to the sun) while considering the actual atmospheric, instrumental, and observational (e.g. the sun position relative to the pointing) parameters, the geolocation and the pointing of the telescope as described in detail in Hüneke [2016]; Hüneke et al. [2017]. Precisely, McArtim is used to simulate the intensity weighted photon path length distribution L_i of photons of a given wavelength and altitude layer i of depth h_i and the absorption coefficient $\beta_{a,i}$ under the assumption of a cloud-free single scattering atmosphere,

$$B_i(\lambda) = -\frac{1}{I(\lambda)h_i}\frac{\delta I(\lambda)}{\delta\beta_{a,i}} \approx \frac{L_i}{h_i} \tag{3.3}$$

[Deutschmann et al., 2011]. The resulting B_i is referred to as box air mass factor and gives a handle on the sensitivity of a trace gas for absorption at altitude i relative to all altitudes. From eq. 3.3 follows directly a key difference of atmospheric Limb and Nadir observation geometries, which are both treated in this thesis. Limited by the observation altitude (here the flight altitude of the research aircraft), the light paths of the observed photons in Nadir direction are for most cases significantly shorter than in Limb direction (compare Fig. 3.5 and sect. 3.1.3). $\mathrm{B_{i,Nadir}}$ (e.g. Fig. 3.8, panel a) is therefore significantly smaller than $\mathrm{B_{i,Limb}}$ (up to 10^2). The measurement sensitivity with respect to the absorption of photons is therefore significantly smaller in the Nadir observation geometry. In particular for the analysis of weakly absorbing trace gases, such as in the present study, this complicates the retrieval and enlarges the measurements uncertainty. This aspect is discussed in more detail in sects. 3.1.3.1 and 3.1.3.2.

For the McArtim simulations, the atmosphere is describe as detailed as possible by a combination of climatological aerosol profiles obtained by LIVAS [Amiridis et al., 2015] and the

Stratospheric Aerosol and Gas Experiment II (SAGE II)[3] as well as temperature, pressure and humidity measurements[4]. Further parameters include the surface albedo (usually 0.3 for continental measurements), the single scattering albedo (SSA), the asymmetry parameter (g), and the a priori assumed vertical altitude profiles of all included trace gases (see below and Fig. 3.4). SSA and g are inferred from the OPAC model (Optical Properties of Aerosols and Clouds; Hess et al. [1998]). Depending on the relative humidity and further air mass characteristics (pristine to polluted), for the different research missions follows SSA≈ 0.68 and g$= 0.85 - 0.99$ (vis) and SSA≈ 0.68 and g$= 0.86 - 0.99$ (UV). The box air mass factors are simulated at 377 nm and 460 nm for the UV and visible spectral ranges, respectively. The application of the simulations performed under a clear-sky assumption into an all-sky, cloudy atmosphere is performed following the scaling method as described above. The validity of this approach has been confirmed in different previous studies (e.g. Knecht [2015]; Hüneke et al. [2017]) and is further analysed in the present thesis based on the ACRIDICON-CHUVA measurements under a complex cloud cover (i.e. shallow stratocumulus and cumulonimbus clouds) over the tropical rainforest, a very moist atmosphere with quickly changing cloud mixture.

The α-factors are inferred from the concentration weighted sum of the simulated air mass factors (Stutz et al. [2017], eq. (11)). To obtain the vertical O_4 profile, the extinction due to $[O_4]_j$ is calculated. For the target gases CH_2O, $C_2H_2O_2$, $C_3H_4O_2{}^*$, in a first step a priori profiles are used based on previous mini-DOAS measurements in similar atmospheric conditions (clean and polluted terrestrial air or remote marine air), and subsequently iterated until convergence is achieved (see below). If previous measurements are not available, an exponentially decaying profile is assumed in a first iteration step. The latter appears justified because of photochemical arguments, the source distribution (mostly surface), the short photochemical lifetimes, the time scales of possible vertical transport as well as when inspecting the profile shapes obtained in the post-analysis (Fig. 5.11). The following section briefly demonstrates the robustness of the retrieved glyoxal concentrations with respect to the necessary a priori assumptions in the radiative transfer (RT) calculations. In a first step, the RT model is run using mini-DOAS a priori glyoxal profiles obtained during previous missions and assuming an exponentially decaying profile above the maximum flight altitude. Secondly, an averaged glyoxal profile is inferred along an example flight track over central Europe on 15 May 2018 from simulations of the global chemical transport model MAGRITTE, that is also used for the TROPOMI glyoxal retrieval (e.g. Bauwens et al. [2016]; Lerot et al. [2021]). Both a priori profiles show notable differences in their absolute mixing ratios as well as in their vertical shape (Fig. 3.4, panels a and b). In the following, iterations of the radiative transfer simulation are performed using consecutively the resulting profiles from both approaches as new a priori profiles (Fig. 3.4, panels a and b). Evidently, even strongly diverging a priori assumptions converge well after the first iteration to a common profile within the error margins. After four iterations, no notable changes are observable any more in the obtained a priori profiles as well as in the resulting mixing ratios (Fig. 3.4, panel c), thus demonstrating the robustness of the scaling method with respect to the necessary a priori assumptions. This insensitivity of the resulting profile towards the assumed a priori profile is a direct consequence of the applied scaling method, because all a priori profiles of the target gas are evaluated relative to the scaling gas (in this study O_4), of which the atmospheric absorption is measured. Without iteration, the scaling method is therefore moderately sensitive to the relative differences in the assumed profile shapes (Fig. 3.4, panel b), but not to the absolute concentrations assumed in the a priori profiles. As demonstrated above, this remaining sensitivity can sufficiently be reduced by performing a second iteration of the radiative transfer model when calculating the α-factors.

---

[3] `https://eosweb.larc.nasa.gov/project/sage3/sage3_table`

[4] During all missions, avionic and climatological measurements were performed by the Basic HALO Measurement And Sensor System (BAHAMAS) operated by the DLR-FX Sensor and Data group [Krautstrunk and Giez, 2012].

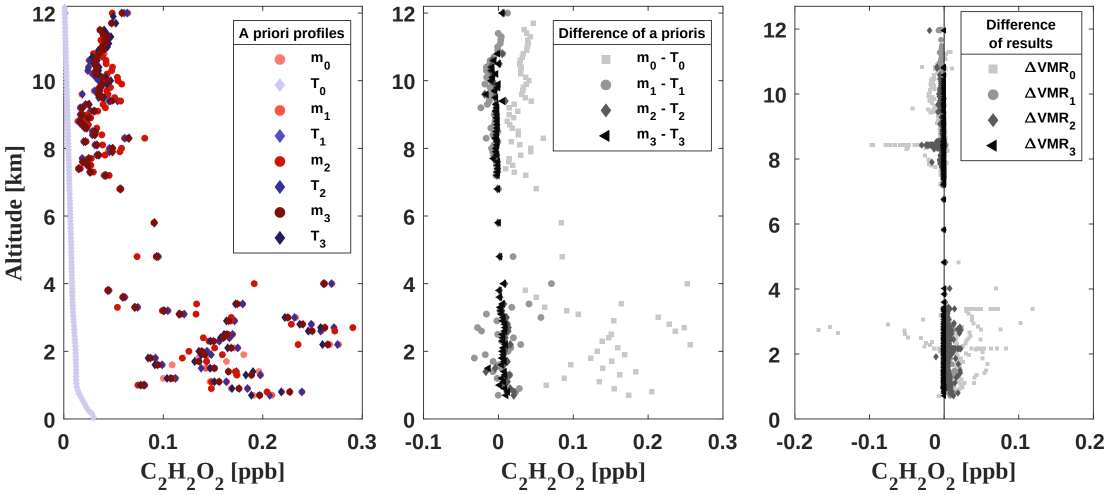

Figure 3.4: Iteration of different a priori glyoxal profiles in α-factor calculations, here for the HALO flight on 15 May 2018 (CoMet mission). Starting a priori profiles are a mean glyoxal profile inferred from previous mini-DOAS measurements in polluted continental air ($m0$), and averaged MAGRITTE CTM simulated glyoxal profiles (T_0) for a TROPOMI overpass over Europe at 13:30 UTC on 15 May 2018 [Lerot et al., 2021]. The a prioris are used in the first iteration of α-factor calculations. The resulting profiles are then used for the following i iterations to obtain the profiles mi and Ti, respectively. The differences of each iteration step in the a priori and the finally resulting profiles (based on the respective α-factor simulation) are plotted in panels b and c.

When needed, the total atmospheric column density of the respective gases is approximated from the Limb measurements by integrating the measured lower and higher quartile profiles in incremental steps of 100 m each (Figs. 5.7 and 5.14).

For the Nadir measurements, the measured Nadir slant column densities $\mathrm{SCD}_{\mathrm{nadir,X}}$ of the trace gas X are converted to vertical column densities $\mathrm{VCD}_{\mathrm{X}}$ according to

$$\mathrm{VCD}_{X,i} = SCD_{nadir,X,i} \cdot \frac{\sum [X]_i \cdot z_i}{\sum [X]_i \cdot z_i \cdot B_i}, \tag{3.4}$$

using box air mass factors B_i simulated by the McArtim model for each layer i of thickness z_i and the same a priori concentrations $[\mathrm{X}]_i$ as used for the Limb measurements.

3.1.3 Averaged atmospheric volume

The average atmospheric volume analysed from each spectrum (i.e the averaging kernel) can be approximated based on the aircraft displacement (vertical and horizontal) during the spectrum integration time as well as the telescope's field of view (0.5° vertical, 3.15° horizontal) and the mean photon path length of the detected photons (Limb) or the measurement altitude (Nadir, clear sky assumption), respectively. The latter two processes are considered in the evaluation and respective RT calculations. Typical light path lengths and approximated averaging volumes as well as a detailed discussion of the implications of airborne Limb measurements, e.g. the origin of the detected photons (below, above, in line-of-sight of the aircraft), or the influence of cloudy sky conditions on the measurements are discussed in the following.

3.1.3.1 Limb viewing geometry

In the Limb viewing geometry, the averaged atmospheric volume mainly depends on the mean photon path lengths PL of the Limb detected photons. PL at the flight altitude j can be

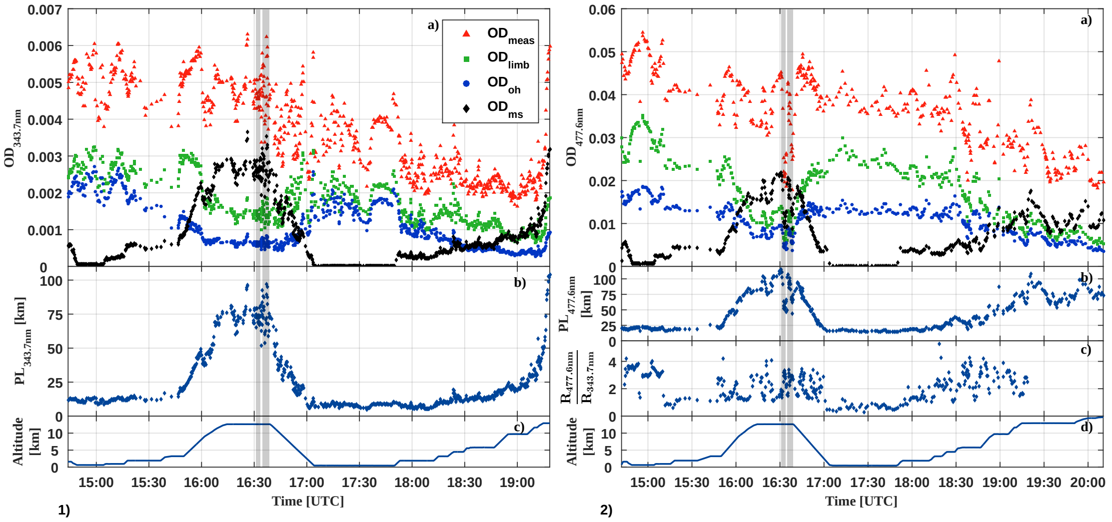

Figure 3.5: Attribution of the total measured optical depth of O_4 at 343.7 nm (panel 1 on the left) and at 477.6 nm (panel 2 on the right) to the various fractions, i.e. absorption from overhead the aircraft (OD_{oh}), from multiple scattering below the aircraft (OD_{ms}), within the line-of-sight of the telescopes (OD_{limb}), and the total measured optical depth of O_4 (OD_{meas}) for the ACRIDICON-CHUVA HALO flight on 16 Sept. 2014 (panels 1a, 2a). The average line-of-sight photon path length inferred from the measured OD_{meas} at 343.7 nm and 477.6 nm, respectively, as a function of the flight time is plotted in panels (1b), (2b). The colour ratio $\frac{R_{343.7}}{R_{477.6}}$ of the measured radiances at 343.7 nm versus 477.6 nm is shown in panel (2c). The flight trajectory of the HALO aircraft is shown in panels (1c) and (2d). The sharp drop of the optical depth between 16:32–16:34 UTC and 16:35–16:39 UTC (grey bars) coincides with the passage of a cumulonimbus cloud in front of the telescopes. For details see the text.

approximated for each single recorded spectrum according to

$$PL_j \approx \frac{OD_{O4,j}}{\epsilon_{O4,j}} \tag{3.5}$$

by comparing the measured (real sky) optical density OD_{O4} and the calculated (clear sky) atmospheric extinction (ϵ_{O4}) of O_4,

$$\epsilon_{O4,j} = \sigma_{O4} \cdot k_{eq} \cdot [O_2]_j^2 = \sigma_{col} \cdot [O_2]_j^2 \,. \tag{3.6}$$

Here, σ_{O4} denotes the absorption cross section of O_4, k_{eq} its equilibrium constant and $[O_2]_j$ the oxygen concentration in the altitude j. The peak collision pair absorption cross section $v\sigma_{col}$ of O_4, i.e. the cross section related to the collisional absorption structures of the O_2-O_2-complex [Pfeilsticker et al., 2001], $\sigma_{col} = \sigma_{O4} \cdot k_{eq}$, is determined by laboratory measurements (e.g. Thalman and Volkamer [2013]). In the visible wavelength range, PL ranges from ~ 10 km (at 2 km altitude) to about ~ 100 km at the maximum flight altitude of the aircraft around 15 km, depending on the wavelength, aerosol concentration and cloud cover. In the UV spectral range, the larger fraction of Rayleigh scattered photons reduces the median upper tropospheric light paths to ~ 75 km (Fig. 3.5, panels 1c and 2c).

Attribution of the observed absorption to different atmospheric layers

Evidently, UV/vis Limb measurements naturally divide the atmosphere into three different layers, which are separated by the different contributions to the total absorption or optical depth. These contributions are (a) the overhead absorption OD_{oh}, (b) the absorption located within the line-of-sight of the telescopes OD_{limb} (of which most, but not all is due to single scattering), and (c) the absorption below the line of sight OD_{ms} (of which the photon paths are necessarily

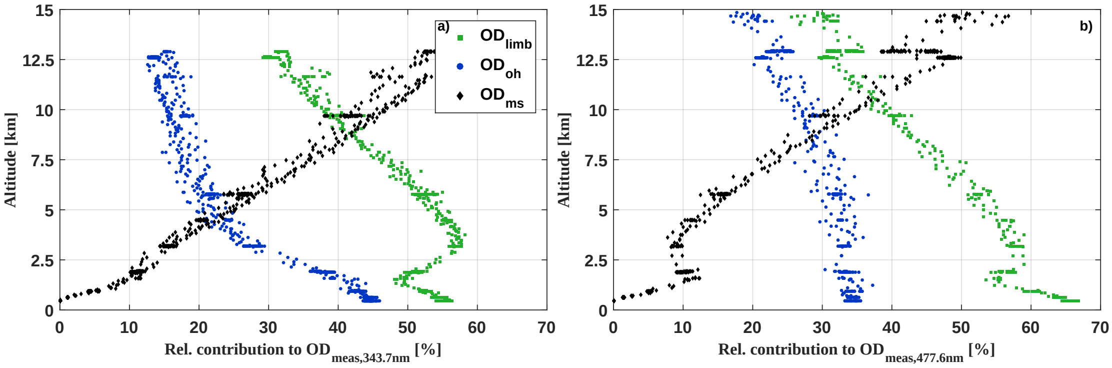

Figure 3.6: Relative contribution to the limb measured optical depth of O_4 at 343.7 nm (panel a) and at 477.6 nm (panel b) due to the absorption overhead the aircraft (OD_{oh}), from multiple scattering (OD_{ms}), and within the line of sight of the telescopes (OD_{limb}) for the ACRIDICON-CHUVA HALO flight on 11 Sept. 2014.

all of higher scattering order). In the following, the significance of the different contributions is exemplarily discussed for O_4. Evidently, the same tri-partitioning applies for all other gases of interest, however differently weighted as expressed by the respective α-factors. For a high-flying aircraft, OD_{oh} has the least uncertainty since O_4 absorption approximately scales with $[O_2]^2$ and the optical state of the overhead atmosphere is well known. Therefore, the remainder of the measured total O_4 absorption has to be due to the varying contributions of OD_{limb} and OD_{ms}, which are mostly modified by the current low level cloud cover and ground albedo (Stutz et al. [2017], Fig. 7). The knowledge of the α-factor however gives a handle on the relative fractions OD_{limb} and OD_{ms}, since contribution OD_{limb} can be calculated from $OD_{limb} = \alpha \cdot OD_{meas}$, and accordingly $OD_{ms} = OD_{meas} - OD_{oh} - OD_{limb}$. Still, the calculated attributions of OD_{limb} and OD_{ms} to OD_{meas} can only be approximated due to the assumptions made regarding the current aerosols distribution and the cloud coverage.

Figure 3.5 illustrates the contributions to OD_{meas} at 343.7 nm (panel 1a) and 477.3 nm (panel 2a) for O_4 as a function of the flight time for a flight over the Amazon rainforest on 16 Sept. 2014. Figure 3.6 shows the same data, but sorted by flight altitude to demonstrate the relative change of the contributions. Up to 10 km altitude and for both investigated wavelengths, the absorption within the line of sight of the telescopes contributes with more than 50% to the total O_4 absorption. A relative minimum can be seen at the top of the planetary boundary layer at approximately 2 km, where often stratocumulus clouds prevail over the Amazon. Further, a maximum of OD_{limb} is visible at about 4 km, most probably a result of the increasing horizontal visibility with altitude and the moderate contribution of reflected multiple scattered photons from the lower atmosphere to the total O_4 absorption. In the upper troposphere, the relative contribution of OD_{limb} to OD_{meas} decreases while the effective horizontal light paths become longer and reach maximum values around 100 km. But given all uncertainties in the details of the actual atmospheric aerosol content, the cloud structure and coverage and their optical properties, it is more reasonable to speak here of an indication rather than a determination of the photon path lengths.

Above uncertainties do not propagate into the uncertainty of the α-factor ratio and hence into the determination of $[X]_j$, provided the gases X and P have sufficiently similar profile shapes to meet the conditions of the equivalence theorem of Irvine [1963] [Knecht, 2015; Hüneke et al., 2017; Stutz et al., 2017]. From the above discussion, it also becomes clear that the airborne UV/vis Limb measurements average over some atmospheric volume, which is determined by the viewing angle of the telescope lenses (0.38°), the light path length, and the aircraft displacement during the time of measurement, both of which are on the order of several kilometres. Typical integration

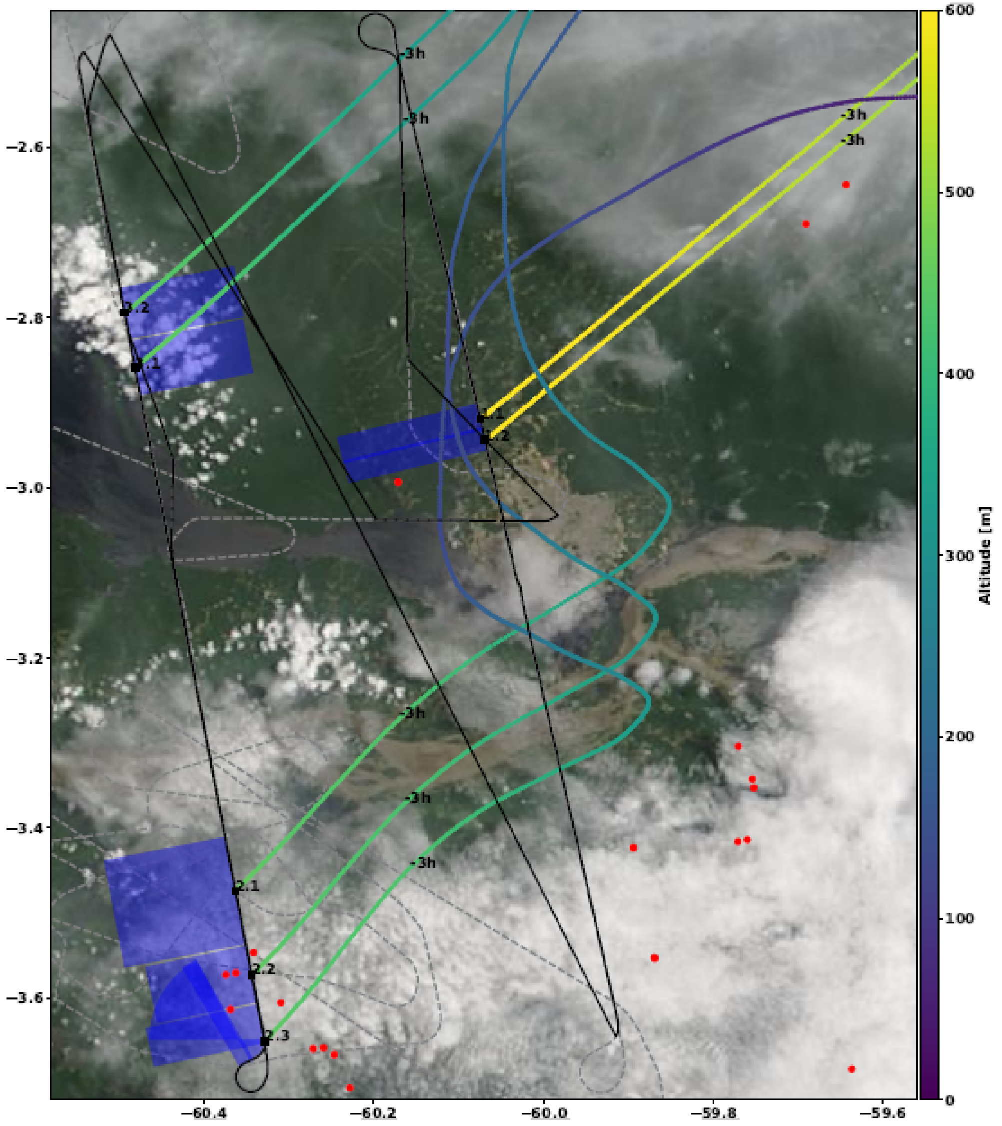

Figure 3.7: Averaged atmospheric volume of example Limb measurements during the ACRIDICON-CHUVA flight on 16 Sept. 2014. The flight trajectories below/above 1000 m altitude are labelled by drawn/dashed lines, respectively. The take-off and landing of the aircraft was from Manaus airport (3.1° S, 60.0° W), located in the centre of the image. The biomass burning events detected by the MCD14 MODIS instrument on the Terra and Aqua satellites are indicated with red dots (not to scale). The biomass events probed by the mini-DOAS instrument are marked by black numbers next to the flight track, according to the labelling of Table 5.2. The blue rectangles approximately indicate the probed air masses in the horizontal plane, where the distance perpendicular to the flight track is given by the O_4 estimated photon path lengths (14 to 19 km), and the along-track distance (3 to 15 km) by the spectrum integration time (33 to 166 s) multiplied by the aircraft ground speed (approximately 95 $\mathrm{m\,s^{-1}}$). For each biomass burning event, 3 h backward air mass trajectories were calculated and plotted colour-coded by the altitude of the airmass. The MODIS satellite image was taken from NASA WORLDVIEW, see `https://worldview.earthdata.nasa.gov/`.

times of the measured co-added sets of skylight spectra range from seconds (under clear sky conditions) to several minutes (during cloudy sky and hazy conditions). In consequence, the along-track resolution of the measurements was typically several kilometres, while the horizontal resolution perpendicular to the aircraft is determined by the radiative transfer parameters (sect. 3.1.2). A two-dimensional visualization of the resulting averaging (or probed) areas per single measurement is indicated for example measurements (labelled with 1–3) of biomass burning plumes over the Amazon rainforest around Manaus by the blue areas in Fig. 3.7 along with corresponding 3 h backwards air masses trajectories of the probed air masses. The resulting sampling volume precludes direct comparisons with in situ measured quantities on spatial scales smaller than the current averaging volume. This is of relevance to the present study, for example when adding information from in situ measurements like CO to the analysis of the data.

3.1.3.2 Nadir viewing geometry

In the Nadir observation mode, the instrument measures the atmospheric column density of the target gases particularly below the aircraft (Fig. 3.8) with a rectangular foot print of $\approx$ 600 m cross-track and several kilometre along-track (FOV 3.15° × 0.38°; [Hüneke, 2016]), depending on the flight altitude, cruise velocity (typically $\sim$ 200 ms^{-1} in the upper troposphere), and signal integration time (up to 1 min). For flight altitudes above 8 km in a moderately humid to dry atmosphere, the typical footprint for a signal integration time of 14 s is 4.2×0.6 km^2. For measurements in a moist atmosphere or over the pristine oceans, occasionally up to 150 spectra were co-added (South Atlantic measurements), thus extending the Nadir along-track resolution in some extreme cases up to 230 km. However, the median Nadir along-track resolution over the South Atlantic is much smaller and on the order of 32 km. The spectral co-adding significantly enlarges the footprint for a minor fraction of the measurements, but at the same time favours the detection limit, which is helpful for monitoring glyoxal at low VCDs, i.e. far away from distinct sources such as over the open ocean. Flight tracks over the ocean (which frequently occurred during the CAFE and SouthTRAC missions) are usually far away from distinct sources of the analysed gases, therefore requiring low detection limits, but at the same time allowing for larger foot-prints. In the other regions, where no or only a few spectra need to co-added, the median Nadir along-track resolution is 4 km (Europe, Mediterranean and East China Sea, Tropical and North Atlantic).

3.1.4 Comparison of airborne and spaceborne Nadir measurements

The comparison of airborne and spaceborne Nadir measurements comes with certain method-based complications. In order to keep such methodological differences small, for the comparison to the TROPOMI satellite measurements the airborne mini-DOAS data need to be filtered for specific parameters, e.g. the flight altitude and the solar zenith angle (SZA). This is discussed in more detail in the following section.

For weakly absorbing substances (as it is the case for glyoxal), the box air mass factors for the satellite and the aircraft Nadir measurements are expected to be similar provided the observation geometry and the assumptions regarding Rayleigh and Mie scattering, and the ground reflection (albedo) are similar. While the assumptions regarding Rayleigh and Mie scattering and the ground reflection are similar for the satellite and airborne measurements discussed in this thesis, the observation geometry is only similar for a high flying aircraft (see below).

In order to understand the relative sensitivity of the Nadir observing satellite and aircraft measurements, it is necessary to inspect the product $[\mathrm{X}]_j \cdot \mathrm{B}_j$ (with $[\mathrm{X}]_j$ being the trace gas concentration and B_j the box air mass factor in the altitude layer j). The product expresses the relative contribution of the absorption (or slant column density) of the altitude layer j to the total absorption (or slant column density; see eq. 3.4 and Fig. 3.8). The a priori glyoxal profiles ($[\mathrm{X}]_j$ in all tropospheric altitudes) assumed in the satellite and the airborne retrieval are similar in shape, but not the same. If the a priori glyoxal profiles used in the satellite retrieval would be used for the airborne measurements, the information on glyoxal obtained from the airborne Limb observations would be ignored. Therefore, the airborne measured a priori profiles are used for the aircraft glyoxal retrieval, while for the satellite retrieval the MAGRITTE CTM a priori profiles are kept for the box air mass factor simulations [Lerot et al., 2021]. In fact, the profile measurements (section 5.1.1) indicate that the actual glyoxal profiles are much more structured in the vertical than any CTM can portray. Therefore, in the box air mass factor simulations, climatological glyoxal profiles are used in which the concentration peaks due to individual plumes are removed. RT simulations show that this removal of the (in altitude localised) glyoxal peaks only slightly changes the total glyoxal vertical column density (sect. 3.1.5).

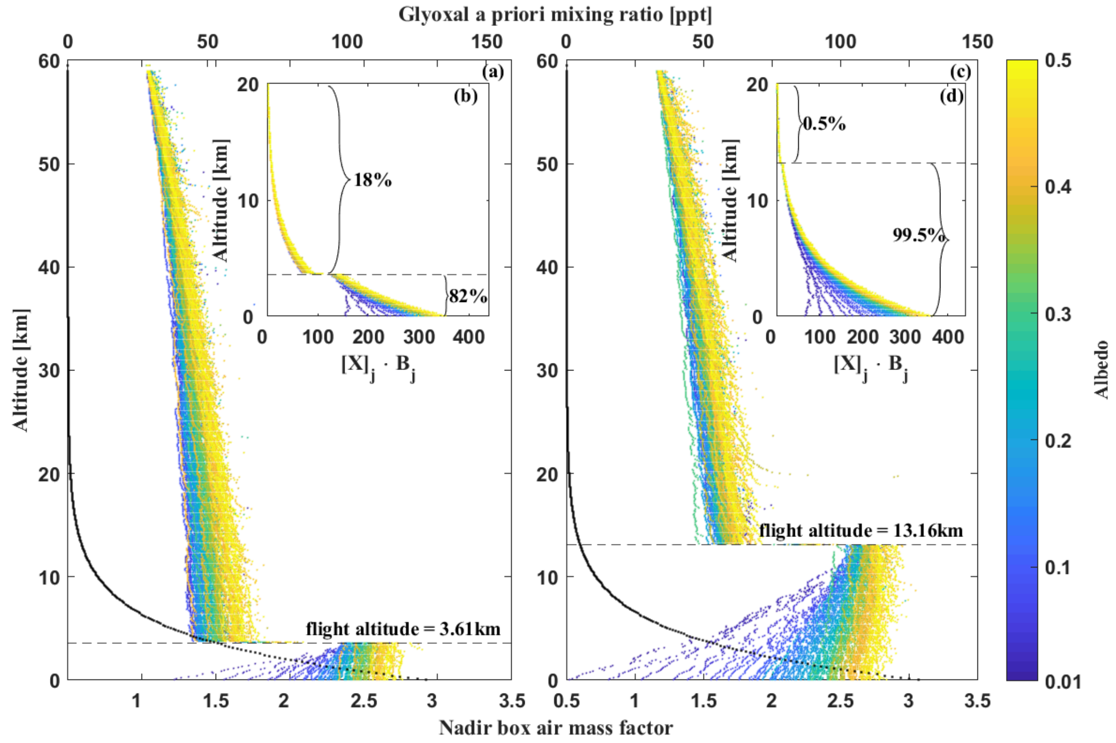

Figure 3.8: Box air mass factors (B_j, lower x-axis pf panels a and c) of two mini-DOAS Nadir measurements in the lower (panels a and b) and upper (panels c and d) troposphere for changing surface albedos between 0.1 and 0.5 (colour-code). Both measurements were performed during a research flight from Oberpfaffenhofen (Germany) to Sal (Cape Verde) on 07 Aug. 2018 (flight CA03, for a detailed flight description see table C.7 and Fig. C.2, panel d). The product of B_j and the assumed a priori glyoxal concentration $[\mathrm{X}]_j$ (upper x-axis of panels a and c, black line) yields the relative contribution of each altitude layer j (panels b and d). Evidently, even airborne Nadir measurements at lower altitudes predominantly, but not exclusively, probe the atmosphere below the flight altitude. This causes the necessary restriction to upper tropospheric flight altitudes for an airborne and spaceborne measurement comparison as discussed in sect. 5.1.2.

Further, the profile measurements often indicate relatively larger glyoxal at lower altitudes than the MAGRITTE CTM predicts (e.g. Fig. 3.4, panel a). In consequence, the box air mass factors as well as the product $[\mathrm{X}]_j \cdot \mathrm{B}_j$ tend to differ for both retrievals. Due to the different assumptions for $[\mathrm{X}]_j$ and B_j in the altitude layers j, the satellite and aircraft retrievals attribute different fractions of the total absorption to each j (see eq. 3). In particular, these differences in

$[X]_j$ and B_j yield different relative fractions $\sum_{j>i}^{j_{max}}[X]_j \cdot B_j$ of the total absorption above the aircraft flight altitude i (Fig. 3.8).

For a high flying aircraft, the similar observation geometries of aircraft and satellite result in a similar sum $\sum_{j_{min}}^{j_{max}}[X]_j \cdot B_j$ and hence a similar detection sensitivity for glyoxal (even though the products of single altitude layers j may be different). However, for low flight altitudes the contributions $[X]_j \cdot B_j$ are largely different. The latter primarily results from the fact that, for Nadir observations B_j is larger (smaller) for altitudes j smaller (greater) than the aircraft flight altitude i as compared to those for the satellite, and less due to differences in the assumed $[X]_j$. Equally, airborne Nadir observations from low altitudes tend to be more sensitive for detecting trace gases in the lower atmosphere, than those performed from the satellite.

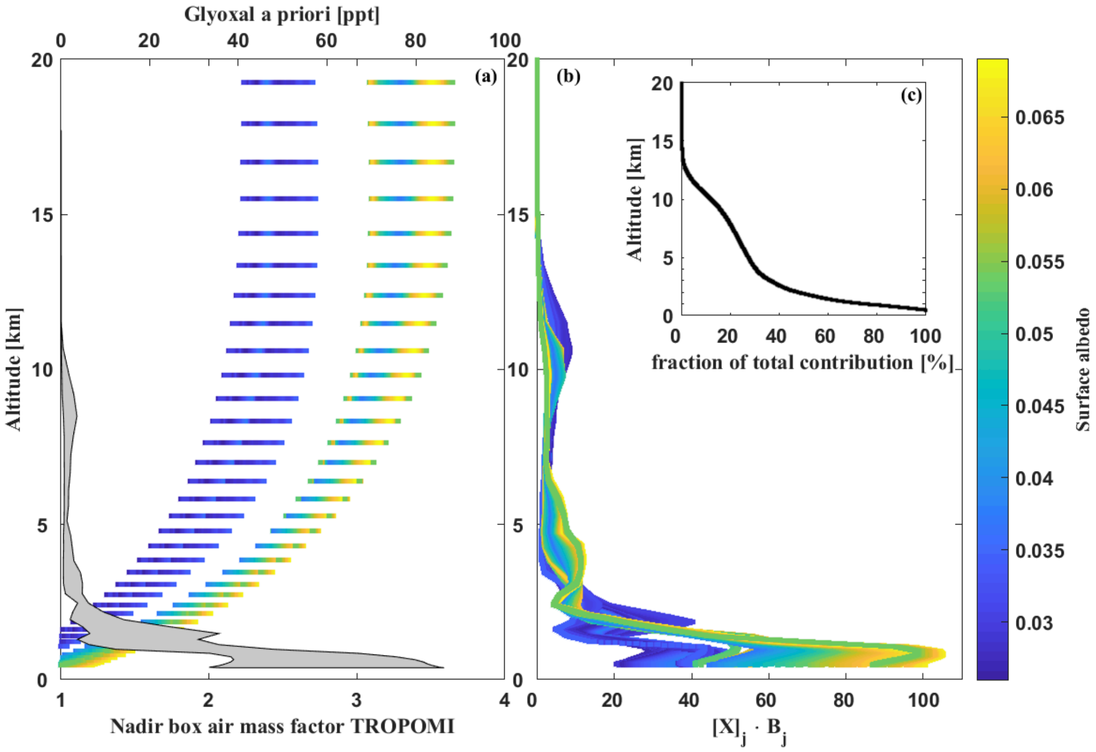

Figure 3.9: Tropospheric box air mass factors (B_j, panel a, lower x-axis) for TROPOMI Nadir observations, colour-coded by the respective surface albedo, and the range (gray area) of a priori glyoxal profiles ($[X]_j$, panel a, upper x-axis) for the continental section of the research flight on 7 Aug. 2018. All B_j and a priori profiles are averaged on a 0.25° × 0.25° area around each mini-DOAS measurement during the flight. The product of B_j and the assumed a priori glyoxal concentration $[X]_j$ yields the relative contribution of the altitude layer j (panel b). Panel (c) shows the relative contribution $\frac{\sum_{i>j}^{TOA}[X]_i \cdot B_i}{\sum_{i=0}^{TOA}[X]_j \cdot B_j}$ as a function of the altitude j (in viewing direction of the satellite, i.e from top down). The two branches of the B_j distribution (panel a) result from a local increase in the simulated surface albedo and AMFs above Spain and western France (Fig. B.1).

In consequence, for an optimal and biased-minimized inter-comparison between satellite and aircraft Nadir observations (which respects the similarities in observation geometry and hence detection sensitivity), the Nadir observations from the high flying aircraft need to be preferred over those performed from a low flying aircraft. Vice versa, airborne Nadir observations from low altitudes tend to be more sensitive for detecting trace gases in the lower atmosphere than those performed from the satellite. Therefore, for the comparison of the mini-DOAS Nadir measurements with satellite observations, only VCDs inferred in > 8 km flight altitude are used, where over 95% of the total contribution $\sum_{j=0}^{TOA}[X]_j \cdot B_j$ is expected below the aircraft (compare Fig. 3.8, panels c and d).

Further, provided that the satellite and the aircraft observations have a similarly sized footprint (which is the case here when not adding individual satellite pixels) and technical outline (FOV, photon detection sensitivity) due to the largely different cruising velocities (Sentinel 5P 7500 $\mathrm{m\,s^{-1}}$ versus aircraft 200 $\mathrm{m\,s^{-1}}$), the aircraft may observe a specific scene about a factor of 37.5 times longer than the satellite, hence it integrates over respectively more photons. Given that the detection limit of both instruments is determined by the photon shot noise, the aircraft measurements are about a factor of six ($\approx \sqrt{37.5}$) times more sensitive for the detection of glyoxal in individual spectra than those of the satellite. Accordingly, to obtain the same limit for glyoxal detection from both instruments, i.e. in order to reduce the noise of the satellite, multiple measurements of the satellite instrument need to be averaged.

Finally, all satellite detected VCDs are strictly filtered for potential cloud and aerosol interferences [Lerot et al., 2021]. As a consequence, for the remaining measurements TROPOMI radiative transfer simulations assume surface albedos of about 0.05 (Fig. 3.9 and Lerot et al. [2021]). Since for the airborne measurements an equivalent filter is neither necessary (for the Limb measurements) nor possible (for the Nadir measurements), a respectively larger all-sky albedo of 0.3 is assumed for the airborne radiative transfer simulations (Fig. 3.8).

3.1.5 Measurement uncertainties

Summing-up all described uncertainties, the precision error of the combined methods in the Limb geometry can be approximately calculated according to eq. (3.2) as

$$[\Delta X]_{j,Limb} = \sqrt{\left(\frac{\Delta\alpha_{R,j}}{\alpha_{R,j}}\right)^2 + \left(\frac{\Delta S_{X,j}}{S_{X,j}}\right)^2 + \left(\frac{\Delta S_{P,j}}{S_{P,j}}\right)^2 + \left(\frac{\Delta P_j}{P_j}\right)^2} \cdot [X]_j\,, \tag{3.7}$$

where $\Delta\alpha_{\mathrm{R,j}}$ accounts for (a) the random and unknown part of the Mie extinction, (b) the small scale variability of the target and scaling gas mixing ratios at flight level and (c) the uncertainty in the sampling contribution as discussed in Figs. 3.5 and 3.6. The slant column errors $\Delta\mathrm{S_{X,j}}$ and $\Delta\mathrm{S_{P,j}}$ account for (a) uncertainty of the inferred Fraunhofer reference SCD and (b) the DOAS fit error. $\Delta\mathrm{P}_j$ accounts for the uncertainty of the in situ mixing ratio of the scaling gas, which in the case of O_4 scales with the air density and is accordingly limited by the measurement uncertainty of pressure and temperature. Additionally, the systematic errors of the individual absorption cross sections need to be added to $\Delta\mathrm{S_{X,j}}$ according to Table 3.1. An extensive discussion of the total error budget of the O_4 scaling can be found in Hüneke [2016].

Important implications of the Limb measurement uncertainties on the data are briefly discussed in the following exemplary for the ACRIDICON-CHUVA measurements. While $\Delta\mathrm{P}_j$ and $\Delta\alpha_{\mathrm{R,j}}$ contribute approximately constantly for changing j to the total error budget, $\Delta\mathrm{S_{X,j}}$ strongly increases with decreasing slant column density. For mixing ratios below 1 ppb (CH_2O), 0.15 ppb ($C_2H_2O_2$), and 1.3 ppb ($C_2H_4O_2{}^*$), the total precision error is strongly dominated by $\Delta\mathrm{S_{X,j}}$. For higher mixing ratios, $\Delta\alpha_{\mathrm{R,j}}$ and $\Delta\mathrm{S_{X,j}}$ contribute in equal parts to the total precision error of $C_2H_2O_2$ and $C_2H_4O_2{}^*$. For CH_2O, $\Delta\alpha_{\mathrm{R,j}}$ is the major error factor for mixing ratios above 1 ppb, and $\Delta\mathrm{S_{X,j}}$ only makes up 30% of the total error. For all gases, $\Delta\mathrm{P}_j$ never exceeds 7% of the total precision error. Due to the strong dependence of $\Delta\mathrm{S_{X,j}}$ on the slant column density and the exponentially decreasing vertical profiles of the gases, the resulting total precision errors $[\Delta\mathrm{X}]_j$ are strongly altitude dependent (Fig. 3.10). They range from 16% to 100% for CH_2O, 17% to 100% for $C_2H_2O_2$, and 16% to 100% for $C_2H_4O_2{}^*$. For measurements of biomass burning plumes below 2 km altitude, the total errors of the analysed biomass burning events are on average 21%

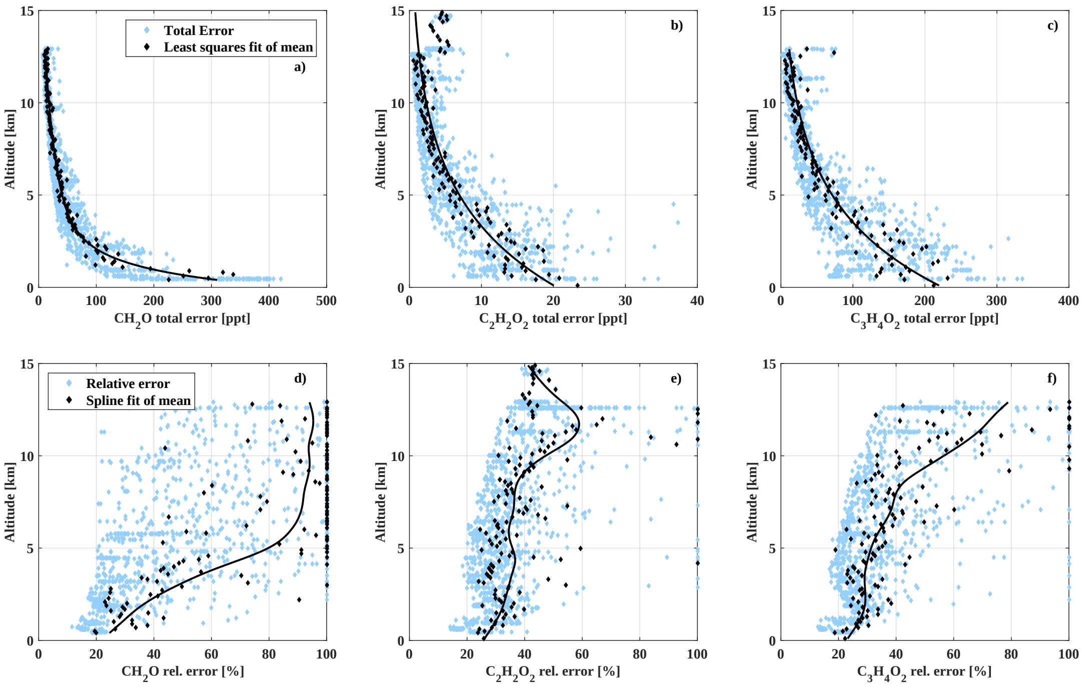

Figure 3.10: Relative and absolute total precision error of all ACRIDICON-CHUVA measurements as a function of the measurement altitude.

for CH_2O (upper and lower limit of the total precision errors are 350 ppt and 740 ppt), 25% for $C_2H_2O_2$ (total errors from 30 ppt to 45 ppt), and 22% for $C_2H_4O_2{}^*$ (total errors from 240 ppt to 560 ppt), respectively.

In the Nadir geometry, the combined precision error is predominantly determined by the uncertainty of the box air mass factors ($\Delta \mathrm{BAMF}_j$) and of the slant column density ($\Delta \mathrm{S}_{\mathrm{X,j}}$). $\Delta \mathrm{BAMF}_j$ is mainly controlled by radiative transfer uncertainties due to deviations of the assumed and actual surface albedo (Fig. 3.8). For all mini-DOAS measurements, an average all-sky albedo of 0.3 is assumed. For clear sky measurements over dark sceneries (e.g. the ocean surface), this may lead to an overestimation of the actual B_j on the order of 0–20%, with the largest deviation in the boundary layer. Equally, for measurements over a very bright cloud or ice cover (e.g. flights over the Antarctic ice shelves), the albedo approximation may cause an underestimation of B_j by up to 20% (Fig. 3.8). However, for all altitudes $[\Delta \mathrm{X}]_{\mathrm{j,Nadir}}$ is dominated by the uncertainty of $\mathrm{S}_{\mathrm{X,j}}$, which contributes on average 65 % to the total precision error. Uncertainties in the assumed a priori profile are minimized by iterating the a priori observations if necessary as described above (i.e. if no prior mini-DOAS measurements in comparable air masses are available). For the a priori glyoxal profiles, distinctive peaks in the observed profiles due to individual emission events are removed (compare Fig. 5.1 and sect. 3.1.4). Based on radiative transfer simulations using glyoxal a priori profiles including and excluding such peak events, this restriction to climatological glyoxal profiles induces median changes in the contribution $[\mathrm{X}]_j \cdot \mathrm{B}_j$ of $< 2\%$.

3.2 Additional instrumentation and model simulations

For the analysis of the mini-DOAS measurements, the present thesis relies on simultaneous observations of additional instruments aboard the HALO aircraft as well as measurements of the satellite instrument TROPOMI and finally glyoxal simulations of the ECHAM/MESSy Atmospheric Chemistry model (EMAC). The additional instruments and the EMAC model simulations are described in more detail below.

3.2.1 AMTEX instrument

The Aero-Laser 5002 vacuum UV resonance fluorescence (AMTEX) instrument performs in situ CO measurements aboard the HALO aircraft at 1 Hz resolution and 1.5 ppb precision [Gerbig et al., 1996, 1999; Huntrieser et al., 2016a,b]. AMTEX samples air at a rate of 40 $\mathrm{mL\,min^{-1}}$ through an inlet mounted on top of the aircraft. The detection of CO is based on resonance fluorescence of the fourth positive CO band around 151 nm by a radio frequency discharge resonance lamp [Gerbig et al., 1996].

This thesis uses AMTEX CO measurements during the ACRIDICON-CHUVA mission in 2014 for a better analysis of the atmospheric composition and biomass burning plume identification.

3.2.2 TROPOspheric Monitoring Instrument

The TROPOspheric Monitoring Instrument (TROPOMI) is a spaceborne Nadir looking imaging spectrometer based on the Copernicus Sentinel-5 Precursor satellite platform. It was initiated to fill the gap between previous (SCIAMACHY [Bovensmann et al., 1999], GOME-2 [Munro et al., 2016], and OMI [Levelt et al., 2006]) and the future Sentinel-4 and Sentinel-5 missions from the Copernicus Earth observation programme by the European Union [Ingmann et al., 2012]. Since its launch in October 2017, TROPOMI provides daily Nadir measurements of solar irradiance and Earthshine radiance spectra by four spectrometers that cover the ultraviolet, visible, and near and shortwave infrared spectral ranges. TROPOMI is located in a low-earth orbit with local equator crossing time of 13:30 LT [Veefkind et al., 2012]. Currently, TROPOMI is the most up-to-date spaceborne instrument to provide Nadir trace gas measurements of the atmosphere, with a remarkable timely (daily global coverage) and above all spatial resolution of $3.5 \times 5.5\ \mathrm{km}^2$ for single observations. Such as the mini-DOAS Nadir spectrometers, TROPOMI exploits backscattered solar light to infer column integrated concentrations, from which vertical column densities can be inferred for the different trace gases. The present study uses TROPOMI glyoxal VCDs for a detailed comparison of airborne and satellite based glyoxal measurements. A detailed technical description of the instrument can be found e.g. in Kleipool et al. [2018]; Ludewig et al. [2020]; Lerot et al. [2021].

3.2.3. ECHAM/MESSy Atmospheric Chemistry model simulations

The glyoxal concentration and VCD measurements performed in this study are compared to glyoxal simulations from the ECHAM/MESSy Atmospheric Chemistry (EMAC) model. According to `https://www.messy-interface.org/`, ”the ECHAM/MESSy Atmospheric Chemistry (EMAC) model is a numerical chemistry and climate simulation system that includes sub-models describing tropospheric and middle atmosphere processes and their interaction with oceans, land and human influences [Jöckel et al., 2010]. It uses the second version of the Modular Earth Submodel System (MESSy2) to link multi-institutional computer codes. The core atmospheric model is the 5th generation European Centre Hamburg general circulation model (ECHAM5; Roeckner et al. [2003]). The present study reports on EMAC (ECHAM5 version 5.3.02, MESSy version 2.55.0) simulations in the T63L90MA resolution, i.e. with a spherical truncation of T63 (corresponding to a quadratic Gaussian grid of $\approx 1.875° \times 1.875°$ in latitude and longitude) with 90 vertical hybrid pressure levels up to 0.01 hPa.”

All simulations were performed by S. Rosanka (Forschungszentrum Jülich, Institute for Energy and Climate Research: Troposphere (IEK-8)) at the Jülich Supercomputing Centre using the Jülich Wizard for European Leadership Science (JUWELS) cluster [Krause, 2019]. The applied model set-up is representative for recent VOC chemistry studies (e.g. Novelli et al. [2020]; Rosanka et al. [2020]; Taraborrelli et al. [2021]; Franco et al. [2021]; Rosanka et al. [2021a]; Pozzer et al. [2022]) and briefly described below.

The atmospheric gas-phase chemistry is based on the Module Efficiently Calculating the Chemistry of the Atmosphere [MECCA; Sander et al., 2019] and the Mainz Organic Mechanism [MOM; Taraborrelli et al., 2009, 2012; Hens et al., 2014; Nölscher et al., 2014; Cabrera-Perez et al., 2016; Sander et al., 2019; Novelli et al., 2020; Pozzer et al., 2022], which considers 43 primary emitted VOC species. Further submodels and datasets include the SCAVenging submodel [SCAV; Tost et al., 2006, 2007; Franco et al., 2021] for aqueous-phase mechanisms, the Model of Emissions of Gases and Aerosols from Nature [MEGAN; Guenther et al., 2006] for biogenic VOC emissions [Sindelarova et al., 2014], the MESSy submodel BIOBURN and the Global Fire Assimilation System (GFAS) for biomass burning emissions [Akagi et al., 2011; Kaiser et al., 2012], the MESSy submodel AIRSEA for VOC air-sea exchange [Pozzer et al., 2006], the Emissions Database for Global Atmospheric Research [EDGAR, v4.3.2; Crippa et al., 2018] for anthropogenic emissions and their vertical profiles [Pozzer et al., 2009], and European Centre for Medium-Range Weather Forecasts (ECMWF) Reanalysis v5 [ERA5; Jöckel et al., 2006; Hersbach et al., 2020] data.

In the present study, all simulations are performed on a 10 min time grid along the aircraft flight tracks. Since of the eight missions only ACRIDICON-CHUVA (2014) and OMO (2015) took place before 2017, the model simulations are performed for the years 2017–2019. This reduces the high computational costs of such high spatial resolution simulations. For the earlier missions ACRIDICON-CHUVA and OMO, the simulations are performed for the year 2017 to enable a climatological comparison.

Chapter 4

Measurements

The following chapter provides an overview of the different measurements and HALO research missions that are included in the analysis. Particular focus is put on the characteristics of the different probed air masses, their ages, photochemical composition and involved transport.

Main parts of this chapter have been published in Kluge et al. [2020], section 3, or are currently under review in Kluge et al. [2022].

4.1 Mini-DOAS measurements

Within the framework of this thesis, trace gas measurements are analysed from eight different airborne research missions conducted in the period between fall 2014 and fall 2019, with personal participation in the six missions between 2017 and 2019. In total, over 100 research flights were performed with the German research aircraft HALO operated by the Deutsches Zentrum für Luft- und Raumfahrt (DLR) in Oberpfaffenhofen, Germany. The scientific flights cover a wide range of geographic areas reaching from the southern tip of South America and Western Antarctica, over the Amazon rainforest, the tropical and northern Atlantic, and Europe to the East China Sea, Taiwan, and the south of the Japanese Island (Fig. 4.1).

4.1.1 Research missions

The following subsection provides brief overviews on all scientific missions that are included in this study. A more detailed description of each mission's objectives, the participating instruments and research groups can be found in the respective mission publications. Special focus is put on observations of biomass burning affected air masses with expectedly high concentrations of the analysed VOCs (ACRIDICON-CHUVA mission, see below). Detailed flight overviews for all missions can be found in appendix C

4.1.1.1 Aerosol, Cloud, Precipitation, and Radiation Interactions and Dynamics of Convective Cloud Systems (ACRIDICON-CHUVA, 2014)

The ACRIDICON-CHUVA[1] mission took place from the operational basis Manaus (Brazil) within the period September and early October 2014 with a total of 14 scientific flights over the Amazon region [Wendisch et al., 2016]. The mission aimed to improve the understanding of tropical deep convective clouds and their interaction with biogenic and anthropogenic aerosols, and also included studies on precipitation formation and air pollution. As the mission took place at the end of the local dry season, extensive probing of fresh and aged biomass burning plumes was

---

[1] `https://acp.copernicus.org/articles/special_issue852.html`

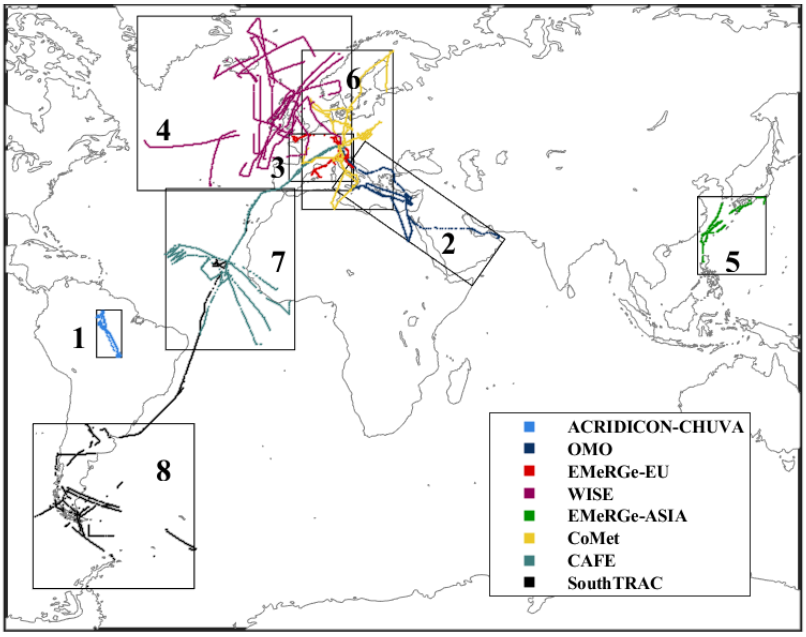

Figure 4.1: The different geographical regions and the flight tracks covered during the eight missions. For simplicity, the missions are numbered according to their temporal order with ACRIDICON-CHUVA (1, red), OMO (2, dark blue), EMeRGe-EU (3, light blue), WISE (4, magenta) EMeRGe-Asia (5, green), CoMet (6, blue), CAFE (7, cyan), SouthTRAC (8, black). The operational bases for the individual missions were Manaus (Brazil) for ACRIDICON-CHUVA, Paphos (Cyprus) for OMO, Oberpfaffenhofen (Germany) for EMeRGe-Europe and CoMet, Shannon (Ireland) for WISE, Tainan (Taiwan) for EMeRGe-Asia, Sal (Cape Verde) for CAFE, and Rio Grande (Argentina) for SouthTRAC. Only flight sections with mini-DOAS measurements are shown.

performed. Due to instrumental instabilities (e.g. difficulties with the spectrometer cooling), mini-DOAS VOC measurements are available only for four of the performed research flights. Despite this limited number of flights, the observations cover a large geographical range between approximately 6° S to 8° N, and 49° W to 63° W and tropospheric altitudes from several hundred meters up to 15 km (Fig. 4.2). The flight sections inside the planetary boundary layer overpassed large agricultural areas (18 and 19 Sept. 2014) as well as the tropical rainforest, the Amazon river delta, and Manaus (9 and 16 Sept. 2014).

4.1.1.2 Oxidation Mechanism Observations (OMO-ASIA, 2015)

The OMO mission was conducted over the eastern Mediterranean Sea, the Arabian Sea and Indian ocean in July and August 2015, with operational bases in Munich (Germany), Paphos (Cyprus), and Gan island (Addu Atoll; Lelieveld et al. [2018]). The mission focused on upper tropospheric chemistry measurements under the influence of the South Asian monsoon. Most sections of the 18 research flights were thus conducted above 10 km flight altitude. Mini-DOAS glyoxal measurements are available for six of the research flights (see table C.2).

4.1.1.3 Effect of Megacities on the Transport and Transformation of Pollutants on the Regional to Global Scales in Europe (EMeRGe-EU, 2017)

The EMeRGe-EU[2] research mission took place in July 2017 with Oberpfaffenhofen (Germany) as the operational mission basis. All seven measurement flights were performed over the central

---

[2] `https://acp.copernicus.org/articles/special_issue1074.html`

European continent and the adjacent coastal regions of the Mediterranean Sea and the English Channel. The mission focused on emission measurements from major European population centres like Barcelona and Paris, or the Po valley in northern Italy [Andrés Hernández et al., 2022]. The EMeRGe-EU mission thus predominantly provides observations within the freshly polluted planetary boundary layer, with flight altitudes reaching down to 0.5 km and rarely exceeding $\sim$ 5 km altitude.

4.1.1.4 Wave-driven ISentropic Exchange in Europe (WISE, 2017)

The WISE[3] mission took place in September to October 2017 over the North Atlantic Ocean and northern European continent and islands. With operational basis in Shannon (Ireland), the research flights were conducted towards Iceland in the North and the Canary Islands in the South, thus covering a large latitudinal range over the North Atlantic Ocean. The mission focused on the analysis of mixing processes between the upper troposphere and lower stratosphere (UT/LS) and the general composition of the UT/LS. The mission thus predominantly provides upper tropospheric and even lower stratospheric observations with very high flight altitudes above 15 km during a total of 15 research flights.

4.1.1.5 Effect of Megacities on the Transport and Transformation of Pollutants on the Regional to Global Scales in Asia (EMeRGe-Asia, 2018)

The second phase of the two EMeRGe[4] missions focused on emission measurements of major population centres in East Asia in March and April 2018. From the operational basis in Tainan (Taiwan), the ten local research flights were conducted towards Japan and South Korea in the North as well as the Philippines south of Taiwan, with measurement altitudes primarily below 5 km to probe relatively fresh anthropogenic emissions. Long flight sections and dives into the marine boundary layer over the East China Sea additionally provide measurements of Ship emissions and fresh to aged pollution plumes [Andrés Hernández et al., 2022].

4.1.1.6 Carbon Dioxide and Methane Mission (CoMet, 2018)

The CoMet[5] mission provides measurements of anthropogenic greenhouse gases over continental Europe from nine research flights in May and June 2018 [Fix et al., 2018]. Particular focus was on the probing of emissions from the Upper Silesian Coal Valley, a region in southern Poland with a very large quantity of Coal-fired Power plants and related industries. Also the Italian Po valley was probed extensively during multiple research flights that covered the lower as well as the upper troposphere.

4.1.1.7 Chemistry of the atmosphere: African Field Experiment (CAFE, 2018)

The CAFE mission took place over the Tropical Atlantic in August and September 2018[6]. From the operational basis Sal (Cape Verde Islands), the marine atmosphere around the equatorial belt (Tropical Atlantic) was probed during 14 research flights predominantly in the upper troposphere, with occasional dives into the marine boundary layer. Research flights along the West African coastline south and north of the Cape Verde islands additionally provide measurements in air masses affected by continental African outflow in the biomass burning season. The latter observations were extended by continental flights towards and over Ghana.

---

[3] `https://acp.copernicus.org/articles/special_issue1061.html`

[4] `https://acp.copernicus.org/articles/special_issue1074.html`

[5] `https://acp.copernicus.org/articles/special_issue400_1034.html`

[6] `https://www.mpic.de/4130589/cafe-africa`

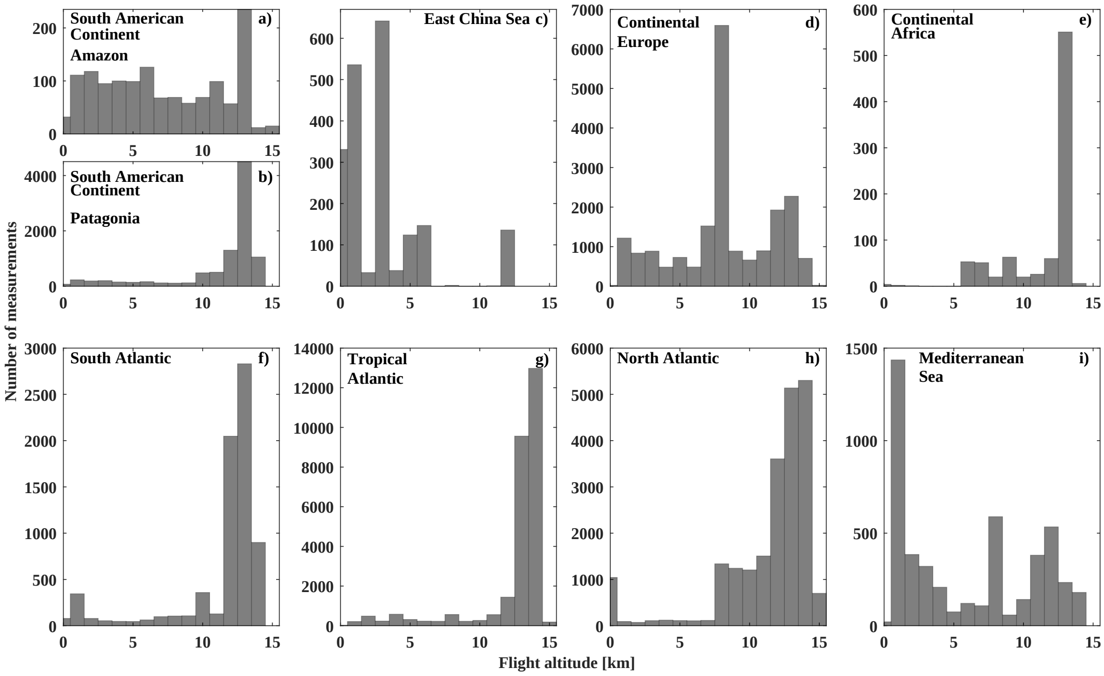

Figure 4.2: Tropospheric coverage of the measurements over the investigated regions. The flight altitudes are averaged on a 1 km grid. During the different missions, the research focus was put on different photochemical regimes in the troposphere, i.e. the planetary and marine boundary layer over the Amazon rainforest, East China and Mediterranean Sea, whereas open oceans like South, Tropical, or North Atlantic were probed predominantly in the upper troposphere or even lower stratosphere.

4.1.1.8 Transport and Composition of the Southern Hemisphere UTLS (SouthTRAC, 2019)

The SouthTRAC mission over Patagonia and Western Antarctica in fall 2019 complements the glyoxal observations with measurements in extremely remote and pristine air masses [Rapp et al., 2021]. From the operational basis Rio Grande (Argentina) on the Tierra del Fuego Peninsula, 15 scientific flights were directed towards the western Antarctica, the East Pacific and the South Atlantic around the Falkland islands. The nine transfer flights of the HALO aircraft from Munich (Germany) to Rio Grande via Sal (Cape Verde) and Buenos Aires (Argentina) additionally provide measurements of air masses located over South Argentina and Patagonia in early austral spring as well as the Brazilian outflow into the coastal Tropical Atlantic at the end of the dry season. The research flights were conducted predominantly in the upper troposphere above 10 km altitude.

4.1.2 Mini-DOAS measurements

Mini-DOAS measurements of the target trace gases are sometimes available only for a fraction of the total flight time. This is mostly a result of (1) flight sections without recorded sunlight spectra due to the over saturation of the CCD detector, e.g. when flying in and adjacent to bright clouds, which frequently occurred e.g. during the SouthTRAC mission, (2) research flights during the night, or (3) spectrometer temperatures being above 3° C preventing a stable spectral imaging (e.g. during EMeRGe-Asia). In total, the present data set consists of 72 research flights with typical duration of 8 to 9 hours each, depending on the flight altitude (and thus fuel consumption) and scientific objectives of the flights. A comprehensive list of all research flights including the

Table 4.1: Coverage of different geographic regions and probed air masses. Flights covering multiple regions (e.g. Continental Europe and the Mediterranean Sea) appear in both categories. Soundings over the East China Sea include measurements over adjacent islands like Taiwan, Japan, and the Philippines. Observations over continental Europe also includes major islands like Great Britain, Ireland, and Iceland.

Region	Air mass types	no. of flights
South Atlantic	pristine marine aged BB plumes	11
Tropical Atlantic	pristine marine aged BB plumes	12
North Atlantic	pristine marine aged pollution (mostly anthropogenic)	16
Mediterranean Sea	fresh–aged pollution (mostly anthropogenic) BB plumes	9
East China Sea	fresh–aged pollution (mostly anthropogenic)	7
South America	pristine terrestrial biogenic emissions (tropical rainforest) fresh–aged BB plumes	14
Europe, North Africa, and Arabian Peninsula	biogenic emissions fresh–aged pollution (mostly anthropogenic) BB plumes	34

geographic coverage, flight duration, probed altitudes and the mini-DOAS measurements as well as figures of all flight tracks can be found in appendix C. In the further analysis, the observations from all missions are combined, sorted according to the respective geographic regions, and further differentiated into characteristic trace gas sources, sinks, and transport processes by categorizing the data based on photochemical markers, air mass back trajectories and satellite observations according to different air mass types (Table 4.1 and section 5.1.1).

4.1.3 Probed air masses types

During the eight research missions, air masses of different origins and compositions, and thus largely different trace gas sources and concentrations were probed. This includes in particular (1) pristine marine air, (2) pristine continental air, (3) biomass burning affected air of different ages, and (4) air affected by fresh or aged anthropogenic emissions.

4.1.3.1 Pristine marine air

Pristine marine air was primarily probed over the North, Tropical, and South Atlantic during the WISE mission in 2017, the CAFE mission in 2018, and the SouthTRAC mission in 2019. During all three missions, long flight sections led through the upper troposphere over the remote oceans, with occasional dives into the marine boundary layer as well as into the airports of Shannon (Ireland), Sal (Cape Verde), or Rio Grande (Argentina). Combined, the three missions cover the Atlantic from Iceland and Scandinavia in the North over the Azores and the equatorial latitudes down to the South Atlantic, Southeast Pacific and the Wedell Sea around the Antarctic Peninsula.

4.1.3.2 Pristine terrestrial air

Pristine terrestrial air masses were probed extensively over the southern part of the South American continent (Patagonia and South Argentina) in austral spring 2019 (SouthTRAC mission). Due to the early season, continental biogenic emissions from vegetation were still very low during the measurements. Due to the remoteness of the region, the influence of anthropogenic emissions on the observations limits to flight sections in the direct surroundings of the approached airports, where also most of the vertical profiling was performed.

4.1.3.3 Air masses affected by fresh or aged biomass burning

Biomass burning plumes of different ages and extents were observed over all regions and throughout all tropospheric altitudes. Especially during ACRIDICON-CHUVA, multiple fresh biomass burning plumes were crossed within the planetary boundary layer above the Amazon rainforest and the surrounding agricultural areas (see sect. 4.1.3.5). Several research flights in the upper troposphere in the same region additionally provide observations of aged plumes and the respective chemical transformation of pollutants therein.

Aged biomass burning plumes advected from continental Africa and Brazil were also probed during multiple flights in the lower as well as upper troposphere over the Tropical Atlantic, e.g. along the east Brazilian and west African coastlines. In the southern hemisphere, biomass burning affected air masses from Australian bush fires in austral spring and summer 2019 (e.g. Kloss et al. [2021]) were detected over the Drake passage around 57° S and 67° W in the upper troposphere on 12 Nov. 2019.

4.1.3.4 Air masses affected by fresh or aged anthropogenic emissions

Air masses affected by recent anthropogenic emissions were probed over the European continent and its northern islands (mostly Ireland and Great Britain) as well as over the adjacent marine regions (North, Baltic and Mediterranean Sea) during the missions EMeRGe-EU in summer 2017, WISE in fall 2017, CoMet in spring 2018, and over Taiwan and the East China Sea during EMeRGe-Asia in spring 2018. The research flights targeted the emissions of major European and Asian cities, e.g. London, Paris, Rome, Marseilles, Barcelona, Manila, and Osaka as well as emissions from industrial areas (e.g. the Ruhr valley and the Upper Silesian Coal basin). During EMeRGe, the research flights focused on fresh pollution plumes in the planetary and marine boundary layer, whereas CoMet provides measurements in the free and upper troposphere over the different cities and the Mediterranean Sea. These thorough continental soundings are complemented by the WISE mission, which focused on flights over the major northern European islands like Ireland, Great Britain, and Iceland as well as the North Atlantic with special focus on fresh anthropogenic emissions over the Irish Sea and the North Channel.

Research flights over the Mediterranean Sea, Egypt, the Arabian Peninsula and Arabian Sea (OMO, EMeRGe-EU, CoMet) as well as in the outflow of mainland China, Japan, Korea, and the Philippines over the East China Sea (EMeRGe-Asia) provide further information on the extent and transport of local pollution. Due to operational reasons, during EMeRGe-Asia profiling from the free troposphere into the boundary layer could only be performed over Taiwan, south of Osaka (Japan), and Manila (Philippines), whereas the free and upper troposphere was probed during the flight sections between Taiwan and South Japan.

4.1.3.5 Air masses affected by biogenic emissions from a tropical rainforest

For the measurements over the Amazon, the analysis focuses on either directly emitted or secondarily formed glyoxal in biomass burning plumes as well as its secondary formation by biogenic precursors emitted from the rainforest. In this region, efficient vertical air mass transport combined with large biogenic emissions at low NO_x and low HO_x concentrations provide an atmospheric background rich in precursor VOCs of the target carbonyls also above the planetary boundary layer. The Amazon rainforest in particular is one of the main global emission sources

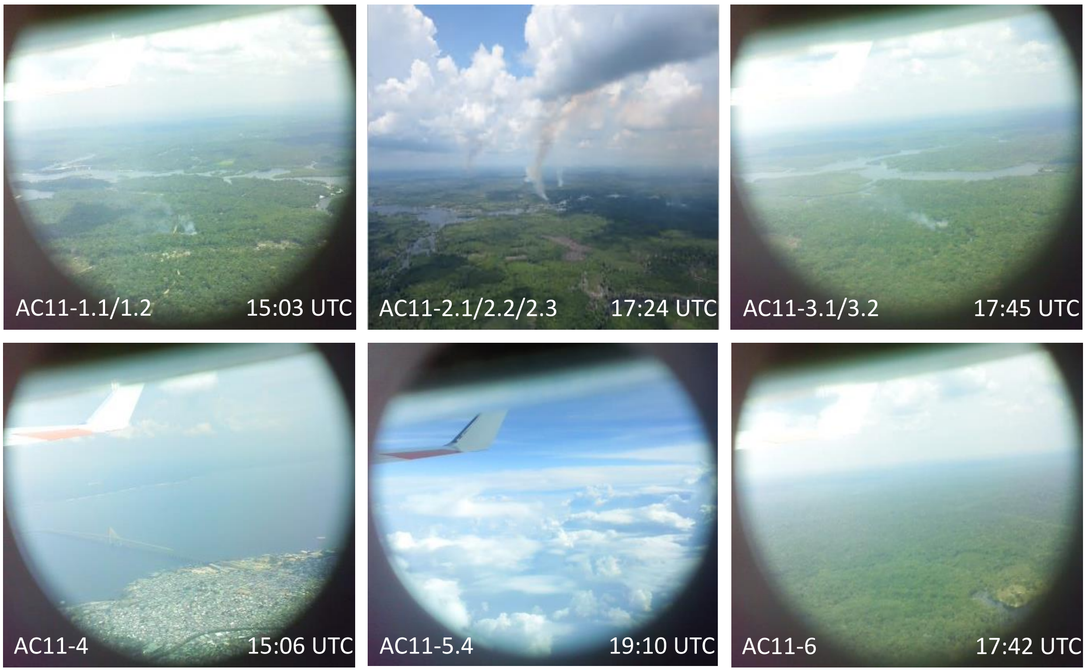

Figure 4.3: Images of the probed atmospheric scenery taken by the mini-DOAS video camera during flight AC11 (events 1–6 as indicated in Fig. 3.7 and 5.13). The second image was taken from the respective flight report. The camera points into the same direction as the three Limb telescopes of the mini-DOAS spectrometer, however with a much larger field of view of ≈ 46° width.

of isoprene, which is the main precursor of all three target gases. A largely extended wildfire season within the rainforest as well as in the surrounding agricultural areas seasonally provides significant additional direct and secondary emission sources of the investigated carbonyls. As a consequence, the region provides a well suited example (in particular during the local dry season) to study the instruments potential with respect to the detection of trace gases with low optical densities in a humid and heavily clouded atmosphere.

The identification of the atmospheric measurement conditions over the rainforest and in particular of each probed biomass burning event is based on visual imagery using the recorded video data stream of the mini-DOAS instrument (Fig. 4.3). In the following, only those measurements are claimed to be affected by biomass burning, for which the actual plumes are visible in the recorded images and in the telescope's line of sight. These events are listed in Table 5.2. Depending on the flight pattern and the integration time of the spectra, some of these plumes were intercepted more than once. In total, eight distinct plumes were probed during twelve individual measurements, all of which were recorded below 2 km flight altitude.

The MODIS instrument on board the Terra and Aqua satellites (MCD14, collection 6, available online from `doi:10.5067/FIRMS/MODIS/MCD14DL.NRT.006`) reports additional fires in the vicinity of the aircraft trajectory, which were not directly located within the field of view of the mini-DOAS telescopes, nor within the larger field of view of the camera. Therefore, these events are not further investigated in the analysis. However, the emissions of these fires are likely to have created an atmospheric background generally affected by differently aged biomass burning emissions within the boundary layer (Fig. 3.7). Further insights into the recent photochemical past of the air masses are provided by 3 h backward air mass trajectories calculated using the

READY (Real-time Environmental Applications and Display sYstem) website of the NOAA HYSPLIT model (`https://www.ready.noaa.gov/HYSPLIT.php`; Stein et al. [2015]; Rolph et al. [2017]). Exemplary 3 h backward trajectories are shown for events AC11-1.2 to AC11-3.2 in Fig. 3.7. They indicate, that prior to detection all air masses did not directly pass over any reported fire, but resided well within the mixed polluted boundary layer and are thus presumably affected by different types of fresh and aged pollution. All identified biomass burning events show large and correlated enhancements of CH_2O, $C_2H_2O_2$, and $C_3H_4O_2{}^*$, with mixing ratios up to 4.0 ppb, 0.26 ppb, and 2.8 ppb, respectively (Fig. 5.13). Due to the differently sized spatial resolutions of both instruments (sect. 3.1.3), the detected peaks in CO and those of CH_2O, $C_2H_2O_2$, and $C_3H_4O_2{}^*$ do not (and are not expected to) strictly correlate. Therefore, in the further analysis emission ratios are not estimated directly with respect to CO.

4.2 TROPOMI measurements

As with the mini-DOAS instrument, the TROPOMI glyoxal retrieval is based on the DOAS method. The data retrieval comprises (1) inferring of SCDs of the target gas from the measured spectra according to the DOAS method, (2) conversion of the SCDs to VCDs based on air mass factors obtained from radiative transfer modelling, (3) application of a background correction to account for systematic retrieval biases.

For the present thesis, S5P TROPOMI glyoxal VCDs for the period 2018–2019 were provided by C. Lerot (Atmospheric reactive gases, Royal Belgian Institute for Space Aeronomy (BIRA-IASB), Brussels, Belgium). A detailed description of the TROPOMI glyoxal retrieval can be found in Lerot et al. [2021] and some key aspects are briefly outlined below.

The TROPOMI DOAS retrieval of glyoxal is based on previous studies on spaceborne glyoxal measurements [Lerot et al., 2010; Alvarado et al., 2014; Chan Miller et al., 2014]. The DOAS spectral fit of the measured optical depths is performed between 435 and 460 nm. It includes absorption cross sections of glyoxal, nitrogen dioxide (220 and 294 nm), ozone (223 K), O_4 (293 K), water vapour (293 K), and liquid water. TROPOMI uses a mean radiance background spectrum of backscattered skylight recorded over the remote Pacific. Additional correction procedures include two pseudo absorbers to account for scene heterogeneity and an empirical correction for measurements affected by strong NO_2 absorption. As described in detail in Lerot et al. [2021], the latter correction is based on a linear regression fit obtained by a representative sensitivity test for glyoxal measurements at $NO_2 > 2 \times 10^{16}$ molec cm^2. The air mass factors are computed with the vector model VLIDORT [Palmer et al., 2001; Spurr and Christi, 2019] and used to convert the SCDs to VCDs. A priori vertical glyoxal profiles are obtained over continents with the BIRA-IASB global chemical transport model MAGRITTE [Müller and Brasseur, 1995]. Over the oceans, a common glyoxal a priori profile based on measurements over the Pacific is applied to all measurements [Volkamer et al., 2015]. Further, all retrievals under cloud cover and at solar zenith angles (SZA) above 70° are filtered out. The latter accounts for the reduced sensitivity due to enhanced Rayleigh scattering, which prevents sensitive glyoxal detection near the surface. The average uncertainty of the retrieved glyoxal VCDs is on the order of $1 \times 10^{14} - 3 \times 10^{14}$ molec cm^{-2} (30–70% for an average VCD of $> 2 \times 10^{14}$ molec cm^{-2}). Due to the low optical density of glyoxal, single spaceborne measurements are affected by noise and spectral interferences. Therefore, the TROPOMI observations at the 0.05° × 0.05° resolution are averaged in this study onto a coarser spatial grid of 0.25° × 0.25°.

The TROPOMI glyoxal retrieval was compared with reasonable agreement to previous spaceborne and MAX-DOAS observations in the recent study by Lerot et al. [2021]. However, MAX-DOAS glyoxal measurements are still sparse and not homogenised. As a result, the

TROPOMI–MAX-DOAS comparison was limited to only nine measurement sites in continental Europe and Asia. Since these MAX-DOAS measurements were performed with different instruments and retrieval algorithms, the comparison may further be affected by the individual measurement and retrieval characteristics. One key scope of the present thesis is therefore a worldwide single instrument comparison of spaceborne and airborne glyoxal observations, both over the continents and different oceans across all latitudes.

Chapter 5

Observations and results

The following chapter discusses the major findings and observations from all measurements in four main steps. Firstly, based on the collocated data from all research missions, tropospheric glyoxal is analysed in (1) pristine marine and terrestrial air (South and North Atlantic and southern Argentina/Patagonia), (2) biomass burning affected air masses (mostly South America and Tropical Atlantic), and (3) recently polluted air both over continents (Europe, South America, and South East Asia) as well as the adjacent marine regions (Mediterranean and East China Sea). The investigation of atmospheric glyoxal in these different air masses, seasons, and regions is further extended by analysing the glyoxal vertical column density measurements during all investigated research missions. In this second part of the chapter, the glyoxal VCDs are also used for a detailed validation of the mini-DOAS airborne glyoxal observations based on collocated glyoxal VCD measurements from the TROPOMI satellite instrument. In a third step all airborne glyoxal measurements of vertical profiles and column densities are used for an evaluation of the portrayal of atmospheric glyoxal by the global photochemical transport model EMAC. Finally, the glyoxal measurements in the biogenic and wildfire affected air masses over the tropical rainforest and the Amazon river delta are analysed in more detail and combined with simultaneous observations of the carbonyls formaldehyde and methylglyoxal.

Main parts of this chapter have been published in Kluge et al. [2020] (section 4 and 5), or are currently under review for publication in Kluge et al. [2022].

5.1 Global observations of glyoxal

In the following section, tropospheric glyoxal is analysed over eight different marine and terrestrial global regions, in air masses of vastly different composition, ages, and altitudes.

5.1.1 Vertical profiles of glyoxal

Based on the combined data from the research missions ACRIDICON-CHUVA, OMO, EMeRGe-EU, WISE, EMeRGe-Asia, CoMet, CAFE, and SouthTRAC, atmospheric glyoxal profiles are inferred in (1) pristine marine air (South, Tropical, North Atlantic), (2) biomass burning affected air (mostly off-coast Africa and South America), and (3) recently polluted air both over continents (Europe, South America, and South-East Asia) as well as adjacent marine regions (e.g. Mediterranean Sea, Irish Sea, and East/South China Sea). The following section firstly discusses the inferred vertical profiles of glyoxal and compares them to previous measurements, before the Nadir VCDs and integrated profiles are inter-compared with collocated TROPOMI glyoxal VCD measurements. Finally, the airborne measurements of glyoxal mixing ratios and VCDs are compared to respective simulations from the EMAC model.

Table 5.1: Observed median, median absolute deviation, and maximum (in brackets) glyoxal mixing ratios [ppt] as a function of different geographic regions, air mass types, and altitude ranges. If available, chemical markers are used for the attribution of the air masses to the different regimes: Polluted air masses are differentiated into fresh or aged biomass burning ($P_{\mathrm{BB-fresh/aged}}$ or P_{BB}, in cases where the plume age is not known), anthropogenic pollution ($P_{\mathrm{anthr.}}$), and mixed pollution (P_{mix}). Further categories consist of air masses rich in bVOC emissions (labelled biogenic, e.g. the tropical rainforest) as well as pristine air.

Region	**Air mass type**		**Glyoxal [ppt]**	
		Lower troposphere 0–3 km	**Free troposphere 3–8 km**	**Upper troposphere 8–15 km**
South Atlantic	pristine	10 ± 10 (139)	3 ± 15 (84)	3 ± 3 (36)
	$P_{\mathrm{BB-aged}}$		33 ± 9 (45)	31 ± 11 (187)
Tropical Atlantic	pristine+$P_{\mathrm{BB-aged}}$	44 ± 27 (382)	13 ± 9 (185)	1 ± 3 (246)
	$P_{\mathrm{BB-aged}}$	58 ± 10 (94)	41 ± 13 (168)	5 ± 10 (3192)
North Atlantic	pristine	19 ± 4 (144)	13 ± 6 (51)	5 ± 4 (191)
	$P_{\mathrm{anthr.}}$			53 ± 54 (2970)
Mediterranean Sea	P_{mix}	279 ± 114 (845)	20 ± 11 (309)	5 ± 4 (87)
	$P_{\mathrm{BB-aged}}$	126 ± 12 (147)		
	$P_{\mathrm{anthr.}}$	182 ± 103 (570)		
South America	pristine	23 ± 20 (223)	24 ± 10 (204)	5 ± 3 (119)
	$P_{\mathrm{BB-aged}}$		96 ± 3 (102)	3 ± 32 (311)
	rainforest	87 ± 15 (476)	36 ± 16 (593)	3 ± 8 (33)
East China Sea	P_{mix}	75 ± 42 (323)	11 ± 15 (340)	2 ± 5 (418)
	$P_{\mathrm{BB-aged}}$	52 ± 21 (301)	29 ± 25 (109)	6 ± 5 (234)
	$P_{\mathrm{anthr.}}$	77 ± 48 (299)	15 ± 11 (474)	
Continental Europe	P_{mix}	51 ± 24 (580)	14 ± 10 (441)	5 ± 5 (493)
	P_{BB}		12 ± 1 (12)	
	$P_{\mathrm{anthr.}}$	399 ± 67 (547)	204 ± 74 (277)	

Figure 5.1 provides an overview of all glyoxal profiles inferred for the eight investigated regions. This includes glyoxal profiles measured over Patagonia and the Amazon rainforest (Fig. 5.1, panel a), East China Sea and Taiwan (panel b), the European continent and its northern islands (panel c), the South Atlantic (panel d), the Tropical Atlantic (panel e), the North Atlantic (panel f), and the Mediterranean Sea (panel g). The corresponding flight tracks as a function of altitude are shown in Fig. 5.2 (panels a, d, g, j, and m) together with the along-track inferred glyoxal mixing ratios (panels b, e, h, k, and n) and glyoxal VCDs (panels c, f, i, l, and o).

As can be seen in Fig. 5.2, lower altitudes were mostly probed in the vicinity of potential emission sources (e.g. large population centres and biomass burning events), whereas the remote oceans were predominantly probed from the upper troposphere (Fig. 5.2 and Sect. 5.1.2). This sampling was motivated by (1) the mission objectives, which often differed from those necessary for in depth glyoxal monitoring, (2) flight track restrictions, which prohibited some of the intended soundings (e.g. over the remote South Atlantic), (3) the required aircraft tracks with narrow curves near airports which prevented a reliable Limb sounding, and (4) instrument malfunctions. Consequently, the marine observations in the lower troposphere over the South and Tropical Atlantic as well as over the Mediterranean Sea, contain a larger fraction of coastal rather than remote ocean soundings. Also the vertical soundings over the Mediterranean Sea and North Atlantic were mostly performed near larger pollution sources (e.g. Marseilles, Barcelona, and Shannon), rather than over the remote sea, leading to a larger fraction of pollution-affected

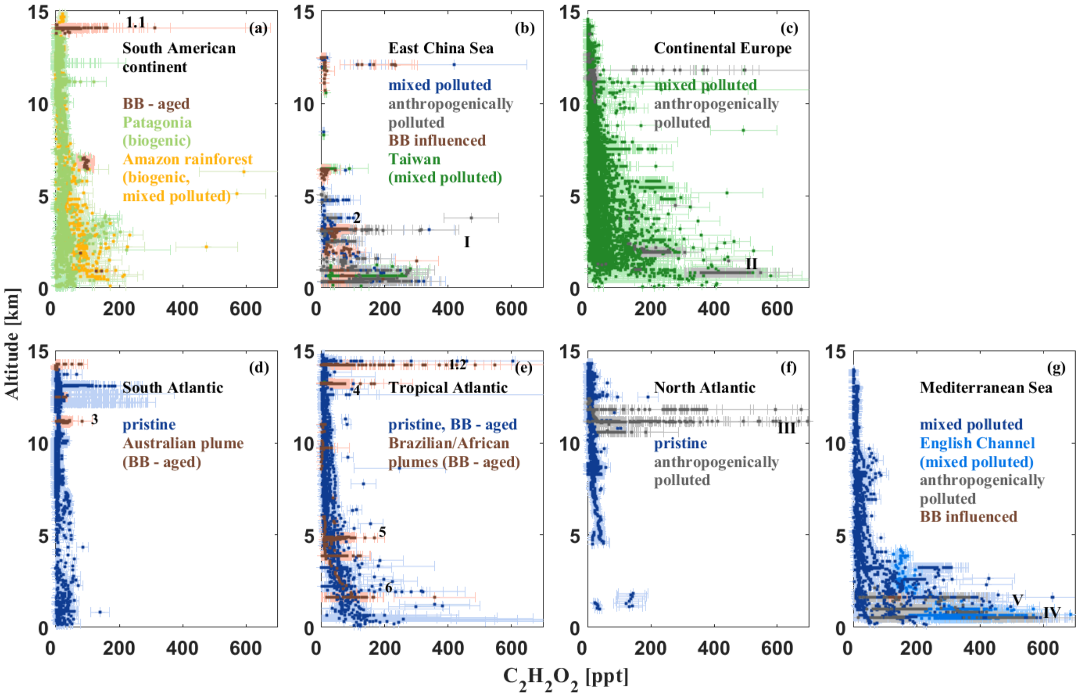

Figure 5.1: Vertical profiles of glyoxal in the different regions: South American continent in fall 2014 and austral spring 2019 (panel a); Taiwan and the East China Sea in spring 2018 (panel b); the European continent in summer and fall 2017 and 2018 (panel c); the South Atlantic in austral spring 2019 (panel d); the Tropical Atlantic and around the Cape Verde Islands in summer 2018 and austral spring 2019 (panel e); the North Atlantic and Irish Sea in fall 2017 (panel f); and the Mediterranean Sea, English channel and North Sea in summer 2015, 2017, and 2018 (panel g). The various marine environments are indicated in blue, terrestrial in green, and rainforest in yellow, while perturbations due to biomass burning (BB) plumes are indicated in brown and city plumes in grey. The Arabic numbers denote encounters with biomass burning plumes and the Roman numerals with plumes of anthropogenic emissions (mostly city plumes). The three largest glyoxal plumes observed are plume 1.2 (panel e) with up to 3192 ppt, plume III with up to 2970 ppt (panel f), and plumes IV and V with up to 845 ppt and 774 ppt, respectively (panel g). All four plumes are not shown in full scale for better comparability with the other profiles. For better visibility of the different profile shapes, occasional negative measurements are not shown (compare to Fig. 5.8).

observations in the planetary boundary layer as compared to higher altitudes. However, this bias is expected to be small for vertical soundings in regions of widely polluted air (e.g. over polluted continental areas) and the East China Sea, where vertical profiles were also inferred over the remote ocean.

Nevertheless these observation related limitations, the glyoxal profiles provide valuable information on the background of glyoxal in various environments around the globe including marine (Fig. 5.1, blue colour) and terrestrial regions (Fig. 5.1, green colour) and the Amazon rainforest (Fig. 5.1, yellow colour) as well as perturbations due to biomass burning (BB) plumes (Fig. 5.1, brown colour) and city plumes (Fig. 5.1, grey colour).

The attribution of the different air masses to the respective emission types is based on markers of typical chemicals emitted by anthropogenic activities and biomass burning. For the EMeRGe-EU and EMeRGe-Asia missions, benzene (C_6H_6), isoprene (C_5H_8), and acetonitrile (CH_3CN) are used to detect anthropogenic pollution or biomass burning affected air masses [Andrés Hernández et al., 2022; Förster et al., 2022; Krüger et al., 2022]. Biomass burning plumes are further identified based on simultaneous measurements of CO [Tadic et al., 2017] and black carbon [Holanda et al., 2020] during CAFE-Africa, and of CO [Müller et al., 2015;

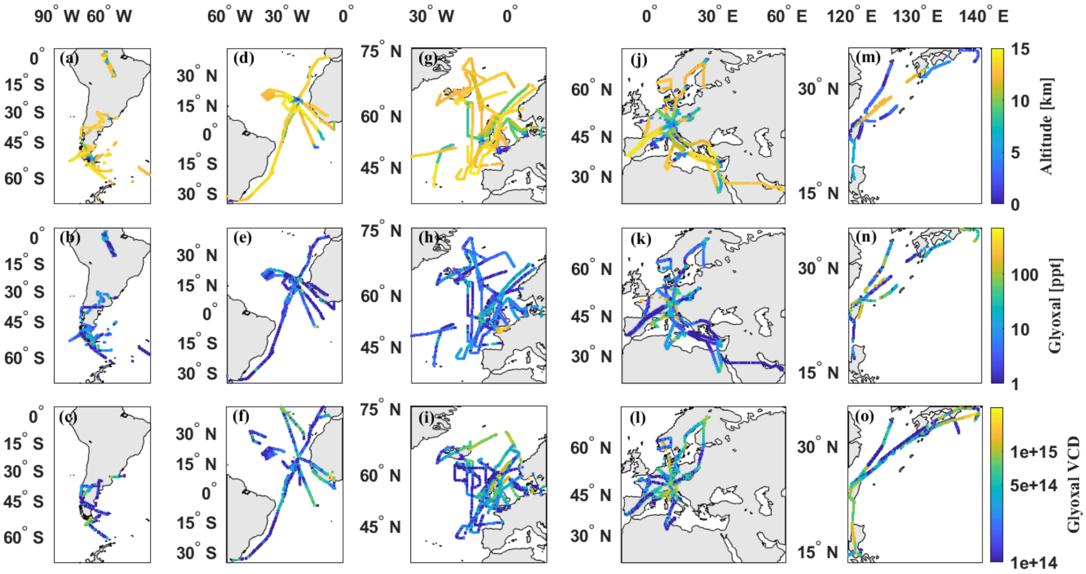

Figure 5.2: Flight trajectories, measured glyoxal mixing ratios, and VCDs are displayed in the top, middle and bottom rows, respectively, from over South America (panels a-c), the Tropical Atlantic (panels d–f), the North Atlantic (panels g–i), Continental Europe (panels j–l), and South-East Asia (panels m–o). Note the logarithmic colour scale in the two lower rows of the panels.

Kunkel et al., 2019], peroxyacetyl nitrate (PAN), ethane (C_2H_6), formic acid (HCOOH), methanol (CH_3OH), ethylene (C_2H_4) [Johansson et al., 2022], and acetylene (C_2H_2) (S. Johansson, private communication, Feb. 2022) during the SouthTRAC mission, and by visual inspection as well as air mass back trajectory calculations for the ACRIDICON-CHUVA mission (Sect. 4.1.3.4.

Evidently, not all of the glyoxal observations can unambiguously be assigned to one of the four encountered air mass types (pristine, biogenic, polluted, or biomass burning affected) as described above, since either no markers for the different regimes were measured during individual flights or entire missions (e.g. CoMet) or a mixture of polluted air masses from different sources was probed, e.g. over continental Europe, the Mediterranean Sea, Taiwan and the East China Sea [Lelieveld et al., 2018; Andrés Hernández et al., 2022].

Table 5.1 provides an overview of glyoxal mixing ratios (median, median absolute deviation and maximum) inferred in the distinctive regimes in the lower, middle and upper troposphere in the different global regions. As expected, most glyoxal is observed in the lower and middle troposphere over Europe, the Mediterranean Sea and Eastern Asia, and the smallest mixing ratios are found over pristine marine (South and North Atlantic) and terrestrial regions (Patagonia). In the upper troposphere, glyoxal mixing ratios are generally only a few ppt in all regions, if not affected by biomass burning or other emission plumes.

Overall, the comparison of the glyoxal measurements with previous findings from varying altitudes, regions and seasons around the globe shows a reasonable good agreement:

(1) Pristine marine air masses were mostly probed over the South Atlantic, with median mixing ratios in the lower, middle, and free troposphere of 10 ppt, 3 ppt, and 3 ppt, respectively (Fig. 5.1, panel d and Fig. 5.2, panels a–c). Over the South Atlantic, glyoxal mixing ratios larger than 100 ppt are exclusively observed in aged biomass burning plumes or near the South American coastline below 3 km altitude, where the enhancements very likely resulted from respective continental outflow of glyoxal and its precursors. Comparable glyoxal mixing ratios of 19 ppt (median) are observed in the planetary boundary layer over the North Atlantic, with slight glyoxal enhancements predominantly observed during ascents and descents into the Shannon airport (Ireland; Fig. 5.2, panels g–i). Also in the middle and free troposphere, the range of observed glyoxal mixing ratios above the pristine South and North Atlantic compares well if not affected by specific emission events (biomass burning for the South and mostly anthropogenic emissions for the North Atlantic, see Fig. 5.1, panels d and f). Glyoxal observations in the remote marine free troposphere and in particular in the free troposphere over the North Atlantic are still sparse, and thus deserve further investigations.

In the pristine marine boundary layer, the glyoxal measurements compare well with observations by Mahajan et al. [2014], who found average glyoxal mixing ratios of typically 25 ppt (upper limit 40 ppt) based on 10 oceanic cruises over the open oceans in different parts of the world. For the South Pacific boundary layer, Lawson et al. [2015] reported glyoxal mixing ratios ranging from 7 to 23 ppt, which is slightly smaller than the median observation in the boundary layer over the Tropical Atlantic of 44 ppt.

In fact, compared to the measurements in pristine marine air (e.g. over the South Atlantic), glyoxal over the Tropical Atlantic below 3 km is found to be on average four times larger (Fig. 5.1, panel e and Fig. 5.2, panels d–f). This observation of moderately elevated glyoxal in the marine lower troposphere in the tropics support previous findings of elevated glyoxal in other regions of the remote marine tropics, e.g. in the lower atmosphere over the East Pacific [Sinreich et al., 2010; Volkamer et al., 2015].

(2) Pristine terrestrial air masses: The median glyoxal mixing ratios over Patagonia and south Argentina (21 ppt) are are only slightly higher than those inferred for the South Atlantic. In contrast to the other investigated terrestrial regions, in the lower and free troposphere over Patagonia glyoxal mixing ratios appear to be approximately constant with altitude. Mixing ratios significantly larger than the median are only observed when approaching population centres, like Buenos Aires or Rio Grande (Argentina). In the upper troposphere and distant from such emission sources of pollutants, glyoxal mixing ratios decrease further to a median of 5 ppt (Fig. 5.1, panel a), which is comparable to air masses investigated in the upper troposphere in the other regions.

The lack of significant ground-based emission sources and thus rather small emission of glyoxal and its precursors results in a close to constant vertical glyoxal profile over south Argentina, in contrast to the measurements over the Amazon rainforest (Fig. 5.1, panel a). There, glyoxal strongly decreases in the free and upper troposphere due to significant enhancements in the boundary layer and the lower middle troposphere that are caused by large direct emissions of glyoxal and its precursors by biomass burning as well as secondary formation from longer-lived precursors emitted from the rainforest (mostly isoprene, see Sect. 5.2). Interestingly, glyoxal in the lower troposphere over the Amazon basin is considerably smaller (median 87 ± 15 ppt) than reported from the tropical rainforest in a rural region of South-East Asia (up to 1.6 ppb; MacDonald et al. [2012]). There, large emissions of isoprene were suspected to yield these high glyoxal mixing ratios.

(3) Air masses affected by biomass burning: Two of the probed biomass burning plumes (Fig. 5.1, brown colour) are documented in the literature. On 12 Nov. 2019, an aged (3–4 days old) biomass burning filament was detected in the upper troposphere and lower stratosphere over the Drake Passage around 57° S and 67° W, that most probably originated from Australian bushfires [Kloss et al., 2021] (Fig. 5.1, panel d, event 3). On this day, elevated glyoxal up to 83 ± 32 ppt was continuously measured during a 280 km long flight section in the upper troposphere south of Patagonia. On 8 Sept. 2019, an extended biomass burning plume was crossed along the south Brazilian and Uruguayan coastlines towards Buenos Aires (Fig. 5.1, panels a and e, event 1.1 and 1.2, and Fig. 5.6, panels c and d). Within this plume, the largest glyoxal mixing ratios among all biomass burning measurements were observed (up to 3192 ppt).

The FIRMS fire map as well as air mass trajectory calculations show that the plume most probably originated from wildfires in south Brazil, Uruguay, Paraguay, and northern Argentina [Johansson et al., 2022] (see Sect. 5.1.2 and Fig. 5.6, panel c).

Based on the chemical markers, at least five more extended biomass burning plumes can be identified from the measurements over the Tropical Atlantic (Fig. 5.1, events 4, 5 and 6) and over the East China Sea (event 2). Additionally, occasionally smaller plumes were probed over the Mediterranean Sea and continental Europe during several research flights (Fig. 5.1, panels c and g). Also the air masses probed over East Asia were frequently influenced by biomass burning plumes and anthropogenic emissions. This is exemplarily indicated for event 2 (Fig. 5.1, panel b), which marks the crossing of polluted air masses off-coast Taipei (Taiwan) on 19 March 2018. Around the Cape Verde Archipelago, extended biomass burning plumes were crossed 400 km south-west of Cape Verde on 17 Aug. 2018 (event 4), later during the same flight between the islands Sal and Praia (event 5) as well as $\sim$ 500 km distant off the Brazilian coast at 1.6 km altitude on 12 Aug. 2018 (event 6). For all these encounters (except event 4), significant enhancements in black carbon and CO were simultaneously detected.

(4) Air masses affected by anthropogenic activities were probed over the East China Sea, continental Europe, the English Channel, and the Irish Sea (Fig. 5.1, panels b, c, f, and g, and Fig. 5.2, panels g–o). In these regions, large glyoxal enhancements were observed in predominantly anthropogenic (and occasionally biomass burning) polluted air masses at all altitudes. These most probably originated from fresh anthropogenic emissions of glyoxal and its precursor into the planetary boundary layer (e.g. plume II with up to 547 ppt, Fig. 5.1, panel c), which were further transported into the upper troposphere (e.g. plume III with up to 2970 ppt, Fig. 5.1, panel f). Plume III was crossed between 10.5 and 12.5 km altitude above the Malin Sea approx. 30 km north of Ireland on 28 Sept. 2017 (Fig. 5.3, panel a). This plume is remarkable because of its particularly high glyoxal mixing ratios despite the high observation altitude. Air mass trajectory calculations show that three to four days prior to the observation these air masses had been transported in a warm conveyor belt originating from the North American lower troposphere. The monitoring of a plume below 3 km altitude above the English Channel on 17 July 2017, which is one of the densest ship routes worldwide, yielded glyoxal mixing ratios up to 774 ppt (Fig. 5.1, panel g, plume V), which is a factor of four times less as compared to the glyoxal enhancement in the presumably much older air in plume III. Anthropogenic pollution in the remaining but not categorized observations (Fig. 5.1, green) cannot be excluded as the air masses are expected to be generally affected by pollution or biogenic emissions over Europe and East Asia [Andrés Hernández et al., 2022]. These plumes can often not unambiguously be attributed to one of the three regimes and are therefore not more specifically categorized in the further analysis.

Interestingly, the measurements in the boundary layer over continental Europe and the East China Sea yield smaller medians than those inferred over the Mediterranean Sea, where glyoxal even exceeds the observations over the Amazon rainforest (Table 5.1 and Fig. 5.1, panels a, b, c and g).

Over continental Europe, the largest mixing ratios of 580 ppt were observed while approaching Munich airport from the west at 671 m flight altitude on 20 July 2017. Constantly enhanced glyoxal mixing ratios were observed especially over northern Italy (Fig. 5.1, panel c, event II, and Fig. 5.3, panel c), where glyoxal increased up to 522 ppt at 836 m altitude (20 July 2017). Based on all research flights in this region, a median of 395 ± 71 ppt glyoxal in the lower troposphere is inferred for May–July 2017/2018. This is much larger than observed in the boundary layer over other European regions, e.g. Catania or Munich, with median glyoxal of 78 ppt and 51 ppt, respectively (Fig. 5.3, panels b and d). Glyoxal in the boundary layer over northern Italy also

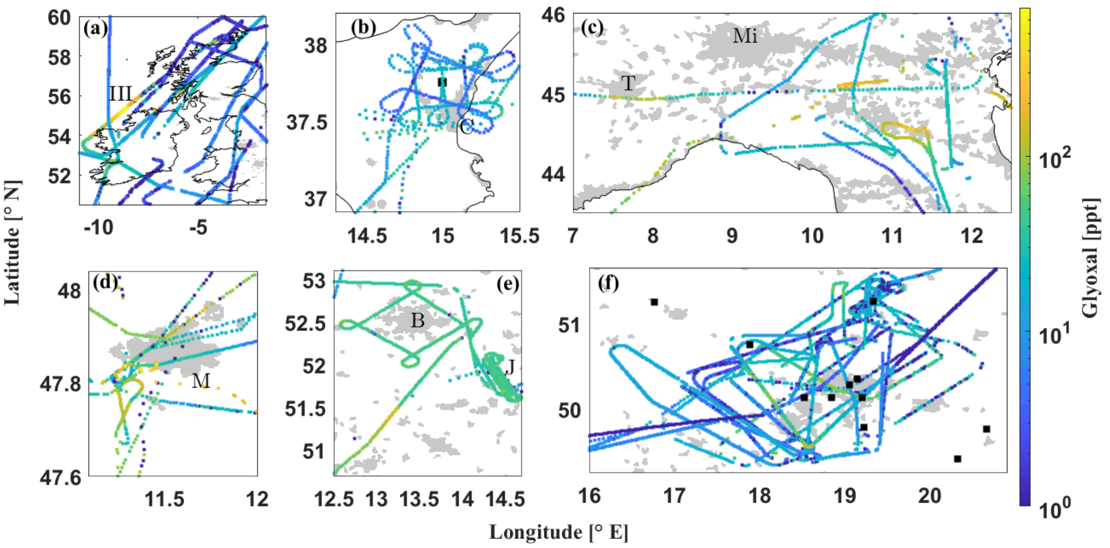

Figure 5.3: Examples of glyoxal measurements displayed over select regions of Europe: (a) over Ireland and Great Britain with the crossing of plume III during a flight leg between the Irish north coast and Scotland; (b) eastern Sicily (Italy) around Catania (C) with the Etna volcano (black square); (c) the Po Valley (Italy) with Turin (T) and Milano (Mi); (d) the Munich (M, Germany) metropolitan area; (e) the Berlin (B, Germany) metropolitan area with the Jänschwalde power plant (J) in the south-east; and (f) the upper Silesian Coal Basin (Poland) with the coal-fired power plants marked by black squares. Note the logarithmic scale of the colour axis. Grey areas mark population centres based on 2002-2003 MODIS satellite images (made with Natural Earth).

exceeded the observations over the Upper Silesian Coal Basin in Poland (41 ± 17 ppt; Fig. 5.3, panel f), which is known as large emitter of anthropogenic pollutants.

Apparently, over Europe the emissions of glyoxal and its precursors from distinctive regional sources of anthropogenic pollutants are, while locally confined, potentially much stronger than those caused by widespread biogenic and biomass burning VOC emissions, e.g. over the Amazonian rainforest (Fig. 5.1, panel a). Still, the median background (25–75% of the data range) is two times larger over the Amazonian rainforest (4–65 ppt) compared to continental Europe (3–27 ppt), as expected due to the steadily larger biogenic emissions there.

The anthropogenic emissions from some larger European coastal cities (Barcelona, Marseilles and the gulf of Venice) were probed during research flights along the Mediterranean coast on 11, 20, and 24 July 2017 (Fig. 5.1, panel g). These soundings are the reason for the possible high-biased glyoxal profile in the lower troposphere over the Mediterranean Sea, since lower altitude measurements were not performed over the remote sea, but within the plumes of coastal cities. During the measurements over the gulf of Venice on 20 July 2017, median mixing ratios of 363 ± 102 ppt were observed between 0.5 and 3.3 km altitude, with a maximum of 845 ± 206 ppt at 500 m altitude presumably caused by VOC emissions from the nearby oil refinery and the oil rigs in the Adriatic Sea. and/or ship traffic (Fig. 5.1, panel g, plume IV). The soundings into the lower troposphere (0.5–3 km) near Barcelona on 24 July 2017 resulted in glyoxal mixing ratios up to 158 ppt (median 111 ppt). While in the lower marine troposphere of the Mediterranean Sea, glyoxal mixing ratios are even larger as over continental Europe, over the remote ocean the vertical profile decreases quickly to a few ppt at higher altitudes. This is most likely a result of the limited vertical transport by the shallow convection over the sea and the limited lifetime of glyoxal and its major precursors.

The glyoxal profiles over Taiwan and the East China Sea (Fig. 5.1, panel b) are dominated by the polluted air masses probed during the ascent/descent into Tainan (Taiwan) airport, the low altitude soundings over Manila (Philippines), and those performed over the East China Sea between 17 March 2018 and 4 April 2018 (Fig. 5.1, panel b, and Fig. 5.2, panels m–o). The identification of the various plume origins indicate encounters of both anthropogenic emissions (e.g. plume I) as well as from biomass burning (e.g. event 2) during the flights. On 19 March 2018, while flying towards the remote East China Sea, enhanced mixing ratios of benzene and toluene indicated growing influence of anthropogenic pollutants in the probed air masses with simultaneous increase of glyoxal up to 179 ppt. Differently to the other marine measurements, lower altitude observations over the East China Sea were obtained not only close to Taiwan, but also over the more remote ocean. Given the larger emissions of pollutants by mainland China and South Korea, it is not surprising that over the East China Sea glyoxal mixing ratios in the lower troposphere significantly exceeded those above the South, Tropical and North Atlantic on average by 31 ppt (Tropical Atlantic) up to 65 ppt (South Atlantic).

Overall, the glyoxal measurements in anthropogenically polluted air masses (Mediterranean Sea, continental Europe, and East China Sea) fall into the range of previous studies in similarly polluted air masses around the globe (e.g. Lee et al. [1998]; Volkamer et al. [2005a, 2007]; Fu et al. [2008]; Sinreich et al. [2010]; Baidar et al. [2013]; Kaiser et al. [2015]; Volkamer et al. [2015]; Min et al. [2016]; Chan Miller et al. [2017]; Kim et al. [2022]).

5.1.2 Inter-comparison of airborne and satellite measured glyoxal VCDs

Vertical column densities of glyoxal were detected with the Nadir observing spectrometers of the mini-DOAS instrument simultaneously to the Limb measured glyoxal mixing ratios. In the following, these Nadir observations and the integrated profiles are used for a detailed validation of the mini-DOAS glyoxal measurements using collocated satellite observations from the TROPOMI instrument. The potential of each observation system as well as its limitations regarding the detection of glyoxal is analysed in the different atmospheric source regimes, i.e. (1) in predominantly pristine air, where both instruments operate close to their detection limits, (2) over largely extended emission events (e.g. during the South American biomass burning season), (3) in locally confined trace gas filaments in otherwise pristine air masses (e.g. small biomass burning plumes in the marine atmosphere), and (4) in air masses generally affected by differently aged biogenic and anthropogenic VOC emissions (e.g. over industrial agglomerations of continental Europe, like the Po Valley or Upper Silesian Coal Basin).

The airborne mini-DOAS Nadir measurements are compared to respective same-day L3 processed glyoxal observations from the TROPOMI satellite instrument [Lerot et al., 2021]. Since the Sentinel-5p spacecraft was launched in October 2017, the comparison focuses on the mini-DOAS measurements from 2018 onward (EMeRGe-Asia, CoMet, CAFE-Africa (all 2018), and SouthTRAC (2019)). Additionally, the measurements over the North Atlantic (WISE, fall 2017) are included to extend the latitudinal coverage of the data set.

As discussed in sect. 3.1.4, in favour of an optimal and biased-minimized inter-comparison between satellite and aircraft Nadir observations (which respects the similarities in observation geometry and hence detection sensitivity), the Nadir observations from the high flying (> 8 km) aircraft are preferred over those performed from the low flying aircraft. In consequence of this altitude restriction, only data collected during two research flights remain for the inter-comparison of the EMeRGe-Asia mission (Fig. 5.4, panel a and Fig. 5.7, panel b). Further, to obtain the same limit for glyoxal detection from both instruments, i.e. in order to reduce the noise in the satellite measurements, the TROPOMI glyoxal VCDs are averaged over a $0.25° \times 0.25°$ grid. Each grid box is centred around the individual footprint of a single mini-DOAS measurement (Fig. 5.5, panel b). Even though the footprints of TROPOMI and mini-DOAS geographically overlap well and only observations from the same day are chosen, the exact timing of the measurements may

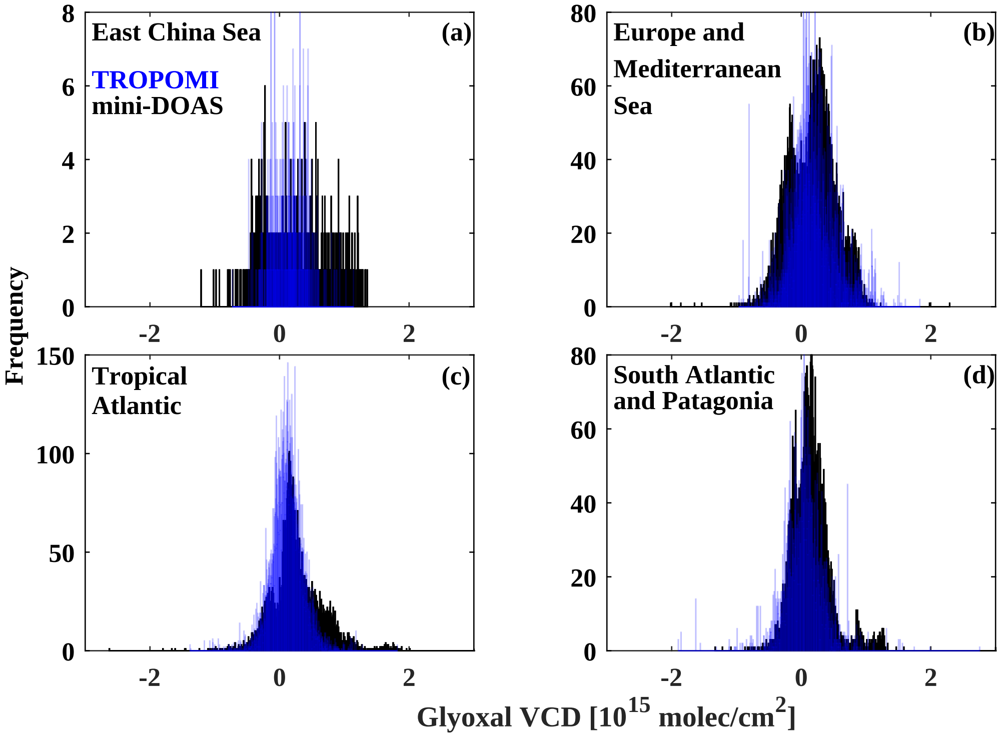

Figure 5.4: Distribution of individual glyoxal VCD measurements from the TROPOMI (blue) and mini-DOAS (black) instruments after the latter are filtered for flight altitudes > 8 km and according to the TROPOMI data for solar zenith angles $< 70°$. The L3 TROPOMI data at a 0.05° resolution are averaged on a $0.25° \times 0.25°$ grid around the mini-DOAS measurement locations (see Fig. 5.5, panel b). Due to low number of airborne measurements > 8 km over East Asia, the altitude filter prevents a thorough statistical analysis of the region (panel a).

differ significantly, which has to be taken into account when comparing specific emission plumes.

As the TROPOMI L3 data are filtered for observations with solar zenith angles $< 70°$ [Lerot et al., 2021], the same filter is applied to the mini-DOAS data. This mostly affects the measurements over the South Atlantic as a consequence of the high geographic latitude and consequently low sun position in the region. The largest remaining difference in the filtering of both data sets is the TROPOMI cloud filter, which cannot be applied to the mini-DOAS observations. However, the analysis of a possible colour index dependency of the airborne Nadir glyoxal measurements (radiance at 620 nm compared to 440 nm) did not show any correlation towards higher or lower biased observations for small (cloudy sky) or large (clear sky) colour indices.

The glyoxal VCDs measured by both instruments generally agree well for all investigated regions (Fig. 5.4), even though the inferred VCDs show the expected statistical scatter including the occurrence of negative VCDs due to the statistical noise of the glyoxal retrieval close to the individual detection limits. In the following, both data sets are more closely compared to highlight their strengths and limitations for the detection of glyoxal in different situations and ranges of VCDs.

(1) The detection of glyoxal in pristine air masses (South Atlantic and southern Argentina) shows a good agreement among both instruments with a corresponding scatter around zero (Fig. 5.4, panel d). In this region, TROPOMI and the mini-DOAS instrument measure slightly elevated median glyoxal VCDs of $(0.5 \pm 1.6) \cdot 10^{14}$ molec cm^{-2} and $(1.1 \pm 1.6) \cdot 10^{14}$ molec cm^{-2}, respectively. Compared to TROPOMI, the mini-DOAS distribution shows a slightly larger right side tail (Fig. 5.4, panel d). This is a result of elevated glyoxal detected from

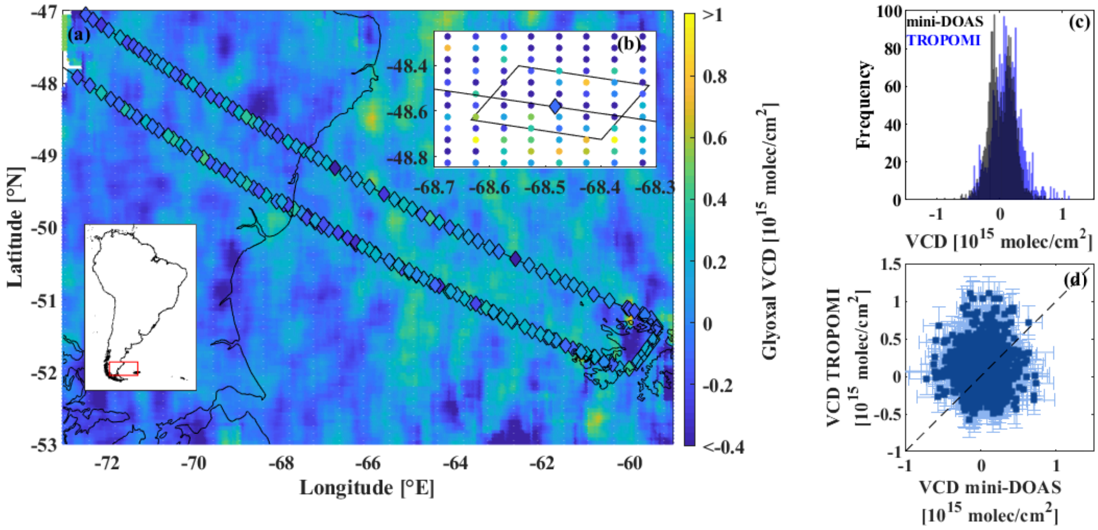

Figure 5.5: Glyoxal measurements in the pristine marine atmosphere over the South Atlantic between southern Patagonia (Argentina) and the Falkland Islands (UK) on 9 Nov. 2019. Panel (a): along-track mini-DOAS glyoxal measurements (diamonds with black contours) with the collocated same-day L3 TROPOMI observations at 0.25° × 0.25° resolution. For better visibility, only every fifth mini-DOAS measurement is shown. Panel (b): spatial gridding of 25 high-resolution TROPOMI measurements around an individual mini-DOAS observation. Panels (c) and (d): Frequency distribution and scatter plot of the inferred glyoxal VCDs from the mini-DOAS instrument versus TROPOMI L3 averaged on 0.25° × 0.25° according to panel (b).

the aircraft (and not captured by TROPOMI) in aged biomass burning plumes from over 20 smaller wildfires in the Chilean Biobio Region located about 100 km north-east of the HALO flight on 15 Nov. 2019. Note that the scatter of TROPOMI data at the high resolution of 0.05° × 0.05° is significantly larger than of the mini-DOAS measurements, even though both instruments have comparable spatial resolutions. Evidently, this is a consequence of the much shorter observing time and hence number of collected photons (about a factor of 6) from an individual pixel for TROPOMI as compared to the mini-DOAS instrument owing to the much higher velocity of the satellite (7500 $\mathrm{m\,s^{-1}}$) as compared to the aircraft (200 $\mathrm{m\,s^{-1}}$; compare sect. 3.1.4). For daily TROPOMI data at 0.25° × 0.25° resolution, this scatter is largely smoothed-out (Fig. 5.5, panel a), thus demonstrating the need to spatially degrade the high resolution TROPOMI glyoxal data in glyoxal inter-comparison studies (Fig. 5.5, panels c and d). The respective gridding of 25 high-resolution TROPOMI measurements around each mini-DOAS observation is shown for an example measurement in Fig. 5.5, panel (b).

(2) The detection of glyoxal in largely extended biomass burning plumes shows generally good agreement among both instruments, even though the differing overpass times and resulting plume displacements may cause some discrepancy in the along-track comparison. Such large plumes were e.g. detected over the gulf of Cadiz along the southern Portuguese coast on 7 Aug. 2018 (Fig. 5.6, panels a and b) as well as over southern Uruguay on 7 Oct. 2019 (Fig. 5.6, panels c and d). Satellite images from the MODIS instruments on the Terra and Aqua satellite taken over the gulf of Cadiz on the same day show a well confined biomass burning plume that was captured by both instruments with a respective increase in glyoxal (Fig. 5.6, panel a). While the TROPOMI detected glyoxal VCDs quickly decrease around the margins of the plume, the mini-DOAS instrument still measured slightly elevated glyoxal VCDs in the margins of the plume (Fig. 5.6, panel b, data below the 1:1 line). This behaviour is especially pronounced towards the open Atlantic west of the plume and might be a result of an apparent degraded sensitivity

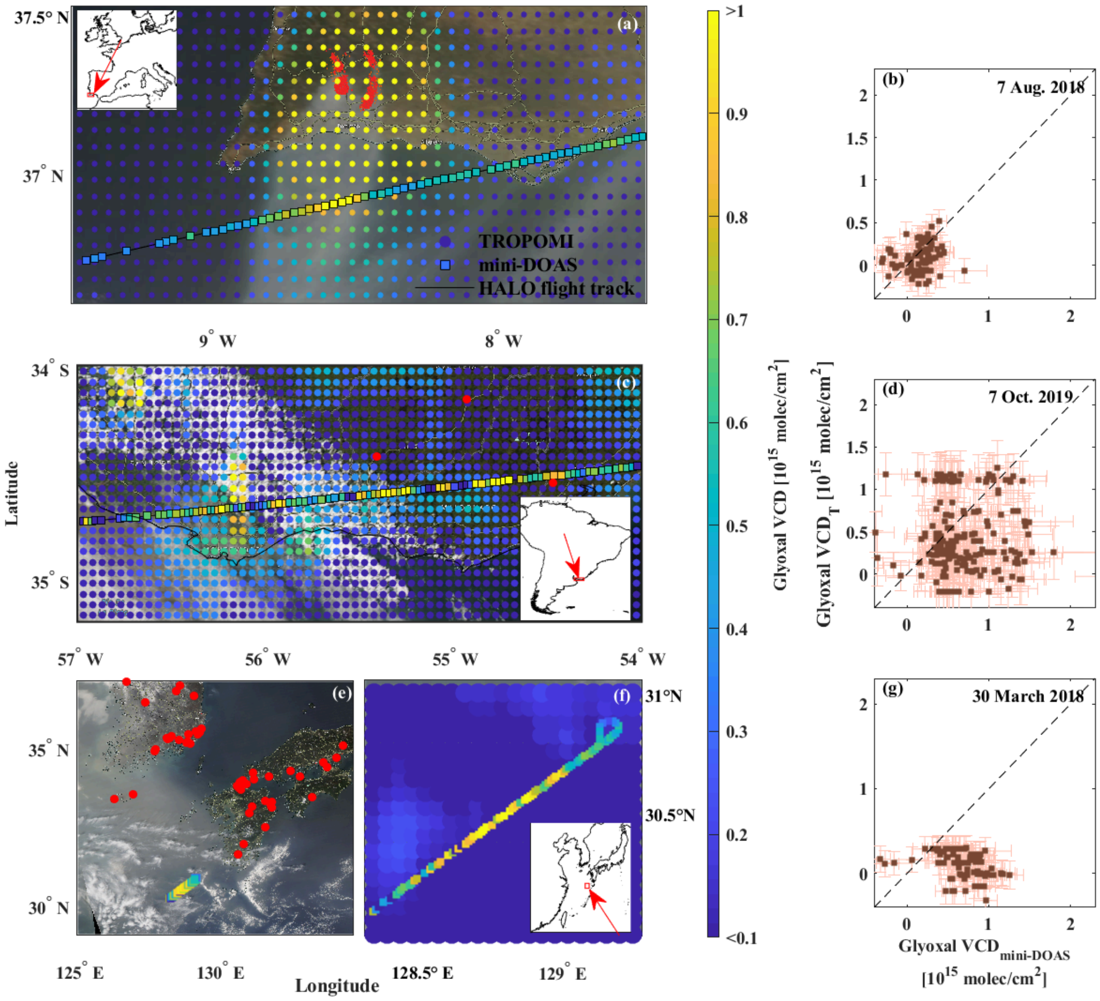

Figure 5.6: Collocated glyoxal VCDs from mini-DOAS observations (diamonds with black contours) and 0.25° × 0.25° resolution L3 TROPOMI observations (squares) in different regions (panels a, c, e, and f) with corresponding scatter plots (panels b, d, and g), where each TROPOMI observation is gridded around the mini-DOAS measurements as exemplary shown in Fig. 5.5, panel (b). For better visibility of the underlying satellite image, the footprints are not to scale. Panels (a) and (b): Monitoring of a glyoxal plume from wildfires in the Serra de Monchique (Algarve, Portugal), detected by TROPOMI and by the mini-DOAS instrument (13 km flight altitude) over the gulf of Cadiz at 13:50 UTC and 11 UTC, respectively, on 7 Aug. 2018. Panels (c) and (d): Overpass of extended biomass burning plumes near the Uruguayan coast region observed by TROPOMI (overpass at 17:00 UTC) and mini-DOAS (8–13 km flight altitude) at 10:45 UTC on 7 Oct. 2019. Panels (e), (f), and (g): Monitoring of a glyoxal plume within the marine boundary layer above the East China Sea, south-west of Japan, on 30 March 2018 at 12:50 UTC (TROPOMI) and 1:40 UTC (mini-DOAS) with the geographic overview (panel e), zoom of the flight track (panel f), and respective scatter plot (panel g). The wildfire data (red circles, not to scale) are derived from MCD14 MODIS observations on the Terra and Aqua satellites. The MODIS satellite images are taken from NASA WORLDVIEW based on the satellite overpasses on 13:48 UTC on 7 Aug. 2018 (panel a), 17:23 UTC on 7 Oct. 2019 (panel c), and 2:30 UTC on 30 March 2018 (panel e).

of TROPOMI to detect small glyoxal enhancements in the lower troposphere over dark water surface, such as the ocean (see Sect. 6).

The glyoxal enhancements over Uruguay on 7 Oct. 2019 cannot be ascribed to a specific but instead to more dispersed plumes due to extended wildfires in central Uruguay and in the north-east of Argentina. Here, the large scatter of the data in Fig. 5.6, panel (d) is primarily a result of the temporal mismatch between the observations of 6 h (overpass mini-DOAS around 10:45 UTC and TROPOMI at 17 UTC).

(3) The detection of glyoxal in small or aged plumes over the oceans with moderately enhanced glyoxal shows sizeable differences between both instruments. Such plumes predominantly originate from continental wildfires and were frequently observed in all regions during all research missions (Fig. 5.1). Over the oceans, such plume encounters can be well distinguished from the pristine surroundings with low glyoxal due to resulting high local concentration gradients. In contrast, for observations over land with generally higher glyoxal concentration in the background, such plume encounters with only moderately enhanced glyoxal are less distinct (Fig. 5.6, panels b, c, and g). During the South Atlantic and Tropical Atlantic flights, the various smaller plumes detected from the aircraft in the upper troposphere were mostly not observed by TROPOMI, e.g. along the south Chilean coast on 15 Nov. 2019 (see Sect. 5.1.1). During the various encounters of biomass burning plumes over the Atlantic, TROPOMI thus detects generally smaller glyoxal VCDs than the mini-DOAS instrument. This causes the right side tail of the mini-DOAS distribution and accordingly a slight increase in the median of the VCD distributions (Fig. 5.4, panels c and d). The same behaviour is observed for plume encounters at lower altitudes, e.g. within the marine boundary layer below 2 km over the East China Sea south of Kyushu island (Japan) on 30 March 2018 (Fig 5.6, panels e, f, and g), or at 1.6 km altitude and $\sim$ 500 km north-east of the Brazilian coast over the Tropical Atlantic on 15 Aug. 2018 (see Sect. 5.1.1), which were both not detected by TROPOMI. Similar observations were made during multiple other occasions, e.g. during biomass burning plume encounters near the Canary Islands on 7 and 15 Aug. 2018 and 7 Sept. 2018, off-coast Brazil on 4 Nov. 2019, along the West African coast on 10 and 31 Aug. and 4 Sept. 2018, and along the coast of Japan east of Osaka on 4 April 2018. Very likely, the undetected increase of glyoxal in such small or low lying biomass burning plumes by TROPOMI is a result of (a) the potentially small vertical extent of some of the low lying plumes and hence their relatively small contribution to the total atmospheric VCD, (b) the small horizontal extent of the plumes, which may just not be detectable by the satellite due to the lower spatial resolution of TROPOMI for co-added pixels, or simply missed due to the temporal mismatch with the airborne observations, (c) an incorrect a priori glyoxal profile in the air mass factor calculations, or (d) a decreased sensitivity of the TROPOMI instrument to low lying plumes over surfaces with low reflectivity (e.g. oceans), or a combination of all these circumstances.

(4) The detection of glyoxal in mixed polluted continental or coastal air masses (e.g. over continental Europe) agrees well between both instruments for upper tropospheric measurements, even though glyoxal VCDs are sometimes underestimated by TROPOMI (e.g. over the Upper Silesian Coal Basin). While the discussion of space and aircraft observations generally focuses on aircraft observations in the upper troposphere (as explained above), the airborne instrument was found to generally measure more glyoxal than the satellite for measurements closely above and within the polluted boundary layer. This is primarily a consequence of the observation geometry, the different a priori assumptions, and the proximity of the measurements to the pollution. At lower flight altitudes, a relatively larger fraction of photons detected by the aircraft instrument will have travelled through the pollution layer than the photons detected by the satellite. Secondly, the mostly larger assumed a priori glyoxal for the airborne observations

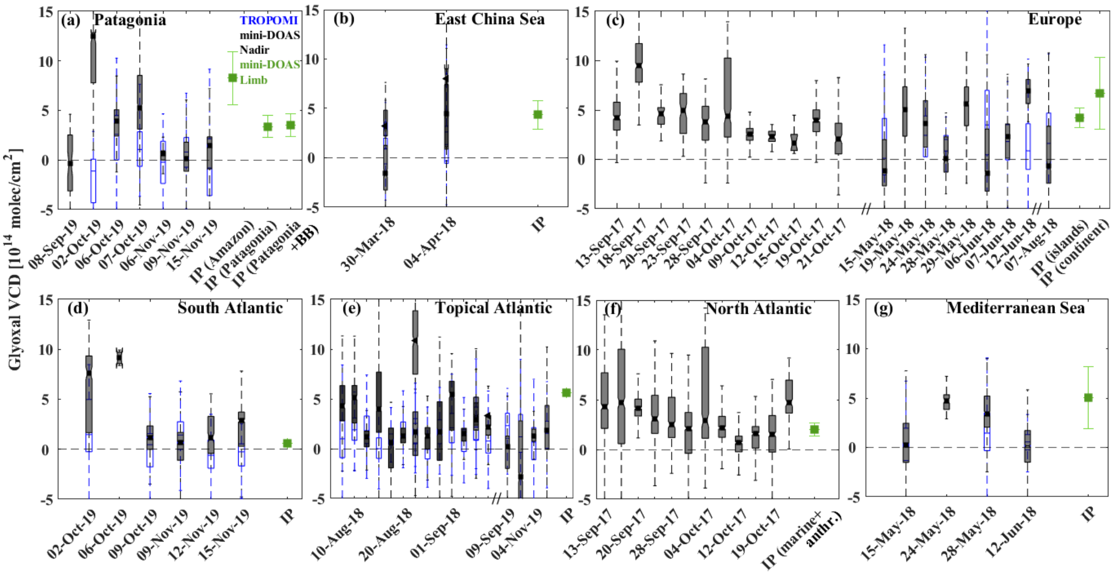

Figure 5.7: Comparison of inferred glyoxal VCDs for TROPOMI (blue) and mini-DOAS measurements (black) for the different regions: South American continent (panel a), East China Sea (panel b), continental Europe and its northern islands (panel c), South Atlantic (panel d), Tropical Atlantic (panel e), North Atlantic (panel f), and the Mediterranean Sea (panel g). The whisker boxes indicate the 25th to 75th percentile ranges and respective medians with in-range minima and maxima. For comparison, also the integrated glyoxal Limb profiles (IP, see Sect. 5.1.1) for the different subsets of data are shown (green squares). For the South American Continent, mini-DOAS VCD measurements are only available for the Patagonia and Argentina SouthTRAC deployments in fall 2019. For the measurements before 2018, TROPOMI data were not yet available.

as compared to MARGRITTE CTM simulations for low altitudes in polluted environments leads to a larger detection sensitivity for glyoxal of the aircraft at these altitudes (Figs. 3.8 and 3.9). This becomes in particular noticeable when the aircraft is close to within the polluted lower atmosphere. For such measurements, the box air mass factors give even more weight to the glyoxal located below the aircraft than to the glyoxal fraction above the aircraft (to which the satellite relatively gives more weight). Over continental Europe, both instruments detected median glyoxal VCDs roughly two to five times larger than over pristine marine environments, such as over the South, Tropical, and North Atlantic (Fig. 5.7, panels c, d, e, f, and g). When probing distinct (mostly anthropogenic) emission sources of glyoxal and its precursors such as over major population centres (e.g. Bologna) or industrial agglomerations (e.g. the Po Valley or the upper Silesian Coal Basin), TROPOMI generally measures smaller VCDs than the mini-DOAS instrument (right side tail in the mini-DOAS distribution in Fig. 5.4, panel b). Accordingly, over the Upper Silesian Coal basin a factor of five times larger glyoxal VCDs are detected by the mini-DOAS instrument ($(7.2 \pm 4.4) \times 10^{14}$ molec cm^{-2}) than by TROPOMI ($(1.3 \pm 2.4) \times 10^{14}$ molec cm^{-2}). The smaller VCDs reported by TROPOMI over populated and industrial areas with a correspondingly increased aerosol load in the boundary layer might be caused by the decreased detectability of glyoxal from space.

Figure 5.7 shows the glyoxal VCDs inferred for collocated flight sections in the different regions and seasons with the median, 25th and 75th percentiles (box edges) and whiskers indicating in-range minima and maxima. Additionally, the glyoxal VCDs inferred from the integrated Limb profiles are compared to the Nadir inferred VCDs (Fig. 5.7, green squares). The VCDs obtained from the integrated vertical glyoxal profiles (IP) are in good agreement to the Nadir measured VCDs, thus providing confidence in the consistency of the airborne glyoxal measurements. In

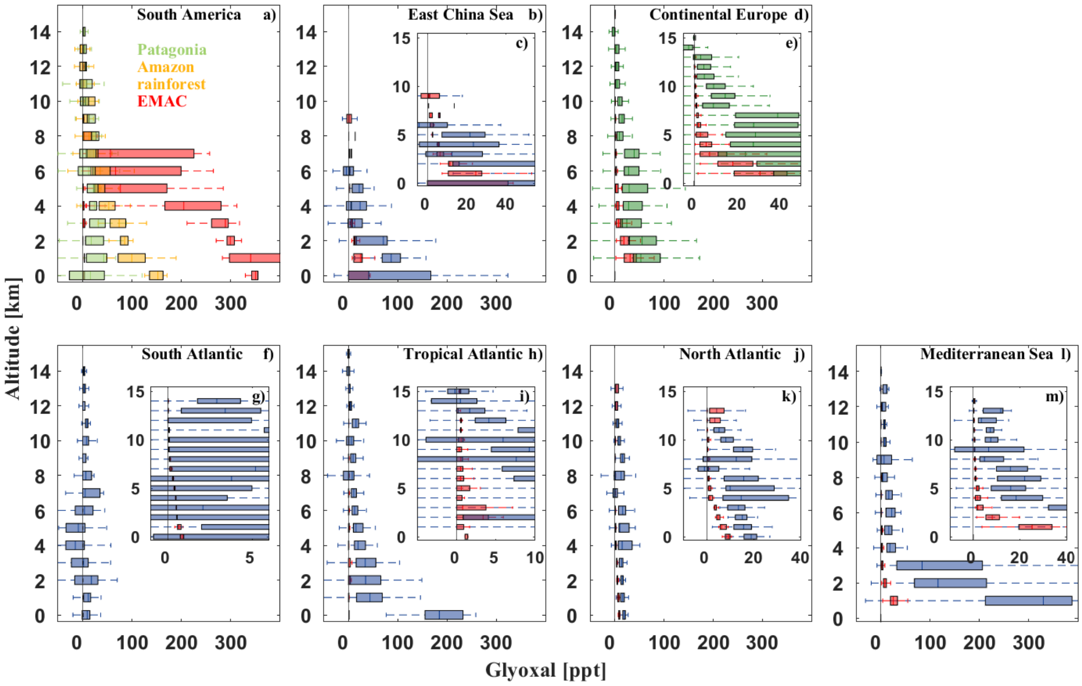

Figure 5.8: Measured and simulated vertical profiles of glyoxal over the different regions (model simulations in red, continental measurements are shown in green, over the rainforest in yellow, and marine observations in blue). For the comparison, only positive valued measurements are considered due to the missing randomness of the model simulations (see text). Since for the measurements over the Amazon rainforest in 2014 and over the Mediterranean and Near East in 2015 no EMAC simulations are available, simulations performed for the year 2017 are used instead (panel b and a minor part of the data in panel h). The data are plotted in 1 km altitude bins for the 25th to 75th percentiles (whisker boxes) with respective medians and with in-range minima and maxima. Identified emission events (see Fig. 5.1 and Sect. 5.1.1) are excluded to enable a climatological comparison of the characteristic background atmosphere of each region.

general, a good agreement is found between the airborne and space-borne glyoxal measurements for all regions and seasons, with the exceptions discussed above.

Even though (aged) biomass burning plumes often only extend over a limited altitude range in the lower and middle troposphere and therefore may only contribute a minor fraction to the total VCDs in background air, they are apparently discernible in airborne observations and in cases of more pronounced pollution or large vertical extent even from space (e.g. Fig. 5.6, panels a and b, and Fig. 5.7, panels a and c).

5.1.3 Inter-comparison of airborne measured and EMAC simulated glyoxal

In the following, the airborne glyoxal measurements are compared to EMAC model simulations provided by S. Rosanka (Forschungszentrum Jülich Institute for Energy and Climate Research: Troposphere (IEK-8)) and performed at the Jülich Supercomputing Centre (sect. 3.1.5). The simulations of glyoxal mixing ratios and VCDs are performed on a 10 min time grid resolution along the flight trajectories based on the settings described in sect. 3.1.5. For the measured versus modelled inter-comparison, VCDs detected at all flight altitudes are included in the analysis. This comes with the advantage of a larger number of available VCD measurements than for the airborne to satellite comparison (in particular over the East China Sea), but at the same time the flight medians slightly change from those compiled for the satellite comparison (Fig. 5.7 and Fig.

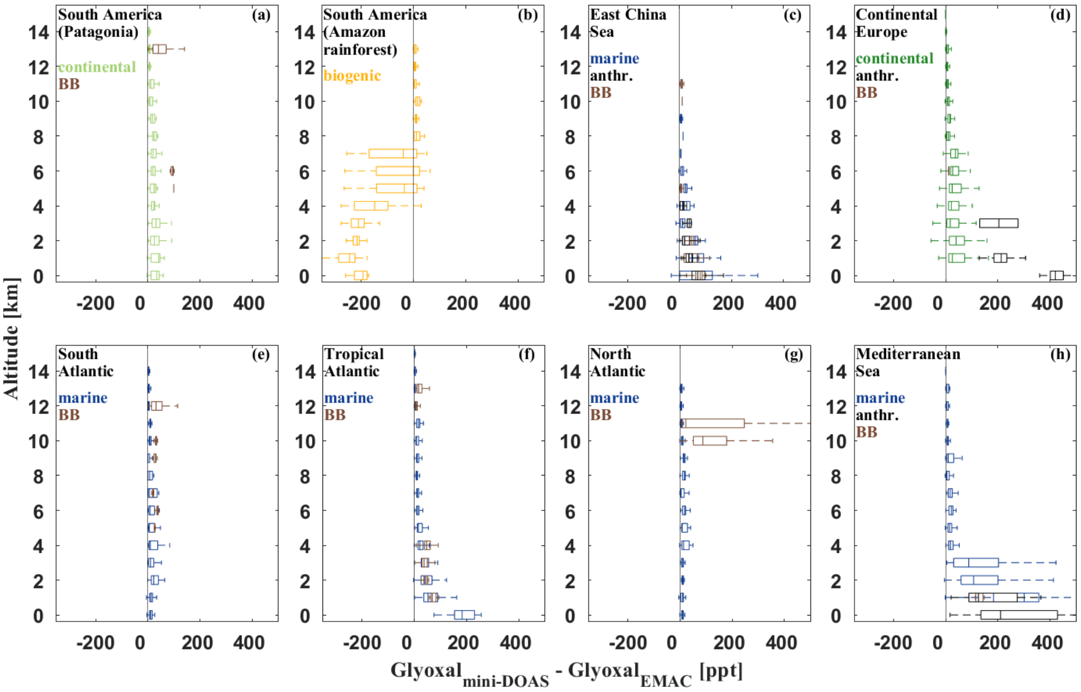

Figure 5.9: Difference of measured airborne and EMAC simulated glyoxal for the different regions (continental measurements are shown in green, over the rainforest in yellow, and marine observations in blue). For the comparison, only positive valued measurements are considered due to the missing randomness of the model simulations (see text). Since for the measurements over the Amazon rainforest in 2014 and over the Mediterranean and Near East in 2015 no EMAC simulations are available, simulations performed for the year 2017 are used instead (panel b and a minor part of the data in panel h). The data are plotted in 1 km altitude bins for the 25th to 75th percentiles (whisker boxes) with respective medians and with in-range minima and maxima. Profiles for identified emission events (see Fig. 5.1 and Sect. 5.1.1) are calculated separately (biomass burning in brown and anthropogenic emissions in black).

5.10). For the comparison, it is distinguished between observations in background air (outside of identified emission events) and observations of elevated glyoxal due to specific emission plumes (see Fig. 5.1 and Sect. 5.1.1). The resulting profiles differentiate the characteristic background glyoxal in each region (green, yellow, and blue in Fig. 5.9) from local glyoxal enhancements due to biomass burning or anthropogenic pollution (brown and black colours, respectively, in Fig. 5.9). Since for low glyoxal concentrations the measurement noise occasionally leads to negative data (see Fig. 5.4 and Fig. 5.10), and the model does not reproduce such measurement noise, negative glyoxal measurements are omitted from the comparison (appendix D, Fig. D.1, black) rather than to keep them in the analysis (appendix D, Fig. D.1, red). The comparison of both approaches however indicates that including or excluding negative measurements causes only minor changes to the results, which are all within the uncertainty of the given median differences in the observations (appendix D, Fig. D.2).

However, the performance of the same comparison including negative glyoxal observations yields only small deviations to the comparison without negative glyoxal, all within the uncertainty range of the inferred median observation to model differences.

For the employed EMAC set-up, simulated glyoxal underestimates measured glyoxal to varying degrees, in agreement with previous findings (e.g. Myriokefalitakis et al. [2008]; Fu et al. [2008]; Stavrakou et al. [2009a]; Walker et al. [2022]; and Figs. 5.9 and 5.10). The best agreement between the model and measurement and thus smallest glyoxal underestimation is generally found for the upper troposphere and in most pristine regions with only little surface emissions or

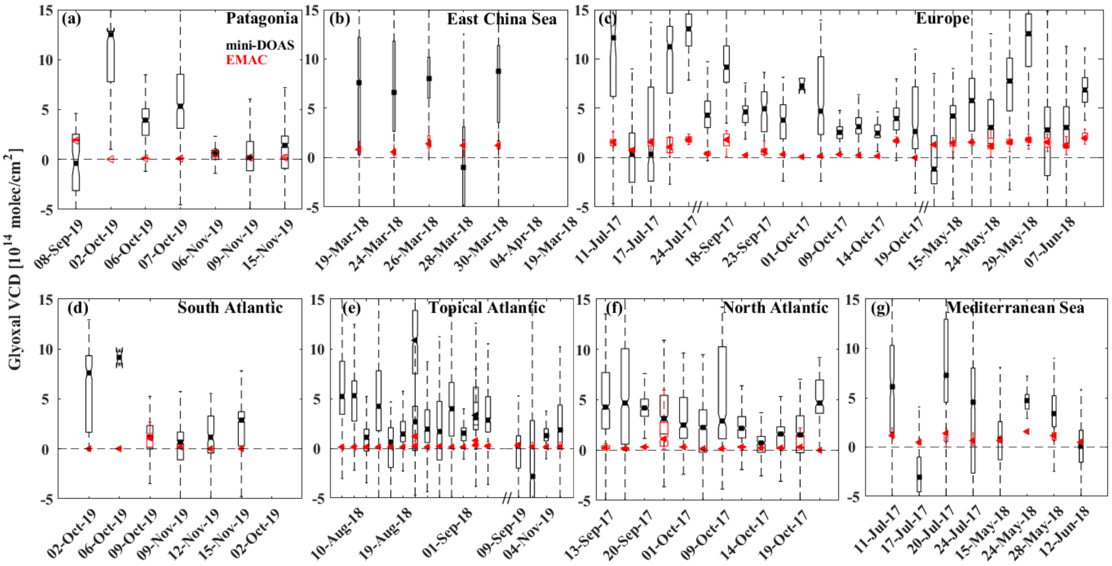

Figure 5.10: Comparison of measured airborne (black) and simulated (red) glyoxal VCDs in the different regions and for all flight altitudes of the measured data.

expected long-range transport of glyoxal and its precursors, i.e. over Patagonia or the North Atlantic (Fig. 5.9, panels a, e, and g, and Fig. 5.10, panels a, d, and f). Larger differences of modelled and measured glyoxal are found for regions with significant biogenic (e.g. tropical rainforests), anthropogenic (e.g. continental Europe, East China or Mediterranean Sea; Fig. 5.9, panels c, d, and h, and Fig. 5.10, panels b, c, and g), or biomass burning related emissions of glyoxal and precursor VOCs (e.g. the Tropical Atlantic, Fig. 5.9, panel f, and Fig. 5.10, panel e). In the mixed polluted background atmosphere over continental Europe, the comparison shows a relatively small glyoxal underestimation by EMAC (Fig. 5.9, panel d, green), whereas measured and modelled glyoxal differ significantly when probing local emission hotspots (e.g. city plumes; Fig. 5.9, panel d, grey) as well as in the mixed polluted marine boundary layer over both the East China and Mediterranean Sea (Fig. 5.9, panels c and h).

The following three key findings are eminent:

(1) Over the tropical rainforest, with its significant surface emissions of biogenic VOCs, the model overestimates glyoxal by a factor of 2–3 in the planetary boundary layer and free troposphere (Fig. 5.9, panel b). At higher altitudes (> 8 km), measured glyoxal exceeds the simulations, as it is also observed for the other investigated regions. This may indicate too strong emissions of short-lived biogenic VOCs (e.g. isoprene) from the rainforest and/or overestimated emissions of longer-lived glyoxal precursor molecules (e.g. aromatics, aliphatic compounds) within the model. In addition, the strong overestimation might point to missing glyoxal loss processes like the uptake and hydration and oligomerization in cloud droplets which have been recently represented in EMAC in the Jülich Aqueous-phase Mechanism of Organic Chemistry [JAMOC; Rosanka et al., 2021b,a].

(2) In distinctive biomass burning or anthropogenic emission plumes (Fig. 5.9, brown and grey), the glyoxal underestimation from the model is found to be larger than outside of the plumes. For example, glyoxal enhancements due to city plumes over Europe are mostly reproduced by the model, however with the magnitude underestimated on average by a factor of 8. The reasons for this underestimated glyoxal in polluted air masses are presently unclear, but may be related to incorrect assumptions regarding the strengths and composition of the anthropogenically emitted mixture of glyoxal producing VOCs. At the same time, the different spatial resolutions of the airborne observations and EMAC (about 209 × 209 km^2) may further amplify the underestimation of individual city plumes by the model.

(3) The findings of enhanced glyoxal in the tropical marine boundary layer are in agreement with previous reports from the Tropical Pacific and Atlantic (e.g. Sinreich et al. [2010]; Walker et al. [2022]), but are not reproduced by the model (Fig. 5.9, panel f). Over the Tropical Atlantic, EMAC simulates an approximately constant vertical profile with much smaller median glyoxal mixing ratios (4 ppt) than observed (44 ppt). In the free and upper troposphere, the simulations and observations outside of biomass burning plumes agree better. Again, this discrepancy may point to missing glyoxal sources related to the organic micro-layer at the sea surface in the model (e.g. Chiu et al. [2017]; Brüggemann et al. [2018]).

5.2 Measurements of formaldehyde, glyoxal, and methylglyoxal over the Amazon rainforest

The second part of this chapter focuses on the measurements over the tropical rainforest and the Amazon river delta. The vertical profiles of the carbonyls formaldehyde, glyoxal, and methylglyoxal are compared and possible precursors of sources are discussed. A particular focus is put on their emissions from biomass burning plumes, which frequently occur during the tropical dry season and can reach large regional extents.

5.2.1 Vertical profiles

Based on all four measurement flights over the Amazon rainforest, the volume mixing ratios of the target gases, and additionally of CO as final and respectively long lived oxidation product of the VOCs, are analysed as a function of the measurement altitude in the troposphere.

5.2.1.1 CO

Below 450 m altitude, CO mixing ratios range from 88.6 ppb to 291.8 ppb (Fig. 5.11, panel a), with a mean of [CO]=188.1 ppb. Within the planetary boundary layer, CO mixing ratios increase from 88.4 ppb to 2308 ppb (mean [CO] = 212.8 ppb), with peak mixing ratios above 500 ppb appearing when biomass burning plumes are directly passed. Lowest [CO] mixing ratios in the range of 55.1 ppb to 231.9 ppb (mean [CO] = 86.3 ppb) are found in the middle troposphere between 6 and 8 km altitude. In the upper troposphere (12–14 km), CO increases from 52.5 ppb to 212.6 ppb (mean [CO] = 134.5 ppb). In the convective tropics, C-shaped CO profiles are a well-known phenomenon, caused by the rapid transport of near surface CO rich air by meso-scale convective systems into the upper troposphere (e.g., Brocchi et al. [2018]; Krysztofiak et al. [2018]). When binning the data in 100 m altitude intervals and averaging over the lower and upper data quartiles within each interval, another maximum forms around the top of the boundary layer. Most likely, this suggests that over the Amazon biomass burning plumes often detrain their pollutants near the top of the boundary layer (e.g. at 17:24 UTC, Fig. 4.3).

5.2.1.2 Formaldehyde

The inferred formaldehyde ranges from 4.5 ppb near the surface to mean mixing ratios of 30 ppt in the upper troposphere (above 10 km). Mixing ratios within the boundary layer and middle troposphere vary significantly (Fig. 5.11, panel b). In part, this might be a manifestation of the direct emission of formaldehyde into the lower part of the atmosphere, or the in situ formation of formaldehyde during the oxidation of bVOCs as well as partly oxidized VOCs (OVOCs). Figure 5.12 puts the present formaldehyde measurements over the Amazon into the context of

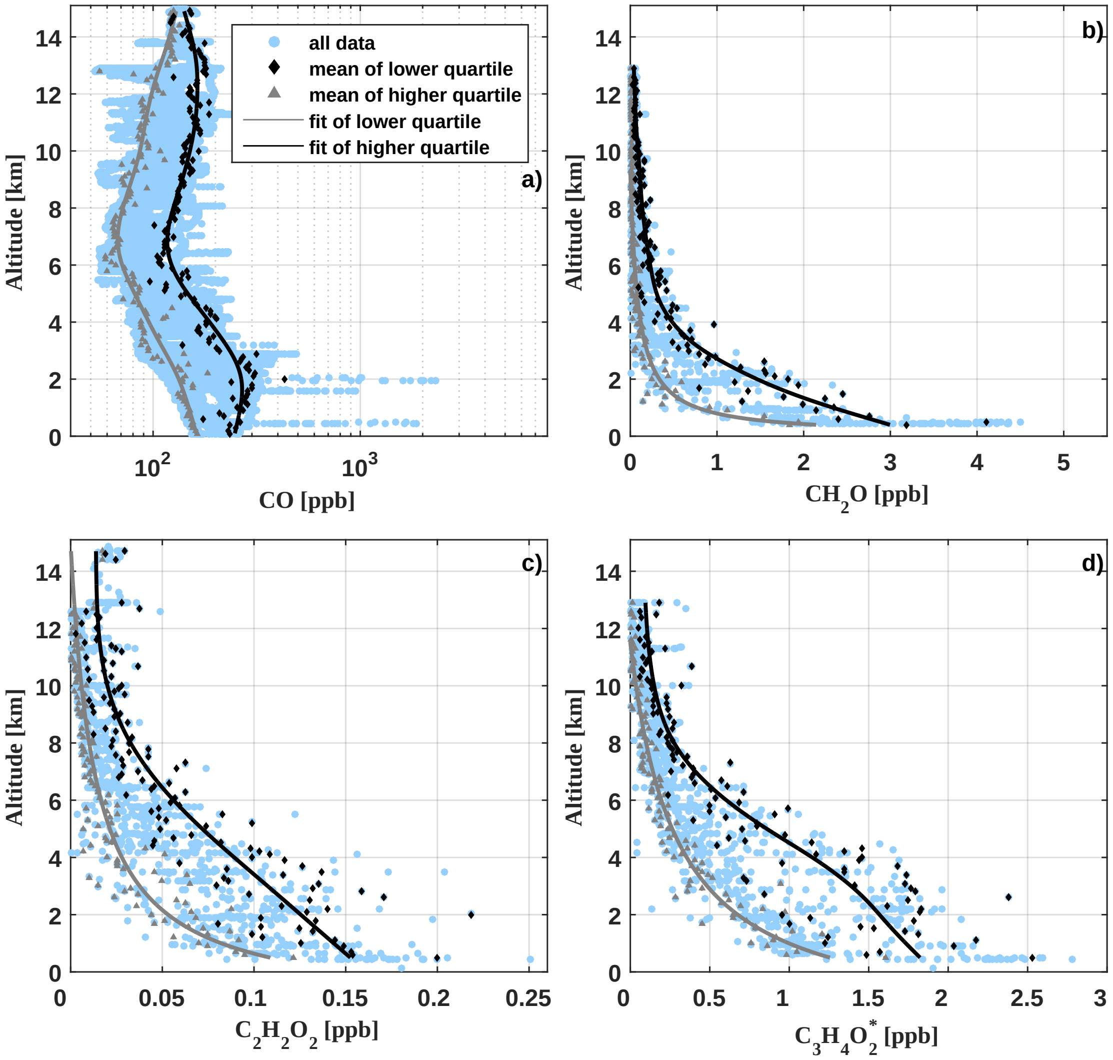

Figure 5.11: Vertical profiles of CO (panel a), formaldehyde (CH_2O, panel b), glyoxal ($C_2H_2O_2$, panel c), and $C_3H_4O_2{}^*$ (panel d) as measured during flights AC09, AC11, AC12, and AC13 (blue circles). Note the logarithmic scale of the x-axis in panel a. For AC09, there are no CO data available. The grey lines indicate a spline fit (panel a) and least squares fits (panel b to d) through the lower quartile of the data (grey triangles) in 100 m altitude bins. The black lines show corresponding fits through the mean of the upper quartile (black diamonds).

previously published formaldehyde observations all over the world. Within this comparison, it is remarkable that the lowest formaldehyde mixing ratios measured over the Amazon are similar to formaldehyde reported by Peters et al. [2012] within the boundary layer and middle troposphere over the West Pacific. The measurements in the upper troposphere compare well to findings from Dufour et al. [2009] and Boeke et al. [2011] over Brazil and North America, respectively. The lowest mixing ratios measured in the middle and upper troposphere may reflect formaldehyde formed during the oxidation of mostly methane and, if available, some residual VOCs, OVOCs, and bVOCs (e.g. Fig. 5.11, panel c for glyoxal and panel d for methylglyoxal), since their photochemical and heterogeneous removal is often slower than the formaldehyde photochemical lifetime of only a few hours [Frost et al., 2002]. In contrast, the largest formaldehyde mixing ratios measured over the Amazon at any altitude appear slightly smaller than the average, and significantly smaller than the maximum mixing ratios reported from the joint SENEX aircraft observations of formaldehyde and glyoxal over North America [Kaiser et al., 2015; Chan Miller et al., 2017].

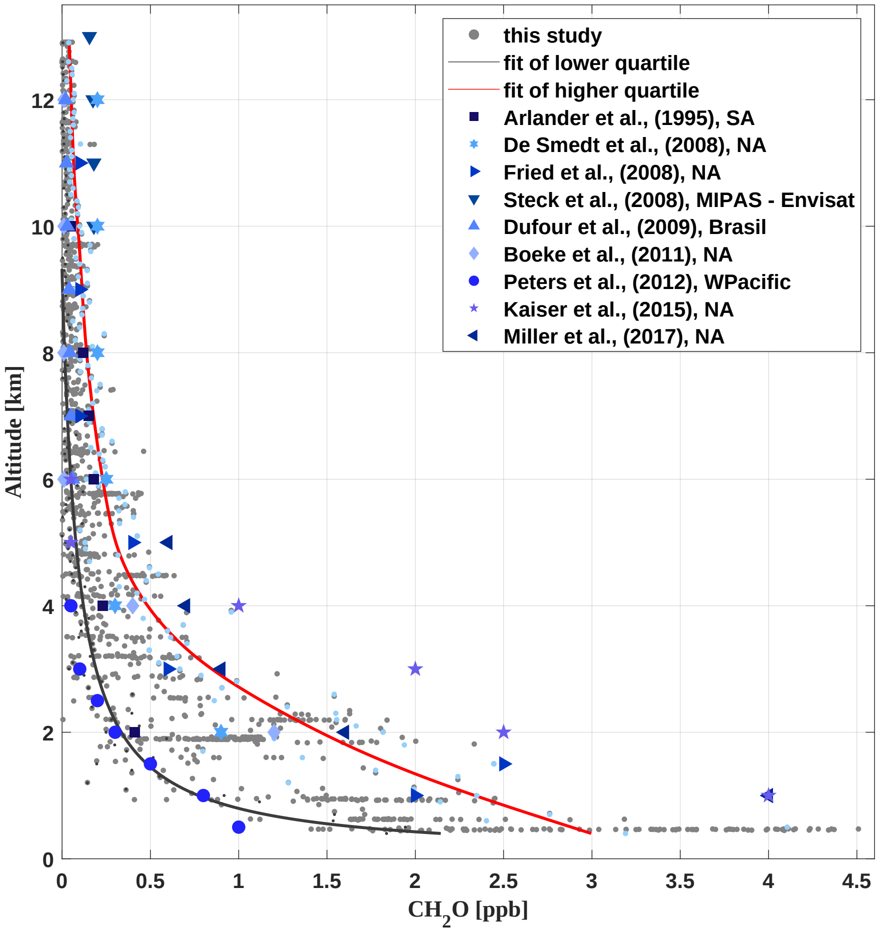

Figure 5.12: Comparison of different formaldehyde measurements available from the literature [Arlander et al., 1995; De Smedt et al., 2008; Fried et al., 2008; Dufour et al., 2009; Steck et al., 2008; Boeke et al., 2011; Peters et al., 2012; Kaiser et al., 2015; Chan Miller et al., 2017] with those of the present study (grey). The geographical regions of the measurements are Brazil, South America (SA), North America (NA), West Pacific (WPacific) and MIPAS-Envisat measurements covering orbit 8164, 14° S/46° W.

5.2.1.3 Glyoxal

Glyoxal mixing ratios range from 85 ppt to 250 ppt below 500 m altitude and decrease in the upper troposphere (12–14 km) to mixing ratios from 5 ppt to about 49 ppt. Close to the ground, the mixing ratios are comparable to those found in the present study over the Tropical Atlantic and much smaller than over continental Europe, the Mediterranean Sea, and the East China Sea. The measurements over the rainforest are further comparable to those observed over North America by Kaiser et al. [2015] and Chan Miller et al. [2017], but much larger than those measured in pristine air masses of the South Pacific (7–23 ppt; Lawson et al. [2015]). Evidently, besides glyoxal formation during the oxidation of bVOCs [Wennberg et al., 2018], a fraction of the near surface and boundary layer glyoxal is certainly due to direct emissions by biomass burning [Zarzana et al., 2018; Andreae, 2019]. In the middle troposphere, the inferred mixing ratios of glyoxal are significantly larger than observations during SENEX (which reach to approximately 6 km altitude) and are also larger in the upper troposphere above 6 km when comparing to data extrapolated from SENEX. Between 6 and 14 km altitude, glyoxal enhancements of up to ≈ 63 ppt become apparent when compared to either the SENEX data or the binned lower quartile of the present data set. Such elevated mixing ratios of glyoxal in the middle and upper troposphere point to an efficient vertical transport of glyoxal and its precursors VOCs, OVOCs, and bVOCs from their emission sources at the ground or to direct formation from longer-lived VOCs (e.g. phenols) [Andreae et al., 2001; Taraborrelli et al., 2021]. Further, glyoxal and $C_3H_4O_2$* present at higher atmospheric altitudes may serve as a marker for the formation of ISOPOO (isoprene peroxy radicals), ISOPOOH (oligomer hydroxyhydroperoxides) and finally IEPOX (isoprene epoxydiols) within the isoprene oxidation chain [Wennberg et al., 2018]. In fact, IEPOX mediated SOA formation in the upper troposphere over the Amazon has been reported from observations made within the framework of the ACRIDICON-CHUVA project [Andreae et al., 2018; Schulz et al., 2018; Liu et al., 2022].

5.2.1.4 Methylglyoxal

The detection of $C_3H_4O_2$*, here taken as the sum of methylglyoxal and larger carbonyls as described previously, appears elusive due to the spectral interference among the different species. Weighting of the measured total absorption for $C_3H_4O_2$* with the relative absorption cross sections of the inferred $C_3H_4O_2$, $C_4H_6O_2$ (biacetyl), and $C_4C_8O_4$ (acetylpropionyl) (Zarzana et al. [2017], Fig. S4) may be indicative of the relative abundance of each species. Based on arguments of Zarzana et al. [2017], a weighting factor of 2.0 ± 0.5 is applied by which the inferred $C_3H_4O_2$* needs to be divided for indicative $C_3H_4O_2$ mixing ratios. However, note that the factor of 2.0 ± 0.5 may largely depend on the precursor concentrations, and thus on the geolocation, altitude, and geophysical regime, and therefore barely provides more than a hint on its true size.

Due to the lack of previous atmospheric $C_3H_4O_2$* (or $C_3H_4O_2$) measurements, it is more difficult to put the inferred $C_3H_4O_2$* profile into the context of previous measurements (Fig. 5.11, panel d). As for the other measured hydrocarbons, the largest $C_3H_4O_2$* mixing ratios between 1.2 ppb and 2.8 ppb (mean [$C_3H_4O_2$*]=1.6 ppb) are found near the ground and within the planetary boundary layer. Below 1 km altitude, the resulting $C_3H_4O_2$ of 0.8 ppb to 2.8 ppb (mean [$C_3H_4O_2$*]=1.5 ppb) are considerably larger than recently reported $C_3H_4O_2$ mixing ratios (28 ppt to 365 ppt) from a Mediterranean site with intense biogenic emissions and low levels of anthropogenic pollutants [Michoud et al., 2018], as well as measurements at Cape Grim (28 ± 11 ppt) and the Chatham Rise (10 ± 10 ppt) in pristine marine air [Lawson et al., 2015]. Therefore, a major fraction of the enhanced $C_3H_4O_2$* is assumed to be related to the oxidation of bVOCs and biomass burning (e.g., Andreae and Merlet [2001]; Akagi et al. [2011]; Stockwell et al. [2015]; Zarzana et al. [2017, 2018]; Andreae [2019]). Evidence that the former is overall the more relevant process (as compared to direct emissions by biomass burning) in the Amazonian troposphere is also provided by the relatively compact clustering of the inferred $C_3H_4O_2$* along the fit of the lower quartile of the data.

Figure 5.13 shows the inferred trace gas mixing ratios of formaldehyde (panel a), glyoxal (panel b), methylglyoxal (panel c), and CO (panel d) during an example flight over the Amazon rainforest on 16. Sept. 2014. Notable are the significant enhancements of all three carbonyls due to several biomass burning plume crossings during the flight.

The measured trace gas mixing ratios are the largest for flight sections within the planetary boundary layer (14:45 to 15:15 UTC and 17:05 to 17:45 UTC), and the lowest in the upper troposphere (16:15 to 16:45 UTC and 19:15 to 20:20 UTC). Notable are the peaks in CO while flying through the Manaus city plume (grey bars) or biomass burning plumes (red bars). Elevated mixing ratios of formaldehyde, glyoxal, and methylglyoxal can be related to biomass burning as well as to air masses of presumably aged background air (labelled with the green bars) as evidenced by the only moderately elevated CO. Here, the numbers (1) to (6) in panel a of Fig. 5.13 denote biomass burning affected air (1–3), air of the Manaus city plume (4), pristine air of the upper troposphere (5), and boundary layer air above the tropical forest (6). Sky images of all six situations (labelled 1 to 6) are shown in Fig. 4.3.

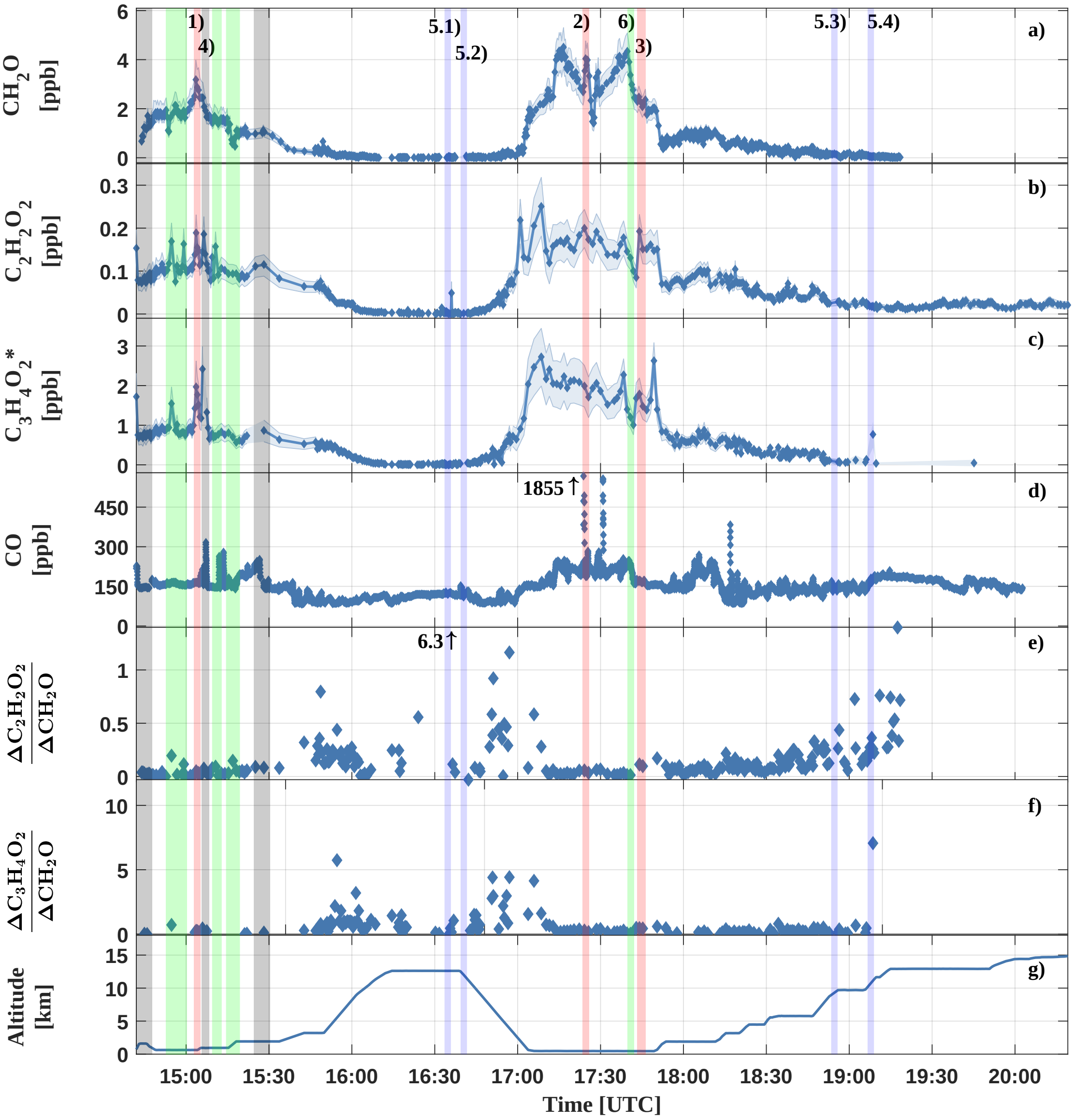

Figure 5.13: Measured mixing ratios of formaldehyde (panel a), glyoxal (panel b), methylglyoxal (panel c), CO (panel d), inferred $R_{GF} = \Delta C_2H_2O_2/\Delta CH_2O$ (panel e), $R_{MF} = \Delta C_3H_4O_2{}^*/\Delta CH_2O$ (panel f), and the height versus time trajectory for the HALO flight AC11 (panel h). The shaded blue area in panels a to c shows the respective measurement uncertainty. All measurements within the Manaus city plume are marked by grey bars (e.g. event AC11-4). Examples for measurements in aged air masses of the upper troposphere are marked in blue (e.g. events AC11-5.1–5.4), and green for the general background atmosphere i.e. tropical forest affected air (e.g. event AC11-6). All measurements of biomass burning plumes are labelled in red (events AC11-1, AC11-2 and AC11-3). The event numbers correspond to the labelling in Table 5.2 and Fig. 3.7.

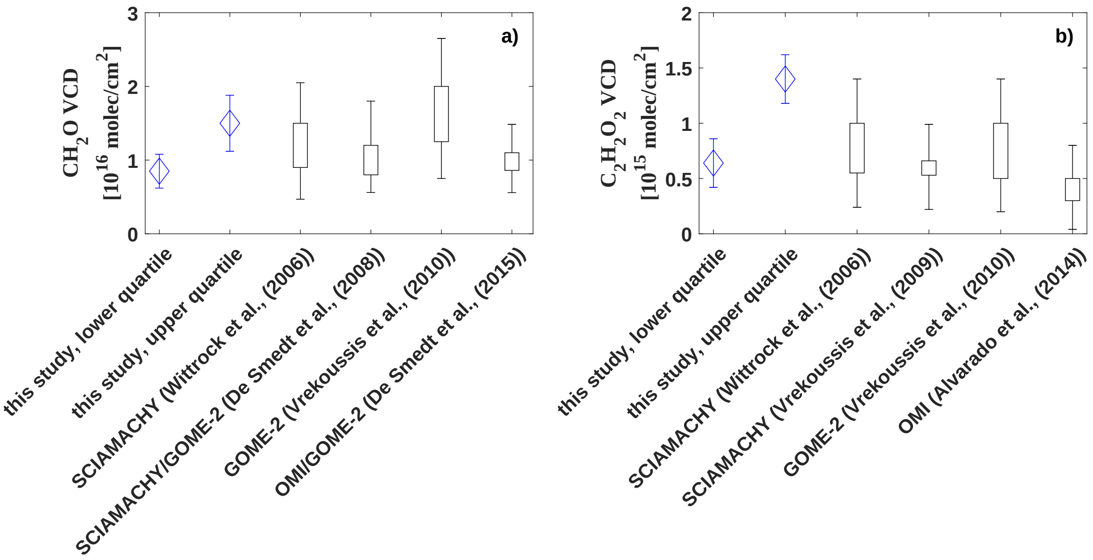

Figure 5.14: Comparison of the integrated total column densities of formaldehyde (CH_2O) and glyoxal ($C_2H_2O_2$). The vertical bars indicate the range of the observed vertical column amounts as reported in the respective studies. The uncertainty range for Wittrock et al. [2006] and Alvarado et al. [2014] was estimated based on Vrekoussis et al. [2009].

5.2.2 Comparison to satellite measurements

Due to the lack of mini-DOAS Nadir measurements during ACRIDICON-CHUVA, no VCD measurements of the target gases were performed over the rainforest. But, since neither formaldehyde nor glyoxal have relevant stratospheric sources, the integration of the profiles should yield their total vertical column density over the investigated region. The uncertainty of the integrated profiles follows from the altitude weighted total error of the measurements as displayed in Fig. 3.10. The observations are compared to respective measurements of the GOME (Global Ozone Monitoring Experiment), SCIAMACHY (SCanning Imaging Absorption spectroMeter for Atmospheric CHartographY), OMI (Ozone Monitoring Instrument), and GOME-2. Combined, they all provide global formaldehyde and glyoxal observations covering more than a decade (Fig. 5.14).

Integration of the formaldehyde profiles yields total column densities of $(0.9 \pm 0.2) \times 10^{16}$ molec cm^{-2} (lower quartile as plotted in Fig. 5.11) to $(1.5 \pm 0.4) \times 10^{16}$ molec cm^{-2} (upper quartile), with a mean of $(1.1 \pm 0.3) \times 10^{16}$ molec cm^{-2} (all data, Fig. 5.14, panel a). Satellite observations generally report enhanced CH_2O VCDs over regions with large biogenic emissions, especially over the Amazon Basin, with maximal enhancements during the dry season. Monthly means of formaldehyde VCDs measured by GOME and SCIAMACHY in the years 1996–2007 over the Amazon report maximal enhancements of $1 - 2 \times 10^{16}$ molec cm^{-2} during the dry season and much smaller vertical column densities of 0.8×10^{16} molec cm^{-2} during the wet season [De Smedt et al., 2008]. The inferred formaldehyde vertical column densities based on the lower quartile agree well with their measurements during the wet season, while the integrated profile of the upper quartile lies within the observations during the dry season. The results agree equally well with SCIAMACHY observations in 2005 over South America with an annual mean formaldehyde VCD of approximately 1.2×10^{16} molec cm^{-2} as reported by Wittrock et al. [2006] and also agree with GOME-2 observations, for which Vrekoussis et al. [2010] report CH_2O VCDs of 1.2 to 1.6×10^{16} molec cm^{-2} over the Amazon Basin for the years 2007 to 2008. Finally, yearly averaged formaldehyde from OMI and GOME-2 observations over Brazil between 2007 and 2013 by De Smedt et al. [2015] agree with the mean of 1.1×10^{16} molec cm^{-2}.

For the central Amazon, the integrated glyoxal profiles range from $(0.6 \pm 0.2) \times 10^{15}$ molec cm^{-2}

(lower quartile) to $(1.4 \pm 0.4) \times 10^{15}$ molec cm^{-2} (upper quartile), with a mean of $(1.0 \pm 0.3) \times 10^{15}$ molec cm^{-2}. Based on SCIAMACHY measurements in the years 2002 to 2007, Vrekoussis et al. [2009] reported seasonal mean glyoxal VCDs of 0.5×10^{15} molec cm^{-2} over northern South America in autumn (Fig. 5.14, panel b). In good agreement with the lower limit, Wittrock et al. [2006] reported slightly higher glyoxal observations from SCIAMACHY of approximately $0.6 - 0.7 \times 10^{15}$ molec cm^{-2} over North Brazil for the year 2005. Corresponding to the mean mini-DOAS VCD, Vrekoussis et al. [2010] further reported average glyoxal VCDs of 0.5×10^{15} molec cm^{-2} ($VCD_{glyoxal,max} = 1 \times 10^{15}$ molec cm^{-2} based on GOME-2 measurements over South America in the years 2007 to 2008. Observations from OMI yield slightly lower monthly mean glyoxal VCDs of 0.3×10^{15} molec cm^{-2} [Alvarado et al., 2014]. The upper quartile glyoxal VCD (indicative of the large amount of direct glyoxal emissions from various biomass burnings into the boundary layer) is larger, but still within the uncertainty range of the SCIAMACHY and GOME-2 observations.

5.2.3 Emission ratios of glyoxal and methylglyoxal

As outlined above, the different air masses probed with the mini-DOAS and AMTEX instruments prevent a definition of emission ratios relative to CO (sects. 3.1.3 and 3.1.5). Instead, the inferred mixing ratios are used to calculate the emission ratios $\mathrm{R}^*_{\mathrm{GF}}$ and $\mathrm{R}^*_{\mathrm{MF}}$ relative to $\mathrm{CH_2O}$, as often done in remote sensing studies (Fu et al. [2008]; Kaiser et al. [2015]; Stavrakou et al. [2016]; Zarzana et al. [2017, 2018], and others). According to the literature, the background uncorrected emission ratio is defined as

$$R^*_{XF} = \frac{[X]}{[CH_2O]}. \tag{5.1}$$

In this study, $[X]$ is either $[\mathrm{C_2H_2O_2}]$ or $[\mathrm{C_3H_4O_2}^*]$, as often used in satellite and modelling studies related to hydrocarbon precursors of the studied species (Fu et al. [2008]; Kaiser et al. [2015], and others). $\mathrm{R}^*_{\mathrm{XF}}$ is calculated for each measurement and analysed with respect to the measurement altitude (Fig. 5.15, panels a and b).

5.2.3.1 $\mathbf{R^*_{GF}}$

$\mathrm{R}^*_{\mathrm{GF}}$ mostly remains smaller than 1.0, with a total mean of $\overline{R}^*_{GF} = 0.35 \pm 0.16$, but reaches maxima $>$ 5.0 during several measurements. Small ratios < 0.05 and large ratios > 1.0 can be observed throughout all analysed flights and nearly all altitudes. The comparison with Kaiser et al. [2015] shows, that the inferred $\mathrm{R}^*_{\mathrm{GF}}$ is notably larger than during most of their in situ measurements at altitudes ranging from the ground up to 6 km over the southeastern US in June–July 2013. The results are in much better agreement with the $\mathrm{R}^*_{\mathrm{GF}}$ inferred by MacDonald et al. [2012] from ground based DOAS measurements for altitudes between 0 and 1000 m over a south-east Asian tropical rainforest in April–July 2008. Their $\mathrm{R}^*_{\mathrm{GF}}$ in the range 0.2 to 0.7 agrees with most of the present measurements as well as with $\overline{R}^*_{GF}$. From measurements above the Kisatchie National Forest and the Mark Twain National Forest in the south-eastern US, Kaiser et al. [2015] conclude characteristically low $\mathrm{R}^*_{\mathrm{GF}}$ in pristine regions with strong isoprene emissions, while regimes dominated by the emission of other monoterpenes appear to have higher $\mathrm{R}^*_{\mathrm{GF}}$. Most of the mini-DOAS measurements took place in pristine air masses above the rainforest and far away from any major population centre or other anthropogenic emission sources. Monoterpene and isoprene emissions over the central Amazon were studied in several investigations (e.g. Helmig et al. [1998] and Kesselmeier et al. [2000]). All these studies reported generally low mixing ratios of monoterpenes compared to isoprene, which comprises 90% of the total VOC budget in the Amazon [Kuhn et al., 2007]. Apparently, emissions of larger monoterpenes, like alpha-pinene, are at least one order of magnitude smaller than isoprene emissions. Approximately the same

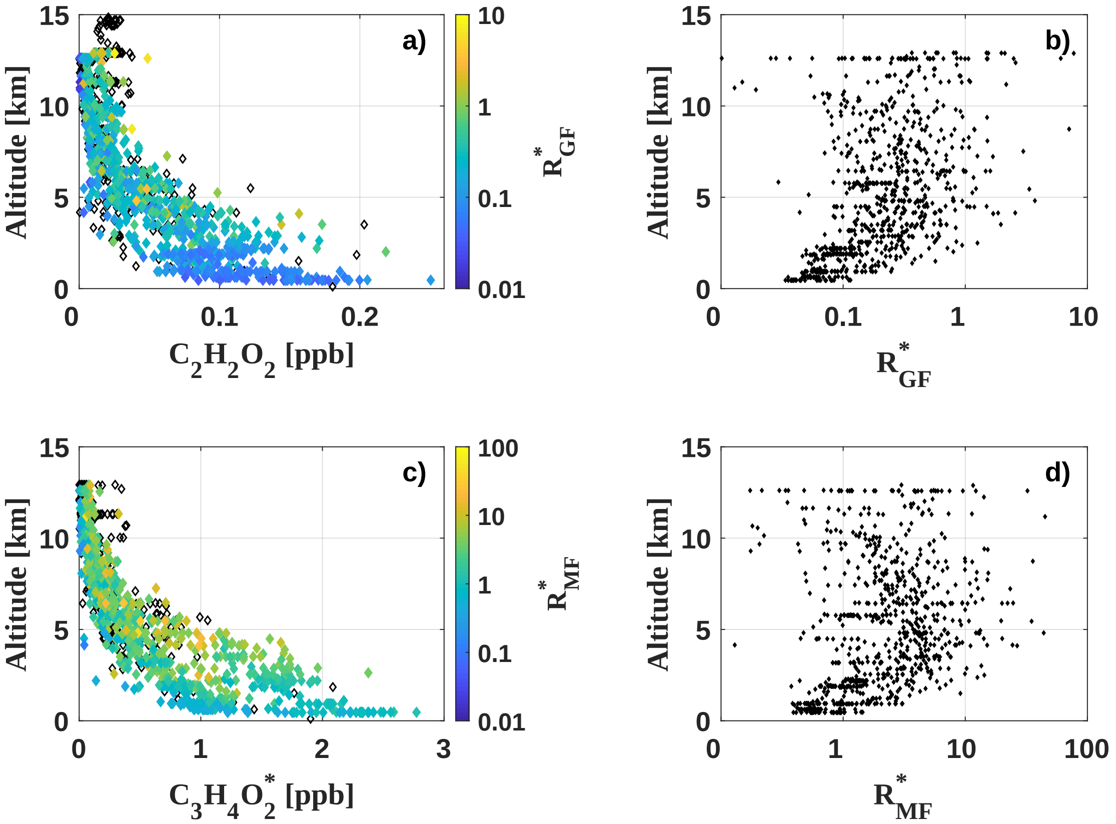

Figure 5.15: Vertical profiles of $C_2H_2O_2$ (panel a) and $C_3H_4O_2^*$ (panel c), colour-coded by the ratios R^*_{GF} and R^*_{MF}, respectively, for each measurement during flights AC09, AC11, AC12, and AC13. Black diamonds indicate measurements with missing CH_2O data (recorded with a different spectrometer) and consequently missing ratios. Panels b and d illustrate the vertical profiles of R^*_{GF} and R^*_{MF} throughout the troposphere. For panels (b) and (d) a logarithmic x-axis has been chosen for a better illustration of the altitude dependence of small R^*_{GF} and R^*_{MF}, respectively.

relation was found for the total monoterpene emissions [Kuhn et al., 2007; Rizzo et al., 2010]. Kaiser et al. [2015] report an approximately 1.2–2.0 times larger glyoxal yield from α- and β-pinene oxidation with respect to CH_2O than from isoprene. Still, the significant predominance of isoprene emissions over the Amazon clearly compensate this relatively smaller yield. Therefore, it is reasonable to conclude that isoprene and not monoterpenes is the dominant precursor of CH_2O and $C_2H_2O_2$ for the observations. Contrary to the measurements of Kaiser et al. [2015] in isoprene rich regimes, the results indicate significantly elevated R^*_{GF} in the troposphere over the Amazon. This is a direct consequence of the much lower CH_2O mixing ratios as compared to those found over the south-eastern US. CH_2O generally does not exceed 1–2 ppb (except for direct measurements in biomass burning or in the Manaus city plume), which is four times less than reported by Kaiser et al. [2015] for air masses probed over the Mark Twain National Forest (ca. 8 ppb). The $C_2H_2O_2$ mixing ratios of typically 100 ppt in the lower troposphere, on the other hand, are comparable to the findings of Kaiser et al. [2015]. As a result, significantly larger R^*_{GF} than from Kaiser et al. [2015] are found in the present study for the pristine troposphere.

Based on the SENEX observations, Chan Miller et al. [2017] reported mean R^*_{GF} of 0.024 below 1 km altitude. Interestingly, Chan Miller et al. [2017] obtained larger R^*_{GF} of up to 0.06 when NO_x was very low (0.1–0.5 ppb). Even though it is not possible to infer NO_x concentrations for all flights due to instrument failures, mini-DOAS NO_2 measurements yield $NO_2 < 1$ ppb for all flights with the exception of direct plume measurements, e.g. of the Manaus city plume and biomass fires. From these overall low NO_2 mixing ratios can be concluded that the measurements during the campaign were generally under very low NO_x conditions. As described in detail by Chan Miller et al. [2017], this could lead to direct glyoxal formation through isoprene peroxy radicals and thus slightly enhanced R^*_{GF} compared to observations under high NO_x. Further, from the measurements over Manaus city, no sizeable influence of anthropogenic VOCs on the inferred R^*_{GF} can be detected. During several low overpasses of the city (< 2 km flight altitude), R^*_{GF} did not show any significant difference to measurements distant from anthropogenic emission sources. Apparently, the relative increases of CH_2O and $C_2H_2O_2$ mixing ratios, i.e their relative source strengths, were similar within the city plume, hence leading to consistent R^*_{GF}.

Finally, the vertical profile of R^*_{GF} indicates slightly elevated ratios above the boundary layer and in the free troposphere (fig. 5.15, panel b). Within the boundary layer, R^*_{GF} remains approximately constant. Both features were previously observed by Kaiser et al. [2015] for altitudes up to 6 km, however less pronounced. The increase in R^*_{GF} between 2–10 km appears most pronounced just above the boundary layer (at about 2 km), where CH_2O and $C_2H_2O_2$ mixing ratios are still significantly above the detection limits. Notably, the correlation of CH_2O and $C_2H_2O_2$ is larger within the boundary layer than in the free troposphere. When discussing the profile shape of R^*_{GF}, one has to keep in mind the very low CH_2O and $C_2H_2O_2$ mixing ratios in the upper troposphere and the increasing influence of measurement noise on the inferred mixing ratios. Above 6 km, mean CH_2O and $C_2H_2O_2$ of only 54 ± 40 ppt and 15 ± 5 ppt, respectively, are observed and accordingly, R^*_{GF} varies on average by 60% among the different measurements within the same altitude range.

5.2.3.2 $\mathbf{R^*_{MF}}$

Generally, R^*_{MF} appears to be approximately 10 times larger than R^*_{GF} (fig. 5.15, panels c and d). $R^*_{MF} < 1$ are observed only for a minority of the measurements and mostly for background $C_3H_4O_2^*$ concentrations. Larger $R^*_{MF} > 1$ are inferred at all altitudes, with a total mean $\overline{R}^*_{MF} = 3.4 \pm 1.6$ and a maximum ratio $R^*_{MF,max} = 45.2 \pm 0.8$. As discussed above for R^*_{GF}, the vertical profile of R^*_{MF} indicates slightly larger R^*_{MF} above the boundary layer and throughout the free troposphere. In the upper troposphere, R^*_{MF} decreases again, leading to a concave curvature of the vertical profile for small R^*_{MF}, as described above for R^*_{GF}. Several studies were published on the emission ratio of $C_3H_4O_2$ to CH_2O (or CO) in biomass burning plumes (e.g. Hays et al. [2002]; Müller et al. [2016]; Zarzana et al. [2017, 2018]). To my knowledge, comparable $C_3H_4O_2$ measurements for air masses of the free troposphere are not yet available.

5.2.4 Normalized excess mixing ratios and emission factors in biomass burning plumes

During the four measurement flights over the Amazonian rainforest, twelve biomass burning plume intercepts were identified based on video imagery (e.g. Fig. 4.3 for events AC11-1.1/1.2 and AC11-3.1/3.2). Most of the plume soundings occurred south of Manaus, and during two extensive flight periods at altitudes below 2 km on 18 and 19 Sept. 2014 (flights AC11 and AC13, Table 5.2). The precise location of all plume intercepts during flight AC11, and the related horizontal averaging kernels of the telescopes are given in Fig. 3.7. As indicated by the backward trajectories, three hours prior to detection all probed air masses moved well within the boundary layer, below 600 m altitude. This residence time if air within the boundary layer is longer than the atmospheric lifetimes of CH_2O, $C_2H_2O_2$ and $C_3H_4O_2$. Consequently, the measured mixing ratios of these gases are a result of fresh emissions from the surface. Each biomass burning plume encounter correlates with significant enhancements in CH_2O, $C_2H_2O_2$ and $C_3H_4O_2{}^*$ over the background by 13 to 400%. Based on the backward trajectories combined with the inspection of

Table 5.2: Inferred normalized excess mixing ratios and emission factors for individual biomass burning events over the Amazon rainforest (range and mean). R_{GF} and R_{MF} are given in mole mole^{-1}.

event	**time [UTC]**	**location**	**altitude [km]**
AC11-1.1	15:03:19–15:03:51	2.9° S, 60.1° W	0.624–0.632
AC11-1.2	15:03:48–15:04:16	2.9° S, 60.1° W	0.615–0.647
AC11-2.1	17:21:06–17:23:31	3.6° S, 60.3° W	0.455–0.471
AC11-2.2	17:23:31–17:24:48	3.6° S, 60.3° W	0.453–0.470
AC11-2.3	17:24:50–17:26:30	3.6° S, 60.3° W	0.452–0.470
AC11-3.1	17:43:27–17:44:41	2.9° S, 60.5° W	0.450–0.456
AC11-3.2	17:44:43–17:45:52	2.8° S, 60.5° W	0.449–0.454
AC13-1	16:33:41–16:34:20	11.0° S, 56.2° W	0.923–0.934
AC13-2	16:34:20–16:34:56	11.1° S, 56.2° W	0.921–0.932
AC13-3	16:35:39–16:36:18	11.2° S, 56.2° W	0.918–0.929
AC13-4	16:37:01–16:37:43	11.2° S, 56.2° W	0.915–0.932
AC13-5	16:52:15–16:53:03	11.2° S, 56.2° W	1.849–1.191

the mini-DOAS video imagery and the short lifetimes of the gases, contributions from other major emission sources (e.g. Manaus city) can largely be excluded. The exact timing, location and altitude of each plume intercept is given in Table 5.2. As indicated by the numbering in column one, some of the plumes were probed more than once, giving a total of eight different biomass burning plumes with 12 encounters (further on called events AC11-1.1 to AC13-5). Due to the lack of respective $C_2H_2O_2$ and $C_3H_4O_2$ measurements, mean background mixing ratios $[X]_{bkg}$ for all three gases are inferred by binning the mini-DOAS data measured elsewhere over the Amazon in 100 m stacks. The mean of the lower data quartile was then calculated for each bin as displayed in Fig. 5.11 (grey lines). As Fig. 5.12 shows for the case of formaldehyde, the such defined background mixing ratios approximately correspond to formaldehyde measurements of pristine air masses above the Western Pacific Ocean [Peters et al., 2012]. In order to detect enhancements due to the plumes, $[X]_{bkg}$ is then subtracted from the measured mixing ratios. From the resulting enhancements, the normalized excess mixing ratio R_{XF} (or NEMR) is calculated according to

$$R_{XF} = \frac{\Delta[X]}{\Delta[CH_2O]} = \frac{[X_{fire}] - [X_{bkg}]}{[CH_2O_{fire}] - [CH_2O_{bkg}]} \tag{5.2}$$

with X being either $C_2H_2O_2$ or $C_3H_4O_2^*$. R_{XF} for each individual biomass burning event as well as the mean and range of R_{GF} and R_{MF} are given in Table 5.2.

5.2.4.1 R_{GF}

R_{GF} ranges between 0.02 and 0.11, with an average of $\overline{R}_{GF} = 0.07\pm0.05$. Repeated measurements of the same biomass burning plumes all agree well within the error, indicating that the respective plumes were mostly constant in their composition throughout the measurements. The plume AC11-3 (Fig. 3.7) yields the highest R_{GF} of 0.10 and 0.11. Unfortunately, the plume was not reported in the MODIS fire database. Therefore, the precise location of the fire is unknown, which prevents a discussion of the results with respect to the distance of the aircraft from the plume. The smallest R_{GF} of 0.02 is found during a plume probing that occurred at a 1 km higher flight altitude as compared to those of the other events.

The presented R_{XF} are consistent with recent laboratory studies on biomass burning emissions by Zarzana et al. [2018] as well as different field measurements and satellite observations by Chan Miller et al. [2014, 2017]; DiGangi et al. [2012]; Wittrock et al. [2006] and Zarzana et al. [2017]. From laboratory measurements, Zarzana et al. [2018] reported an average R_{GF} of 0.068

Table 5.2: Continued.

event	$\mathrm{R}_{\mathbf{GF}}$	$\mathrm{R}_{\mathbf{MF}}$	$\mathrm{EF}_{\mathbf{G}}$ $\left[\mathbf{g\ kg^{-1}}\right]$	$\mathrm{EF}_{\mathbf{M}}$ $\left[\mathbf{g\ kg^{-1}}\right]$
AC11-1.1	$0\ 05 \pm 0\ 03$	0.09 ± 0.13	0.23 ± 0.13	0.50 ± 0.76
AC11-1.2	0.03 ± 0.02	0.11 ± 0.16	0.16 ± 0.12	0.65 ± 0.94
AC11-2.1	0.06 ± 0.04	0.86 ± 0.39	0.26 ± 0.19	4.96 ± 2.6
AC11-2.2	0.06 ± 0.04	0.66 ± 0.31	0.26 ± 0.18	3.8 ± 2.04
AC11-2.3	0.03 ± 0.03	0.51 ± 0.26	0.16 ± 0.15	2.93 ± 1.68
AC11-3.1	0.11 ± 0.10	1.50 ± 0.60	0.52 ± 0.47	8.64 ± 4.13
AC11-3.2	0.10 ± 0.11	1.30 ± 0.70	0.45 ± 0.52	7.49 ± 4.49
AC13-1	0.04 ± 0.05	1.20 ± 0.60	0.18 ± 0.23	6.91 ± 3.90
AC13-2	0.08 ± 0.07	1.40 ± 0.70	0.37 ± 0.34	8.06 ± 4.55
AC13-3	0.03 ± 0.04	0.76 ± 0.43	0.13 ± 0.17	4.35 ± 2.73
AC13-4	0.05 ± 0.04	0.81 ± 0.43	0.23 ± 0.19	4.67 ± 2.76
AC13-5	0.02 ± 0.02	0.56 ± 0.27	0.11 ± 0.10	3.25 ± 1.77
Range	0.02–0.11	0.09–1.50	0.11–0.52	0.50–8.64
Mean	0.07 ± 0.05	0.98 ± 0.42	0.25 ± 0.23	4.70 ± 2.70

for fresh emissions and different kinds of fuels. Without further knowledge on the fuels burned during the observed events, no firm conclusions on the photochemistry within the fire plumes can be made. While different fuel types may lead to changing emission factors of glyoxal, Zarzana et al. [2018] observed only little variance in R_{GF} for different fuel types. The correlation of $\mathrm{C_2H_2O_2}$ and $\mathrm{CH_2O}$ seems to be consistent for different kinds of fuel. The lack of knowledge of the exact fuels burned in each fire can therefore not be addressed when comparing R_{GF} of the different plumes and intercepts. Hays et al. [2002] reported R_{GF} on the order of approximately 2.5 to 3 for Palmae and Poaceae. This is a factor of 35–42 times larger than found by Zarzana et al. [2018] and in the present study. McDonald et al. [2000] reported even up to 57 times larger R_{GF} of $\mathrm{R}_{\mathrm{GF}} = 4$ as compared to $\overline{R}_{GF} = 0.07 \pm 0.05$ of the present study or $\mathrm{R}_{\mathrm{GF}} = 0.068$ as found by Zarzana et al. [2018]. In the present study, $\mathrm{R}_{\mathrm{GF}} > 1$ were only observed for the background-uncorrected $\mathrm{R}^{*}_{\mathrm{GF}}$ in the free troposphere.

During recent field measurements over the US, Zarzana et al. [2017] report R_{GF} in the range 0.008 to 0.110. Due to the very nature of airborne plume measurements, it is unknown by how much the measurements differ with respect to plume age, air mass origin, atmospheric composition, or the measurement distance to the plume. Despite the very different atmospheric backgrounds and conditions, the present measurements over the rainforest agree reasonably well with their findings.

Measurements in an aged biomass burning plume yield slightly smaller R_{GF} of 0.02 to 0.03 [DiGangi et al., 2012]. Of all events, event AC13-5 is most likely the oldest plume measured. This is a consequence of the high flight altitude in combination with the distance of the plume from the aircraft during the measurement. AC13-5 has the smallest R_{GF} of only 0.02, which agrees with the findings of DiGangi et al. [2012]. It cannot be concluded by how much this plume measurement is influenced by the atmospheric background. The air masses in the boundary layer are generally highly polluted with biomass burning emission of different ages. It is therefore unclear how much these differently aged emissions influenced the individual plume measurements. Therefore, a distinct relationship between R_{GF} and the plume ages cannot be inferred, which, due to the mixing within the boundary layer may flatten out on time scales between several minutes to hours during all measurements.

5.2.4.2 $\mathbf{R}_{\mathbf{MF}}$

R_{MF} ranges between 0.09 and 1.50, with an average of $\overline{R}_{MF} = (0.98 \pm 0.42)$. Three of the eight probed plumes yield $\mathrm{R_{MF}} > 1$ (both measurements of AC11-3, AC13-1, and AC13-2). All the other plumes yield $\mathrm{R_{MF}} < 1$, in the range of 0.09 to 0.86. For event AC11-1, $\mathrm{R_{GF}}$ is comparable to the other inferred $\mathrm{R_{GF}}$, while $\mathrm{R_{MF}}$ is significantly smaller than the average $\overline{R}_{MF}$ by approximately a factor of 10. Based on the video imagery, the size of the observed plumes as well as the estimated distance to the aircraft are comparable during events AC11-1 and AC11-3 (Fig. 4.3). Still, they yield very different normalized excess mixing ratios. In fact, the largest $\mathrm{R_{MF}}$ and $\mathrm{R_{GF}}$ are obtained during event AC11-3. Accordingly, the emission of $C_2H_2O_2$ and $C_3H_4O_2^*$ with respect to CH_2O is the highest within this biomass burning plume. Interestingly, this is not related to the size and quantity of the biomass burning events monitored by the mini-DOAS instrument. The highest emissions (i.e. the largest plumes) were observed during event AC11-2, where three different large fires were simultaneously detected in a otherwise hazy atmosphere rich in fresh emissions (Fig. 4.3). These plumes were also recorded by MCD14 on MODIS (Fig. 3.7, red dots in the field of view of event 2.2).

Laboratory measurements report $\mathrm{R_{MF}}$ approximately between 1 and 2 for different kinds of fuels [Hays et al., 2002]. This is the upper range of the mini-DOAS observations. Instead of $\mathrm{R_{MF}}$, Zarzana et al. [2018] report the ratio $C_3H_4O_2$ to $C_2H_2O_2$ (R_{MG}) to be on the order of 1.7–2.5 for burning rice straw and different kinds of canopy. The mini-DOAS measurements yield $\mathrm{R_{MG}}$ in the range 1–3, with the exception of event AC11-1, where $\mathrm{R_{MG}} < 1$ due to the small $C_3H_4O_2{}^*$ mixing ratios. Event AC11-3 yields $\mathrm{R_{MG}} = 1$ during both measurements. This reflects the correlated strong enhancement of both gases within the biomass burning plumes.

5.2.4.3 Biomass burning emission factors

According to Andreae [2019], the biomass burning emission factors for $C_2H_2O_2$ and $C_3H_4O_2^*$ are defined by the normalized excess mixing ratio $\mathrm{R_{XF}}$ as

$$EF_X = R_{XF} \frac{MW_X}{MW_{CH_2O}} EF_{CH_2O} \tag{5.3}$$

using the molecular weight MW of each species, and the mean emission factor EF_{CH_2O} of the reference trace gas CH_2O. As the latter was not measured during the campaign, the EF_{CH_2O} of the recent comprehensive compilation by Andreae [2019] is used. It reports EF_{CH_2O} with respect to different combustion processes and fuel types. For tropical forest fires, Andreae [2019] inferred mean $EF_{CH_2O} = 2.4 \pm 0.63$ g(formaldehyde) $\mathrm{kg^{-1}}$(fuel). The resulting $\mathrm{EF_G}$ and $\mathrm{EF_M}$ are listed in Table 5.2 for each biomass burning plume intercept in units of g(target species) $\mathrm{kg^{-1}}$(fuel).

$\mathrm{EF_G}$ ranges from 0.11 to 0.52 g glyoxal per kg of fuel burned with a mean emission factor of (0.25 ± 0.23) $\mathrm{g\,kg^{-1}}$. According to its high $\mathrm{R_{GF}}$, event AC11-3 yields the highest emission factors of 0.52 and 0.45 $\mathrm{g\,kg^{-1}}$. Five out of the twelve plume encounters yield $\mathrm{EF_G}$ of less than 0.2 $\mathrm{g\,kg^{-1}}$.

Corresponding to the largest $\mathrm{EF_G}$, Andreae [2019] estimated $\mathrm{EF_G} = 0.5\ \mathrm{g\,kg^{-1}}$ for tropical forest fires. With $\mathrm{EF_G} = 0.24\ \mathrm{g\,kg^{-1}}$, the same study reported glyoxal emissions from open-air burns of agricultural residues to be approximately 50% lower than those of tropical forest fires. All biomass burning events encountered during flight AC13 were located between 11.0–11.2° S and 56.2° W. While other parts of the measurement flight were located over rainforest, this region is largely dominated by agricultural activities. $\mathrm{EF_G}$ of events AC13-1 to AC13-5 ranges from 0.11 to 0.37 $\mathrm{g\,kg^{-1}}$. Assuming that the biomass burning plumes were dominated by agricultural residues during these measurements, a corresponding mean emission factor of $\mathrm{EF_G} = (0.25 \pm 0.23)$ g glyoxal per kg of open-air burns of agricultural residues is inferred. The range of $\mathrm{EF_G}$ further agrees with laboratory measurements by Zarzana et al. [2018], who reported $\mathrm{EF_G}$ in the range of 0.06 to 0.55 $\mathrm{g\,kg^{-1}}$ depending on the fuel type.

EF_M ranges between 0.5 and 8.64 g methylglyoxal per kg of fuel burned, with a mean emission factor of $(4.68 \pm 2.7)\ \text{g}\,\text{kg}^{-1}$. For each biomass burning event, EF_M is at least twice as high as EF_G. The largest EF_M were found during flight AC13, i.e. for fires dominated by agricultural residues. Even after applying the correction factor of 2 on the inferred EF_M, the resulting EF_M are significantly larger than reported by Zarzana et al. [2018] from laboratory measurements. They found maximal emission factors of approximately $2\ \text{g}\,\text{kg}^{-1}$ for burns of duff. While their absolute EF_M are much lower, their results were equally variable as in the present study, with EF_M ranging from 0.11 to $2.0\ \text{g}\,\text{kg}^{-1}$.

Chapter 6

Discussion

The following chapter summarizes and discusses the major findings. Firstly, the atmospheric profile of glyoxal is investigated based on the near global observations in different altitudes, air masses, regions, and seasons and put into context with current research. Based on all measurements, unanswered questions regarding the geographical and vertical distribution of glyoxal (especially in the marine atmosphere) and the resulting deficiencies in its representation by photochemical transport models are addressed. Secondly, the atmospheric profiles of formaldehyde, glyoxal, and methylglyoxal are analysed in the troposphere above the tropical rainforest, which is known as large emitter of bVOCs. Based on the regional measurements at the end of the dry season, when biomass burning reaches its yearly maximum, the impact of biomass burning on the atmospheric concentrations of the target gases is analysed in this bVOC rich regime. Main parts of this chapter have been published in Kluge et al. [2020], section 5 and 6, or are currently under review for publication in Kluge et al. [2022].

(1) Glyoxal over different global regions: When placing the glyoxal measurements over the different terrestrial regions in context with the observations over the different oceans around the globe, in particular those over the tropical rainforest, it is remarkable that local anthropogenic or biomass burning emissions cause larger glyoxal concentrations in the boundary layer over many regions than those observed over the Amazon rainforest. In particular in the boundary layer over anthropogenically polluted regions (e.g. the coastal regions of the Mediterranean Sea and the English Channel, over the East China Sea, and also continental Europe), glyoxal mixing ratios are up to a factor of three times larger than over the Amazon rainforest. The detailed comparison of the airborne glyoxal VCD measurements all around the globe with satellite TROPOMI observations of glyoxal overall show a good agreement for measurements in (a) pristine air with low glyoxal mixing ratios near the detection limits of the instruments, (b) polluted air masses with high glyoxal mixing ratios (e.g. major emission plumes), and (c) continental air of mixed pollution sources. Exceptions to this overall good agreement are those observations (a) over land with an increased aerosol load in the boundary layer, (b) of low lying plumes (mostly biomass burning) over the ocean with its low reflectivity in the visible wavelengths, and (c) of pollution plumes over the oceans with a limited vertical or horizontal extent irrespective of their altitude. For TROPOMI, this also leads to underestimated glyoxal in the marine surroundings of larger emission plumes. A systematic comparison of the global mini-DOAS glyoxal measurements to previous air- or shipborne measurements in the same regions, seasons, and altitudes, in particular in the remote marine free and upper troposphere, is complicated by the limited number of respective studies. In this respect, the present observations provide a unique and novel data set of glyoxal measurements covering a large number of so far poorly explored (or even unexplored) regions and altitude ranges with different pollution levels around the globe. In particular, the data provide new insights into the vertical profiles of glyoxal and its potential precursors in different pristine marine regions. Moreover, they provide further evidence of elevated glyoxal in aged and long-range transported biomass burning plumes, similar to past studies that reported much larger glyoxal mixing ratios than expected. These two aspects of the measurements are discussed in more detail in the following.

(1) The measurements confirm previous reports of (at least) occasionally elevated glyoxal (1–140 ppt) in the marine boundary layer over the remote ocean (e.g. Zhou and Mopper [1990]; Sinreich et al. [2010]; Coburn et al. [2014]; Mahajan et al. [2014]; Lawson et al. [2015]; Volkamer et al. [2015]; Chiu et al. [2017]; Walker et al. [2022]). The measurements further confirm observations of elevated glyoxal in the marine boundary layer over tropical oceans as compared to the marine boundary layer at higher latitudes. In fact, the mini-DOAS measurements yield two to four times more glyoxal in the marine boundary layer of the tropics as compared to the South or North Atlantic (Fig. 5.1 and Table 5.1). The comparable large range of observed glyoxal mixing ratios in different marine regions is indicative for the large variety of the types and transport history of the investigated air masses (Table 5.1). Yet, given the short lifetime of glyoxal in the sunlit atmosphere of ~ 2 h [Koch and Moortgat, 1998; Volkamer et al., 2005a; Tadić et al., 2006; Fu et al., 2008; Wennberg et al., 2018], the observation of elevated glyoxal in the tropical marine atmosphere requires rather large and potentially variable sources in the range 0.5 $\mathrm{ppt\,h^{-1}}$ to 70 $\mathrm{ppt\,h^{-1}}$, if glyoxal is derived from the photochemical decay of its organic precursor substances. In the past, two major explanations for the yet unexplained glyoxal over marine regions have been discussed, i.e. either (a) the transport of longer-lived glyoxal precursor species from land-based sources into the remote marine atmosphere, and/or (b) the emissions of glyoxal and/or its organic precursors from the ocean:

(a) Based on co-located measurements of glyoxal and some of its main known precursors like isoprene and the monoterpenes, Lawson et al. [2015] estimated their potential contribution to glyoxal in the marine boundary layer to be of the order of 10%. Additional long-lived glyoxal precursor molecules (e.g. aromatics, acetylene, or larger VOCs) have been suggested to explain the discrepancy between observed and expected glyoxal in the pristine marine boundary layer, but conclusive answers had not yet been found (e.g. Sinreich et al. [2010]; Rinaldi et al. [2011]; Coburn et al. [2014]; Mahajan et al. [2014]; Lawson et al. [2015]; Chiu et al. [2017]; Walker et al. [2022]). The here performed comparison of the vertical glyoxal profiles above the tropical Atlantic to those over the mid- and high-latitude Atlantic clearly shows that the relative enhancement of glyoxal is restricted to the tropical marine boundary layer. At higher altitudes (i.e. the tropical free and upper troposphere), the glyoxal profiles over different regions of the Atlantic are similar. This finding strongly points to a marine glyoxal source in the tropics rather than long-range transport of glyoxal and its precursors from terrestrial emissions. In fact, if the latter process was the dominant glyoxal precursor in the observed marine air masses, elevated glyoxal would also be expected to occur at higher altitudes and latitudes, and not exclusively in the tropical boundary layer.

(b) Direct emissions of significant amounts of glyoxal from the oceans could also be convincingly ruled out, primarily because of its high water solubility (effective Henry's law coefficient $\mathrm{H^{cp}} = 4100\ \mathrm{mol\,m^{-3}\,P^{-1}}$, Sander [2015]) and the observation that the daytime flux of glyoxal is directed from the atmosphere into the ocean [Zhou and Mopper, 1990; Coburn et al., 2014; Chiu et al., 2017; Zhu and Kieber, 2019]. Potentially relevant glyoxal precursor molecules include glycolaldehyde and acetaldehyde. However, their contribution to the atmospheric glyoxal budget is poorly constrained. For instance, acetaldehyde is largely produced in seawater [Zhu and Kieber, 2020] and a net flux to the atmosphere is expected [Zhu and Kieber, 2019]. Estimates of the global oceanic source of acetaldehyde range from 34 to 57 $\mathrm{Tg\,yr^{-1}}$ [Millet et al., 2010; Wang et al., 2019]. Usually global atmospheric models neglect this source, as is the case in the EMAC simulation performed in this study. However, even when this marine source of acetaldehyde is taken into account atmospheric models still underestimate observations in the boundary layer and free troposphere [Wang et al., 2019]. The implied significant and widespread missing source of acetaldehyde may therefore be relevant for the global glyoxal budget. Direct oceanic emissions of unsaturated aliphatic or additional aromatic glyoxal precursor species besides acetylene (e.g. benzene, toluene, ethylbenzene, or xylenes) have also been found to be insufficient to explain the observed glyoxal concentrations in the marine environment of the tropics [Xiao et al., 2007; Mahajan et al., 2014], even though their potential source strengths have recently been reported to be larger than previously thought [Rocco et al., 2021]. At night, NO_3 may oxidise some organic VOCs (e.g. toluene) and thus build-up a certain glyoxal level until dawn, but the potential production rate is far too small to explain the observed glyoxal concentrations both at night and during the daytime [Coburn et al., 2014; Walker et al., 2022].

In contrast, recent laboratory experiments have shown that UV light-initiated reactions at the sea surface organic microlayer involving DOC (dissolved organic carbon) may lead to the production of significant amounts of VOCs of low solubility, e.g. fatty (heptanoic, octanoic) and nonanoic (NA) acids, and thus of secondarily formed oxidised VOCs like glyoxal and its precursors [Ciuraru et al., 2015; Chiu et al., 2017]. From their study, Chiu et al. [2017] concluded that the ozonolysis of 2-nonenal is most likely the primary chemical mechanism to produce significant amounts glyoxal in the marine atmosphere, and that this source can potentially sustain tens of ppt of glyoxal over the ocean. In addition, a recent study by Brüggemann et al. [2018] discusses an abiotic source of organic vapours emitted by photochemical reactions of the amphiphilic compounds forming surfactants at the sea surface. In their study, they determined global emissions to be 23.2–91.9 $\mathrm{TgC\,yr^{-1}}$ of these organic vapours due to interfacial photochemistry, of which 1.11 (0.70–1.52) $\mathrm{Tg\,yr^{-1}}$ are attributed to emissions of isoprene. Though potentially relevant for organic aerosol mass over the remote ocean [Brüggemann et al., 2018], at this point it is unclear how much this organic vapour may ultimately contribute to the elevated glyoxal observed over the tropical oceans.

In conclusion, the low-to-high latitudinal gradient of glyoxal and the comparably low concentrations in the free troposphere also above the biologically active tropics provide some evidence that indeed the emissions of DOC related VOCs from the oceanic micro-layer and their photochemical decay rather than long-range transport of long-lived glyoxal precursors from land is primarily responsible for the elevated glyoxal in the pristine marine atmosphere of the tropics. A more detailed discussion of potentially relevant glyoxal precursor molecules suitable to explain the observations of elevated glyoxal in the marine (and in particular tropical) environment and how they are represented in the global circulation chemical model EMAC is beyond the scope of the present thesis, but will be subject of an accompanying study by Rosanka et al., (manuscript in preparation, 2022).

(2) Further, the observations of enhanced glyoxal in aged biomass burning plumes both over land and the ocean confirm recent reports of enhanced glyoxal in aged biomass burning plumes that have been transported for at least several days (e.g. Alvarado et al. [2020]). Such plumes were observed on multiple occasions over the South (one event), North (one event), and Tropical Atlantic (multiple events, see Sect. 5.1.1) within the framework of the present study. Again, due to the short atmospheric lifetime of glyoxal during daytime, the glyoxal detected in these aged biomass burning plumes was necessarily secondarily formed from direct or multi-generation oxidation of yet unidentified longer-lived VOC precursor species (e.g. benzene, acetylene, or aromatics), which were co-emitted during the wildfires. Details on how the primary emitted and secondary formed glyoxal-producing VOCs evolve in aged biomass burning plumes still need to be explored before more firm conclusions on the fate of glyoxal and its potential to form secondary aerosols in these aged biomass burning plumes can be drawn. However, there is growing evidence that a significant fraction of glyoxal in such pollution plumes may result from the oxidation of aromatic compounds that are produced during the evaporation of organic aerosols [Palm et al., 2020]. Since this potential additional glyoxal source is currently not accounted for by EMAC, its consideration may also improve the existing model underestimation of ozone production by biomass burning emissions [Bourgeois et al., 2021]. Since biomass burning is much more frequent in the tropics than at higher latitudes, the glyoxal formed in these aged biomass burning plumes from long-lived precursors may also enhance the observed low to high latitude gradient of glyoxal in the lower marine atmosphere.

In summary, the present study confirms recent findings on glyoxal in the atmosphere, but it also offers new aspects on how widespread elevated glyoxal occurs in the atmosphere. This emphasizes the potential role glyoxal may play in the oxidation of VOCs, the oxidative capacity of the atmosphere and hence ozone formation, and on its importance in secondary aerosol formation.

(2) Formaldehyde, glyoxal, and methylglyoxal over the Amazon rainforest: It is remarkable that even though formaldehyde, glyoxal, and methylglyoxal have a common dominant source (isoprene) and similar lifetime against their main sink (photolysis), their relative profile shapes over the tropical rainforest are different. Especially above the boundary layer, the inferred formaldehyde mixing ratios decrease faster with increasing altitude than the vertical profiles of glyoxal and methylglyoxal do. This raises the question as to whether the relative contribution of the different precursor gases, their sinks due to photolysis and reaction with OH radicals in a low-NO_x, high-VOC, and low-HO_x environment or the different efficiencies regarding the uptake into aerosols or cloud particles may alter the relative profile shapes of the three species:

Over the rainforest, the observed formaldehyde mixing ratios in the lower and free troposphere range from those previously reported over the remote Pacific [Peters et al., 2012] (lower quartile) to those measured over continental North and South America [Kaiser et al., 2015] (upper quartile). A good agreement with previous satellite measurements is found for the lower and upper range of profile integrated formaldehyde [Wittrock et al., 2006; De Smedt et al., 2008; Vrekoussis et al., 2009, 2010; Alvarado et al., 2014; De Smedt et al., 2015]. The lower quartile of the measured mixing ratios appears to result from the oxidation of methane and to a lesser degree of VOCs (mostly isoprene). In the lower troposphere, enhanced formaldehyde mixing ratios have two major contributions: direct emissions, e.g. from biomass burning, and secondary formation during the degradation of short-lived VOCs, like isoprene. In the middle and upper tropical troposphere, formaldehyde seems to have more constant sources and sinks (mainly photolysis) than in the lower troposphere.

In contrast to formaldehyde, for $C_2H_2O_2$ and $C_3H_4O_2{}^*$ significant enhancements above the inferred backgrounds are observed in the free troposphere . As for formaldehyde, a good agreement with earlier spaceborne observations is also found for the lower and upper range of profile integrated glyoxal [Wittrock et al., 2006; De Smedt et al., 2008; Vrekoussis et al., 2009, 2010; Alvarado et al., 2014; De Smedt et al., 2015]. After applying a correction factor of 2.0 ± 0.5 to the measured $C_3H_4O_2{}^*$ mixing ratios as discussed above, methylglyoxal exceeds the inferred glyoxal mixing ratios by up to a factor of five for all measurements. A significant fraction of the research flights was conducted above the remote rainforest and was at least partly free of fires and plumes. Because of this and the comparatively different shape of the formaldehyde profile, not all of the observed enhancements of glyoxal and methylglyoxal in the free troposphere can be attributed to direct emissions from biomass burning. The compact clustering as well as the smooth decrease of the lower quartile mixing ratios with altitude provide evidence as to the type and sink of the precursor molecules. Apparently, these precursors should have lifetimes of at least several days, and should either be constantly emitted by the biosphere (e.g. isoprene and acetone) or occasionally during biomass burning (e.g. acetylene, aromatics) before being vertically transported. The major known precursors of formaldehyde, glyoxal, and methylglyoxal over the rainforest are discussed in more detail in the following:

As their dominant source, isoprene globally accounts for 67%, 47%, and 79% of the annual sources of formaldehyde, glyoxal, and methylglyoxal [Fu et al., 2008], respectively, leading to their rapidly decreasing vertical profiles. As argued by Fu et al. [2008] and Fu et al. [2019] (Fig. 6, panel a), the oxidation of isoprene under high isoprene, low NO_x, and the resulting low HO_X concentrations may be delayed by hours or even several days (sect. 2.2.1). This prolonged lifetime combined with the efficient vertical atmospheric transport in the tropics leads to some oxidation of isoprene above the boundary layer. As a consequence, the in situ formation of glyoxal and methylglyoxal and finally formaldehyde from isoprene oxidation may contribute significantly to the observed enhanced mixing ratios in the free troposphere. The methylglyoxal enhancements in the middle troposphere are approximately five times larger than the observed glyoxal mixing ratios. Molar yields of glyoxal and methylglyoxal from second and third generation isoprene oxidation combined, are 6.2% and 34%, respectively [Fu et al., 2008]. Therefore, the in situ formation of methylglyoxal from isoprene oxidation is expected to be approximately five times larger than the respective glyoxal production. In accordance with the present observations, this should lead to five times larger methylglyoxal mixing ratios compared to glyoxal in the free troposphere. The present glyoxal and methylglyoxal observations are thus strongly indicative for a significant upwards transport of isoprene into the free troposphere above the tropical rainforest, where they may ultimately serve as sources of ozone and secondary organic aerosols.

Besides their common dominant precursor, additional sources for precursors of the gases differently influence their local distribution. For formaldehyde, these sources are mostly combustion processes and oxidation of other biogenic/anthropogenic hydrocarbons [Lee et al., 1998; Liu et al., 2007; Fortems-Cheiney et al., 2012], for glyoxal oxidation of acetylene, and for methylglyoxal oxidation of acetone [Fu et al., 2008]). All these precursors might differently contribute in the present measurements and hence cause differences in the inferred profiles. A recent study additionally discussed the oxidation of aromatics as possible relevant source of atmospheric glyoxal and methylglyoxal [Taraborrelli et al., 2021]. While acetylene is mostly an anthropogenically emitted trace gas, acetone additionally has direct biogenic sources [Fu et al., 2008]. Both gases have a long lifetime of up to 18 and 22 days, respectively [Fu et al., 2008]. Therefore, vertically transported acetylene from ground-based combustion processes might be a further source of the observed glyoxal in the free troposphere over the rainforest. While acetone is also emitted in biomass burning processes (one fifth of the total global acetone budget [Pöschl et al., 2001]), an equally large source of acetone emissions is decomposing plant material (10^{-4} $\mathrm{g\,g^{-1}}$ [Warneke et al., 1999]). The remaining acetone is to a large part an oxidation product of hydrocarbons and also an oxidation product of isoprene under low NO_x conditions, which are typical for air above rainforests [Warneke et al., 2001]. Mean acetone mixing ratios in the boundary layer above tropical rainforests are of the order of 2 ppb [Pöschl et al., 2001]. Besides isoprene oxidation, a fraction of the observed methylglyoxal enhancements in the free troposphere might therefore be a direct or secondary (through the oxidation of hydroacetone) product of acetone oxidation above the boundary layer or a result of longer-lived oxidized aromatics [Taraborrelli et al., 2021].

Further, the water solubility of the measured gases is largely different ($H^{cp} = 32\mathrm{mol\,m^{-3}\,Pa^{-1}}$ for formaldehyde, $H^{cp} = 4100\mathrm{mol\,m^{-3}\,Pa^{-1}}$ for glyoxal, and $H^{cp} = 370\mathrm{mol\,m^{-3}\,Pa^{-1}}$ for methylglyoxal; Sander [2015]), but significantly smaller for formaldehyde than for glyoxal. Heterogeneous uptake is therefore not a reasonable explanation for the relative depletion of formaldehyde over glyoxal and methylglyoxal in the middle troposphere.

The different and changing fractions of the short and long-lived precursors relevant for the formation of formaldehyde as compared to those of glyoxal and methylglyoxal are also expressed by the altitude dependence of R^*_{GF} and R^*_{MF}. The increasing fraction of glyoxal and methylglyoxal relative to formaldehyde in the middle and upper troposphere over the Amazon rainforest require significant sources for both gases which are supposed to result from the oxidation of longer-lived VOCs [Schulz et al., 2018]. In fact, since both gases are known to contribute to SOA formation, the elevated mixing ratios of glyoxal and methylglyoxal in the upper troposphere lend further support to the proposed SOA formation from products of isoprene oxidation as observed by Schulz et al. [2018]; Andreae et al. [2018] and Williamson et al. [2019] over the Amazon Basin and generally over the forested tropics.

The detection of all three gases in biomass burning plumes are correlated and show moderate to strong enhancements. The inferred R_{GF} in the range of 0.02–0.11 ($\overline{R}_{GF}$=0.07) for the observed biomass burning events agree well with previous studies, both in the field over North America [Zarzana et al., 2017] as well as in the laboratory fuel study [Zarzana et al., 2018]. It is further in agreement with R_{GF} inferred from satellite measurements [Chan Miller et al., 2014, 2017; DiGangi et al., 2012; Wittrock et al., 2006]. For R_{MF}, a range of 0.09 to 1.5 with $\overline{R}_{MF}$=0.98 is inferred over the rainforest (or respectively smaller results when correcting the $C_3H_4O_2^*$ mixing ratios by a factor of 2.0 ± 0.5). This range overlaps with the lower end of the range of normalized excess mixing ratios previously reported for different types of fuels in the laboratory [Hays et al., 2002]. The presented study as well as the measurements by Hays et al. [2002] indicate a slightly larger R_{MF} than reported by Zarzana et al. [2018] based on R_{MG} and R_{GF} observations (∼0.1–0.5). However, this difference of the observed ranges may in part be a result of additional dicarbonyls which might differently affect the present retrieval and that of the study by Zarzana et al. [2018]. In fact, when correcting R_{MF} by a factor of 2, the results agree much better with the measurements by Zarzana et al. [2018]. Based on R_{GF} and R_{MF} and average emission factors for formaldehyde estimated by Andreae [2019], emission factors in the range of 0.11–0.52 ($\overline{EF}_G = (0.25 \pm 0.23)$ g kg^{-1}) for glyoxal and 0.5–8.6 ($\overline{EF}_M = (4.7 \pm 2.7)$ g kg^{-1}) for methylglyoxal are inferred for the probed biomass burning events over the Amazon. The inferred EF_G agrees well with the range reported from laboratory measurements [Zarzana et al., 2018]. Notably, EF_M is significantly larger than found in their study, also when correcting the results for possibly included additional dicarbonyls.

Chapter 7

Conclusions

The present thesis reports on novel airborne measurements of glyoxal mixing ratios and vertical column densities performed during 72 research flights with the German research aircraft DLR HALO over different global regions between 2014 and 2019. The observations made over the Amazon rainforest are complemented by simultaneous airborne measurements of formaldehyde and methylglyoxal. Combined, the analysed data set consists of the first simultaneous measurements of formaldehyde, glyoxal, and methylglyoxal over a tropical rainforest as well as a unique compilation of worldwide airborne glyoxal measurements, both in the Limb as well and in the Nadir viewing geometry. Combined, the data may offer new information onto the atmospheric abundance, profiles, and potential underestimated or unknown sources of glyoxal in the terrestrial and marine atmosphere. The detailed analysis of the carbonyls formaldehyde, glyoxal, and methylglyoxal over one of the largest tropical rainforests as well as in both fresh and aged biomass burning plumes further provides observational constraints on the still largely uncertain source strength of such fires for glyoxal and methylglyoxal.

Due to the lack of respective airborne glyoxal mixing ratio or VCD measurements in most regions and altitudes, the directly measured (Nadir) and profile integrated (Limb) column densities of glyoxal are compared to collocated measurements from space by the TROPOMI instrument on the Copernicus Sentinel-5 Precursor satellite. Based on this unique data set with respect to geographical and seasonal coverage, an in-depth evaluation of the strengths and weaknesses of each observation technique is made. Overall a good agreement is found among the two data sets, with the exception of airborne observations of faint glyoxal plumes occurring over surfaces of low reflectivity and plumes in lower altitudes (i.e. in the marine or planetary boundary layer), which appear elusive for detection from space.

Both types of airborne glyoxal measurements, i.e. total atmospheric column densities from Nadir and vertical concentrations profiles from Limb observations, are further compared to glyoxal simulations of the global atmosphere-chemistry model EMAC. The comparison of measured and simulated glyoxal point to several deficits in the current representation of the photochemistry of glyoxal and its precursor species in respective models. The general underestimation of glyoxal found in the simulations over land and oceans has already been recognized in previous studies, most of which were based on past satellite observations (e.g. Fu et al. [2008]; Myriokefalitakis et al. [2008]; Stavrakou et al. [2009a]). Most of those studies rely on comparisons of climatologies (i.e yearly or seasonal averages) rather than on comparisons of direct measurements such as those performed in the present study. As a result, the discrepancies between observations and modelling unravelled in the present thesis are even more pronounced than previously reported in other studies. In particular, the present comparison includes not only the regionally and seasonally characteristic glyoxal mixing ratios, but also measurements of glyoxal in biomass burning and anthropogenic plumes. For the latter, the glyoxal underestimation of the employed set-up of the EMAC model is found to be even larger than outside of specific emission events.

The airborne glyoxal observations confirm key findings related to atmospheric glyoxal reported in other recent studies, specifically the occurrence of elevated glyoxal in aged biomass burning plumes [Alvarado et al., 2020] and in the marine boundary layer of the tropics [Sinreich et al., 2010; Rinaldi et al., 2011; Coburn et al., 2014; Mahajan et al., 2014; Lawson et al., 2015; Chiu et al., 2017; Walker et al., 2022]. In addition, the present measurements provide novel insights into various aspects of atmospheric glyoxal, e.g. its height distribution in rarely or yet unprobed air mass types or those elusive for glyoxal detection from space. Remarkable are the differences of the marine glyoxal profiles at changing latitudes and over different oceans as well as the frequency of pollution plume observations throughout all regions and altitudes. Among other aspects, these observations clearly indicate the need to re-evaluate assumptions on geographically uniform or even negligible glyoxal mixing ratios in the marine atmosphere.

Over the Amazon rainforest, a suite of different secondary sources of formaldehyde, glyoxal, and methylglyoxal with different atmospheric lifetimes cause relative differences in their vertical profile shapes. These differences are particular pronounced above the boundary layer. Notable in this respect are the slightly elevated mixing ratios of glyoxal and methylglyoxal in the free troposphere as compared to formaldehyde. These are presumably a result of upwards transport of isoprene and (to a minor degree) additional precursor VOCs like acetone (methylglyoxal), acetylene (glyoxal) or aromatics (both gases). In contrast, the predominant source of formaldehyde in the upper troposphere is the oxidation of methane versus its constant sink by photolysis. As glyoxal and methylglyoxal are both known as significant SOA precursors, the observed enhancements of both gases in the free troposphere support recent claims of upper tropospheric SOA formation from isoprene oxidation products [Andreae et al., 2018; Schulz et al., 2018; Williamson et al., 2019; Liu et al., 2022] as well as of potential upwards transport of isoprene and its oxidation products into the tropical free troposphere [Fu et al., 2019].

If available, the measurements reported here of the three carbonyls over the tropical rainforest are compared to previous studies. However, those were mostly performed over other regions of the globe outside of the characteristic low HO_X, low NO_X, high VOC air observed over a tropical rainforest. In particular, measurements of upper tropospheric glyoxal and in general of methylglyoxal are still rare. This prevents a thorough comparison of the present measurements to those of other studies. Therefore, in addition a climatological comparison of the integrated vertical formaldehyde and glyoxal profiles to previous satellite observations over the same regions was performed. Overall a good agreement between both types of measurement was found. For methylglyoxal, satellite observations are not yet available. As a result, in particular the methylglyoxal measurements over the Amazon rainforest are currently still standing alone. In this respect, the present observations provide important new insights into the atmospheric profile and (upper limit) mixing ratios of methylglyoxal, nonetheless the discussed uncertainties the DOAS detection of methylglyoxal is affected off.

In and close to biomass burning plumes, all three carbonyls expectedly show notable enhancements, which exceed their average mixing ratios due to emissions of their biogenic precursors from the rainforest. The emission of glyoxal from tropical forest fires of 0.16–0.52 $\mathrm{g_{glyoxal}\,kg_{fuel}^{-1}}$ appears to be larger than from agricultural fires (0.11–0.37 $\mathrm{g\,kg^{-1}}$). The observed glyoxal emissions from tropical forest fires are on average 40% smaller than recently estimated by Andreae [2019]. However, due to the lack of respective studies, Andreae [2019] did not include information from field observations in the estimates. Contrary to the comparison to Andreae [2019], the present observations are in good agreement to a laboratory study by Zarzana et al. [2018]. For all fires, the inferred methylglyoxal emissions (0.25–4.32 $\mathrm{g\,kg^{-1}}$) are considerably larger than those of glyoxal. Again, this agrees with the observations by Zarzana et al. [2018], but is contrary to the report of Andreae [2019], who estimated slightly larger glyoxal than methylglyoxal emissions for all fuel types besides agricultural residues. This large range of reported methylglyoxal emissions from a still limited number of studies demonstrates the need for additional field observations of both its pyrogenic and biogenic source strengths.

In summary, the combined glyoxal data over the rainforest and other global regions point to some major deficits in our current understanding of atmospheric glyoxal. When combined, these deficits point to multiple causes for the current glyoxal underestimation, which are do not result from the disregard of a single glyoxal precursor molecule, source, or single chemical pathway, but potentially from a suite of glyoxal precursor molecules and formation processes. This conjecture is supported by the observed deficits in explaining the measured glyoxal in vastly different types of air masses, i.e. in (a) anthropogenic plumes of larger agglomerations, (b) aged polluted air masses forming the continental glyoxal background, (c) pristine air masses of the marine boundary layer in the tropics, (d) the pristine marine atmosphere (e.g. South and North Atlantic), and (e) aged biomass burning plumes. The present observations thus provide novel insights on the required emission strengths, concentration and lifetimes of the possible different glyoxal producing precursors and their intermediates necessary to close the apparent gap between observations and models.

In this respect, it is noteworthy to acknowledge that deficits in understanding atmospheric glyoxal ultimately indicate a more fundamental deficiency in the current knowledge of the photochemistry and emissions of carbonyl forming VOCs in the atmosphere, with a variety of consequences, e.g. for the oxidative capacity of the atmosphere.

Moreover, since glyoxal is known to support secondary organic aerosol (SOA) formation, the finding of an overall larger glyoxal concentration in both the polluted and pristine atmosphere provides evidence for an overall more significant and widespread role that glyoxal may play in global SOA formation than is currently assumed. Since the potential SOA formation mechanisms from glyoxal are not yet fully understood, the implications of generally larger glyoxal concentrations than currently accounted for by CTMs, in particular in the tropical marine boundary layer, cannot be precisely quantified. However, even in polluted regimes (urban, industrial), model studies attributed a notable 1–15% of SOA to glyoxal uptake [Knote et al., 2014]. The present study indicates that this fraction may be a lower bound only and in particular in the tropical marine boundary layer it may be notably larger.

The present study as well as previous research on atmospheric glyoxal thus strongly motivates a reevaluation of the current understanding of the carbonyl forming VOC photochemistry and its implications, e.g. for the oxidative capacity of the atmosphere, the formation of ozone and of secondary formed aerosols, both of which impact human health, the atmospheric radiative balance, and hence the global climate.

Acronyms

AMTEX Aero-Laser 5002 vacuum UV resonance fluorescence instrument.

BAHAMAS Basic HALO Measurement And Sensor System.

bVOC biogenic VOC.

CAFE Chemistry of the atmosphere: African Field Experiment.

CoMet Carbon dioxide and Methane Mission.

CTM Chemical Transport Model.

DLR Deutsches Zentrum für Luft- und Raumfahrt.

DOAS Differential Optical Absorption Spectroscopy.

dSCD differential Slant Column Density.

ECMWF European Centre for Medium-Range Weather Forecasts.

EDGAR Emissions Database for Global Atmospheric Research.

EMAC ECHAM/MESSY Atmospheric Chemistry.

EMeRGe-Asia Effect of Megacities on the Transport and Transformation of Pollutants on The regional to Global Scales in Asia.

EMeRGe-EU Effect of Megacities on the Transport and Transformation of Pollutants on The regional to Global Scales in Europe.

FOV Field Of View.

FWHM Full Width at Half Maximum.

GFAS Global Fire Assimilation System.

GOME Global Ozone Monitoring Experiment.

HALO High Altitude and LOng range.

IPCC Intergovernmental Panel on Climate Change.

ITCZ InterTropical Convergence Zone.

MECCA Module Efficiently Calculating the Chemistry of the Atmosphere.

MEGAN Model of Emissions of Gases and Aerosols from Nature.

MOM Mainz Organic Mechnism.

NMHC non-methane hydrocarbon.

NMVOC non-methane VOC.

OMI Ozone Monitoring Instrument.

OMO Oxidation mechanism Observations.

OPAC Optical Properties of Aerosols and Clouds.

OVOC oxygenated VOC.

READY Real-time Environmental Aplications and Display sYstem.

RT Radiative Transfer.

SCAV SCAVenging submodel.

SCD Slant Column Density.

SCIAMACHY Scanning Imaging Absorption Spectrometer for Atmospheric Chartography.

SOA Secondary Organic Aerosols.

SouthTRAC Transport and Composition of the Southern Hemisphere UTLS.

SSA Single Scattering Albedo.

TROPOMI TROPOspheric Monitoring Instrument.

UV UltraViolet.

VOC Volatile Organic Compound.

WISE Wave-driven ISentropic Exchange in Europe.

WMO World Meteorological Organisation.

Publications by the Author

Within the framework of this thesis the following article was published by a refereed journal:

Kluge, Flora, et al. "Profiling of formaldehyde, glyoxal, methylglyoxal, and CO over the Amazon: normalized excess mixing ratios and related emission factors in biomass burning plumes", Atmospheric chemistry and Physics 20.20 (2020): 12363-12389. `https://doi.org/10.5194/acp-20-12363-2020`

Within the framework of this thesis the following article was submitted to a refereed journal:

Kluge, Flora, et al. "Airborne glyoxal measurements in the marine and continental atmosphere: Comparison with TROPOMI observations and EMAC simulations." Atmospheric Chemistry and Physics Discussions (2022): 1-46.

Within the framework of this thesis the following co-authored articles were published by a refereed journal:

Nussbaumer, Clara M., et al. "Modification of a conventional photolytic converter for improving aircraft measurements of NO2 via chemiluminescence." Atmospheric measurement techniques 14.10 (2021): 6759-6776.

Rotermund, Meike K., et al. "Organic and inorganic bromine measurements around the extratropical tropopause and lowermost stratosphere: Insights into the transport pathways and total bromine." Atmospheric chemistry and Physics 21.20 (2021): 15375-15407. `https://doi.org/10.5194/acp-21-15375-2021`

Andrés Hernández, M. Dolores, et al. "Overview: On the transport and transformation of pollutants in the outflow of major population centres–observational data from the EMeRGe European intensive operational period in summer 2017." Atmospheric Chemistry and Physics 22.9 (2022): 5877-5924.

Within the framework of this thesis the following co-authored article was submitted to a refereed journal:

George, Midhun, et al. "On the understanding of tropospheric fast photochemistry: airborne observations of peroxy radicals during the EMeRGe-Europe campaign." Atmospheric Chemistry and Physics Discussions (2022): 1-36.

Acknowledgments

First of all, special thanks are given to Christophe Lerot for the provision of the TROPOMI glyoxal data and the great help in analysing and interpreting the air- versus spaceborne measurements. Equally, I thank Simon Rosanka and Domenico Taraborrelli for the performance of the EMAC glyoxal simulations for multiple years and research missions and the discussion of the results and their implications together with Klaus Pfeilsticker.

I am grateful to Michael Lichtenstern, Hans Schlager, Eric Förster, Peter Hoor, Heiko Bozem, Sören Johansson, Horst Fischer, Mira Pöhlker, Bruna Holanda, Ovid Krüger, Christopher Pöhlker, Thomas Klimach, Meinrat Andreae, and Ulrich Pöschl for sharing their data with me and to Steven Brown (NOAA Earth System Research Laboratory) for his helpful discussion of the ACRIDICON-CHUVA measurements and conclusions.

Further, I acknowledge that this thesis contains modified Copernicus Sentinel-5 Precursor satellite data (2018–2019) and the use of imagery from the NASA Worldview application (`https://worldview.earthdata.nasa.gov/`, last access: 19 May 2022), part of the NASA Earth Observing System Data and Information System (EOSDIS), the use of data products and imagery from the Land, Atmosphere Near real-time Capability for EOS (LANCE) system operated by NASA's Earth Science Data and Information System (ESDIS) with funding provided by NASA Headquarters, and finally the NOAA Air Resources Laboratory (ARL) for the provision of the HYSPLIT transport and dispersion model and READY website (`https://www.ready.noaa.gov/index.php`, last access: 30 June 2022), all of which were used in this thesis.

Appendix A

Exemplary DOAS retrievals

Figures A.1–A.3 show the detailed DOAS retrievals for five example spectra based on the settings described in tables 3.1 and 3.2 and sects. 3.1.1.2–3.1.1.4.

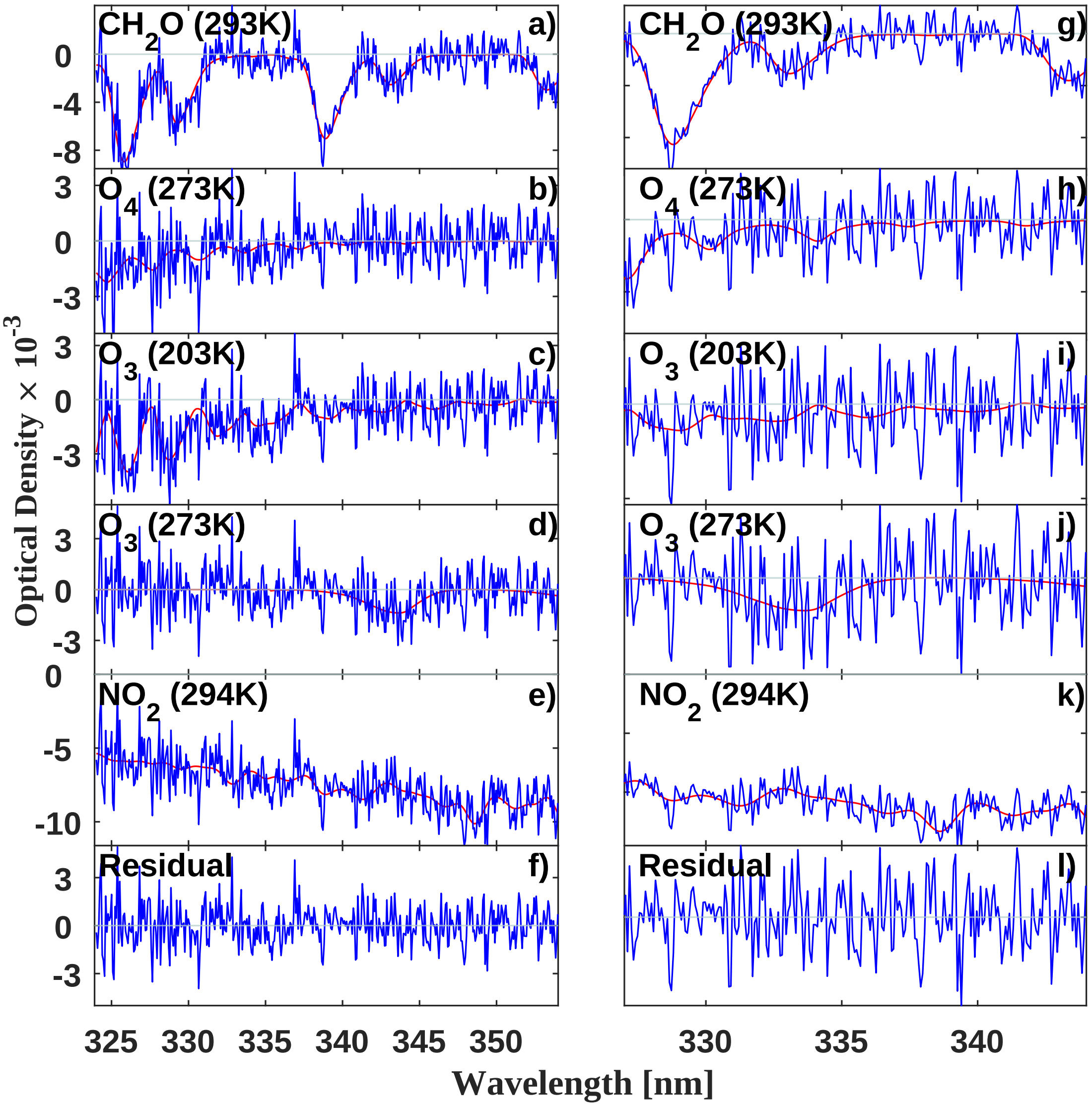

Figure A.1: Spectral retrieval of formaldehyde based on two different wavelength ranges from 320 to 354 nm (left column, S/N= 25) and 337 to 354 nm (right column, S/N= 13), respectively, for the measurement at 17:16 UTC on 11 Sept. 2014 (ACRIDICON-CHUVA research flight AC11). The traces shown in blue are the inferred atmospheric spectra together with the residual spectral structures, the red line shows the reference spectra of the respective gases.

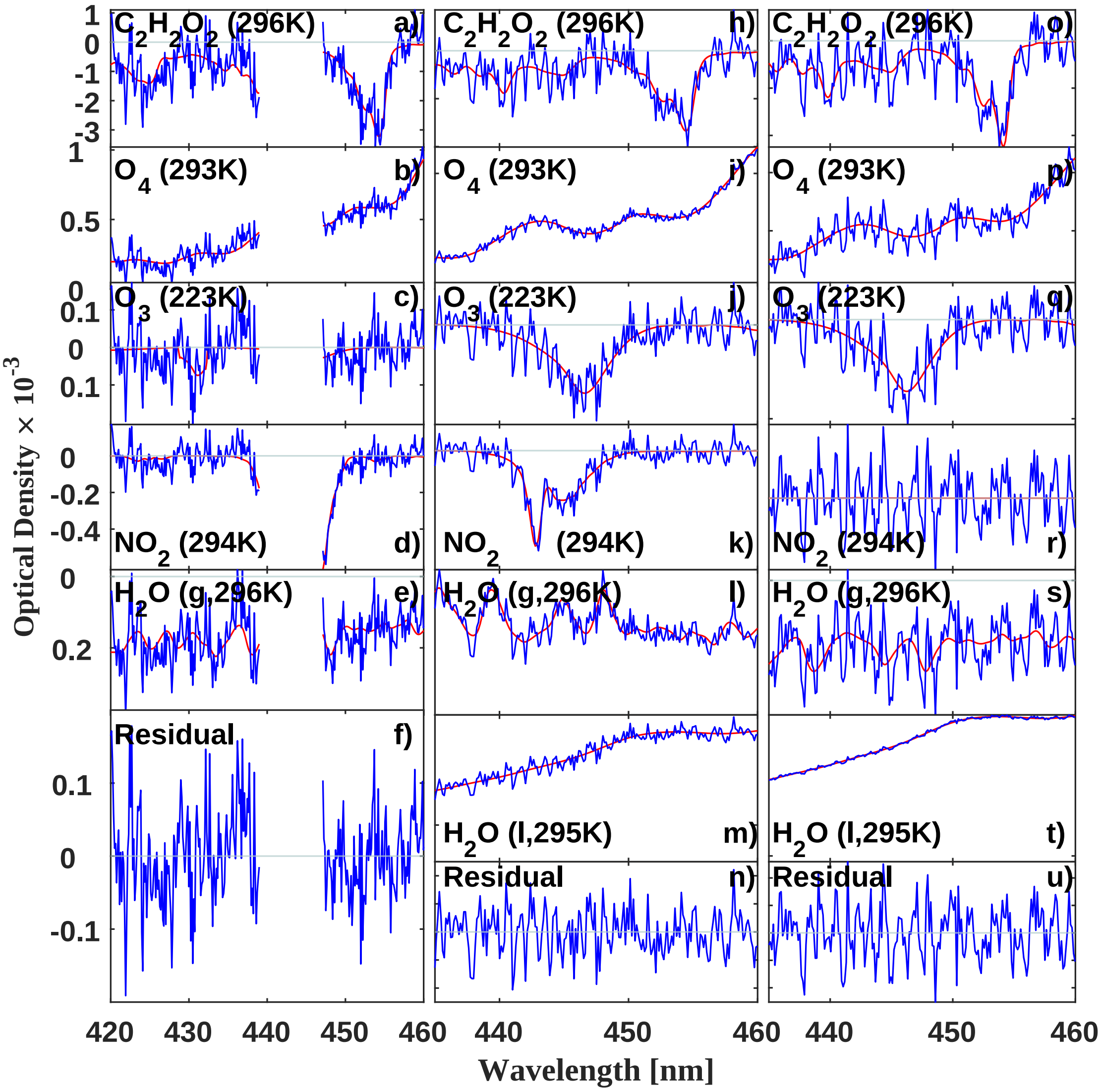

Figure A.2: Spectral retrieval of glyoxal based on the different employed retrieval settings and spectrometers according to table 3.2. For the measurements above the tropical rainforest $C_2H_2O_2$ is simultaneously fitted over two separated spectral windows, ranging from 420 nm to 439 nm and 447 nm to 465 nm, respectively (left column). Over all other regions, a continuous wavelength range of 330 (or 335) to 360 nm is chosen (Limb glyoxal retrieval in the middle column, Nadir retrieval in the right column). The traces shown in blue are the inferred atmospheric spectra together with the residual spectral structures, the red line shows the reference spectra of the respective gases. From left to right, the corresponding signal to noise ratios of each measurement are 8, 2, and 8. The spectra were measured at 15:06 UTC on 11 Sept. 2014 (research flight AC09, left column), 15:21 UTC on 28 Sept. 2017 (research flight W07, middle column), and 10:33 UTC on 07 Aug. 2018 (research flight CA03, right column).

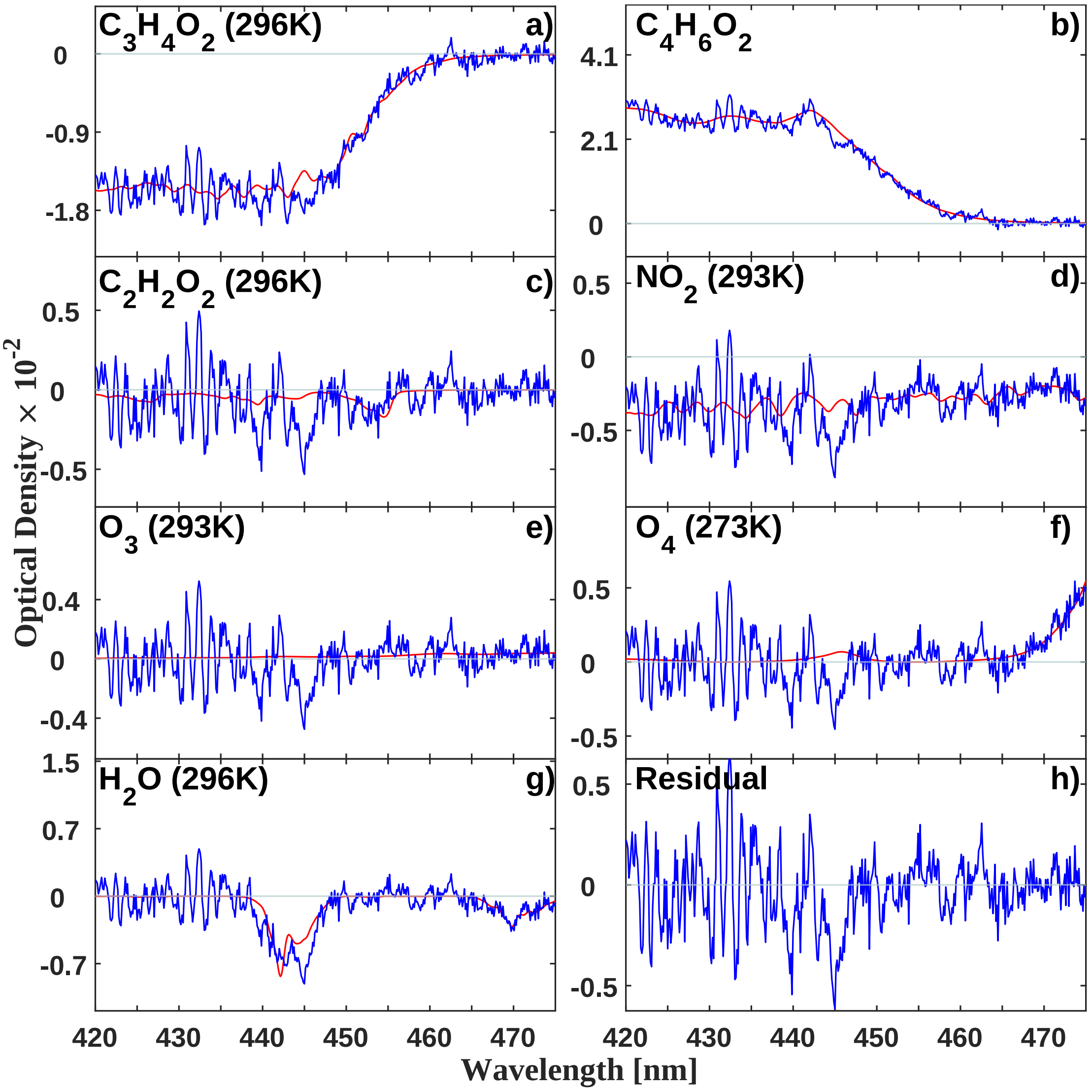

Figure A.3: Exemplary spectral retrieval of methylglyoxal (S/N= 7) for the measurement at 14:53 UTC on 11 Sept. 2014 (ACRIDICON-CHUVA research flight AC11). The traces shown in blue are the inferred atmospheric spectra together with the residual spectral structures, the red line shows the reference spectra of the respective gases.

Appendix B

TROPOMI air mass factors

In order to calculate the TROPOMI box air mass factors (exemplarily for 7 Aug. 2018 in Fig. 3.9), the MAGRITTE CTM simulated air mass factors (Fig. B.1, panel b) are averaged on a 0.25° × 0.25° grid around the HALO flight track (Fig. B.1, red line) and multiplied by the averaging kernel of each TROPOMI measurement.

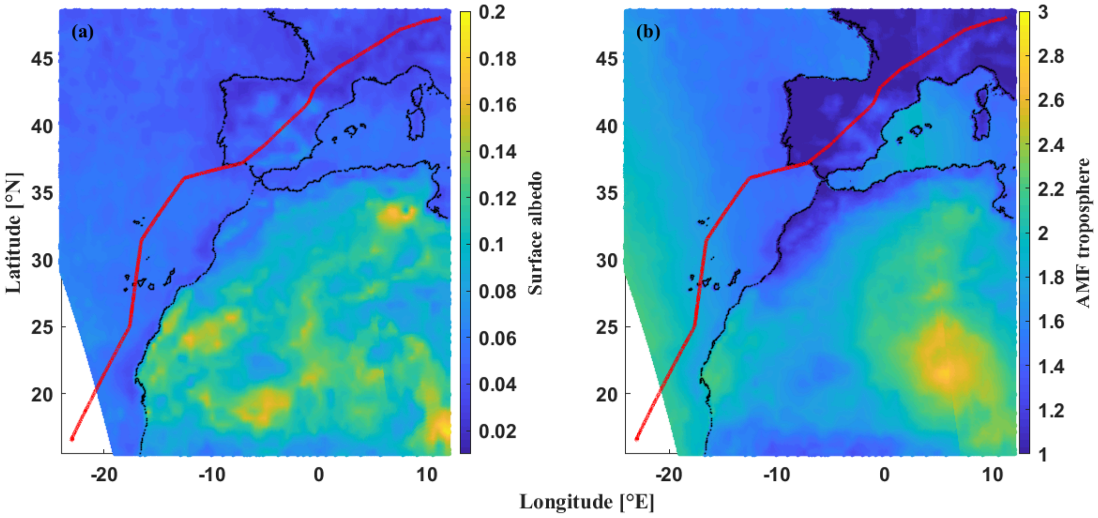

Figure B.1: MAGRITTE CTM simulations of surface albedo and air mass factors of S5p orbit no. 4230 and 4229 on 7 Aug. 2018 along the flight track of the Halo research flight CA03 from Oberpfaffenhofen (Germany) to Sal (Cape Verde, red line). Copyright: Contains modified Copernicus Sentinel data (2018), processed and provided by BIRA-IASB.

Appendix C

Mission overview

The following chapter provides detailed descriptions and flight tracks of all research flights along with an overview of the mini-DOAS measurements addressed within the present thesis. All mini-DOAS measurements are archived in the HALO data depository (`https://doi.org/10.17616/R39Q0T`, re3data.org [2022]) and can be accessed upon signing a data protocol.

In the following (tables C.1–C.8), research flights with available and analysed mini-DOAS measurements of the noted trace gases are marked *yes*. Missing mini-DOAS measurements of a trace gas due to technical instrument failures are marked *technical* (e.g. too high spectrometer temperatures, see sect. 3.1), due to unsuccessful DOAS retrievals *DOAS*, due to constant atmospheric profiling of the mini-DOAS Limb telescopes *profiling*, due to night flights *night*, and due to instrument shut-down *no meas.*. Abbreviations indicate Oberpfaffenhofen (*OP*), Cape Verde (*CV*), Rio Grande (*RG*), Buenos Aires (*BA*), and Argentina (*Arg.*). The aircraft flight altitudes are given as height above the WGS84 ellipsoid (height above sea level for ACRIDICON-CHUVA and OMO) based on onboard measurements of the BAHAMAS instrument [Krautstrunk and Giez, 2012].

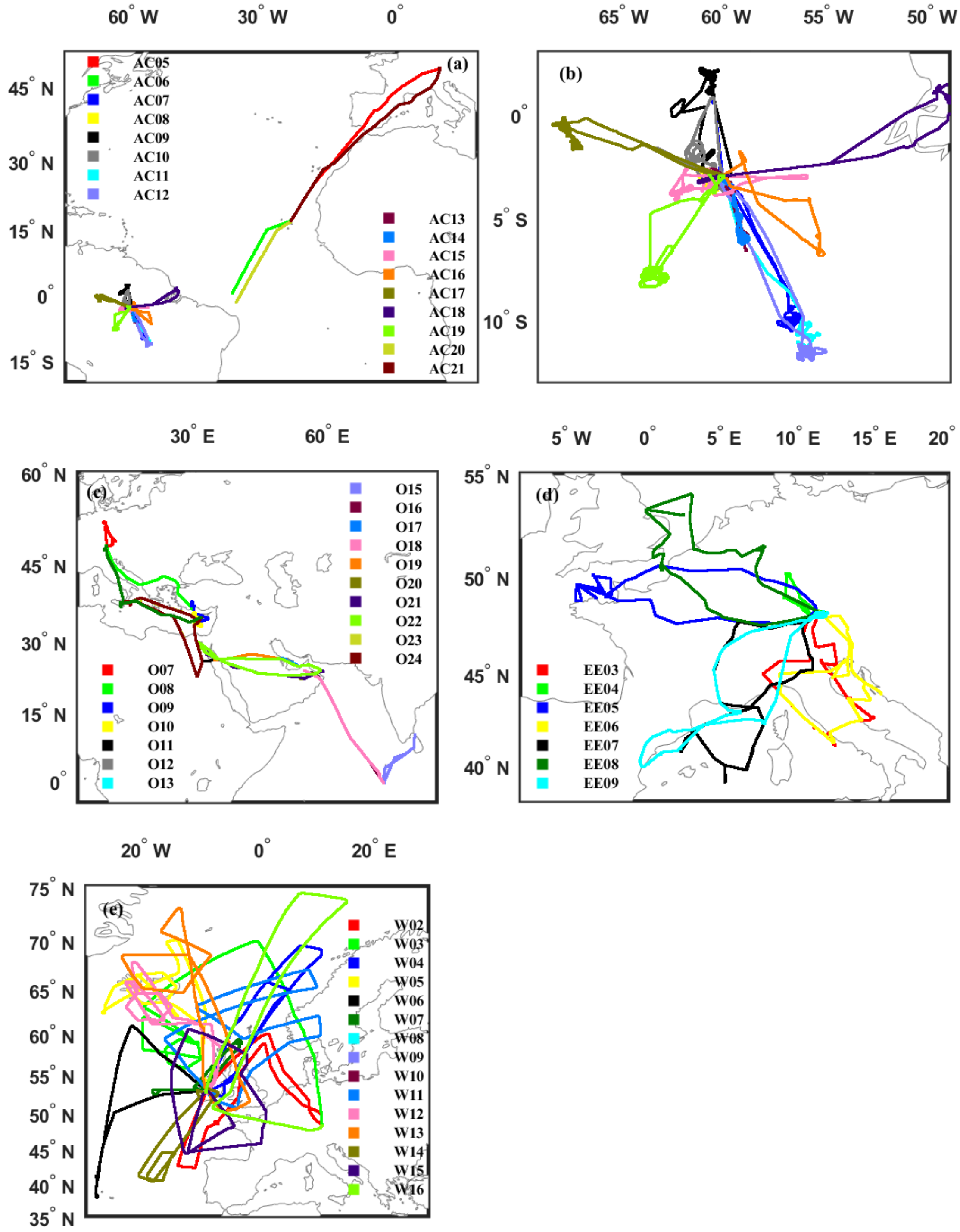

Figure C.1: Flight track overview of all research and transfer flights of the HALO missions ACRIDICON-CHUVA (overview, panel a and zoom on the local research flights, panel b), OMO (panel c), EMeRGe-EU (panel d), and WISE (panel e).

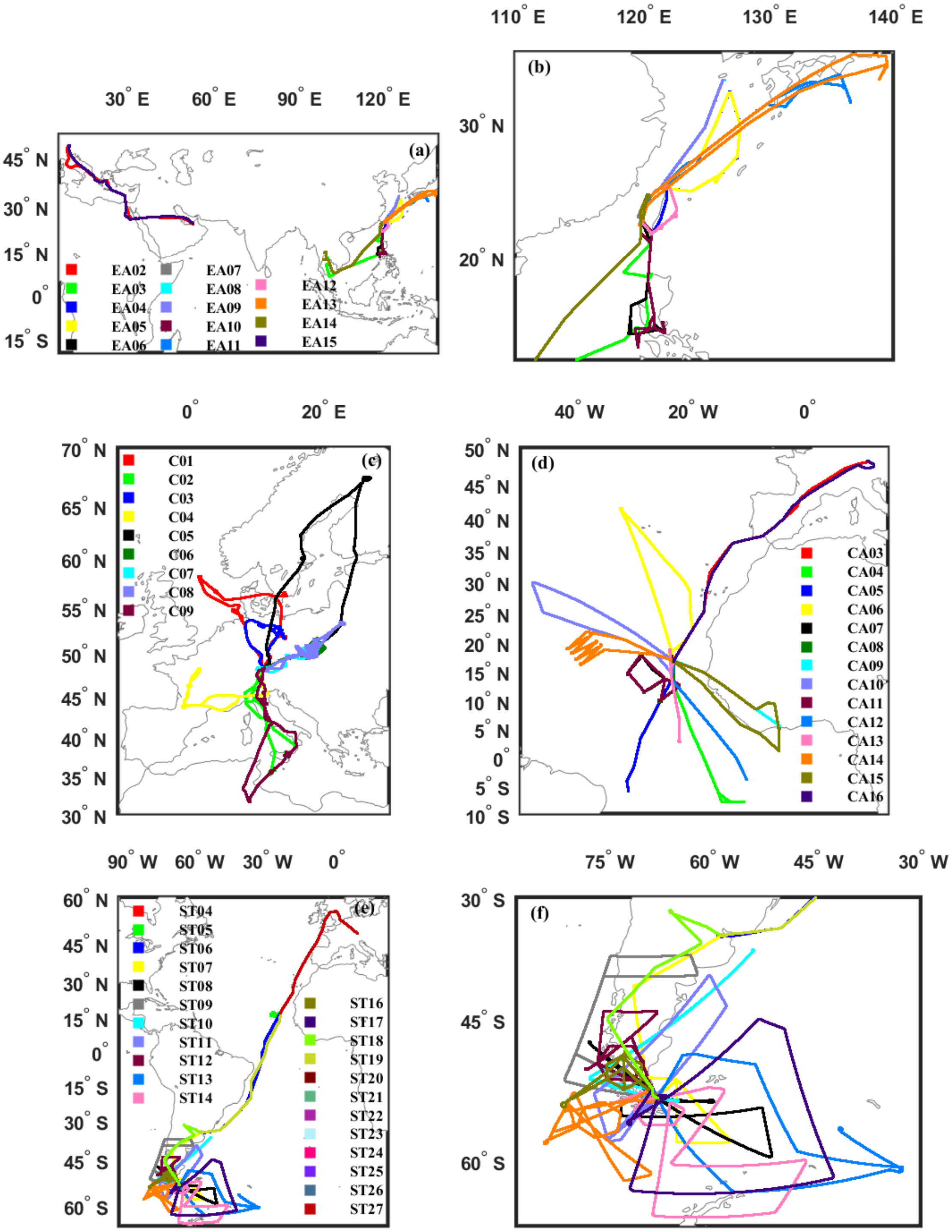

Figure C.2: Flight tracks of all research and transfer flights of the HALO missions EMeRGe-Asia (overview, panel a and zoom on the local research flights, panel b), CoMet (panel c), CAFE (panel d), and SouthTRAC (overview, panel e and zoom on the local research flights, panel f).

Table C.1: ACRIDICON-CHUVA mission (2014) with focus on the tropical rainforest around Manaus city.

Flight ID	**Date**	**Take-off and landing**	**Geographic focus**
AC05	01.09.2014	OP (Germany)–Sal (Cape Verde)	Transfer Germany – Cape Verde
AC06	02.09.2014	Sal (Cape Verde)–Manaus (Brazil)	Transfer Cape Verde – Brazil
AC07	06.09.2014	Manaus (Brazil)	Rainforest
AC08	09.09.2014	Manaus (Brazil)	Amazon river delta
AC09	11.09.2014	Manaus (Brazil)	Rainforest
AC11	16.09.2014	Manaus (Brazil)	Rainforest
AC12	18.09.2014	Manaus (Brazil)	Rainforest
AC13	19.09.2014	Manaus (Brazil)	Rainforest
AC14	21.09.2014	Manaus (Brazil)	Rainforest
AC15	23.09.2014	Manaus (Brazil)	Rainforest
AC16	25.09.2014	Manaus (Brazil)	Amazon river delta
AC17	27.09.2014	Manaus (Brazil)	Rainforest
AC18	28.09.2014	Manaus (Brazil)	Rainforest
AC19	30.09.2014	Manaus (Brazil)	Amazon river delta
AC20	01.10.2014	Manaus (Brazil)	Rainforest
AC21	03.10.2014	Manaus (Brazil)–Sal (Cape Verde)	Transfer Brazil–Cape Verde
AC22	04.10.2014	Sal (Cape Verde) – OP (Germany)	Transfer Cape Verde – Germany

Table C.1: Continued.

Flight ID	**Time [UTC]**	**Predominant (max) flight altitude [km]**	**mini-DOAS measurements**			
			Formaldehyde	**Glyoxal (Limb)**	**Glyoxal (Nadir)**	**Methylglyoxal**
AC05	10:00 – 16:10	13 (13)	DOAS	DOAS	no meas.	DOAS
AC06	15:00 – 18:00	13 (13)	DOAS	DOAS	no meas.	DOAS
AC07	16:00 – 23:20	2 (13)	technical	technical	no meas.	technical
AC08	15:00 – 20:20	3 (13.8)	profiling	profiling	no meas.	profiling
AC09	14:40 – 20:20	11 (12.6)	yes	yes	no meas.	yes
AC11	14:40 – 21:50	13 (15)	yes	yes	no meas.	yes
AC12	15:00 – 20:50	4 (13.8)	yes	yes	no meas.	yes
AC13	15:00 – 21:10	13 (13)	yes	yes	no meas.	yes
AC14	15:00 – 22:00	3 (15)	no meas.	no meas.	no meas.	no meas.
AC15	10:30 – 17:30	1 (13.8)	technical	technical	no meas.	technical
AC16	14:30 – 21:10	1 (13.2)	no meas.	no meas.	no meas.	no meas.
AC17	15:00 – 20:30	4 (8)	no meas.	no meas.	no meas.	no meas.
AC18	14:40 – 21:10	5 (14.4)	no meas.	no meas.	no meas.	no meas.
AC19	15:00 – 22:00	2 (13.8)	no meas.	no meas.	no meas.	no meas.
AC20	15:00 – 21:50	14 (14.4)	no meas	no meas.	no meas.	no meas.
AC21	15:50 – 19:10	14 (14)	no meas.	no meas.	no meas.	no meas.
AC22	10:00 – 16:00	13 (13.8)	no meas.	no meas.	no meas.	no meas.

Table C.2: OMO mission (2015) with changing mission bases in Cyprus, Bahrain, and the Maldives.

Flight ID	**Date**	**Take-off and landing**	**Geographic focus**
O07	16.07.2015	OP (Germany)	Germany
O08	21.07.2015	OP (Germany)–Paphos (Cyprus)	Transfer Germany–Cyprus
O09	25.07.2015	Paphos (Cyprus)	Mediterranean Sea around Cyprus
O10	28.07.2015	Paphos (Cyprus)	Mediterranean Sea around Cyprus
O11	01.08.2015	Paphos (Cyprus)–Gan (Maldives)	Cyprus–Maldives
O12	06.08.2015	Gan (Maldives)–Bahrain (Bahrain)	Maldives–Bahrain
O13	06.08.2015	Bahrain (Bahrain)–Gan (Maldives)	Bahrain–Maldives
O14	08.08.2015	Gan (Maldives)	Gan (Maldives)
O15	09.08.2015	Gan (Maldives)–Bahrain (Bahrain)	Maldives–Bahrain
O16	09.08.2015	Bahrain (Bahrain)–Gan (Maldives)	Bahrain–Maldives
O17	10.08.2015	Gan (Maldives)–Bahrain (Bahrain)	Maldives–Bahrain
O18	10.08.2015	Bahrain (Bahrain)–Paphos (Cyprus)	Bahrain–Cyprus
O19	13.08.2015	Paphos (Cyprus)	Saudi Arabian Peninsula
O20	15.08.2015	Paphos (Cyprus)	Saudi Arabian Peninsula
O21	18.08.2015	Paphos (Cyprus)	Saudi Arabian Peninsula
O22	23.08.2015	Paphos (Cyprus)–Sal (Cape Verde)	Mediterranean Sea
O23	25.08.2015	Paphos (Cyprus)	Mediterranean Sea
O24	27.08.2015	Paphos (Cyprus)–OP (Germany)	Transfer Cyprus–Germany

Table C.2: Continued.

Flight ID	**Time** [**UTC**]	**Predominant (max) flight altitude** [**km**]	**mini-DOAS measurements**
			Glyoxal (Limb)
O07	10:00 – 12:40	1 (14.5)	DOAS
O08	09:00 – 12:30	11 (14.6)	yes
O09	06:00 – 11:10	12 (14.6)	DOAS
O10	06:10 - 14:00	4 (15.1)	yes
O11	06:10 - 14:00	14 (14.5)	DOAS
O12	02:00 – 06:40	1 (11.4)	no meas.
O13	07:50 – 13:00	7 (11.5)	no meas.
O14	07:30 – 11:30	14 (14.4)	no meas.
O15	01:50 – 06:30	12 (13.9)	no meas.
O16	07:40 – 12:30	9 (9)	no meas.
O17	04:50 – 09:30	12 (13.9)	no meas.
O18	11:00 – 14:30	12 (12.4)	no meas.
O19	06:00 – 15:00	13 (15.2)	no meas.
O20	05:50 – 15:00	13 (13.3)	no meas.
O21	06:10 – 15:10	13 (15)	yes
O22	06:00 – 12:40	14 (14)	yes
O23	06:10 – 14:40	3 (14)	yes
O24	08:40 – 14:30	3 (13.7)	yes

Table C.3: EMeRGe-EU mission (2017) with focus on low-altitude central European measurements.

Flight ID	**Date**	**Take-off and landing**	**Geographic focus**
E03	11.07.2017	OP (Germany)	Germany
E04	13.07.2017	OP (Germany)	Germany
E05	17.07.2017	OP (Germany)	France
E06	20.07.2017	OP (Germany)	Italy
E07	24.07.2017	OP (Germany)	Mediterranean Sea
E08	26.07.2017	OP (Germany)	English Channel
E09	28.07.2017	OP (Germany)	Mediterranean Sea

Table C.3: Continued.

Flight ID	**Time [UTC]**	**Predominant (max) flight altitude [km]**	**mini-DOAS measurements**	
			Glyoxal (Limb)	**Glyoxal (Nadir)**
E03	10:00–16:30	1 (7.6)	yes	yes
E04	10:40–15:00	1 (7.3)	yes	yes
E05	10:30–18:30	1 (6.4)	yes	yes
E06	08:50–17:30	1 (9.6)	yes	yes
E07	09:40–18:20	1 (6.3)	yes	yes
E08	07:50–15:20	1 (7.5)	technical	technical
E09	10:00–18:30	3 (8)	technical	technical

Table C.4: WISE mission (2017) with focus on upper tropospheric-lower stratospheric North Atlantic measurements.

Flight ID	**Date**	**Take-off and landing**	**Geographic focus**
W02	13.09.2017	OP (Germany)–Shannon (Ireland)	North Sea and North Atlantic
W03	18.09.2017	Shannon (Ireland)	North Atlantic, Iceland
W04	20.09.2017	Shannon (Ireland)	North Atlantic (Norwegian Sea)
W05	23.09.2017	Shannon (Ireland)	North Atlantic, Iceland
W06	27.09.2017	Shannon (Ireland)	North Atlantic Sea
W07	28.09.2017	Shannon (Ireland)	Irish Sea
W08	01.10.2017	Shannon (Ireland)	North Atlantic
W09	04.10.2017	Shannon (Ireland)	Norwegian Sea
W10	07.10.2017	Shannon (Ireland)	North Atlantic
W11	09.10.2017	Shannon (Ireland)	North Atlantic
W12	12.10.2017	Shannon (Ireland)	North Atlantic, Iceland
W13	14.10.2017	Shannon (Ireland)	North Atlantic, Iceland
W14	15.10.2017	Shannon (Ireland)	North Atlantic
W15	19.10.2017	Shannon (Ireland)	North Atlantic around Ireland
W16	21.10.2017	Shannon (Ireland)–OP (Germany)	Norwegian Sea, Germany

Table C.4: Continued.

Flight ID	**Time [UTC]**	**Predominant (max) flight altitude [km]**	**mini-DOAS measurements**	
			Glyoxal (Limb)	**Glyoxal (Nadir)**
W02	08:30–18:00	14 (14.6)	yes	yes
W03	08:00–17:30	13 (14)	yes	yes
W04	07:20–17:00	13 (14.6)	DOAS	yes
W05	08:00–17:00	14 (14)	yes	yes
W06	07:30–16:30	14 (14.3)	yes	DOAS
W07	13:00–21:00	11 (14.5)	yes	yes
W08	12:00–22:00	14 (15)	yes	yes
W09	09:30–13:00	15 (15)	yes	yes
W10	12:40–20:30	13 (14.7)	yes	technical
W11	08:30–17:30	14 (14.5)	yes	yes
W12	10:00–19:00	14 (14.7)	DOAS	yes
W13	08:30–17:30	14 (14.8)	yes	yes
W14	13:00–19:00	13 (14.7)	yes	yes
W15	09:00–17:30	12 (14.7)	yes	yes
W16	04:30–13:00	13 (14.7)	yes	yes

Table C.5: EMeRGe-Asia mission (2018) with focus on low-altitude measurements over the East China Sea and its neighbouring islands.

Flight ID	**Date**	**Take-off and landing**	**Geographic focus**
EA02	10.03.2018	OP (Germany)–Abu Dhabi (UAE)	Transfer Germany–UAE
EA03	12.03.2018	Rayong (Thailand)–Tainan (Taiwan)	Transfer Thailand–Taiwan
W04	17.03.2018	Tainan (Taiwan)	East China Sea
EA05	19.03.2018	Tainan (Taiwan)	East China Sea
EA06	20.03.2018	Tainan (Taiwan)	Philippines
EA07	22.03.2018	Tainan (Taiwan)	East China Sea around Taiwan
EA08	24.03.2018	Tainan (Taiwan)	South Japan
EA09	26.03.2018	Tainan (Taiwan)	South Japan
EA10	28.03.2018	Tainan (Taiwan)	Philippines
EA11	30.03.2018	Tainan (Taiwan)	South Japan
EA12	03.04.2018	Tainan (Taiwan)	East China Sea around Taiwan
EA13	04.04.2018	Tainan (Taiwan)	South Japan
EA14	07.04.2018	Tainan (Taiwan)–Rayong (Thailand)	Transfer Taiwan – Thailand
EA15	09.04.2018	Abu Dhabi (UAE)–OP (Germany)	Transfer Thailand – Germany

Table C.5: Continued.

Flight ID	Time [UTC]	Predominant (max) flight altitude [km]	mini-DOAS measurements	
			Glyoxal (Limb)	**Glyoxal (Nadir)**
EA02	07:40–15:30	13 (13)	DOAS	DOAS
EA03	04:50–11:20	13 (13.9)	no meas.	no meas.
EA04	01:00–09:50	3 (5)	yes	DOAS
EA05	00:20–08:30	3 (8)	yes	DOAS
EA06	23:50–06:40	1 (6.8)	yes	DOAS
EA07	03:50–09:30	1 (4.7)	no meas.	no meas.
EA08	01:00–09:50	3 (3.2)	yes	yes
EA09	00:20–09:30	1 (4.7)	yes	yes
EA10	00:00–08:30	1 (6.5	yes	yes
EA11	00:00–09:30	12 (12.5)	yes	yes
EA12	00:30–06:30	1 (12.6)	no meas.	no meas.
EA13	00:30–09:30	12 (12.5)	yes	yes
EA14	01:00–08:40	2 (13)	no meas.	no meas.
EA15	06:00–14:40	13 (13)	no meas.	no meas.

Table C.6: CoMet mission (2018) with focus on continental Europe measurements and European industrial hotspots.

Flight ID	Date	Take-off and landing	Geographic focus
C01	15.05.2018	OP (Germany)	Germany, North and East Sea
C02	19.05.2018	OP (Germany)	Italy and Tyrrhenian Sea
C03	23.05.2018	OP (Germany)	Germany
C04	24.05.2018	OP (Germany)	North Italy and South France
C05	28.05.2018	OP (Germany)	Scandinavian coasts
C06	29.05.2018	OP (Germany)	Upper Silesian Coal Basin
C07	06.06.2018	OP (Germany)	Upper Silesian Coal Basin
C08	07.06.2018	OP (Germany)	Upper Silesian Coal Basin
C09	12.06.2018	OP (Germany)	Italy and Tunisia

Table C.6: Continued.

Flight ID	Time [UTC]	Predominant (max) flight altitude [km]	mini-DOAS measurements	
			Glyoxal (Limb)	**Glyoxal (Nadir)**
C01	07:50 – 17:20	13 (13.1)	yes	yes
C02	09:30 – 16:30	8 (13.4)	yes	yes
C03	06:30 – 11:30	7 (12.7)	yes	yes
C04	06:30 – 14:00	13 (13.4)	yes	yes
C05	05:00 – 14	12 (12.5)	yes	yes
C06	06:50 – 13:30	8 (9.5)	yes	yes
C07	08:50 – 15:30	8 (12.2)	yes	yes
C08	07:40 – 15:10	8 (14)	yes	yes
C09	09:20 – 17:00	13 (13.1)	yes	yes

Table C.7: CAFE mission (2018) with focus on upper tropospheric measurements over the Tropical Atlantic.

Flight ID	**Date**	**Take-off and landing**	**Geographic focus**
CA03	07.08.2018	OP (Germany)–Sal (Cape Verde)	Transfer Germany –Cape Verde
CA04	10.08.2018	Sal (Cape Verde)	Tropical Atlantic, West African coast
CA05	12.08.2018	Sal (Cape Verde)	Tropical Atlantic towards Brazil
CA06	15.08.2018	Sal (Cape Verde)	Tropical Atlantic and Azores
CA07	17.08.2018	Sal (Cape Verde)	Tropical Atlantic around Cape Verde
CA08	19.08.2018	Sal (Cape Verde)	Tropical Atlantic around Cape Verde
CA09	22.08.2018	Sal (Cape Verde)	Ghana
CA10	24.08.2018	Sal (Cape Verde)	Tropical Atlantic
CA11	26.08.2018	Sal (Cape Verde)	Tropical Atlantic around Cape Verde
CA12	29.08.2018	Sal (Cape Verde)	Tropical Atlantic, West African coast
CA13	31.08.2018	Sal (Cape Verde)	Tropical Atlantic
CA14	02.09.2018	Sal (Cape Verde)	Tropical Atlantic
CA15	04.09.2018	Sal (Cape Verde)	Ghana
CA16	07.09.2018	Sal (Cape Verde)–OP (Germany)	Transfer Cape Verde–Germany

Table C.7: Continued.

Flight ID	**Time** [UTC]	**Predominant (max) flight altitude** [km]	**mini-DOAS measurements**	
			Glyoxal (Limb)	**Glyoxal (Nadir)**
CAFE03	08:30 – 14:50	13 (14.8)	yes	yes
CAFE04	10:00 – 19:30	12 (15)	yes	yes
CAFE05	10:00 – 19:00	11 (14.4)	yes	yes
CAFE06	10:00 – 19:00	13 (14.5)	DOAS	yes
CAFE07	10:20 – 19:00	14 (14.6)	yes	yes
CAFE08	04:00 – 13:00	13 (4.5)	yes	yes
CAFE09	09:40 – 12:50	13 (13.3)	DOAS	yes
CAFE10	10:00 – 18:40	13 (14.5)	DOAS	yes
CAFE11	16:00 – 01:40	11 (14.5)	night	night
CAFE12	10:00 – 19:00	13 (14.5)	yes	yes
CAFE13	10:00 – 19:30	13 (14.5)	DOAS	yes
CAFE14	10:30 – 19:40	13 (14.4)	yes	yes
CAFE15	10:00 – 19:00	13 (13.9)	yes	yes
CAFE16	10:00 – 16:20	14 (14.2)	yes	yes

Table C.8: SouthTRAC mission (2019) with focus on upper tropospheric measurements over the South Atlantic and northern Antarctica.

Flight ID	**Date (2019)**	**Take-off and landing**	**Geographic focus**
ST04	06.09	OP (Germany)–Sal (CV)	Transfer Germany–Cape Verde
ST05	06.09	Sal (Cape Verde)	Tropical Atlantic around Cape Verde
ST06	08.09	Sal (CV)–BA (Arg.)	Transfer Cape Verde–Argentina
ST07	09.09	BA (Arg.)–RG (Arg.)	Transfer BA–Tierra del Fuego
ST08	11.09	Rio Grande (Argentina)	South Atlantic (Drake Passage)
ST09	13.09	Rio Grande (Argentina)	South Pacific (Strait of Magellan)
ST10	16.09	Rio Grande (Argentina)	South Atlantic (Argentine Sea)
ST11	18.09	Rio Grande (Argentina)	South Atlantic (Strait of Magellan, Argentine Sea)
ST12	20.09	Rio Grande (Argentina)	South Pacific (Chilean Sea)
ST13	24.08	Rio Grande (Argentina)	South Atlantic (Drake Passage, North Antarctica)
ST14	26.09	Rio Grande (Argentina)	South Atlantic (Drake Passage, North Antarctica)
ST15	29.09	Rio Grande (Argentina)	South Pacific
ST16	30.09	Rio Grande (Argentina)	Patagonia, Strait of Magellan
ST17	02.10	Rio Grande (Argentina)	South Atlantic (Drake Passage, North Antarctica)
ST18	06.10	RG (Arg.)–BA (Arg.)	Transfer Tierra del Fuego–BA
ST19	07.10	BA (Arg.)–Sal (CV)	Transfer BA–Sal (Cape Verde)
ST20	09.10	Sal (CV)–OP (Germany)	Transfer Cape Verde–Germany
ST21	02.11	OP (Germany)–Sal (CV)	Transfer Germany–Cape Verde
ST22	04.11	Sal (CV)–BA (Arg.)	Transfer Cape Verde–Argentina
ST23	06.11	BA (Arg.)–RG (Arg.)	Transfer BA–Tierra del Fuego
ST24	09.11	Rio Grande (Argentina)	South Atlantic (Argentine Sea, Patagonia)
ST25	12.11	Rio Grande (Argentina)	South Atlantic (Drake Passage, North Antarctica)
ST26	15.11	Rio Grande (Argentina)	Patagonia
ST27	16.11	Rio Grande (Argentina)	Strait of Magellan

Table C.8: Continued.

Flight ID	**Time [UTC]**	**Predominant (max) flight altitude [km]**	**mini-DOAS measurements**	
			Glyoxal (Limb)	**Glyoxal (Nadir)**
ST04	07:00–13:30	14 (14.5)	night	night
ST05	14:30–17:40	14 (14,5)	yes	DOAS
ST06	04:00–14:00	14 (14.3)	yes	yes
ST07	07:00–13:40	13 (13.8)	yes	yes
ST08	23:00–07:20	12 (13.9)	night	night
ST09	23:00–07:50	13 (14)	night	night
ST10	23:00–07:40	13 (13.5)	night	night
ST11	23:00–07:00	12 (13.5)	night	night
ST12	23:00–08:00	13 (13.8)	night	night
ST13	14:00–23:30	12 (14.3)	DOAS	DOAS
ST14	23:30–08:30	13 (14.2)	yes	yes
ST15	15:30–24:00	13 (13.5)	yes	DOAS
ST16	16:00–22:00	13 (13.8)	yes	yes
ST17	15:00–23:40	13 (14)	yes	yes
ST18	13:00–18:00	13 (14)	yes	yes
ST19	15:40–00:20	13 (13.5)	yes	yes
ST20	10:00–17:00	13 (14.4)	no meas.	no meas.
ST21	16:30–00:40	13 (14.3)	yes	yes
ST22	10:00–19:30	14 (13.8)	yes	yes
ST23	15:00–22:20	13 (13.3)	yes	yes
ST24	11:00–20:00	13 (14)	yes	yes
ST25	11:10–20:00	11 (14.2)	yes	yes
ST26	17:00–02:00	14 (14.2)	yes	yes
ST27	18:00–18:30	6 (6)	yes	DOAS

Appendix D

Mini-DOAS–EMAC comparison

Figures D.1 and D.2 show the impact of negative observations on the comparison of the glyoxal measurements to the model simulations. Clearly, the statistically derived occasional negative glyoxal has no significant effect on the performed comparison.

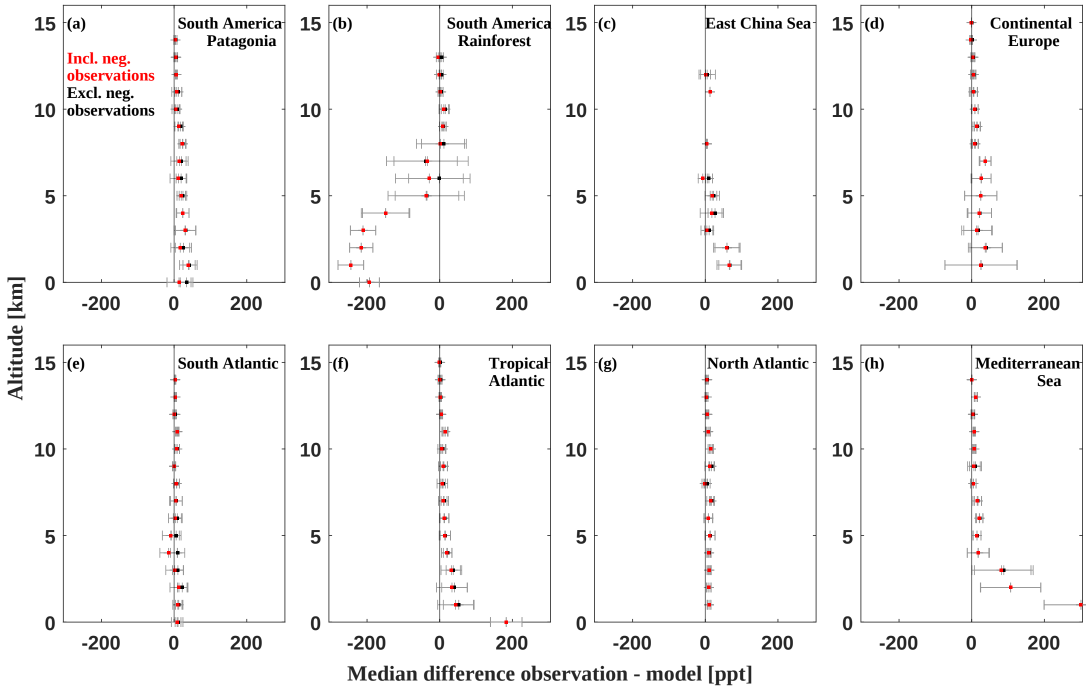

Figure D.1: Median difference of observed and simulated glyoxal in the different regions including negative observations (red) and excluding negative observations (black).

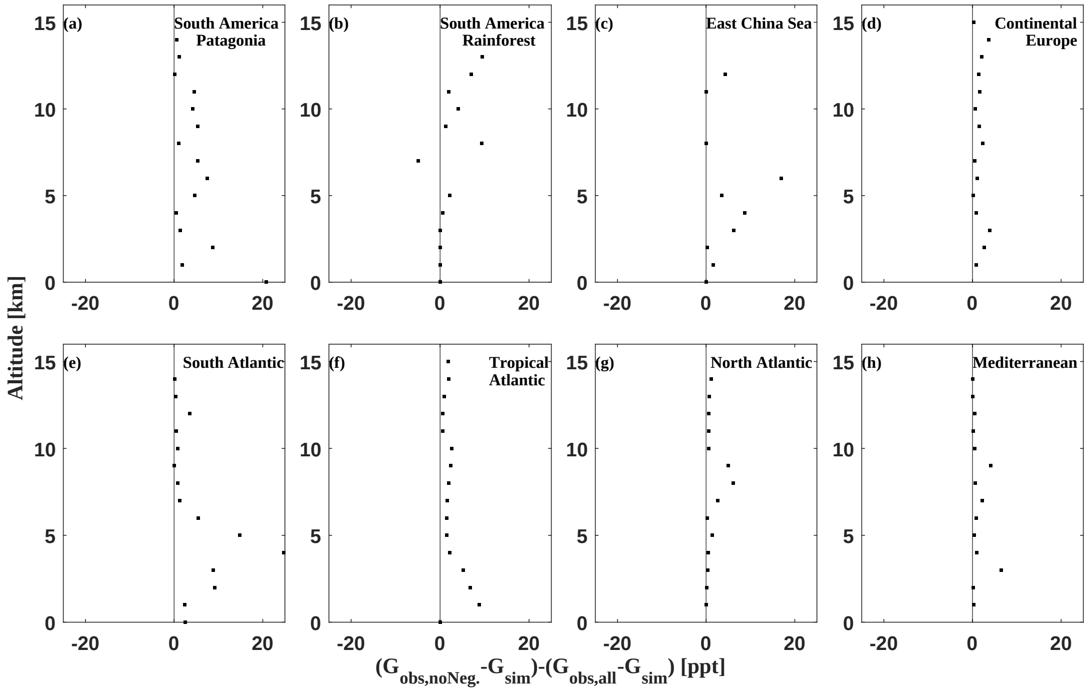

Figure D.2: Difference of the observation - model glyoxal (G) comparison including ($G_{obs,noNeg} - G_{sim}$) and excluding negative observations ($G_{obs,all} - G_{sim}$).

Bibliography

Aiken, A. C., Decarlo, P. F., Kroll, J. H., Worsnop, D. R., Huffman, J. A., Docherty, K. S., Ulbrich, I. M., Mohr, C., Kimmel, J. R., Sueper, D., et al.: O/C and OM/OC ratios of primary, secondary, and ambient organic aerosols with high-resolution time-of-flight aerosol mass spectrometry, Environmental science & technology, 42, 4478–4485, 2008.

Akagi, S. K., Yokelson, R. J., Wiedinmyer, C., Alvarado, M. J., Reid, J. S., Karl, T., Crounse, J. D., and Wennberg, P. O.: Emission factors for open and domestic biomass burning for use in atmospheric models, Atmospheric Chemistry and Physics, 11, 4039–4072, https://doi.org/10.5194/acp-11-4039-2011, URL `https://www.atmos-chem-phys.net/11/4039/2011/`, 2011.

Albrecht, B. A.: Aerosols, cloud microphysics, and fractional cloudiness, Science, 245, 1227–1230, 1989.

Altshuller, A.: Natural volatile organic substances and their effect on air quality in the United States, Atmospheric Environment (1967), 17, 2131–2165, 1983.

Alvarado, L., Richter, A., Vrekoussis, M., Wittrock, F., Hilboll, A., Schreier, S., and Burrows, J.: An improved glyoxal retrieval from OMI measurements, Atmospheric Measurement Techniques, 7, 4133, 2014.

Alvarado, L. M., Richter, A., Vrekoussis, M., Hilboll, A., Hedegaard, A. B. K., Schneising, O., and Burrows, J. P.: Unexpected long-range transport of glyoxal and formaldehyde observed from the Copernicus Sentinel-5 Precursor satellite during the 2018 Canadian wildfires, Atmospheric Chemistry and Physics, 20, 2057–2057, 2020.

Amiridis, V., Marinou, E., Tsekeri, A., Wandinger, U., Schwarz, A., Giannakaki, E., Mamouri, R., Kokkalis, P., Binietoglou, I., Solomos, S., Herekakis, T., Kazadzis, S., Gerasopoulos, E., Proestakis, E., Kottas, M., Balis, D., Papayannis, A., Kontoes, C., Kourtidis, K., Papagiannopoulos, N., Mona, L., Pappalardo, G., Le Rille, O., and Ansmann, A.: LIVAS: a 3-D multi-wavelength aerosol/cloud database based on CALIPSO and EARLINET, Atmospheric Chemistry and Physics, 15, 7127–7153, https://doi.org/10.5194/acp-15-7127-2015, URL `https://www.atmos-chem-phys.net/15/7127/2015/`, 2015.

Andreae, M. and Merlet, P.: Emission of trace gases and aerosols from biomass burning, Global Biogeochemical Cycles, 15, 955–96, https://doi.org/10.1029/2000GB001382, URL `https://agupubs.onlinelibrary.wiley.com/doi/abs/10.1029/2000GB001382`, 2001.

Andreae, M. O.: Biomass burning-Its history, use, and distribution and its impact on environmental quality and global climate, in: Global biomass burning-Atmospheric, climatic, and biospheric implications, 1991.

Andreae, M. O.: Climatic effects of changing atmospheric aerosol levels, World survey of climatology, 16, 347–398, 1995.

Andreae, M. O.: Emission of trace gases and aerosols from biomass burning–an updated assessment, Atmospheric Chemistry and Physics, 19, 8523–8546, 2019.

Andreae, M. O., Artaxo, P., Fischer, H., Freitas, S. R., Grégoire, J.-M., Hansel, A., Hoor, P., Kormann, R., Krejci, R., Lange, L., Lelieveld, J., Lindinger, W., Longo, K., Peters, W., de Reus, M., Scheeren, B., Silva Dias, M. A. F., Ström, J., van Velthoven, P. F. J., and Williams, J.: Transport of biomass burning smoke to the upper troposphere by deep convection in the equatorial region, Geophysical Research Letters, 28, 951–954, https://doi.org/10.1029/2000GL012391, URL `https://agupubs.onlinelibrary.wiley.com/doi/abs/10.1029/2000GL012391`, 2001.

Andreae, M. O., Afchine, A., Albrecht, R., Holanda, B. A., Artaxo, P., Barbosa, H. M., Borrmann, S., Cecchini, M. A., Costa, A., Dollner, M., et al.: Aerosol characteristics and particle production in the upper troposphere over the Amazon Basin, Atmospheric Chemistry and Physics, 18, 921–961, 2018.

Andrés Hernández, M. D., Hilboll, A., Ziereis, H., Förster, E., Krüger, O. O., Kaiser, K., Schneider, J., Barnaba, F., Vrekoussis, M., Schmidt, J., et al.: Overview: On the transport and transformation of pollutants in the outflow of major population centres–observational data from the EMeRGe European intensive operational period in summer 2017, Atmospheric Chemistry and Physics, 22, 5877–5924, 2022.

Archibald, A., Levine, J. G., Abraham, N., Cooke, M., Edwards, P., Heard, D., Jenkin, M., Karunaharan, A., Pike, R., Monks, P., et al.: Impacts of HOx regeneration and recycling in the oxidation of isoprene: Consequences for the composition of past, present and future atmospheres, Geophysical Research Letters, 38, 2011.

Archibald, A., Neu, J., Elshorbany, Y., Cooper, O., Young, P., Akiyoshi, H., Cox, R., Coyle, M., Derwent, R., Deushi, M., et al.: Tropospheric Ozone Assessment ReportA critical review of changes in the tropospheric ozone burden and budget from 1850 to 2100, Elementa: Science of the Anthropocene, 8, 2020.

Arlander, D. W., Brüning, D., Schmidt, U., and Ehhalt, D. H.: The tropospheric distribution of formaldehyde during TROPOZ II, Journal of Atmospheric Chemistry, 22, 251–269, 1995.

Atkinson, R.: Atmospheric chemistry of VOCs and NOx, Atmospheric environment, 34, 2063–2101, 2000.

Atkinson, R., Baulch, D. L., Cox, R. A., Crowley, J. N., Hampson, R. F., Hynes, R. G., Jenkin, M. E., Rossi, M. J., and Troe, J.: Evaluated kinetic and photochemical data for atmospheric chemistry: Volume I, Atmospheric Chemistry and Physics, 4, 1461–1738, https://doi.org/10.5194/acp-4-1461-2004, URL `https://acp.copernicus.org/articles/4/1461/2004/`, 2004.

Atkinson, R., Baulch, D. L., Cox, R. A., Crowley, J. N., Hampson, R. F., Hynes, R. G., Jenkin, M. E., Rossi, M. J., Troe, J., and Subcommittee, I.: Evaluated kinetic and photochemical data for atmospheric chemistry: Volume II - gas phase reactions of organic species, Atmospheric Chemistry and Physics, 6, 3625–4055, https://doi.org/10.5194/acp-6-3625-2006, URL `https://acp.copernicus.org/articles/6/3625/2006/`, 2006.

Aumont, B., Szopa, S., and Madronich, S.: Modelling the evolution of organic carbon during its gas-phase tropospheric oxidation: development of an explicit model based on a self generating approach, Atmospheric Chemistry and Physics, 5, 2497–2517, 2005.

Baidar, S., Oetjen, H., Coburn, S., Dix, B., Ortega, I., Sinreich, R., and Volkamer, R.: The CU Airborne MAX-DOAS instrument: Vertical profiling of aerosol extinction and trace gases, Atmospheric Measurement Techniques, 6, 719–739, 2013.

Barkley, M. P., Palmer, P. I., Kuhn, U., Kesselmeier, J., Chance, K., Kurosu, T. P., Martin, R. V., Helmig, D., and Guenther, A.: Net ecosystem fluxes of isoprene over tropical South America inferred from Global Ozone Monitoring Experiment (GOME) observations of HCHO columns, Journal of Geophysical Research: Atmospheres, 113, 2008.

Barkley, M. P., Smedt, I. D., Van Roozendael, M., Kurosu, T. P., Chance, K., Arneth, A., Hagberg, D., Guenther, A., Paulot, F., Marais, E., et al.: Top-down isoprene emissions over tropical South America inferred from SCIAMACHY and OMI formaldehyde columns, Journal of Geophysical Research: Atmospheres, 118, 6849–6868, 2013.

Bates, D. R. and Nicolet, M.: Atmospheric hydrogen, Publications of the Astronomical Society of the Pacific, 62, 106–110, 1950.

Bauwens, M., Stavrakou, T., Müller, J.-F., De Smedt, I., Van Roozendael, M., Van Der Werf, G. R., Wiedinmyer, C., Kaiser, J. W., Sindelarova, K., and Guenther, A.: Nine years of global hydrocarbon emissions based on source inversion of OMI formaldehyde observations, Atmospheric Chemistry and Physics, 16, 10 133–10 158, 2016.

Behrens, L. K., Hilboll, A., Richter, A., Peters, E., Alvarado, L., Kalisz Hedegaard, A. B., Wittrock, F., Burrows, J. P., and Vrekoussis, M.: Detection of outflow of formaldehyde and glyoxal from the African continent to the Atlantic Ocean with a MAX-DOAS instrument, Atmospheric Chemistry and Physics, 19, 10 257–10 278, 2019.

Boeke, N. L., Marshall, J. D., Alvarez, S., Chance, K. V., Fried, A., Kurosu, T. P., Rappenglück, B., Richter, D., Walega, J., Weibring, P., et al.: Formaldehyde columns from the Ozone Monitoring Instrument: Urban versus background levels and evaluation using aircraft data and a global model, Journal of Geophysical Research: Atmospheres, 116, 2011.

Borbon, A., Ruiz, M., Bechara, J., Aumont, B., Chong, M., Huntrieser, H., Mari, C., Reeves, C. E., Scialom, G., Hamburger, T., Stark, H., Afif, C., Jambert, C., Mills, G., Schlager, H., and Perros, P. E.: Transport and chemistry of formaldehyde by mesoscale convective systems in West Africa during AMMA 2006, Journal of Geophysical Research: Atmospheres, 117, https://doi.org/10.1029/2011JD017121, URL `https://agupubs.onlinelibrary.wiley.com/doi/abs/10.1029/2011JD017121`, 2012.

Bourgeois, I., Peischl, J., Neuman, J. A., Brown, S. S., Thompson, C. R., Aikin, K. C., Allen, H. M., Angot, H., Apel, E. C., Baublitz, C. B., et al.: Large contribution of biomass burning emissions to ozone throughout the global remote troposphere, Proceedings of the National Academy of Sciences, 118, 2021.

Bovensmann, H., Burrows, J., Buchwitz, M., Frerick, J., Noel, S., Rozanov, V., Chance, K., and Goede, A.: SCIAMACHY: Mission objectives and measurement modes, Journal of the atmospheric sciences, 56, 127–150, 1999.

Brasseur, G. and Solomon, S.: Aeronomy of the Middle Atmosphere–Chemistry and Physics of the Stratosphere and Mesosphere, Atmospheric and Oceanographic Sciences Library 32, Springer, PO Box, 17, 3300, 2005a.

Brasseur, G. P. and Solomon, S.: Dynamics and Transport, Springer, 2005b.

Brocchi, V., Krysztofiak, G., Catoire, V., Guth, J., Marecal, V., Zbinden, R., Amraoui, L. E., Dulac, F., and Ricaud, P.: Intercontinental transport of biomass burning pollutants over the Mediterranean Basin during the summer 2014 ChArMEx-GLAM airborne campaign, Atmospheric Chemistry and Physics, 18, 6887–6906, 2018.

Brüggemann, M., Hayeck, N., and George, C.: Interfacial photochemistry at the ocean surface is a global source of organic vapors and aerosols, Nature communications, 9, 1–8, 2018.

Cabrera-Perez, D., Taraborrelli, D., Sander, R., and Pozzer, A.: Global atmospheric budget of simple monocyclic aromatic compounds, Atmospheric Chemistry and Physics, 16, 6931–6947, 2016.

Calvert, J. G.: Hydrocarbon involvement in photochemical smog formation in Los Angeles atmosphere, Environmental Science & Technology, 10, 256–262, 1976.

Calvert, J. G., Atkinson, R., Becker, K. H., Kamens, R. M., Seinfeld, J. H., Wallington, T. H., and Yarwood, G.: The mechanisms of atmospheric oxidation of the aromatic hydrocarbons, 2002.

Camredon, M., Aumont, B., Lee-Taylor, J., and Madronich, S.: The SOA/VOC/NO x system: an explicit model of secondary organic aerosol formation, Atmospheric Chemistry and Physics, 7, 5599–5610, 2007.

Carslaw, K., Boucher, O., Spracklen, D., Mann, G., Rae, J., Woodward, S., and Kulmala, M.: A review of natural aerosol interactions and feedbacks within the Earth system, Atmospheric Chemistry and Physics, 10, 1701–1737, 2010.

Carter, W. P. and Atkinson, R.: Development and evaluation of a detailed mechanism for the atmospheric reactions of isoprene and NOx, International Journal of Chemical Kinetics, 28, 497–530, 1996.

Chan Miller, C., Gonzalez Abad, G., Wang, H., Liu, X., Kurosu, T., Jacob, D., and Chance, K.: Glyoxal retrieval from the ozone monitoring instrument, Atmospheric Measurement Techniques, 7, 3891–3907, 2014.

Chan Miller, C., Jacob, D. J., Marais, E. A., Yu, K., Travis, K. R., Kim, P. S., Fisher, J. A., Zhu, L., Wolfe, G. M., Hanisco, T. F., et al.: Glyoxal yield from isoprene oxidation and relation to formaldehyde: chemical mechanism, constraints from SENEX aircraft observations, and interpretation of OMI satellite data, Atmospheric Chemistry and Physics, 17, 8725–8738, 2017.

Chance, K. and Orphal, J.: Revised ultraviolet absorption cross sections of H2CO for the HITRAN database, Journal of Quantitative Spectroscopy and Radiative Transfer, 112, 1509–1510, 2011.

Chance, K., Palmer, P. I., Spurr, R. J., Martin, R. V., Kurosu, T. P., and Jacob, D. J.: Satellite observations of formaldehyde over North America from GOME, Geophysical Research Letters, 27, 3461–3464, 2000.

Chapman, S.: The photochemistry of atmospheric oxygen, Reports on Progress in Physics, 9, 92, 1942.

Chiu, R., Tinel, L., Gonzalez, L., Ciuraru, R., Bernard, F., George, C., and Volkamer, R.: UV photochemistry of carboxylic acids at the air-sea boundary: A relevant source of glyoxal and other oxygenated VOC in the marine atmosphere, Geophysical Research Letters, 44, 1079–1087, 2017.

Churkina, G., Kuik, F., Bonn, B., Lauer, A., Grote, R., Tomiak, K., and Butler, T. M.: Effect of VOC emissions from vegetation on air quality in Berlin during a heatwave, Environmental Science & Technology, 51, 6120–6130, 2017.

Ciuraru, R., Fine, L., Pinxteren, M. v., D'Anna, B., Herrmann, H., and George, C.: Unravelling new processes at interfaces: photochemical isoprene production at the sea surface, Environmental science & technology, 49, 13 199–13 205, 2015.

Coburn, S., Ortega, I., Thalman, R., Blomquist, B., Fairall, C., and Volkamer, R.: Measurements of diurnal variations and eddy covariance (EC) fluxes of glyoxal in the tropical marine boundary layer: description of the Fast LED-CE-DOAS instrument, Atmospheric Measurement Techniques, 7, 3579–3595, 2014.

Cooke, M., Utembe, S., Carbajo, P. G., Archibald, A., Orr-Ewing, A., Jenkin, M., Derwent, R., Lary, D., and Shallcross, D.: Impacts of formaldehyde photolysis rates on tropospheric chemistry, Atmospheric Science Letters, 11, 33–38, 2010.

Cooper, O. R., Parrish, D., Ziemke, J., Balashov, N., Cupeiro, M., Galbally, I., Gilge, S., Horowitz, L., Jensen, N., Lamarque, J.-F., et al.: Global distribution and trends of tropospheric ozone: An observation-based reviewGlobal distribution and trends of tropospheric ozone, Elementa: Science of the Anthropocene, 2, 2014.

Corrigan, C. and Novakov, T.: Cloud condensation nucleus activity of organic compounds: a laboratory study, Atmospheric Environment, 33, 2661–2668, 1999.

Council, N. R. et al.: Rethinking the ozone problem in urban and regional air pollution, National Academies Press, 1992.

Crippa, M., Guizzardi, D., Muntean, M., Schaaf, E., Dentener, F., Van Aardenne, J. A., Monni, S., Doering, U., Olivier, J. G., Pagliari, V., et al.: Gridded emissions of air pollutants for the period 1970–2012 within EDGAR v4. 3.2, Earth Syst. Sci. Data, 10, 1987–2013, 2018.

Crutzen, P. J.: Tropospheric ozone: An overview, Tropospheric ozone, pp. 3–32, 1988.

Crutzen, P. J. and Andreae, M. O.: Biomass Burning in the Tropics: Impact on Atmospheric Chemistry and Biogeochemical Cycles, Science, 250, 1669–1678, https://doi.org/10.1126/science.250.4988.1669, URL `http://science.sciencemag.org/content/250/4988/1669`, 1990.

Crutzen, P. J., Heidt, L. E., Krasnec, J. P., Pollock, W. H., and Seiler, W.: Biomass burning as a source of atmospheric gases CO, H2, N2O, NO, CH3Cl and COS, Nature, 282, 253–256, 1979.

Dalsøren, S. B., Myhre, G., Hodnebrog, Ø., Myhre, C. L., Stohl, A., Pisso, I., Schwietzke, S., Höglund-Isaksson, L., Helmig, D., Reimann, S., et al.: Discrepancy between simulated and observed ethane and propane levels explained by underestimated fossil emissions, Nature Geoscience, 11, 178–184, 2018.

Dayan, C., Fredj, E., Misztal, P. K., Gabay, M., Guenther, A. B., and Tas, E.: Emission of biogenic volatile organic compounds from warm and oligotrophic seawater in the Eastern Mediterranean, Atmospheric Chemistry and Physics, 20, 12 741–12 759, 2020.

de Serves, C.: Gas phase formaldehyde and peroxide measurements in the Arctic atmosphere, Journal of Geophysical Research: Atmospheres, 99, 25 391–25 398, 1994.

De Smedt, I., Müller, J.-F., Stavrakou, T., van der A, R., Eskes, H., and Van Roozendael, M.: Twelve years of global observations of formaldehyde in the troposphere using GOME and SCIAMACHY sensors, Atmospheric Chemistry and Physics, 8, 4947–4963, https://doi.org/10.5194/acp-8-4947-2008, URL `https://www.atmos-chem-phys.net/8/4947/2008/`, 2008.

De Smedt, I., Stavrakou, T., Hendrick, F., Danckaert, T., Vlemmix, T., Pinardi, G., Theys, N., Lerot, C., Gielen, C., Vigouroux, C., Hermans, C., Fayt, C., Veefkind, P., Müller, J.-F., and Van Roozendael, M.: Diurnal, seasonal and long-term variations of global formaldehyde columns inferred from combined OMI and GOME-2 observations, Atmospheric Chemistry and Physics, 15, 12 519–12 545, https://doi.org/10.5194/acp-15-12519-2015, URL `https://www.atmos-chem-phys.net/15/12519/2015/`, 2015.

Deutschmann, T., Beirle, S., Frieß, U., Grzegorski, M., Kern, C., Kritten, L., Platt, U., Prados-Román, C., Puķı, J., Wagner, T., et al.: The Monte Carlo atmospheric radiative transfer model McArtim: Introduction and validation of Jacobians and 3D features, Journal of Quantitative Spectroscopy and Radiative Transfer, 112, 1119–1137, 2011.

Dibble, T. S.: Failures and limitations of quantum chemistry for two key problems in the atmospheric chemistry of peroxy radicals, Atmospheric Environment, 42, 5837–5848, 2008.

Dickerson, R., Kondragunta, S., Stenchikov, G., Civerolo, K., Doddridge, B., and Holben, B.: The impact of aerosols on solar ultraviolet radiation and photochemical smog, science, 278, 827–830, 1997.

Didan, K.: MODIS/Aqua Vegetation Indices Monthly L3 Global 1km SIN Grid V061., distributed by NASA EOSDIS Land Processes DAAC, https://doi.org/https://doi.org/10.5067/MODIS/MYD13A3.061.Accessed2022-06-18, 2021.

DiGangi, J., Henry, S., Kammrath, A., Boyle, E., Kaser, L., Schnitzhofer, R., Graus, M., Turnipseed, A., Park, J., Weber, R., et al.: Observations of glyoxal and formaldehyde as metrics for the anthropogenic impact on rural photochemistry, Atmospheric Chemistry and Physics, 12, 9529–9543, 2012.

Dufour, G., Szopa, S., Barkley, M. P., Boone, C. D., Perrin, A., Palmer, P. I., and Bernath, P. F.: Global upper-tropospheric formaldehyde: seasonal cycles observed by the ACE-FTS satellite instrument, Atmospheric Chemistry and Physics, 9, 3893–3910, https://doi.org/10.5194/acp-9-3893-2009, URL `https://www.atmos-chem-phys.net/9/3893/2009/`, 2009.

Fan, W., Chen, T., Zhu, Z., Zhang, H., Qiu, Y., and Yin, D.: A review of secondary organic aerosols formation focusing on organosulfates and organic nitrates, Journal of Hazardous Materials, p. 128406, 2022.

Finlayson-Pitts, B. J. and J. N. Pitts, J.: Atmospheric chemistry : fundamentals and experimental techniques, Wiley and Sons, New York, 1986.

Fiore, A. M., Levy Ii, H., and Jaffe, D.: North American isoprene influence on intercontinental ozone pollution, Atmospheric Chemistry and Physics, 11, 1697–1710, 2011.

Fishman, J. and Seiler, W.: Correlative nature of ozone and carbon monoxide in the troposphere: Implications for the tropospheric ozone budget, Journal of Geophysical Research: Oceans, 88, 3662–3670, 1983.

Fishman, J., Watson, C. E., Larsen, J. C., and Logan, J. A.: Distribution of tropospheric ozone determined from satellite data, Journal of Geophysical Research: Atmospheres, 95, 3599–3617, 1990.

Fishman, J., Hoell Jr, J. M., Bendura, R. D., McNeal, R. J., and Kirchhoff, V. W.: NASA GTE trace a experiment (September–October 1992): Overview, Journal of Geophysical Research: Atmospheres, 101, 23 865–23 879, 1996.

Fittschen, C.: The reaction of peroxy radicals with OH radicals, Chemical Physics Letters, 725, 102–108, 2019.

Fix, A., Amediek, A., Bovensmann, H., Ehret, G., Gerbig, C., Gerilowski, K., Pfeilsticker, K., Roiger, A., and Zöger, M.: CoMet: An airborne mission to simultaneously measure CO2 and CH4 using lidar, passive remote sensing, and in-situ techniques, in: EPJ Web of Conferences, vol. 176, p. 02003, EDP Sciences, 2018.

Förster, E., Bönisch, H., Neumaier, M., Obersteiner, F., Zahn, A., Hilboll, A., Kalisz Hedegaard, A. B., Daskalakis, N., Poulidis, A. P., Vrekoussis, M., et al.: Chemical and dynamical identification of emission outflows during the HALO campaign EMeRGe in Europe and Asia, Atmospheric Chemistry and Physics Discussions, pp. 1–37, 2022.

Fortems-Cheiney, A., Chevallier, F., Pison, I., Bousquet, P., Saunois, M., Szopa, S., Cressot, C., Kurosu, T. P., Chance, K., and Fried, A.: The formaldehyde budget as seen by a global-scale multi-constraint and multi-species inversion system, Atmospheric Chemistry and Physics, 12, 6699–6721, https://doi.org/10.5194/acp-12-6699-2012, URL `https://www.atmos-chem-phys.net/12/6699/2012/`, 2012.

Franco, B., Blumenstock, T., Cho, C., Clarisse, L., Clerbaux, C., Coheur, P.-F., De Mazière, M., De Smedt, I., Dorn, H.-P., Emmerichs, T., et al.: Ubiquitous atmospheric production of organic acids mediated by cloud droplets, Nature, 593, 233–237, 2021.

French, N. H., Goovaerts, P., and Kasischke, E. S.: Uncertainty in estimating carbon emissions from boreal forest fires, Journal of Geophysical Research: Atmospheres, 109, 2004.

Fried, A., McKeen, S., Sewell, S., Harder, J., Henry, B., Goldan, P., Kuster, W., Williams, E., Baumann, K., Shetter, R., et al.: Photochemistry of formaldehyde during the 1993 Tropospheric OH Photochemistry Experiment, Journal of Geophysical Research: Atmospheres, 102, 6283–6296, 1997.

Fried, A., Olson, J. R., Walega, J. G., Crawford, J. H., Chen, G., Weibring, P., Richter, D., Roller, C., Tittel, F., Porter, M., Fuelberg, H., Halland, J., Bertram, T. H., Cohen, R. C., Pickering, K., Heikes, B. G., Snow, J. A., Shen, H., O'Sullivan, D. W., Brune, W. H., Ren, X., Blake, D. R., Blake, N., Sachse, G., Diskin, G. S., Podolske, J., Vay, S. A., Shetter, R. E., Hall, S. R., Anderson, B. E., Thornhill, L., Clarke, A. D., McNaughton, C. S., Singh, H. B., Avery, M. A., Huey, G., Kim, S., and Millet, D. B.: Role of convection in redistributing formaldehyde to the upper troposphere over North America and the North Atlantic during the summer 2004 INTEX campaign, Journal of Geophysical Research: Atmospheres, 113, https://doi.org/10.1029/2007JD009760, URL `https://agupubs.onlinelibrary.wiley.com/doi/abs/10.1029/2007JD009760`, 2008.

Friedfeld, S., Fraser, M., Ensor, K., Tribble, S., Rehle, D., Leleux, D., and Tittel, F.: Statistical analysis of primary and secondary atmospheric formaldehyde, Atmospheric Environment, 36, 4767–4775, 2002.

Frost, G. J., Fried, A., Lee, Y.-N., Wert, B., Henry, B., Drummond, J. R., Evans, M. J., Fehsenfeld, F. C., Goldan, P. D., Holloway, J. S., Hübler, G., Jakoubek, R., Jobson, B. T., Knapp, K., Kuster, W. C., Roberts, J., Rudolph, J., Ryerson, T. B., Stohl, A., Stroud, C., Sueper, D. T., Trainer, M., and Williams, J.: Comparisons of box model calculations and measurements of formaldehyde from the 1997 North Atlantic Regional Experiment, Journal of Geophysical Research: Atmospheres, 107, ACH 3–1–ACH 3–12, https://doi.org/10.

1029/2001JD000896, URL `https://agupubs.onlinelibrary.wiley.com/doi/abs/10.1029/2001JD000896`, 2002.

Fu, D., Millet, D. B., Wells, K. C., Payne, V. H., Yu, S., Guenther, A., and Eldering, A.: Direct retrieval of isoprene from satellite-based infrared measurements, Nature Communications, 10, 1–12, 2019.

Fu, T.-M., Jacob, D. J., Wittrock, F., Burrows, J. P., Vrekoussis, M., and Henze, D. K.: Global budgets of atmospheric glyoxal and methylglyoxal, and implications for formation of secondary organic aerosols, Journal of geophysical research: atmospheres, 113, 2008.

G. Myhre, D. Shindell, F.-M. B. W. C. J. F. J. H. D. K. J.-F. L. D. L. B. M. T. N. A. R. G. S. T. T. and Zhang, H.: Climate Change 2013: The Physical Science Basis. Contribution of Working Group I to the Fifth Assessment Report of the Intergovernmental Panel on Climate Change, 2013.

Gerbig, C., Kley, D., Volz-Thomas, A., Kent, J., Dewey, K., and McKenna, D. S.: Fast response resonance fluorescence CO measurements a the C-130: Instrument characterization and measurements made during North Atlantic Regional Experiment 1993, Journal of Geophysical Research: Atmospheres, 101, 29 229–29 238, 1996.

Gerbig, C., Schmitgen, S., Kley, D., Volz-Thomas, A., Dewey, K., and Haaks, D.: An improved fast-response vacuum-UV resonance fluorescence CO instrument, Journal of Geophysical Research: Atmospheres, 104, 1699–1704, 1999.

Giglio, L., Boschetti, L., Roy, D. P., Humber, M. L., and Justice, C. O.: The Collection 6 MODIS burned area mapping algorithm and product, Remote sensing of environment, 217, 72–85, 2018.

Goosse, H., BARRIAT, P.-Y., LOUTRE, M.-F., and ZUNZ, V.: Introduction to climate dynamics and climate modeling, Centre de recherche sur la Terre et le climat Georges Lemaître-UCLouvain, 2010.

Greenblatt, G. D., Orlando, J. J., Burkholder, J. B., and Ravishankara, A.: Absorption measurements of oxygen between 330 and 1140 nm, Journal of Geophysical Research: Atmospheres, 95, 18 577–18 582, 1990.

Grosjean, E., de Andrade, J. B., and Grosjean, D.: Carbonyl products of the gas-phase reaction of ozone with simple alkenes, Environmental science & technology, 30, 975–983, 1996.

Gu, D., Guenther, A. B., Shilling, J. E., Yu, H., Huang, M., Zhao, C., Yang, Q., Martin, S. T., Artaxo, P., Kim, S., Seco, R., Stavrakou, T., Longo, K. M., Tóta, J., Ferreira de Souza, R. A., Vega, O., Liu, Y., Shrivastava, M., Alves, E. G., Santos, F. C., Leng, G., and Hu, Z.: Airborne observations reveal elevational gradient in tropical forest isoprene emissions, Nature Communications, 8, 1–7, 2017.

Gu, S., Guenther, A., and Faiola, C.: Effects of Anthropogenic and Biogenic Volatile Organic Compounds on Los Angeles Air Quality, Environmental Science & Technology, 55, 12 191–12 201, 2021.

Guenther, A., Hewitt, C. N., Erickson, D., Fall, R., Geron, C., Graedel, T., Harley, P., Klinger, L., Lerdau, M., McKay, W., et al.: A global model of natural volatile organic compound emissions, Journal of Geophysical Research: Atmospheres, 100, 8873–8892, 1995.

Guenther, A., Karl, T., Harley, P., Wiedinmyer, C., Palmer, P. I., and Geron, C.: Estimates of global terrestrial isoprene emissions using MEGAN (Model of Emissions of Gases and Aerosols from Nature), Atmospheric Chemistry and Physics, 6, 3181–3210, 2006.

Haagen-Smit, A., Darley, E. F., Zaitlin, M., Hull, H., and Noble, W.: Investigation on injury to plants from air pollution in the Los Angeles area, Plant Physiology, 27, 18, 1952.

Hao, W. M. and Liu, M.-H.: Spatial and temporal distribution of tropical biomass burning, Global biogeochemical cycles, 8, 495–503, 1994.

Hartley, W.: XXI.—On the absorption of solar rays by atmospheric ozone, Journal of the Chemical Society, Transactions, 39, 111–128, 1881.

Hays, M. D., Geron, C. D., Linna, K. J., Smith, N. D., and Schauer, J. J.: Speciation of Gas-Phase and Fine Particle Emissions from Burning of Foliar Fuels, Environmental Science & Technology, 36, 2281–2295, https://doi.org/10.1021/es0111683, URL `https://doi.org/10.1021/es0111683`, pMID: 12075778, 2002.

Heald, C. L., Jacob, D. J., Park, R. J., Alexander, B., Fairlie, T. D., Yantosca, R. M., and Chu, D. A.: Transpacific transport of Asian anthropogenic aerosols and its impact on surface air quality in the United States, Journal of Geophysical Research: Atmospheres, 111, 2006.

Heck, W. W., Taylor, O., Adams, R., Bingham, G., Miller, J., Preston, E., and Weinstein, L.: Assessment of crop loss from ozone, Journal of the Air Pollution Control Association, 32, 353–361, 1982.

Helmig, D., Balsley, B., Davis, K., Kuck, L. R., Jensen, M., Bognar, J., Smith Jr, T., Arrieta, R. V., Rodríguez, R., and Birks, J. W.: Vertical profiling and determination of landscape fluxes of biogenic nonmethane hydrocarbons within the planetary boundary layer in the Peruvian Amazon, Journal of Geophysical Research: Atmospheres, 103, 25 519–25 532, 1998.

Hens, K., Novelli, A., Martinez, M., Auld, J., Axinte, R., Bohn, B., Fischer, H., Keronen, P., Kubistin, D., Nölscher, A., et al.: Observation and modelling of HO x radicals in a boreal forest, Atmospheric Chemistry and Physics, 14, 8723–8747, 2014.

Hersbach, H., Bell, B., Berrisford, P., Hirahara, S., Horányi, A., Muñoz-Sabater, J., Nicolas, J., Peubey, C., Radu, R., Schepers, D., et al.: The ERA5 global reanalysis, Quarterly Journal of the Royal Meteorological Society, 146, 1999–2049, 2020.

Hess, M., Koepke, P., and Schult, I.: Optical properties of aerosols and clouds: The software package OPAC, Bulletin of the American meteorological society, 79, 831–844, 1998.

Hewitt, C., Ashworth, K., Boynard, A., Guenther, A., Langford, B., MacKenzie, A., Misztal, P., Nemitz, E., Owen, S., Possell, M., et al.: Ground-level ozone influenced by circadian control of isoprene emissions, Nature geoscience, 4, 671–674, 2011.

Hoelzemann, J. J., Schultz, M. G., Brasseur, G. P., Granier, C., and Simon, M.: Global Wildland Fire Emission Model (GWEM): Evaluating the use of global area burnt satellite data, Journal of Geophysical Research: Atmospheres, 109, 2004.

Hoffmann, T., Odum, J. R., Bowman, F., Collins, D., Klockow, D., Flagan, R. C., and Seinfeld, J. H.: Formation of organic aerosols from the oxidation of biogenic hydrocarbons, Journal of Atmospheric Chemistry, 26, 189–222, 1997.

Holanda, B. A., Pöhlker, M. L., Walter, D., Saturno, J., Sörgel, M., Ditas, J., Ditas, F., Schulz, C., Franco, M. A., Wang, Q., et al.: Influx of African biomass burning aerosol during the Amazonian dry season through layered transatlantic transport of black carbon-rich smoke, Atmospheric Chemistry and Physics, 20, 4757–4785, 2020.

Hoque, H., Irie, H., and Damiani, A.: First MAX-DOAS Observations of Formaldehyde and Glyoxal in Phimai, Thailand, Journal of Geophysical Research: Atmospheres, 123, 9957–9975, 2018.

Horowitz, A., Meller, R., and Moortgat, G. K.: The UV–VIS absorption cross sections of the α-dicarbonyl compounds: pyruvic acid, biacetyl and glyoxal, Journal of Photochemistry and Photobiology A: Chemistry, 146, 19–27, 2001.

Hoyle, C. R., Boy, M., Donahue, N. M., Fry, J. L., Glasius, M., Guenther, A., Hallar, A. G., Huff Hartz, K., Petters, M. D., Petäjä, T., et al.: A review of the anthropogenic influence on biogenic secondary organic aerosol, Atmospheric Chemistry and Physics, 11, 321–343, 2011.

Hüneke, T.: The scaling method applied to HALO measurements: Inferring absolute trace gas concentrations from airborne limb spectroscopy under all sky conditions, Phd, University of Heidelberg, Heidelberg, Germany, 2016.

Hüneke, T., Aderhold, O.-A., Bounin, J., Dorf, M., Gentry, E., Grossmann, K., Grooß, J.-U., Hoor, P., Jöckel, P., Kenntner, M., et al.: The novel HALO mini-DOAS instrument: inferring trace gas concentrations from airborne UV/visible limb spectroscopy under all skies using the scaling method, Atmospheric Measurement Techniques, 10, 4209–4234, 2017.

Huntrieser, H., Lichtenstern, M., Scheibe, M., Aufmhoff, H., Schlager, H., Pucik, T., Minikin, A., Weinzierl, B., Heimerl, K., Fütterer, D., Rappenglück, B., Ackermann, L., Pickering, K. E., Cummings, K. A., Biggerstaff, M. I., Betten, D. P., Honomichl, S., and Barth, M. C.: On the origin of pronounced O3 gradients in the thunderstorm outflow region during DC3, Journal of Geophysical Research: Atmospheres, 121, 6600–6637, https://doi.org/10.1002/2015JD024279, URL `https://agupubs.onlinelibrary.wiley.com/doi/abs/10.1002/2015JD024279`, 2016a.

Huntrieser, H., Lichtenstern, M., Scheibe, M., Aufmhoff, H., Schlager, H., Pucik, T., Minikin, A., Weinzierl, B., Heimerl, K., Pollack, I. B., Peischl, J., Ryerson, T. B., Weinheimer, A. J., Honomichl, S., Ridley, B. A., Biggerstaff, M. I., Betten, D. P., Hair, J. W., Butler, C. F., Schwartz, M. J., and Barth, M. C.: Injection of lightning-produced NOx, water vapor, wildfire emissions, and stratospheric air to the UT/LS as observed from DC3 measurements, Journal of Geophysical Research: Atmospheres, 121, 6638–6668, https://doi.org/10.1002/2015JD024273, URL `https://agupubs.onlinelibrary.wiley.com/doi/abs/10.1002/2015JD024273`, 2016b.

Ingmann, P., Veihelmann, B., Langen, J., Lamarre, D., Stark, H., and Courrèges-Lacoste, G. B.: Requirements for the GMES Atmosphere Service and ESA's implementation concept: Sentinels-4/-5 and-5p, Remote Sensing of Environment, 120, 58–69, 2012.

IPCC, T.: Climate change 2001: synthesis report, Intergovernmental Panel on Climate Change (IPCC), Geneva, Switzerland, 2001.

Irvine, W. M.: The formation of absorption bands and the distribution of photon optical paths in a scattering atmosphere, Bulletin of the Astronomical Institutes of the Netherlands, 17, 266, 1963.

Ito, A. and Penner, J. E.: Global estimates of biomass burning emissions based on satellite imagery for the year 2000, Journal of Geophysical Research: Atmospheres, 109, 2004.

Jacob, D. J., Heikes, E., Fan, S.-M., Logan, J. A., Mauzerall, D., Bradshaw, J., Singh, H., Gregory, G., Talbot, R., Blake, D., et al.: Origin of ozone and NOx in the tropical troposphere: A photochemical analysis of aircraft observations over the South Atlantic basin, Journal of Geophysical Research: Atmospheres, 101, 24 235–24 250, 1996.

Jaeglé, L., Jacob, D. J., Brune, W., Tan, D., Faloona, I., Weinheimer, A., Ridley, B., Campos, T., and Sachse, G.: Sources of HOx and production of ozone in the upper troposphere over the United States, Geophysical Research Letters, 25, 1709–1712, 1998.

Jaeglé, L., Jacob, D. J., Brune, W. H., and Wennberg, P. O.: Chemistry of HOx radicals in the upper troposphere, Atmospheric Environment, 35, 469–489, 2001.

Jaffe, D., Bertschi, I., Jaeglé, L., Novelli, P., Reid, J. S., Tanimoto, H., Vingarzan, R., and Westphal, D. L.: Long-range transport of Siberian biomass burning emissions and impact on surface ozone in western North America, Geophysical research letters, 31, 2004.

Jang, M. and Kamens, R. M.: Atmospheric secondary aerosol formation by heterogeneous reactions of aldehydes in the presence of a sulfuric acid aerosol catalyst, Environmental Science & Technology, 35, 4758–4766, 2001.

Jenkin, M., Young, J., and Rickard, A.: The MCM v3. 3.1 degradation scheme for isoprene, Atmospheric Chemistry and Physics, 15, 11 433–11 459, 2015.

Jöckel, P., Tost, H., Pozzer, A., Brühl, C., Buchholz, J., Ganzeveld, L., Hoor, P., Kerkweg, A., Lawrence, M., Sander, R., et al.: The atmospheric chemistry general circulation model ECHAM5/MESSy1: consistent simulation of ozone from the surface to the mesosphere, Atmospheric Chemistry and Physics, 6, 5067–5104, 2006.

Jöckel, P., Kerkweg, A., Pozzer, A., Sander, R., Tost, H., Riede, H., Baumgaertner, A., Gromov, S., and Kern, B.: Development cycle 2 of the modular earth submodel system (MESSy2), Geoscientific Model Development, 3, 717–752, 2010.

Johansson, S., Wetzel, G., Friedl-Vallon, F., Glatthor, N., Höpfner, M., Kleinert, A., Neubert, T., Sinnhuber, B.-M., and Ungermann, J.: Biomass burning pollution in the South Atlantic upper troposphere: GLORIA trace gas observations and evaluation of the CAMS model, Atmospheric Chemistry and Physics, 22, 3675–3691, 2022.

Kaiser, J., Heil, A., Andreae, M., Benedetti, A., Chubarova, N., Jones, L., Morcrette, J.-J., Razinger, M., Schultz, M., Suttie, M., et al.: Biomass burning emissions estimated with a global fire assimilation system based on observed fire radiative power, Biogeosciences, 9, 527–554, 2012.

Kaiser, J., Wolfe, G., Min, K., Brown, S., Miller, C., Jacob, D., DeGouw, J., Graus, M., Hanisco, T., Holloway, J., et al.: Reassessing the ratio of glyoxal to formaldehyde as an indicator of hydrocarbon precursor speciation, Atmospheric Chemistry and Physics, 15, 7571–7583, 2015.

Kanakidou, M., Seinfeld, J., Pandis, S., Barnes, I., Dentener, F. J., Facchini, M. C., Van Dingenen, R., Ervens, B., Nenes, A., Nielsen, C., et al.: Organic aerosol and global climate modelling: a review, Atmospheric Chemistry and Physics, 5, 1053–1123, 2005.

Kawamura, K., Okuzawa, K., Aggarwal, S., Irie, H., Kanaya, Y., and Wang, Z.: Determination of gaseous and particulate carbonyls (glycolaldehyde, hydroxyacetone, glyoxal, methylglyoxal, nonanal and decanal) in the atmosphere at Mt. Tai, Atmospheric Chemistry and Physics, 13, 5369–5380, 2013.

Kean, A. J., Grosjean, E., Grosjean, D., and Harley, R. A.: On-road measurement of carbonyls in California light-duty vehicle emissions, Environmental science & technology, 35, 4198–4204, 2001.

Kesselmeier, J., Kuhn, U., Wolf, A., Andreae, M., Ciccioli, P., Brancaleoni, E., Frattoni, M., Guenther, A., Greenberg, J., De Castro Vasconcellos, P., de Oliva, T., Tavares, T., and Artaxo, P.: Atmospheric volatile organic compounds (VOC) at a remote tropical forest site in central Amazonia, Atmospheric Environment, 34, 4063 – 4072, https://doi.org/https://doi.org/10.1016/S1352-2310(00)00186-2, URL `http://www.sciencedirect.com/science/article/pii/S1352231000001862`, 2000.

Kesselmeier, J., Kuhn, U., Rottenberger, S., Biesenthal, T., Wolf, A., Schebeske, G., Andreae, M., Ciccioli, P., Brancaleoni, E., Frattoni, M., et al.: Concentrations and species composition of atmospheric volatile organic compounds (VOCs) as observed during the wet and dry season in Rondonia (Amazonia), Journal of Geophysical Research: Atmospheres, 107, LBA–20, 2002.

Kim, D., Cho, C., Jeong, S., Lee, S., Nault, B. A., Campuzano-Jost, P., Day, D. A., Schroder, J. C., Jimenez, J. L., Volkamer, R., et al.: Field observational constraints on the controllers in glyoxal (CHOCHO) reactive uptake to aerosol, Atmospheric Chemistry and Physics, 22, 805–821, 2022.

Kleipool, Q., Ludewig, A., Babić, L., Bartstra, R., Braak, R., Dierssen, W., Dewitte, P.-J., Kenter, P., Landzaat, R., Leloux, J., et al.: Pre-launch calibration results of the TROPOMI payload on-board the Sentinel-5 Precursor satellite, Atmospheric Measurement Techniques, 11, 6439–6479, 2018.

Kloss, C., Sellitto, P., Von Hobe, M., Berthet, G., Smale, D., Krysztofiak, G., Xue, C., Qiu, C., Jégou, F., Ouerghemmi, I., et al.: Australian Fires 2019–2020: Tropospheric and Stratospheric Pollution Throughout the Whole Fire Season, Front, Environ. Sci, 9, 10–3389, 2021.

Kluge, F., Hüneke, T., Knecht, M., Lichtenstern, M., Rotermund, M., Schlager, H., Schreiner, B., and Pfeilsticker, K.: Profiling of formaldehyde, glyoxal, methylglyoxal, and CO over the Amazon: normalized excess mixing ratios and related emission factors in biomass burning plumes, Atmospheric Chemistry and Physics, 20, 12 363–12 389, 2020.

Kluge, F., Hüneke, T., Lerot, C., Rosanka, S., Rotermund, M. K., Taraborrelli, D., Weyland, B., and Pfeilsticker, K.: Airborne glyoxal measurements in the marine and continental atmosphere: Comparison with TROPOMI observations and EMAC simulations, Atmospheric Chemistry and Physics Discussions, 2022, 1–46, https://doi.org/10.5194/acp-2022-416, URL `https://acp.copernicus.org/preprints/acp-2022-416/`, 2022.

Knecht, M.: Simulation of radiative field modification due to tropical clouds, Master thesis, Institut für Umweltphysik, Universität Heidelberg, URL `http://www.iup.uni-heidelberg.de/institut/forschung/groups/atmosphere/stratosphere/publications/pdf/MA_thesis_Matthias_final.pdf`, 2015.

Knote, C., Hodzic, A., Jimenez, J., Volkamer, R., Orlando, J., Baidar, S., Brioude, J., Fast, J., Gentner, D., Goldstein, A., et al.: Simulation of semi-explicit mechanisms of SOA formation from glyoxal in aerosol in a 3-D model, Atmospheric Chemistry and Physics, 14, 6213–6239, 2014.

Koch, S. and Moortgat, G. K.: Photochemistry of methylglyoxal in the vapor phase, The Journal of Physical Chemistry A, 102, 9142–9153, 1998.

Koppmann, R., Bauer, R., Johnen, F., Plass, C., and Rudolph, J.: The distribution of light nonmethane hydrocarbons over the mid-Atlantic: Results of the Polarstern cruise ANT VII/1, Journal of atmospheric chemistry, 15, 215–234, 1992.

Koppmann, R., Von Czapiewski, K., and Reid, J.: A review of biomass burning emissions, part I: gaseous emissions of carbon monoxide, methane, volatile organic compounds, and nitrogen containing compounds, Atmospheric chemistry and physics discussions, 5, 10 455–10 516, 2005.

Krause, D.: JUWELS: Modular Tier-0/1 supercomputer at the Jülich supercomputing centre, Journal of large-scale research facilities JLSRF, 5, 135, 2019.

Krautstrunk, M. and Giez, A.: The transition from FALCON to HALO era airborne atmospheric research, in: Atmospheric physics, pp. 609–624, Springer, 2012.

Kroll, J. H. and Seinfeld, J. H.: Chemistry of secondary organic aerosol: Formation and evolution of low-volatility organics in the atmosphere, Atmospheric Environment, 42, 3593–3624, 2008.

Kroll, J. H., Ng, N. L., Murphy, S. M., Varutbangkul, V., Flagan, R. C., and Seinfeld, J. H.: Chamber studies of secondary organic aerosol growth by reactive uptake of simple carbonyl compounds, Journal of Geophysical Research: Atmospheres, 110, 2005.

Krüger, O. O., Holanda, B. A., Chowdhury, S., Pozzer, A., Walter, D., Pöhlker, C., Andrés Hernández, M. D., Burrows, J. P., Voigt, C., Lelieveld, J., et al.: Black carbon aerosol reductions during COVID-19 confinement quantified by aircraft measurements over Europe, Atmospheric Chemistry and Physics Discussions, pp. 1–36, 2022.

Krysztofiak, G., Catoire, V., Hamer, P. D., Marécal, V., Robert, C., Engel, A., Bönisch, H., Grossmann, K., Quack, B., Atlas, E., and Pfeilsticker, K.: Evidence of convective transport in tropical West Pacific region during SHIVA experiment, Atmospheric Science Letters, 19, e798, https://doi.org/10.1002/asl.798, URL `https://rmets.onlinelibrary.wiley.com/doi/abs/10.1002/asl.798`, 2018.

Kuhn, U., Andreae, M., Ammann, C., Araújo, A., Brancaleoni, E., Ciccioli, P., Dindorf, T., Frattoni, M., Gatti, L., Ganzeveld, L., et al.: Isoprene and monoterpene fluxes from Central Amazonian rainforest inferred from tower-based and airborne measurements, and implications on the atmospheric chemistry and the local carbon budget, Atmospheric Chemistry and Physics, 7, 2855–2879, 2007.

Kunkel, D., Hoor, P., Kaluza, T., Ungermann, J., Kluschat, B., Giez, A., Lachnitt, H.-C., Kaufmann, M., and Riese, M.: Evidence of small-scale quasi-isentropic mixing in ridges of extratropical baroclinic waves, Atmospheric Chemistry and Physics, 19, 12 607–12 630, 2019.

Landau, A., Allin, E. J., and Welsh, H.: The absorption spectrum of solid oxygen in the wavelength region from 12,000 Å to 3300 Å, Spectrochimica Acta, 18, 1–19, 1962.

Lathiere, J., Hauglustaine, D., Friend, A., Noblet-Ducoudré, D., Viovy, N., Folberth, G., et al.: Impact of climate variability and land use changes on global biogenic volatile organic compound emissions, Atmospheric Chemistry and Physics, 6, 2129–2146, 2006.

Lawson, S., Selleck, P., Galbally, I., Keywood, M., Harvey, M., Lerot, C., Helmig, D., and Ristovski, Z.: Seasonal in situ observations of glyoxal and methylglyoxal over the temperate oceans of the Southern Hemisphere, Atmospheric Chemistry and Physics, 15, 223–240, 2015.

Lee, K.-Y., Kwak, K.-H., Ryu, Y.-H., Lee, S.-H., and Baik, J.-J.: Impacts of biogenic isoprene emission on ozone air quality in the Seoul metropolitan area, Atmospheric Environment, 96, 209–219, 2014.

Lee, M., Heikes, B. G., Jacob, D. J., Sachse, G., and Anderson, B.: Hydrogen peroxide, organic hydroperoxide, and formaldehyde as primary pollutants from biomass burning, Journal of Geophysical Research: Atmospheres, 102, 1301–1309, 1997.

Lee, Y.-N., Zhou, X., Kleinman, L., Nunnermacker, L., Springston, S., Daum, P., Newman, L., Keigley, W., Holdren, M., Spicer, C., et al.: Atmospheric chemistry and distribution of formaldehyde and several multioxygenated carbonyl compounds during the 1995 Nashville/Middle Tennessee Ozone Study, Journal of Geophysical Research: Atmospheres, 103, 22 449–22 462, 1998.

Leighton, P.: Photochemistry of air pollution, Elsevier, 1961.

Lelieveld, J., Evans, J. S., Fnais, M., Giannadaki, D., and Pozzer, A.: The contribution of outdoor air pollution sources to premature mortality on a global scale, Nature, 525, 367–371, 2015.

Lelieveld, J., Bourtsoukidis, E., Brühl, C., Fischer, H., Fuchs, H., Harder, H., Hofzumahaus, A., Holland, F., Marno, D., Neumaier, M., et al.: The South Asian monsoon—pollution pump and purifier, Science, 361, 270–273, 2018.

Lelieveld, J., Klingmüller, K., Pozzer, A., Burnett, R., Haines, A., and Ramanathan, V.: Effects of fossil fuel and total anthropogenic emission removal on public health and climate, Proceedings of the National Academy of Sciences, 116, 7192–7197, 2019.

Lerot, C., Stavrakou, T., De Smedt, I., Müller, J.-F., and Van Roozendael, M.: Glyoxal vertical columns from GOME-2 backscattered light measurements and comparisons with a global model, Atmospheric Chemistry and Physics, 10, 12 059–12 072, 2010.

Lerot, C., Hendrick, F., Van Roozendael, M., Alvarado, L., Richter, A., De Smedt, I., Theys, N., Vlietinck, J., Yu, H., Van Gent, J., et al.: Glyoxal tropospheric column retrievals from TROPOMI–multi-satellite intercomparison and ground-based validation, Atmospheric Measurement Techniques, 14, 7775–7807, 2021.

Levelt, P. F., Van Den Oord, G. H., Dobber, M. R., Malkki, A., Visser, H., De Vries, J., Stammes, P., Lundell, J. O., and Saari, H.: The ozone monitoring instrument, IEEE Transactions on geoscience and remote sensing, 44, 1093–1101, 2006.

Levy, H.: Normal atmosphere: Large radical and formaldehyde concentrations predicted, Science, 173, 141–143, 1971.

Li, J., Mao, J., Min, K.-E., Washenfelder, R. A., Brown, S. S., Kaiser, J., Keutsch, F. N., Volkamer, R., Wolfe, G. M., Hanisco, T. F., et al.: Observational constraints on glyoxal production from isoprene oxidation and its contribution to organic aerosol over the Southeast United States, Journal of Geophysical Research: Atmospheres, 121, 9849–9861, 2016.

Liao, J., Hanisco, T. F., Wolfe, G. M., St Clair, J., Jimenez, J. L., Campuzano-Jost, P., Nault, B. A., Fried, A., Marais, E. A., Gonzalez Abad, G., et al.: Towards a satellite formaldehyde–in situ hybrid estimate for organic aerosol abundance, Atmospheric Chemistry and Physics, 19, 2765–2785, 2019.

Liggio, J., Li, S.-M., and McLaren, R.: Heterogeneous reactions of glyoxal on particulate matter: Identification of acetals and sulfate esters, Environmental science & technology, 39, 1532–1541, 2005a.

Liggio, J., Li, S.-M., and McLaren, R.: Reactive uptake of glyoxal by particulate matter, Journal of Geophysical Research: Atmospheres, 110, 2005b.

Lim, C. Y., Hagan, D. H., Coggon, M. M., Koss, A. R., Sekimoto, K., de Gouw, J., Warneke, C., Cappa, C. D., and Kroll, J. H.: Secondary organic aerosol formation from biomass burning emissions, Atmos. Chem. Phys, 19, 12 797–12 809, 2019.

Lim, Y., Tan, Y., and Turpin, B.: Chemical insights, explicit chemistry, and yields of secondary organic aerosol from OH radical oxidation of methylglyoxal and glyoxal in the aqueous phase, Atmospheric Chemistry and Physics, 13, 8651–8667, 2013.

Ling, Z., Xie, Q., Shao, M., Wang, Z., Wang, T., Guo, H., and Wang, X.: Formation and sink of glyoxal and methylglyoxal in a polluted subtropical environment: observation-based photochemical analysis and impact evaluation, Atmospheric Chemistry and Physics, 20, 11 451–11 467, 2020.

Liu, J., Li, X., Li, D., Xu, R., Gao, Y., Chen, S., Liu, Y., Zhao, G., Wang, H., Wang, H., et al.: Observations of glyoxal and methylglyoxal in a suburban area of the Yangtze River Delta, China, Atmospheric Environment, 238, 117 727, 2020.

Liu, J., Li, X., Tan, Z., Wang, W., Yang, Y., Zhu, Y., Yang, S., Song, M., Chen, S., Wang, H., et al.: Assessing the Ratios of Formaldehyde and Glyoxal to NO2 as Indicators of O3–NO x–VOC Sensitivity, Environmental Science & Technology, 55, 10 935–10 945, 2021.

Liu, L., Flatøy, F., Ordóñez, C., Braathen, G. O., Hak, C., Junkermann, W., Andreani-Aksoyoglu, S., Mellqvist, J., Galle, B., Prévôt, A. S. H., and Isaksen, I.: Photochemical modelling in the Po basin with focus on formaldehyde and ozone, Atmospheric Chemistry and Physics, 7, 121–137, URL `https://hal.archives-ouvertes.fr/hal-00296104`, 2007.

Liu, Y., Su, H., Wang, S., Wei, C., Tao, W., Pöhlker, M. L., Pöhlker, C., Holanda, B. A., Krüger, O. O., Hoffmann, T., et al.: Strong particle production and condensational growth in the upper troposphere sustained by biogenic VOCs from the canopy of the Amazon Basin, Atmospheric Chemistry and Physics Discussions, pp. 1–34, 2022.

Liu, Z., Wang, Y., Vrekoussis, M., Richter, A., Wittrock, F., Burrows, J. P., Shao, M., Chang, C.-C., Liu, S.-C., Wang, H., et al.: Exploring the missing source of glyoxal (CHOCHO) over China, Geophysical Research Letters, 39, 2012.

Logan, J. A.: Tropospheric ozone: Seasonal behavior, trends, and anthropogenic influence, Journal of Geophysical Research: Atmospheres, 90, 10 463–10 482, 1985.

Logan, J. A., Prather, M. J., Wofsy, S. C., and McElroy, M. B.: Tropospheric chemistry: A global perspective, Journal of Geophysical Research: Oceans, 86, 7210–7254, 1981.

Ludewig, A., Kleipool, Q., Bartstra, R., Landzaat, R., Leloux, J., Loots, E., Meijering, P., van der Plas, E., Rozemeijer, N., Vonk, F., et al.: In-flight calibration results of the TROPOMI payload on board the Sentinel-5 Precursor satellite, Atmospheric Measurement Techniques, 13, 3561–3580, 2020.

Luecken, D., Hutzell, W., Strum, M., and Pouliot, G.: Regional sources of atmospheric formaldehyde and acetaldehyde, and implications for atmospheric modeling, Atmospheric Environment, 47, 477–490, 2012.

Lv, S., Gong, D., Ding, Y., Lin, Y., Wang, H., Ding, H., Wu, G., He, C., Zhou, L., Liu, S., et al.: Elevated levels of glyoxal and methylglyoxal at a remote mountain site in southern China: Prompt in-situ formation combined with strong regional transport, Science of the Total Environment, 672, 869–882, 2019.

MacDonald, S., Oetjen, H., Mahajan, A., Whalley, L., Edwards, P., Heard, D., Jones, C., and Plane, J.: DOAS measurements of formaldehyde and glyoxal above a south-east Asian tropical rainforest, Atmospheric Chemistry and Physics, 12, 5949–5962, 2012.

Magneron, I., Thevenet, R., Mellouki, A., Le Bras, G., Moortgat, G., and Wirtz, K.: A study of the photolysis and OH-initiated oxidation of acrolein and trans-crotonaldehyde, The Journal of Physical Chemistry A, 106, 2526–2537, 2002.

Mahajan, A. S., Prados-Roman, C., Hay, T. D., Lampel, J., Pöhler, D., Groβmann, K., Tschritter, J., Frieß, U., Platt, U., Johnston, P., et al.: Glyoxal observations in the global marine boundary layer, Journal of Geophysical Research: Atmospheres, 119, 6160–6169, 2014.

Mahilang, M., Deb, M. K., and Pervez, S.: Biogenic secondary organic aerosols: A review on formation mechanism, analytical challenges and environmental impacts, Chemosphere, 262, 127 771, 2021.

McCormick, R. A. and Ludwig, J. H.: Climate modification by atmospheric aerosols, Science, 156, 1358–1359, 1967.

McDonald, B. C., De Gouw, J. A., Gilman, J. B., Jathar, S. H., Akherati, A., Cappa, C. D., Jimenez, J. L., Lee-Taylor, J., Hayes, P. L., McKeen, S. A., et al.: Volatile chemical products emerging as largest petrochemical source of urban organic emissions, Science, 359, 760–764, 2018.

McDonald, J. D., Zielinska, B., Fujita, E. M., Sagebiel, J. C., Chow, J. C., and Watson, J. G.: Fine Particle and Gaseous Emission Rates from Residential Wood Combustion, Environmental Science & Technology, 34, 2080–2091, https://doi.org/10.1021/es9909632, URL `https://doi.org/10.1021/es9909632`, 2000.

Meller, R., Raber, W., Crowley, J., Jenkin, M., and Moortgat, G.: The UV-visible absorption spectrum of methylglyoxal, Journal of Photochemistry and Photobiology A: Chemistry, 62, 163–171, 1991.

Meteorology, W.: A Three-Dimensional Science: Second Session of the Commission for Aerology, WMO bull, 6, 137, 1957.

Michoud, V., Sauvage, S., Léonardis, T., Fronval, I., Kukui, A., Locoge, N., and Dusanter, S.: Field measurements of methylglyoxal using proton transfer reaction time-of-flight mass spectrometry and comparison to the DNPH–HPLC–UV method, Atmospheric Measurement Techniques, 11, 5729–5740, https://doi.org/10.5194/amt-11-5729-2018, URL `https://www.atmos-meas-tech.net/11/5729/2018/`, 2018.

Miller, W. L. and Moran, M. A.: Interaction of photochemical and microbial processes in the degradation of refractory dissolved organic matter from a coastal marine environment, Limnology and Oceanography, 42, 1317–1324, 1997.

Millet, D. B., Guenther, A., Siegel, D. A., Nelson, N. B., Singh, H. B., de Gouw, J. A., Warneke, C., Williams, J., Eerdekens, G., Sinha, V., et al.: Global atmospheric budget of acetaldehyde: 3-D model analysis and constraints from in-situ and satellite observations, Atmospheric Chemistry and Physics, 10, 3405–3425, 2010.

Min, K.-E., Washenfelder, R., Dubé, W., Langford, A., Edwards, P., Zarzana, K., Stutz, J., Lu, K., Rohrer, F., Zhang, Y., et al.: A broadband cavity enhanced absorption spectrometer for aircraft measurements of glyoxal, methylglyoxal, nitrous acid, nitrogen dioxide, and water vapor, Atmospheric Measurement Techniques, 9, 423–440, 2016.

Mitsuishi, K., Iwasaki, M., Takeuchi, M., Okochi, H., Kato, S., Ohira, S.-I., and Toda, K.: Diurnal variations in partitioning of atmospheric glyoxal and methylglyoxal between gas and particles at the ground level and in the free troposphere, ACS Earth and Space Chemistry, 2, 915–924, 2018.

Monks, P. S.: Gas-phase radical chemistry in the troposphere, Chemical Society Reviews, 34, 376–395, 2005.

Monks, P. S., Archibald, A., Colette, A., Cooper, O., Coyle, M., Derwent, R., Fowler, D., Granier, C., Law, K. S., Mills, G., et al.: Tropospheric ozone and its precursors from the urban to the global scale from air quality to short-lived climate forcer, Atmospheric Chemistry and Physics, 15, 8889–8973, 2015.

Moule, D. and Walsh, A.: Ultraviolet spectra and excited states of formaldehyde, Chemical Reviews, 75, 67–84, 1975.

Müller, J.-F. and Brasseur, G.: IMAGES: A three-dimensional chemical transport model of the global troposphere, Journal of Geophysical Research: Atmospheres, 100, 16 445–16 490, 1995.

Müller, M., Anderson, B. E., Beyersdorf, A. J., Crawford, J. H., Diskin, G. S., Eichler, P., Fried, A., Keutsch, F. N., Mikoviny, T., Thornhill, K. L., et al.: In situ measurements and modeling of reactive trace gases in a small biomass burning plume, Atmospheric Chemistry and Physics, 16, 3813–3824, 2016.

Müller, S., Hoor, P., Berkes, F., Bozem, H., Klingebiel, M., Reutter, P., Smit, H., Wendisch, M., Spichtinger, P., and Borrmann, S.: In situ detection of stratosphere-troposphere exchange of cirrus particles in the midlatitudes, Geophysical research letters, 42, 949–955, 2015.

Munger, J. W., Jacob, D. J., Daube, B. C., Horowitz, L., Keene, W., and Heikes, B. G.: Formaldehyde, glyoxal, and methylglyoxal in air and cloudwater at a rural mountain site in central Virginia, Journal of Geophysical Research: Atmospheres, 100, 9325–9333, 1995.

Munro, R., Lang, R., Klaes, D., Poli, G., Retscher, C., Lindstrot, R., Huckle, R., Lacan, A., Grzegorski, M., Holdak, A., et al.: The GOME-2 instrument on the Metop series of satellites: instrument design, calibration, and level 1 data processing–an overview, Atmospheric Measurement Techniques, 9, 1279–1301, 2016.

Myriokefalitakis, S., Vrekoussis, M., Tsigaridis, K., Wittrock, F., Richter, A., Brühl, C., Volkamer, R., Burrows, J., and Kanakidou, M.: The influence of natural and anthropogenic secondary sources on the glyoxal global distribution, Atmospheric Chemistry and Physics, 8, 4965–4981, 2008.

Newland, M. J., Mouchel-Vallon, C., Valorso, R., Aumont, B., Vereecken, L., Jenkin, M. E., and Rickard, A. R.: Estimation of mechanistic parameters in the gas-phase reactions of ozone with alkenes for use in automated mechanism construction, Atmospheric Chemistry and Physics, 22, 6167–6195, 2022.

Nishino, N., Arey, J., and Atkinson, R.: Formation yields of glyoxal and methylglyoxal from the gas-phase OH radical-initiated reactions of toluene, xylenes, and trimethylbenzenes as a function of NO2 concentration, The Journal of Physical Chemistry A, 114, 10 140–10 147, 2010.

Nölscher, A., Butler, T., Auld, J., Veres, P., Muñoz, A., Taraborrelli, D., Vereecken, L., Lelieveld, J., and Williams, J.: Using total OH reactivity to assess isoprene photooxidation via measurement and model, Atmospheric Environment, 89, 453–463, 2014.

Novakov, T. and Penner, J.: Large contribution of organic aerosols to cloud-condensation-nuclei concentrations, Nature, 365, 823–826, 1993.

Novelli, A., Vereecken, L., Bohn, B., Dorn, H.-P., Gkatzelis, G. I., Hofzumahaus, A., Holland, F., Reimer, D., Rohrer, F., Rosanka, S., et al.: Importance of isomerization reactions for OH radical regeneration from the photo-oxidation of isoprene investigated in the atmospheric simulation chamber SAPHIR, Atmospheric Chemistry and Physics, 20, 3333–3355, 2020.

Opacka, B. and Müller, J.: MEGAN-MOHYCAN global isoprene emissions accounting for space-based land cover changes [ALBERI dataset][Data set]. Royal Belgian Institute for Space Aeronomy (BIRA-IASB), Brussels, Belgium, https://doi.org/https://doi.org/10.18758/71021062, 2021.

Orlando, J. J. and Tyndall, G. S.: Laboratory studies of organic peroxy radical chemistry: an overview with emphasis on recent issues of atmospheric significance, Chemical Society Reviews, 41, 6294–6317, 2012.

Ostro, B. and Chestnut, L.: Assessing the health benefits of reducing particulate matter air pollution in the United States, Environmental research, 76, 94–106, 1998.

P.A. Arias, e. a.: Technical Summary. In Climate Change 2021: The Physical Science Basis. Contribution of Working Group I to the Sixth Assessment Report of the Intergovernmental Panel on Climate Change, https://doi.org/doi:10.1017/9781009157896.002, 2021.

Palm, B. B., Peng, Q., Fredrickson, C. D., Lee, B. H., Garofalo, L. A., Pothier, M. A., Kreidenweis, S. M., Farmer, D. K., Pokhrel, R. P., Shen, Y., et al.: Quantification of organic aerosol and brown carbon evolution in fresh wildfire plumes, Proceedings of the National Academy of Sciences, 117, 29 469–29 477, 2020.

Palmer, P. I., Jacob, D. J., Chance, K., Martin, R. V., Spurr, R. J., Kurosu, T. P., Bey, I., Yantosca, R., Fiore, A., and Li, Q.: Air mass factor formulation for spectroscopic measurements from satellites: Application to formaldehyde retrievals from the Global Ozone Monitoring Experiment, Journal of Geophysical Research: Atmospheres, 106, 14 539–14 550, 2001.

Palmer, P. I., Jacob, D. J., Fiore, A. M., Martin, R. V., Chance, K., and Kurosu, T. P.: Mapping isoprene emissions over North America using formaldehyde column observations from space, Journal of Geophysical Research: Atmospheres, 108, 2003.

Palmer, P. I., Abbot, D. S., Fu, T.-M., Jacob, D. J., Chance, K., Kurosu, T. P., Guenther, A., Wiedinmyer, C., Stanton, J. C., Pilling, M. J., et al.: Quantifying the seasonal and interannual variability of North American isoprene emissions using satellite observations of the formaldehyde column, Journal of Geophysical Research: Atmospheres, 111, 2006.

Pandis, S. N., Paulson, S. E., Seinfeld, J. H., and Flagan, R. C.: Aerosol formation in the photooxidation of isoprene and β-pinene, Atmospheric Environment. Part A. General Topics, 25, 997–1008, 1991.

Parrish, D., Murphy, P., Albritton, D., and Fehsenfeld, F.: The measurement of the photodissociation rate of NO2 in the atmosphere, Atmospheric Environment (1967), 17, 1365–1379, 1983.

Parrish, D., Ryerson, T., Mellqvist, J., Johansson, J., Fried, A., Richter, D., Walega, J., Washenfelder, R. d., De Gouw, J., Peischl, J., et al.: Primary and secondary sources of formaldehyde in urban atmospheres: Houston Texas region, Atmospheric Chemistry and Physics, 12, 3273–3288, 2012.

Paulot, F., Henze, D., and Wennberg, P.: Impact of the isoprene photochemical cascade on tropical ozone, Atmospheric Chemistry and Physics, 12, 1307–1325, 2012.

Peters, E., Wittrock, F., Großmann, K., Frieß, U., Richter, A., and Burrows, J. P.: Formaldehyde and nitrogen dioxide over the remote western Pacific Ocean: SCIAMACHY and GOME-2 validation using ship-based MAX-DOAS observations, Atmospheric Chemistry and Physics, 12, 11 179–11 197, https://doi.org/10.5194/acp-12-11179-2012, URL `https://www.atmos-chem-phys.net/12/11179/2012/`, 2012.

Pfeilsticker, K., Bösch, H., Camy-Peyret, C., Fitzenberger, R., Harder, H., and Osterkamp, H.: First atmospheric profile measurements of UV/visible O4 absorption band intensities: Implications for the spectroscopy, and the formation enthalpy of the O2-O2 dimer, Geophysical research letters, 28, 4595–4598, 2001.

Pfister, G., Emmons, L., Hess, P., Lamarque, J.-F., Orlando, J., Walters, S., Guenther, A., Palmer, P., and Lawrence, P.: Contribution of isoprene to chemical budgets: A model tracer study with the NCAR CTM MOZART-4, Journal of Geophysical Research: Atmospheres, 113, 2008.

Platt, U. and Stutz, J.: Differential Optical Absorption Spectroscopy (DOAS), Principle and Applications, no. ISBN 978-3-642-05946-9 in ISSN 1610-1677, Springer Verlag, Heidelberg, https://doi.org/10.1007/978-3-540-75776-40, 2008.

Plum, C. N., Sanhueza, E., Atkinson, R., Carter, W. P., and Pitts, J. N.: Hydroxyl radical rate constants and photolysis rates of. alpha.-dicarbonyls, Environmental Science & Technology, 17, 479–484, 1983.

Polyansky, O. L., Kyuberis, A. A., Zobov, N. F., Tennyson, J., Yurchenko, S. N., and Lodi, L.: ExoMol molecular line lists XXX: a complete high-accuracy line list for water, Monthly Notices of the Royal Astronomical Society, 480, 2597–2608, 2018.

Pope, R. M. and Fry, E. S.: Absorption spectrum (380–700 nm) of pure water. II. Integrating cavity measurements, Applied optics, 36, 8710–8723, 1997.

Pöschl, U., Williams, J., Hoor, P., Fischer, H., Crutzen, P., Warneke, C., Holzinger, R., Hansel, A., Jordan, A., Lindinger, W., Scheeren, H. A., Peters, W., and Lelieveld, J.: High acetone concentrations throughout the 0–12 km altitude range over the tropical rainforest in Surinam, Journal of atmospheric chemistry, 38, 115–132, 2001.

Pozzer, A., Jöckel, P., Sander, R., Williams, J., Ganzeveld, L., and Lelieveld, J.: The MESSy-submodel AIRSEA calculating the air-sea exchange of chemical species, Atmospheric Chemistry and Physics, 6, 5435–5444, 2006.

Pozzer, A., Jöckel, P., and Van Aardenne, J.: The influence of the vertical distribution of emissions on tropospheric chemistry, Atmospheric Chemistry and physics, 9, 9417–9432, 2009.

Pozzer, A., Reifenberg, S. F., Kumar, V., Franco, B., Kohl, M., Taraborrelli, D., Gromov, S., Ehrhart, S., Jöckel, P., Sander, R., et al.: Simulation of organics in the atmosphere: evaluation of EMACv2. 54 with the Mainz Organic Mechanism (MOM) coupled to the ORACLE (v1. 0) submodel, Geoscientific Model Development, 15, 2673–2710, 2022.

Radke, L. F., Hegg, D. A., Hobbs, P. V., Nance, J. D., Lyons, J. H., Laursen, K. K., Weiss, R. E., Riggan, P. J., and Ward, D. E.: Particulate and trace gas emissions from large biomass fire in North America, In Levine, JS (ed.) Global Biomass Burning: Atmospheric, Climatic, and Biospheric Implications. The MIT Press, Cambridge, Massachusetts. pp. 209-216, pp. 209–216, 1991.

Rapp, M., Kaifler, B., Dörnbrack, A., Gisinger, S., Mixa, T., Reichert, R., Kaifler, N., Knobloch, S., Eckert, R., Wildmann, N., et al.: SOUTHTRAC-GW: An airborne field campaign to explore gravity wave dynamics at the world's strongest hotspot, Bulletin of the American Meteorological Society, 102, E871–E893, 2021.

re3data.org: HALO database; editing status 2021-11-17; re3data.org - Registry of Research Data Repositories., https://doi.org/http://doi.org/10.17616/R39Q0T, 2022.

Reid, J., Koppmann, R., Eck, T., and Eleuterio, D.: A review of biomass burning emissions part II: intensive physical properties of biomass burning particles, Atmospheric chemistry and physics, 5, 799–825, 2005.

Rinaldi, M., Decesari, S., Carbone, C., Finessi, E., Fuzzi, S., Ceburnis, D., O'Dowd, C. D., Sciare, J., Burrows, J. P., Vrekoussis, M., et al.: Evidence of a natural marine source of oxalic acid and a possible link to glyoxal, Journal of Geophysical Research: Atmospheres, 116, 2011.

Rizzo, L., Artaxo, P., Karl, T., Guenther, A., and Greenberg, J.: Aerosol properties, in-canopy gradients, turbulent fluxes and VOC concentrations at a pristine forest site in Amazonia, Atmospheric Environment, 44, 503–511, 2010.

Rocco, M., Dunne, E., Peltola, M., Barr, N., Williams, J., Colomb, A., Safi, K., Saint-Macary, A., Marriner, A., Deppeler, S., et al.: Oceanic phytoplankton are a potentially important source of benzenoids to the remote marine atmosphere, Communications Earth & Environment, 2, 1–8, 2021.

Roeckner, E., Bäuml, G., Bonaventura, L., Brokopf, R., Esch, M., Giorgetta, M., Hagemann, S., Kirchner, I., Kornblueh, L., Manzini, E., et al.: The atmospheric general circulation model ECHAM 5. PART I: Model description, 2003.

Roelofs, G.-J. and Lelieveld, J.: Tropospheric ozone simulation with a chemistry-general circulation model: Influence of higher hydrocarbon chemistry, Journal of Geophysical Research: Atmospheres, 105, 22 697–22 712, 2000.

Rolph, G., Stein, A., and Stunder, B.: Real-time environmental applications and display system: READY, Environmental Modelling & Software, 95, 210–228, 2017.

Rosanka, S., Vu, G. H., Nguyen, H. M., Pham, T. V., Javed, U., Taraborrelli, D., and Vereecken, L.: Atmospheric chemical loss processes of isocyanic acid (HNCO): a combined theoretical kinetic and global modelling study, Atmospheric Chemistry and Physics, 20, 6671–6686, 2020.

Rosanka, S., Sander, R., Franco, B., Wespes, C., Wahner, A., and Taraborrelli, D.: Oxidation of low-molecular-weight organic compounds in cloud droplets: global impact on tropospheric oxidants, Atmospheric chemistry and physics, 21, 9909–9930, 2021a.

Rosanka, S., Sander, R., Wahner, A., and Taraborrelli, D.: Oxidation of low-molecular-weight organic compounds in cloud droplets: development of the Jülich Aqueous-phase Mechanism of Organic Chemistry (JAMOC) in CAABA/MECCA (version 4.5. 0), Geoscientific Model Development, 14, 4103–4115, 2021b.

Rotermund, M. K., Bense, V., Chipperfield, M. P., Engel, A., Grooß, J.-U., Hoor, P., Hüneke, T., Keber, T., Kluge, F., Schreiner, B., et al.: Organic and inorganic bromine measurements around the extratropical tropopause and lowermost stratosphere: Insights into the transport pathways and total bromine, Atmospheric Chemistry and Physics, 21, 15 375–15 407, 2021.

Rothman, L. S., Gordon, I. E., Barbe, A., Benner, D. C., Bernath, P. F., Birk, M., Boudon, V., Brown, L. R., Campargue, A., Champion, J.-P., et al.: The HITRAN 2008 molecular spectroscopic database, Journal of Quantitative Spectroscopy and Radiative Transfer, 110, 533–572, 2009.

Sander, R.: Compilation of Henry's law constants (version 4.0) for water as solvent, Atmospheric Chemistry and Physics, 15, 4399–4981, 2015.

Sander, R., Baumgaertner, A., Cabrera-Perez, D., Frank, F., Gromov, S., Grooß, J.-U., Harder, H., Huijnen, V., Jöckel, P., Karydis, V. A., et al.: The community atmospheric chemistry box model CAABA/MECCA-4.0, Geoscientific model development, 12, 1365–1385, 2019.

Saunders, S. M., Jenkin, M. E., Derwent, R., and Pilling, M.: Protocol for the development of the Master Chemical Mechanism, MCM v3 (Part A): tropospheric degradation of non-aromatic volatile organic compounds, Atmospheric Chemistry and Physics, 3, 161–180, 2003.

Schaefer, T., Van Pinxteren, D., and Herrmann, H.: Multiphase chemistry of glyoxal: Revised kinetics of the alkyl radical reaction with molecular oxygen and the reaction of glyoxal with OH, NO3, and SO4–in aqueous solution, Environmental Science & Technology, 49, 343–350, 2015.

Schulz, C., Schneider, J., Amorim Holanda, B., Appel, O., Costa, A., Sá, S. S. d., Dreiling, V., Fütterer, D., Jurkat-Witschas, T., Klimach, T., et al.: Aircraft-based observations of isoprene-epoxydiol-derived secondary organic aerosol (IEPOX-SOA) in the tropical upper troposphere over the Amazon region, Atmospheric Chemistry and Physics, 18, 14 979–15 001, 2018.

Seiler, W. and Crutzen, P. J.: Estimates of gross and net fluxes of carbon between the biosphere and the atmosphere from biomass burning, Climatic change, 2, 207–247, 1980.

Seinfeld, J. H. and Pandis, S. N.: Atmospheric chemistry and physics : from air pollution to climate change, ISBN 9780471720171, J. Wiley & Sons, Inc., third edition edn., 2013.

Seinfeld, J. H., Bretherton, C., Carslaw, K. S., Coe, H., DeMott, P. J., Dunlea, E. J., Feingold, G., Ghan, S., Guenther, A. B., Kahn, R., et al.: Improving our fundamental understanding of the role of aerosol- cloud interactions in the climate system, Proceedings of the National Academy of Sciences, 113, 5781–5790, 2016.

Serdyuchenko, A., Gorshelev, V., Weber, M., Chehade, W., and Burrows, J. P.: High spectral resolution ozone absorption cross-sections–Part 2: Temperature dependence, Atmospheric Measurement Techniques, 7, 625–636, 2014.

Shi, Y., Zang, S., Matsunaga, T., and Yamaguchi, Y.: A multi-year and high-resolution inventory of biomass burning emissions in tropical continents from 2001–2017 based on satellite observations, Journal of Cleaner Production, 270, 122 511, 2020.

Sillman, S.: The relation between ozone, NOx and hydrocarbons in urban and polluted rural environments, Atmospheric Environment, 33, 1821–1845, 1999.

Sillman, S. and He, D.: Some theoretical results concerning O3-NOx-VOC chemistry and NOx-VOC indicators, Journal of Geophysical Research: Atmospheres, 107, ACH–26, 2002.

Sillman, S., Logan, J. A., and Wofsy, S. C.: The sensitivity of ozone to nitrogen oxides and hydrocarbons in regional ozone episodes, Journal of Geophysical Research: Atmospheres, 95, 1837–1851, 1990.

Silva, S. J., Heald, C. L., and Li, M.: Space-Based Constraints on Terrestrial Glyoxal Production, Journal of Geophysical Research: Atmospheres, 123, 13–583, 2018.

Sindelarova, K., Granier, C., Bouarar, I., Guenther, A., Tilmes, S., Stavrakou, T., Müller, J.-F., Kuhn, U., Stefani, P., and Knorr, W.: Global data set of biogenic VOC emissions calculated by the MEGAN model over the last 30 years, Atmospheric Chemistry and Physics, 14, 9317–9341, 2014.

Sinreich, R., Coburn, S., Dix, B., and Volkamer, R.: Ship-based detection of glyoxal over the remote tropical Pacific Ocean, Atmospheric Chemistry and Physics, 10, 11 359–11 371, 2010.

Sitch, S., Cox, P., Collins, W., and Huntingford, C.: Indirect radiative forcing of climate change through ozone effects on the land-carbon sink, Nature, 448, 791–794, 2007.

Situ, S., Guenther, A., Wang, X., Jiang, X., Turnipseed, A., Wu, Z., and Bai, J.: Impacts of seasonal and regional variability in biogenic VOC emissions on surface ozone in the Pearl River delta region, China, Atmospheric Chemistry and Physics, 13, 11 803–11 817, 2013.

Sporre, M. K., Blichner, S. M., Karset, I. H., Makkonen, R., and Berntsen, T. K.: BVOC–aerosol–climate feedbacks investigated using NorESM, Atmospheric Chemistry and Physics, 19, 4763–4782, 2019.

Spurr, R. and Christi, M.: The LIDORT and VLIDORT linearized scalar and vector discrete ordinate radiative transfer models: Updates in the last 10 years, in: Springer series in light scattering, pp. 1–62, Springer, 2019.

Stavrakou, T., Müller, J.-F., De Smedt, I., Van Roozendael, M., Kanakidou, M., Vrekoussis, M., Wittrock, F., Richter, A., and Burrows, J.: The continental source of glyoxal estimated by the synergistic use of spaceborne measurements and inverse modelling, Atmospheric Chemistry and Physics, 9, 8431–8446, 2009a.

Stavrakou, T., Müller, J.-F., De Smedt, I., Van Roozendael, M., Van Der Werf, G., Giglio, L., and Guenther, A.: Evaluating the performance of pyrogenic and biogenic emission inventories against one decade of space-based formaldehyde columns, Atmospheric Chemistry and Physics, 9, 1037–1060, 2009b.

Stavrakou, T., Müller, J.-F., Bauwens, M., De Smedt, I., Lerot, C., Van Roozendael, M., Coheur, P.-F., Clerbaux, C., Boersma, K., Van Der A, R., et al.: Substantial underestimation of post-harvest burning emissions in the North China Plain revealed by multi-species space observations, Scientific Reports, 6, 1–11, 2016.

Steck, T., Glatthor, N., von Clarmann, T., Fischer, H., Flaud, J. M., Funke, B., Grabowski, U., Höpfner, M., Kellmann, S., Linden, A., Perrin, A., and Stiller, G. P.: Retrieval of global upper tropospheric and stratospheric formaldehyde (H_2CO) distributions from high-resolution MIPAS-Envisat spectra, Atmospheric Chemistry and Physics, 8, 463–470, https://doi.org/10.5194/acp-8-463-2008, URL `https://www.atmos-chem-phys.net/8/463/2008/`, 2008.

Stein, A., Draxler, R. R., Rolph, G. D., Stunder, B. J., Cohen, M., and Ngan, F.: NOAA's HYSPLIT atmospheric transport and dispersion modeling system, Bulletin of the American Meteorological Society, 96, 2059–2077, 2015.

Stevenson, D., Young, P., Naik, V., Lamarque, J.-F., Shindell, D. T., Voulgarakis, A., Skeie, R. B., Dalsoren, S. B., Myhre, G., Berntsen, T. K., et al.: Tropospheric ozone changes, radiative forcing and attribution to emissions in the Atmospheric Chemistry and Climate Model Intercomparison Project (ACCMIP), Atmospheric Chemistry and Physics, 13, 3063–3085, 2013.

Stockwell, C., Veres, P., Williams, J., and Yokelson, R.: Characterization of biomass burning emissions from cooking fires, peat, crop residue, and other fuels with high-resolution proton-transfer-reaction time-of-flight mass spectrometry, Atmospheric Chemistry and Physics, 15, 845–865, 2015.

Stutz, J., Werner, B., Spolaor, M., Scalone, L., Festa, J., Tsai, C., Cheung, R., Colosimo, S. F., Tricoli, U., Raecke, R., et al.: A new Differential Optical Absorption Spectroscopy instrument to study atmospheric chemistry from a high-altitude unmanned aircraft, Atmospheric Measurement Techniques, 10, 1017–1042, 2017.

Tadic, I., Parchatka, U., Königstedt, R., and Fischer, H.: In-flight stability of quantum cascade laser-based infrared absorption spectroscopy measurements of atmospheric carbon monoxide, Applied Physics B, 123, 1–9, 2017.

Tadić, J., Moortgat, G. K., and Wirtz, K.: Photolysis of glyoxal in air, Journal of Photochemistry and Photobiology A: Chemistry, 177, 116–124, 2006.

Tagaris, E., Sotiropoulou, R., Gounaris, N., Andronopoulos, S., and Vlachogiannis, D.: Impact of biogenic emissions on ozone and fine particles over Europe: Comparing effects of temperature increase and a potential anthropogenic NOx emissions abatement strategy, Atmospheric Environment, 98, 214–223, 2014.

Tan, Z., Lu, K., Dong, H., Hu, M., Li, X., Liu, Y., Lu, S., Shao, M., Su, R., Wang, H., et al.: Explicit diagnosis of the local ozone production rate and the ozone-NOx-VOC sensitivities, Science bulletin, 63, 1067–1076, 2018.

Taraborrelli, D., Lawrence, M., Butler, T., Sander, R., and Lelieveld, J.: Mainz Isoprene Mechanism 2 (MIM2): an isoprene oxidation mechanism for regional and global atmospheric modelling, Atmospheric Chemistry and Physics, 9, 2751–2777, 2009.

Taraborrelli, D., Lawrence, M. G., Crowley, J., Dillon, T., Gromov, S., Groß, C., Vereecken, L., and Lelieveld, J.: Hydroxyl radical buffered by isoprene oxidation over tropical forests, Nature Geoscience, 5, 190–193, 2012.

Taraborrelli, D., Cabrera-Perez, D., Bacer, S., Gromov, S., Lelieveld, J., Sander, R., and Pozzer, A.: Influence of aromatics on tropospheric gas-phase composition, Atmospheric Chemistry and Physics, 21, 2615–2636, 2021.

Thalman, R. and Volkamer, R.: Temperature dependent absorption cross-sections of O 2–O 2 collision pairs between 340 and 630 nm and at atmospherically relevant pressure, Physical chemistry chemical physics, 15, 15 371–15 381, 2013.

Thalman, R., Baeza-Romero, M. T., Ball, S. M., Borrás, E., Daniels, M. J. S., Goodall, I. C. A., Henry, S. B., Karl, T., Keutsch, F. N., Kim, S., Mak, J., Monks, P. S., Muñoz, A., Orlando, J., Peppe, S., Rickard, A. R., Ródenas, M., Sánchez, P., Seco, R., Su, L., Tyndall, G., Vázquez, M., Vera, T., Waxman, E., and Volkamer, R.: Instrument intercomparison of glyoxal, methyl glyoxal and NO_2 under simulated atmospheric conditions, Atmospheric Measurement Techniques, 8, 1835–1862, https://doi.org/10.5194/amt-8-1835-2015, URL `https://www.atmos-meas-tech.net/8/1835/2015/`, 2015.

Theys, N., Volkamer, R., Müller, J.-F., Zarzana, K. J., Kille, N., Clarisse, L., De Smedt, I., Lerot, C., Finkenzeller, H., Hendrick, F., et al.: Global nitrous acid emissions and levels of regional oxidants enhanced by wildfires, Nature geoscience, 13, 681–686, 2020.

Thomas, W., Hegels, E., Slijkhuis, S., Spurr, R., and Chance, K.: Detection of biomass burning combustion products in Southeast Asia from backscatter data taken by the GOME spectrometer, Geophysical Research Letters, 25, 1317–1320, 1998.

Thuillier, G., Hersé, M., Simon, P., Labs, D., Mandel, H., and Gillotay, D.: Solar Radiometry and Solar Spectral Irradiance-Observation of the solar spectral irradiance from 200 nm to 870 nm during the ATLAS 1 and ATLAS 2 missions by the SOLSPEC spectrometer, Metrologia-Sevres, 35, 689–696, 1998.

Tost, H., Jöckel, P., Kerkweg, A., Sander, R., and Lelieveld, J.: A new comprehensive SCAVenging submodel for global atmospheric chemistry modelling, Atmospheric Chemistry and Physics, 6, 565–574, 2006.

Tost, H., Jöckel, P., Kerkweg, A., Pozzer, A., Sander, R., and Lelieveld, J.: Global cloud and precipitation chemistry and wet deposition: tropospheric model simulations with ECHAM5/MESSy1, Atmospheric Chemistry and Physics, 7, 2733–2757, 2007.

Twomey, S.: Pollution and the planetary albedo, Atmospheric Environment (1967), 8, 1251–1256, 1974.

Twomey, S. A., Piepgrass, M., and Wolfe, T.: An assessment of the impact of pollution on global cloud albedo, Tellus B, 36, 356–366, 1984.

Van Der Werf, G. R., Randerson, J. T., Collatz, G. J., Giglio, L., Kasibhatla, P. S., Arellano Jr, A. F., Olsen, S. C., and Kasischke, E. S.: Continental-scale partitioning of fire emissions during the 1997 to 2001 El Nino/La Nina period, Science, 303, 73–76, 2004.

Van Dingenen, R., Dentener, F. J., Raes, F., Krol, M. C., Emberson, L., and Cofala, J.: The global impact of ozone on agricultural crop yields under current and future air quality legislation, Atmospheric Environment, 43, 604–618, 2009.

Vandaele, A. C., Hermans, C., Simon, P. C., Carleer, M., Colin, R., Fally, S., Merienne, M.-F., Jenouvrier, A., and Coquart, B.: Measurements of the NO2 absorption cross-section from 42 000 cm- 1 to 10 000 cm- 1 (238–1000 nm) at 220 K and 294 K, Journal of Quantitative Spectroscopy and Radiative Transfer, 59, 171–184, 1998.

Veefkind, J., Aben, I., McMullan, K., Förster, H., De Vries, J., Otter, G., Claas, J., Eskes, H., De Haan, J., Kleipool, Q., et al.: TROPOMI on the ESA Sentinel-5 Precursor: A GMES mission for global observations of the atmospheric composition for climate, air quality and ozone layer applications, Remote sensing of environment, 120, 70–83, 2012.

Volkamer, R., Platt, U., and Wirtz, K.: Primary and secondary glyoxal formation from aromatics: experimental evidence for the bicycloalkyl- radical pathway from benzene, toluene, and p-xylene, The Journal of Physical Chemistry A, 105, 7865–7874, 2001.

Volkamer, R., Molina, L. T., Molina, M. J., Shirley, T., and Brune, W. H.: DOAS measurement of glyoxal as an indicator for fast VOC chemistry in urban air, Geophysical Research Letters, 32, 2005a.

Volkamer, R., Spietz, P., Burrows, J., and Platt, U.: High-resolution absorption cross-section of glyoxal in the UV–vis and IR spectral ranges, Journal of Photochemistry and Photobiology A: Chemistry, 172, 35–46, 2005b.

Volkamer, R., Jimenez, J. L., San Martini, F., Dzepina, K., Zhang, Q., Salcedo, D., Molina, L. T., Worsnop, D. R., and Molina, M. J.: Secondary organic aerosol formation from anthropogenic air pollution: Rapid and higher than expected, Geophysical Research Letters, 33, 2006.

Volkamer, R., San Martini, F., Molina, L. T., Salcedo, D., Jimenez, J. L., and Molina, M. J.: A missing sink for gas-phase glyoxal in Mexico City: Formation of secondary organic aerosol, Geophysical Research Letters, 34, 2007.

Volkamer, R., Baidar, S., Campos, T. L., Coburn, S., DiGangi, J. P., Dix, B., Eloranta, E. W., Koenig, T. K., Morley, B., Ortega, I., et al.: Aircraft measurements of BrO, IO, glyoxal, NO 2, H 2 O, O 2–O 2 and aerosol extinction profiles in the tropics: Comparison with aircraft-/ship-based in situ and lidar measurements, Atmospheric Measurement Techniques, 8, 2121–2148, 2015.

Vrekoussis, M., Wittrock, F., Richter, A., and Burrows, J.: Temporal and spatial variability of glyoxal as observed from space, Atmospheric Chemistry and Physics, 9, 4485–4504, 2009.

Vrekoussis, M., Wittrock, F., Richter, A., and Burrows, J.: GOME-2 observations of oxygenated VOCs: what can we learn from the ratio glyoxal to formaldehyde on a global scale?, Atmospheric Chemistry and Physics, 10, 10 145–10 160, 2010.

Wagner, V., von Glasow, R., Fischer, H., and Crutzen, P. J.: Are CH2O measurements in the marine boundary layer suitable for testing the current understanding of CH4 photooxidation?: A model study, Journal of Geophysical Research: Atmospheres, 107, ACH 3–1–ACH 3–14, https://doi.org/10.1029/2001JD000722, URL `https://agupubs.onlinelibrary.wiley.com/doi/abs/10.1029/2001JD000722`, 2002.

Walker, H., Stone, D., Ingham, T., Hackenberg, S., Cryer, D., Punjabi, S., Read, K., Lee, J., Whalley, L., Spracklen, D. V., et al.: Observations and modelling of glyoxal in the tropical Atlantic marine boundary layer, Atmospheric Chemistry and Physics, 22, 5535–5557, 2022.

Wallington, T. J., Seinfeld, J. H., and Barker, J. R.: 100 Years of progress in gas-phase atmospheric chemistry research, Meteorological Monographs, 59, 10–1, 2019.

Wang, M. and Fu, Q.: Stratosphere-Troposphere Exchange of Air Masses and Ozone Concentrations Based on Reanalyses and Observations, Journal of Geophysical Research: Atmospheres, 126, e2021JD035 159, 2021.

Wang, M., Shao, M., Chen, W., Yuan, B., Lu, S., Zhang, Q., Zeng, L., and Wang, Q.: Atmospheric nanoparticles formed from heterogeneous reactions of organics, Nature Geoscience, 3, 238–24, https://doi.org/10.1038/ngeo778, URL `https://www.nature.com/articles/ngeo778`, 2010.

Wang, S., Hornbrook, R. S., Hills, A., Emmons, L. K., Tilmes, S., Lamarque, J.-F., Jimenez, J. L., Campuzano-Jost, P., Nault, B. A., Crounse, J. D., et al.: Atmospheric acetaldehyde: Importance of air-sea exchange and a missing source in the remote troposphere, Geophysical research letters, 46, 5601–5613, 2019.

Warneke, C., Karl, T., Judmaier, H., Hansel, A., Jordan, A., Lindinger, W., and Crutzen, P. J.: Acetone, methanol, and other partially oxidized volatile organic emissions from dead plant matter by abiological processes: Significance for atmospheric HOx chemistry, Global Biogeochemical Cycles, 13, 9–17, 1999.

Warneke, C., Holzinger, R., Hansel, A., Jordan, A., Lindinger, W., Pöschl, U., Williams, J., Hoor, P., Fischer, H., Crutzen, P., Scheeren, H. A., and Lelieveld, J.: Isoprene and its oxidation products methyl vinyl ketone, methacrolein, and isoprene related peroxides measured online over the tropical rain forest of Surinam in March 1998, Journal of Atmospheric Chemistry, 38, 167–185, 2001.

Wei, P.-S., Chiu, H.-H., Hsieh, Y.-C., Yen, D.-L., Lee, C., Tsai, Y.-C., and Ting, T.-C.: Absorption coefficient of water vapor across atmospheric troposphere layer, Heliyon, 5, e01 145, 2019.

Wendisch, M., Pöschl, U., Andreae, M. O., Machado, L. A., Albrecht, R., Schlager, H., Rosenfeld, D., Martin, S. T., Abdelmonem, A., Afchine, A., et al.: ACRIDICON–CHUVA campaign: Studying tropical deep convective clouds and precipitation over Amazonia using the new German research aircraft HALO, Bulletin of the American Meteorological Society, 97, 1885–1908, 2016.

Wennberg, P., Hanisco, T., Jaegle, L., Jacob, D., Hintsa, E., Lanzendorf, E., Anderson, J., Gao, R.-S., Keim, E., Donnelly, S., et al.: Hydrogen radicals, nitrogen radicals, and the production of O3 in the upper troposphere, science, 279, 49–53, 1998.

Wennberg, P. O., Bates, K. H., Crounse, J. D., Dodson, L. G., McVay, R. C., Mertens, L. A., Nguyen, T. B., Praske, E., Schwantes, R. H., Smarte, M. D., et al.: Gas-phase reactions of isoprene and its major oxidation products, Chemical reviews, 118, 3337–3390, 2018.

Went, F. W.: Blue hazes in the atmosphere, Nature, 187, 641–643, 1960.

Werner, B., Stutz, J., Spolaor, M., Scalone, L., Raecke, R., Festa, J., Colosimo, S. F., Cheung, R., Tsai, C., Hossaini, R., et al.: Probing the subtropical lowermost stratosphere and the tropical upper troposphere and tropopause layer for inorganic bromine, Atmospheric Chemistry and Physics, 17, 1161–1186, 2017.

Williams, J.: Organic trace gases in the atmosphere: an overview, Environmental Chemistry, 1, 125–136, 2004.

Williamson, C. J., Kupc, A., Axisa, D., Bilsback, K. R., Bui, T., Campuzano-Jost, P., Dollner, M., Froyd, K. D., Hodshire, A. L., Jimenez, J. L., Kodros, J. K., Luo, G., Murphy, D. M., Nault, B. A., Ray, E. A., Weinzierl, B., Wilson, J. C., Yu, F., Yu, P., Pierce, J. R., and Brock, C. A.: A large source of cloud condensation nuclei from new particle formation in the tropics, Nature, 574, 399–403, 2019.

Wittrock, F., Richter, A., Oetjen, H., Burrows, J. P., Kanakidou, M., Myriokefalitakis, S., Volkamer, R., Beirle, S., Platt, U., and Wagner, T.: Simultaneous global observations of glyoxal and formaldehyde from space, Geophysical Research Letters, 33, 2006.

Wolfe, G., Kaiser, J., Hanisco, T., Keutsch, F., De Gouw, J., Gilman, J., Graus, M., Hatch, C., Holloway, J., Horowitz, L., et al.: Formaldehyde production from isoprene oxidation across NO x regimes, Atmospheric chemistry and physics, 16, 2597–2610, 2016.

Xiao, Y., Jacob, D. J., and Turquety, S.: Atmospheric acetylene and its relationship with CO as an indicator of air mass age, Journal of Geophysical Research: Atmospheres, 112, 2007.

Yang, X., Yuan, B., Peng, Z., Peng, Y., Wu, C., Yang, S., Li, J., and Shao, M.: Inter-comparisons of VOC oxidation mechanisms based on box model: A focus on OH reactivity, Journal of Environmental Sciences, 114, 286–296, 2022.

Young, P., Archibald, A., Bowman, K., Lamarque, J.-F., Naik, V., Stevenson, D., Tilmes, S., Voulgarakis, A., Wild, O., Bergmann, D., et al.: Pre-industrial to end 21st century projections of tropospheric ozone from the Atmospheric Chemistry and Climate Model Intercomparison Project (ACCMIP), Atmospheric Chemistry and Physics, 13, 2063–2090, 2013.

Zare, A., Christensen, J., Gross, A., Irannejad, P., Glasius, M., and Brandt, J.: Quantifying the contributions of natural emissions to ozone and total fine PM concentrations in the Northern Hemisphere, Atmospheric Chemistry and Physics, 14, 2735–2756, 2014.

Zarzana, K. J., Min, K.-E., Washenfelder, R. A., Kaiser, J., Krawiec-Thayer, M., Peischl, J., Neuman, J. A., Nowak, J. B., Wagner, N. L., Dubè, W. P., et al.: Emissions of glyoxal and other carbonyl compounds from agricultural biomass burning plumes sampled by aircraft, Environmental science & technology, 51, 11 761–11 770, 2017.

Zarzana, K. J., Selimovic, V., Koss, A. R., Sekimoto, K., Coggon, M. M., Yuan, B., Dubé, W. P., Yokelson, R. J., Warneke, C., De Gouw, J. A., et al.: Primary emissions of glyoxal and methylglyoxal from laboratory measurements of open biomass burning, Atmospheric Chemistry and Physics, 18, 15 451–15 470, 2018.

Zhang, R., Gen, M., Fu, T.-M., and Chan, C. K.: Production of formate via oxidation of glyoxal promoted by particulate nitrate photolysis, Environmental Science & Technology, 55, 5711–5720, 2021.

Zhao, J., Levitt, N. P., Zhang, R., and Chen, J.: Heterogeneous reactions of methylglyoxal in acidic media: Implications for secondary organic aerosol formation, Environmental science & technology, 40, 7682–7687, 2006.

Zhou, S., Gonzalez, L., Leithead, A., Finewax, Z., Thalman, R., Vlasenko, A., Vagle, S., Miller, L., Li, S.-M., Bureekul, S., et al.: Formation of gas-phase carbonyls from heterogeneous oxidation of polyunsaturated fatty acids at the air–water interface and of the sea surface microlayer, Atmospheric Chemistry and Physics, 14, 1371–1384, 2014.

Zhou, X. and Mopper, K.: Apparent partition coefficients of 15 carbonyl compounds between air and seawater and between air and freshwater; implications for air-sea exchange, Environmental science & technology, 24, 1864–1869, 1990.

Zhu, J., Penner, J. E., Yu, F., Sillman, S., Andreae, M. O., and Coe, H.: Decrease in radiative forcing by organic aerosol nucleation, climate, and land use change, Nature communications, 10, 1–7, 2019a.

Zhu, L., Kellis, D., and Ding, C.-F.: Photolysis of glyoxal at 193, 248, 308 and 351 nm, Chemical physics letters, 257, 487–491, 1996.

Zhu, S., Mac Kinnon, M., Shaffer, B. P., Samuelsen, G., Brouwer, J., and Dabdub, D.: An uncertainty for clean air: Air quality modeling implications of underestimating VOC emissions in urban inventories, Atmospheric Environment, 211, 256–267, 2019b.

Zhu, Y. and Kieber, D. J.: Concentrations and photochemistry of acetaldehyde, glyoxal, and methylglyoxal in the Northwest Atlantic Ocean, Environmental science & technology, 53, 9512–9521, 2019.

Zhu, Y. and Kieber, D. J.: Global model for depth-dependent carbonyl photochemical production rates in seawater, Global Biogeochemical Cycles, 34, e2019GB006 431, 2020.